Energy Level Engineering in Colloidal Quantum Dot Solar Cells

by

Patrick Richard Brown

Submitted to the Department of Physics
in partial fulfillment of the requirements for the degree of

Doctor of Philosophy

at the

MASSACHUSETTS INSTITUTE OF TECHNOLOGY

June 2016

Author .....
Department of Physics
April 27, 2016

Certified by .....
Vladimir Bulović
Professor of Electrical Engineering and Computer Science
Thesis Supervisor

Certified by .....
Pablo Jarillo-Herrero
Professor of Physics
Thesis Supervisor

Accepted by .....
Nergis Mavalvala
Associate Department Head for Education

Energy Level Engineering in Colloidal Quantum Dot Solar Cells

by

Patrick Richard Brown

Submitted to the Department of Physics
on April 27, 2016, in partial fulfillment of the
requirements for the degree of
Doctor of Philosophy

Abstract

Lead sulfide colloidal quantum dots (PbS QDs) possess a uniquely tunable set of electronic properties that has generated considerable interest in their use as active materials in lightweight, flexible, solution-processed photovoltaics. The bandgap of PbS QDs can be tuned across the entire range relevant for solar cells through modification of the QD size, and a range of other QD electronic properties can be modified through control of the chemical ligands bound to the QD surface. In this thesis we demonstrate how control of the energy level profile within PbS QD solar cells can be used to understand and improve their operation.

First, we demonstrate that improvements in power conversion efficiency may be attained for ZnO / PbS QD heterojunction photovoltaics through the incorporation of a MoO_3 interlayer between the PbS QD film and the top-contact anode. The deep-work-function MoO_3 layer mitigates a Schottky junction that would otherwise form at the PbS / anode interface, resulting in performance improvements for devices employing a range of different anode materials.

Then, we demonstrate how the tunable bandgap of PbS QDs can be used to elucidate charge- and exciton-transfer processes within hybrid organic / QD photovoltaic devices that demonstrate singlet exciton fission. We find that PbS QDs can accept electrons from triplets generated by singlet fission in pentacene and act as low-bandgap light absorbers complementary to the singlet fission material, and we explore the dependence of the triplet dissociation process on the energy levels of the QDs.

Finally, we show that the energy levels of lead sulfide QDs, measured by ultraviolet photoelectron spectroscopy, shift by up to 0.9 eV between different chemical ligand treatments. The directions of these energy shifts match the results of density functional theory calculations and scale with the ligand dipole moment, and trends in the performance of photovoltaic devices employing ligand-modified QD films are consistent with the measured energy level shifts.

These studies identify energy level shifts resulting from interface modification, QD bandgap modification through size control, and ligand-induced surface dipoles as means of predictably controlling the electronic properties of colloidal QD films and as

versatile adjustable parameters in the performance optimization of QD optoelectronic devices.

Thesis Supervisor: Vladimir Bulović
Title: Professor of Electrical Engineering and Computer Science

Thesis Supervisor: Pablo Jarillo-Herrero
Title: Professor of Physics

Acknowledgments

It is a great pleasure to be able to thank the many people who have contributed so positively to my time in graduate school.

I am enormously indebted to my research advisor, Vladimir Bulović. I have tremendous appreciation for the freedom Vladimir has given me throughout my PhD, both within and outside the lab, to pursue the projects that I found most meaningful and interesting. Vladimir's enthusiasm, creativity, and energy seem to know no bounds, and I always wanted to be ready to answer his perennial hallway question of "Hey, what's cookin'?" with an interesting new result that would get an "Oh, that is so cool." Vladimir's healthy skepticism and attention to detail made me a better scientist, and he made the whole process more fun than I had imagined grad school could be.

I would also like to thank the rest of my thesis committee—Pablo Jarillo-Herrero, Isaac Chuang, Bob Jaffe, and Marc Kastner—for their insightful questions and guidance. I'd particularly like to thank Pablo for believing in me and convincing me that the MIT condensed matter physics department could make a great home for me throughout my graduate studies.

I've been incredibly privileged to be able to benefit from close interactions with a number of other professors during my time at MIT. Moungi Bawendi has been a deep source of knowledge and experience on everything related to quantum dots, and I've greatly appreciated the opportunity to work closely with his group. Marc Baldo was very generous with the use of his UPS system, without which the second half of my PhD and some of my most interesting results would not have been possible. Marc's attention to detail and strong level of engagement in our collaborative projects have also been incredibly helpful. Jeff Grossman demonstrated an enthusiasm for our quantum dot work that rivaled Vladimir's, and it's been a great experience working closely with his group. Jessika Trancik gave me the opportunity to become involved in a rewarding project that tied together many of my diverse interests, and I've learned a great deal from our interactions.

I would like to express my enormous gratitude for all of my mentors and friends within the Organic and Nanostructured Electronics lab. Alexi Arango taught me how solar cells work and how to keep the lab operational. Ni Zhao and Richard Lunt took over where Alexi left off, and greatly expanded my understanding of organic optoelectronics. I'm grateful to Richard for pushing me to succeed in research and making me a better writer, instilling in me an appreciation for concision and precision. Trisha Andrew added greatly to our group with her deep knowledge of chemistry,

easy laughter, and healthy skepticism. Tim Osedach seemed to have the answer to any lab-related question beyond my knowledge, and always contributed unexpected insights and perspectives to our conversations. Geoffrey Supran has been my partner in crime since we both joined ONElab in the fall of 2009. I still remember running into Geoffrey in lab late at night during our first year, each asking what the other was doing there—and doing the same thing a few years later in the Google docs of Fossil Free MIT. Geoffrey's inspiring dedication and commitment have always pushed me to excel. Joel Jean—who I could thank in about five different places in these Acknowledgments—has been my closest partner in every part of my graduate school experience, from labwork and the Solar Study to Fossil Free MIT and the INDC project, and from our shared office to our house. Joel always seems to be a step ahead of me, and his organization, critical thinking, and friendship are a continual inspiration.

I'd like to thank everyone who I've had the privilege to call labmates—Gleb, Yasu, Liz, Kathy, Kathy, Apoorva, Wendi, Farnaz, Eletha, Katherine, Melany, Mengfei, Tony, Tom, Parag, Jill, Sarah, Annie, Jonas, Josué, Andrea, Ko, Sam, Garrett, Petar, Antonio, Giovanni, Rich, Anna, Maddalena, Will, Corinne, Sulinya, Mandy, Christina, Costi, Vanessa, and others, whose deep thinking, openness to collaboration, and willingness to drop everything to help keep the lab running (including at midnight when we suddenly discover the lab under an inch of water) has made ONElab such a great place to work. Joel and Apoorva are great officemates, and are always ready to roll out some fun when we need a break from the blizzard of experiments, or to dive into the countless interesting physics questions that come up in everyday lab-life. And of course, I'm happy to thank our amazing administrative assistants, Monica Pegis and Sam Farrell, who keep the trains running on time, the gloveboxes running on liquid nitrogen, and the evaporators running on molybdenum oxide.

In addition to the members of ONElab, I've also had the great privilege to work with a number of excellent collaborators at MIT. Donghun Kim and Priya Jadhav were central to two of my projects, and major parts of this thesis would have been missing without them. Our complementary work together felt like the perfect collaboration, and our projects were more than the sum of their parts. It's been a great pleasure to watch Donghun turn what might otherwise have been hand-waving explanations into precise atomistic calculations and shed more light on the often confusing world of quantum dots.

The Bawendi group has often felt like my lab away from lab, and I've learned a great amount from my collaborators there. It's been a pleasure throughout my PhD to

talk science with Darcy Grinolds. Darcy is a wonderful listener, and her keen ability to ask insightful questions, coupled with her expertise in both the chemistry of quantum dots and the physics of semiconductor devices, has often reminded me how exciting science can be. My other collaborators in the Bawendi lab—Chia-Hao, Jenn, Dave, Brian, Liang-Yi, Scott, Dan, Russ, and many others—have taught me much of what I know about quantum dot chemistry, and have always made me feel welcome. The whole quantum dot solar cell team, spanning the Bulović, Bawendi, Grossman, and Gradečak groups, has been great to interact with and share questions and ideas with. Our collaborators within ONElab—Matt, Noemie, Hyesung, Sehoon, Dave, Nick, and many others—have also greatly enriched my experience and expanded my knowledge. Matt Klug is one of the most appreciative collaborators I've had the pleasure to work with. Gökşin Kavlak and Magdalena Klemun were also very supportive and fun to work with throughout the INDC project. I'm also happy to thank the Solar Study team members, who taught me much of what I know about solar power beyond the physics of photovoltaics. My experience as part of the Solar Study forced me to reexamine many of my own preconceptions and reinforce my reasoning, and made me a better scientist and advocate in the process.

In addition to all of my wonderful colleagues at MIT, I am enormously indebted to my professors and mentors during my undergraduate studies at Notre Dame. Chief among these is my undergraduate research advisor, Prashant Kamat, who first got me hooked on research, taught me to pipette and write scientific papers, and advocated for me at every opportunity. Prashant is an incredible undergraduate mentor who puts his students and their futures first. I also thank the prevous members of the Kamat group, particularly Kevin Tvrdy, Kensuke Takechi, and Ryan Muszynski, as well as Prof. Ken Kuno, for helping guide my first forays into research. I was privileged to have a series of outstanding professors at Notre Dame, including Chris Kolda, Seth Brown, Umesh Garg, Rich Taylor, Marya Lieberman, Bruce Bunker, Doug Miller, and Dennis Jacobs, among many others, who inspired me through their teaching and got me hooked on chemistry and physics—and were completely understanding and encouraging when I couldn't choose between the two. And I'd like to thank Scott Johnson, my high school astronomy teacher, who first taught me how cool science can be.

And of course, I have to thank the many people who have enriched my life outside the lab. I'm particularly happy to thank my friends and comrades in Fossil Free MIT—Jeremy, Ioana, Ben, Daniel, Tse Yang, Becky, Josué, Jordan, Raphael, Rachel, Dalia, Shirin, Pri, Maggie, Elisa, Stephanie, Ben, Jennifer, Geoffrey, Joel, Alison, Michael,

Britta, Siva, Ploy, Nina, Sam, Matt, Tatjana, Jane, Eirik, and everyone else who has put so much time and effort into pushing for climate leadership at MIT. This amazing group continues to inspire me, and I can't wait to see what more comes out of this committed, passionate, and thoughtful collection of leaders in the future. I also have to thank the whole Boston climate crew—Marla, Farhad, Craig, Shea, Ben, Alli, Dorian, Devyn, Emily, Ben, Rachel, Nathan, Adam, Mark, Peter, Greg, Vanessa, Sophie, Vanessa, Jay, Ken, Tim, Eli, Eli, Rohan, Lisa, John, Rachel, Murtaza, Collin, Will, Varshini, Nathan, Malcolm, Joshua, Jeff, and many others, who give me such hope for the future.

I thank my roommates—Jordan, Matthew, An Son, Jo, Joel, and Jenn—who helped keep me sane, whether through board games, excellent food, deep conversation, or all three at once. I'm particularly grateful to Jordan Chesin, who adopted me into his wide circle of friends, always finds the fun parts of life, and helped make sure I was doing more than work. And I thank my friends from Notre Dame and NREL, especially Dominic, Mark, Thomas, Chris, Jimmy, Ben, Packy, Keaton, Andrew, Brennan, Ryan, James, Michael, Jennie, Ashley, Ben, Michael, Doug, and Heena, who have continued to be there for me throughout grad school and who remind me that I always have a home back at the dome or up in the mountains.

My deep gratitude goes to Alison Takemura, whose joy, peace, and compassion have enriched my life, and whose level-headedness and support have helped me through some of my toughest moments. And my deepest thanks go to my family, John, Dianne, and Claire Brown, who have taught me so much, and whose unconditional support has always kept me going.

I also gratefully acknowledge my funding sources: the Fannie and John Hertz Foundation, which supported me throughout five years of my graduate studies; the National Science Foundation, which supported me with a Graduate Research Fellowship; and the Department of Energy Solar America Program and Samsung Advanced Institute of Technology, which supported the quantum dot work in our group.

Contents

List of Figures

List of Tables

Chapter 1

Introduction

Portions of this chapter are adapted with permission from MIT Energy Initiative, "Chapter 6 – PV Scaling and Materials Use," in *The Future of Solar Energy*, [31] copyright 2015 Massachusetts Institute of Technology; with permission from Trancik, J. E.; Brown, P. R.; Jean, J.; Kavlak, G.; Klemun, M. *Technology improvement and emissions reductions as mutually reinforcing efforts: Observations from the global development of solar and wind energy*, **2015**; [13] and from Ref. [64] with permission from The Royal Society of Chemistry.

1.1 Motivation

1.1.1 Climate change

The magnitude and urgency of the crisis of anthropogenic climate change are difficult to overstate, yet can also be difficult to fully grasp. Excellent reviews of the science of anthropogenic climate change, [95] the current and projected impact of climate change on human well being, [96, 97] and climate change mitigation pathways [5] are available elsewhere; we do not seek to provide a deep review of the issue here, but simply to provide an idea of the magnitude and urgency of the threat and the necessary response.

Figure 1-1 shows a reconstruction of the global surface temperature of the

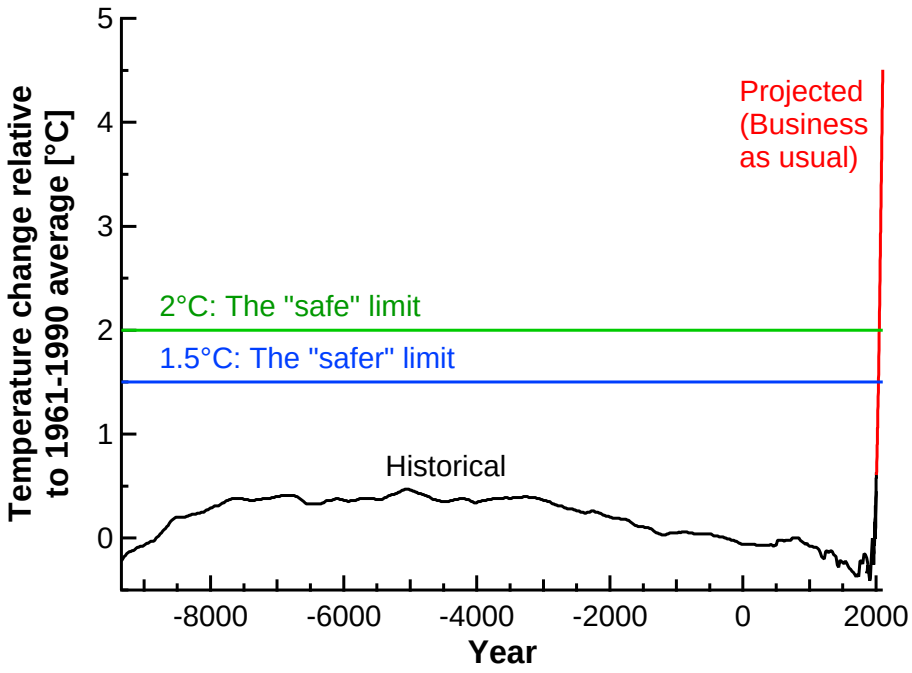

Figure 1-1: **Global surface temperature throughout human civilization.** Historical data (black) are from Marcott et al. and IPCC AR5 WGI. [1, 2] Projected data (red) are from IPCC AR5 WGI. [2] Format inspired by Romm. [3]

earth over the past 11 300 yr (black curve)—roughly the amount of time since the development of agriculture, commonly referred to as the beginning of human civilization. [1] Global average temperature throughout the history of human civilization has been remarkably stable, staying within ±0.5 °C of the 1961–1990 average. The rate of change of temperature has also been low—at least until around the year 1950, when anthropogenic climate change started to become observable. Figure 1-1 also shows the projected temperature rise through the year 2100 under "business as usual" conditions, which roughly correspond to a situation in which the rate of annual anthropogenic carbon emissions undergoes continued growth at historical rates before leveling off around the year 2100 at a level ∼2.4 times higher than today (see **Figure 1-2**). [i] [2]

[i] The concept of "business as usual" is admittedly vague from a system dynamics standpoint, as it excludes the stabilizing feedbacks (the detrimental impact of climate change and global instability on GDP and population growth, or the effects of a mobilization to mitigate climate change spurred by its increasingly observable effects) that would tend to force emissions growth downwards over time. In a sense, when the boundaries of a system are large enough, the future will always be "business as usual". The scenario which we here label "business as usual" follows the usual convention and refers to the RCP8.5 scenario considered in IPCC AR5 (>1000 ppm CO_2(eq) atmospheric concentration in 2100, with a total radiative forcing of +8.5 W m^{-2}). [95]

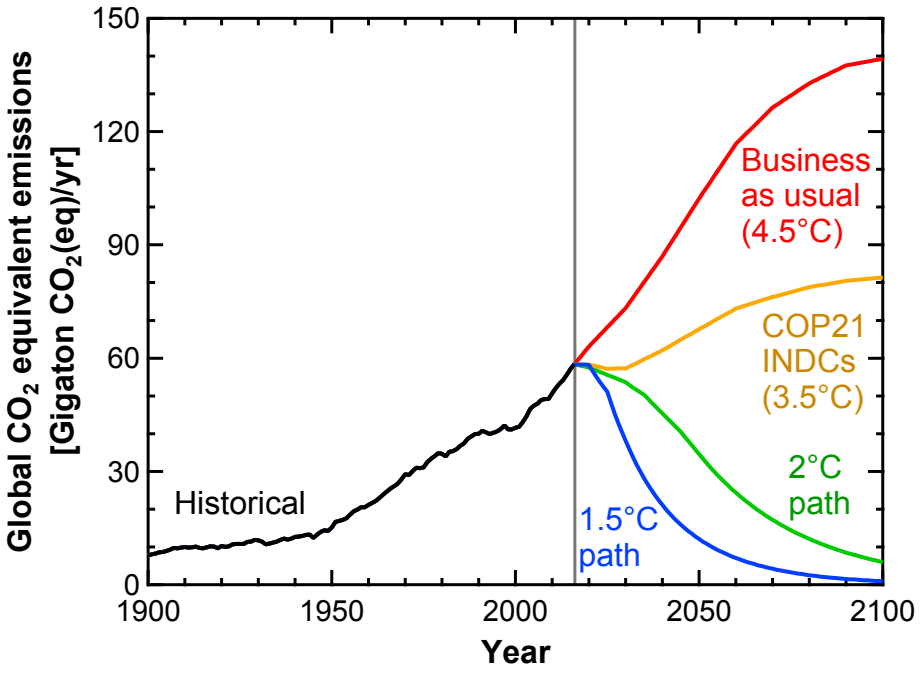

Figure 1-2: **Historical and projected CO_2 emissions.** Data are from Climate Interactive. [4, 5] "COP21 INDCs" refers to a future scenario where the Intended Nationally Determined Contributions stated by member countries at the COP21 conference are met without any further emissions cuts.

Such conditions are projected to lead to global temperatures roughly 4.5 °C higher than preindustrial conditions. Both the temperature and rate of temperature change that are projected under business as usual—as well as the positions of coastlines, the frequency and severity of major storms, the regional levels of rainfall and boundaries of agricultural and habitable zones—are well outside the values seen throughout the history of human civilization. [96, 97]

The future projected by climate models under business as usual conditions is not written in stone, of course. The international agreement reached in Paris in November 2015 at the 21st meeting of the Conference of the Parties to the U.N. Framework Convention on Climate Change (COP21) aims to hold "the increase in global average temperature to well below 2 °C above pre-industrial levels and to pursue efforts to limit the temperature increase to 1.5 °C above pre-industrial levels". [98] What would it take to limit global temperature rise to these levels? Excess carbon dioxide is removed from the atmosphere by natural processes on multiple timescales, but a

significant fraction—ranging from 20–60 % in different models—of anthropogenic CO_2 emissions will persist in the atmosphere for hundreds or thousands of years. [99, 100] As such, stabilization at any temperature target on a human timescale ultimately requires net anthropogenic carbon emissions to fall to zero. **Figure 1-2** gives an idea of the rate of emissions reduction that is required to achieve different temperature targets. To stabilize global temperatures at 2 °C, annual emissions must *fall* at roughly the same rate at which they have *risen* throughout the industrial era—while the population continues to grow and standards of living continue to improve. Stabilizing temperatures at 1.5 °C would require an even faster drop in emissions, with many models requiring net negative anthropogenic carbon emissions before the end of this century. Maintaining a reasonable (even 50 %) chance of keeping global temperature rise below 2 °C will require leaving the majority of the world's fossil fuel reserves unburned. [101, 102, 103]

1.1.2 Why solar?

Multiple factors conspire to make solar energy one of the few primary energy sources suitable for large-scale use in a carbon-constrained world. Solar photovoltaics (PV) has a particularly low lifecycle carbon emission intensity, [5, 104] a critical requirement given the necessary rate of decarbonization noted in Section 1.1.1. And as discussed in Chapter 2, the solar resource is immense; the technical potential of solar power generation dwarfs that of all other terrestrial energy sources.

At the same time, solar power currently generates only ∼1 % of the world's electricity, and as shown in **Figure 1-3**, it is currently one of the more expensive means for generating electricity. Yet these snapshots of the current capacity and cost of solar PV do not capture the incredible rate of change that these metrics have demonstrated over the past decades and continue to demonstrate today. **Figure 1-4** shows the evolution of the price of PV modules and the cost of PV-generated electricity over time. The price of solar modules has fallen by more than a factor of 100 since the late 1970's, and global cumulative PV capacity has grown from ∼1 GW_p in 2000 to over 227 GW_p today, with 50 GW_p added in 2015 alone. [105] Taken together, the

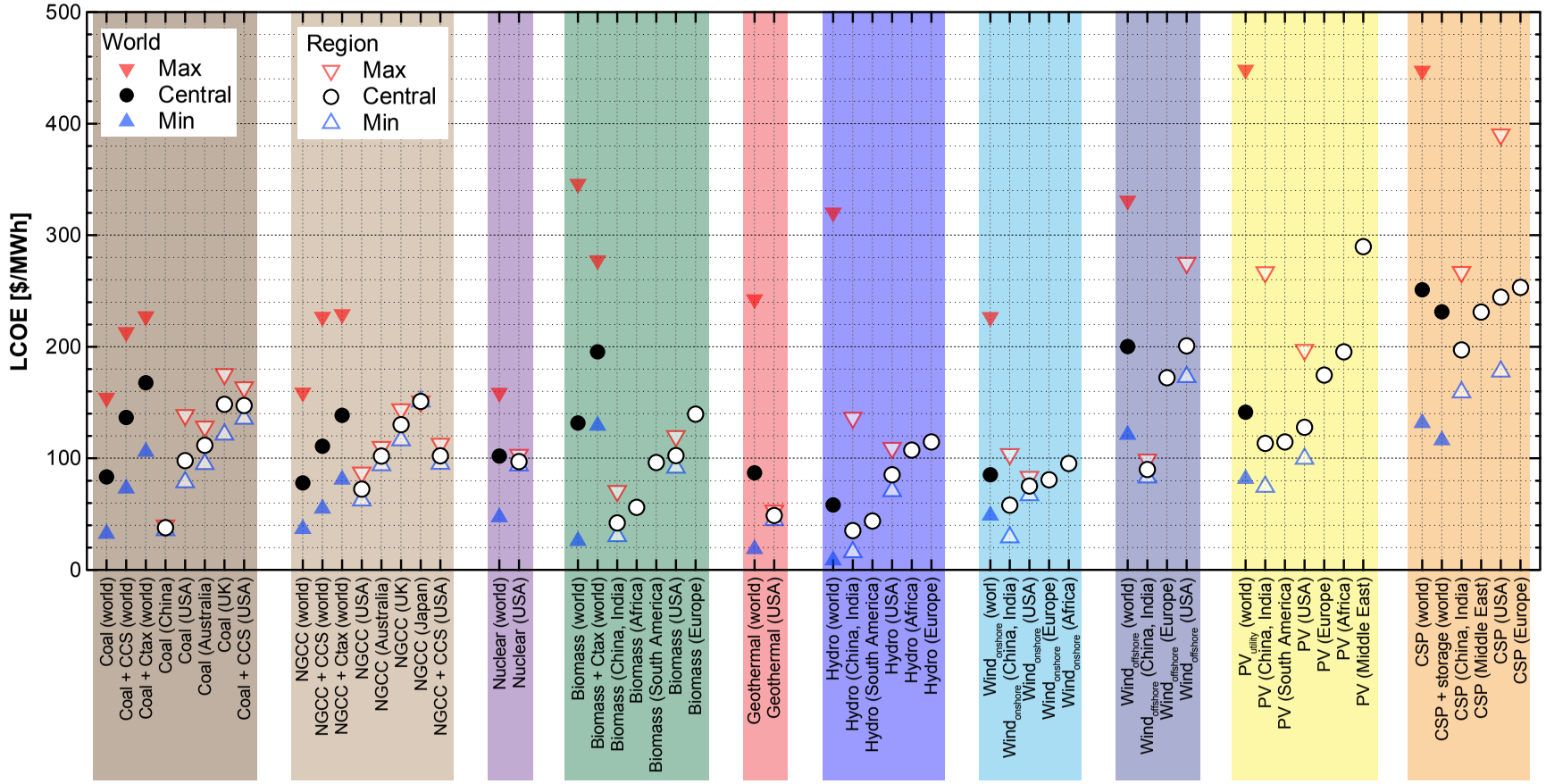

Figure 1-3: **Levelized cost of energy (LCOE) of different energy generation technologies.** Global (filled symbols) and regional (empty symbols) average LCOE in $/MWh (2014 U.S. dollars) for different energy generation technologies. Black and white symbols represent central values for 2012–2014, red triangles represent maxima, and blue triangles represent minima. Data are average values taken, where available, from IPCC AR5 WGIII, IRENA 2015, EIA 2015, and World Energy Council 2013. [5, 6, 7, 8] "Ctax" refers to a carbon price of $100/ton CO_2, and is taken from IPCC AR5 WGIII. [5]

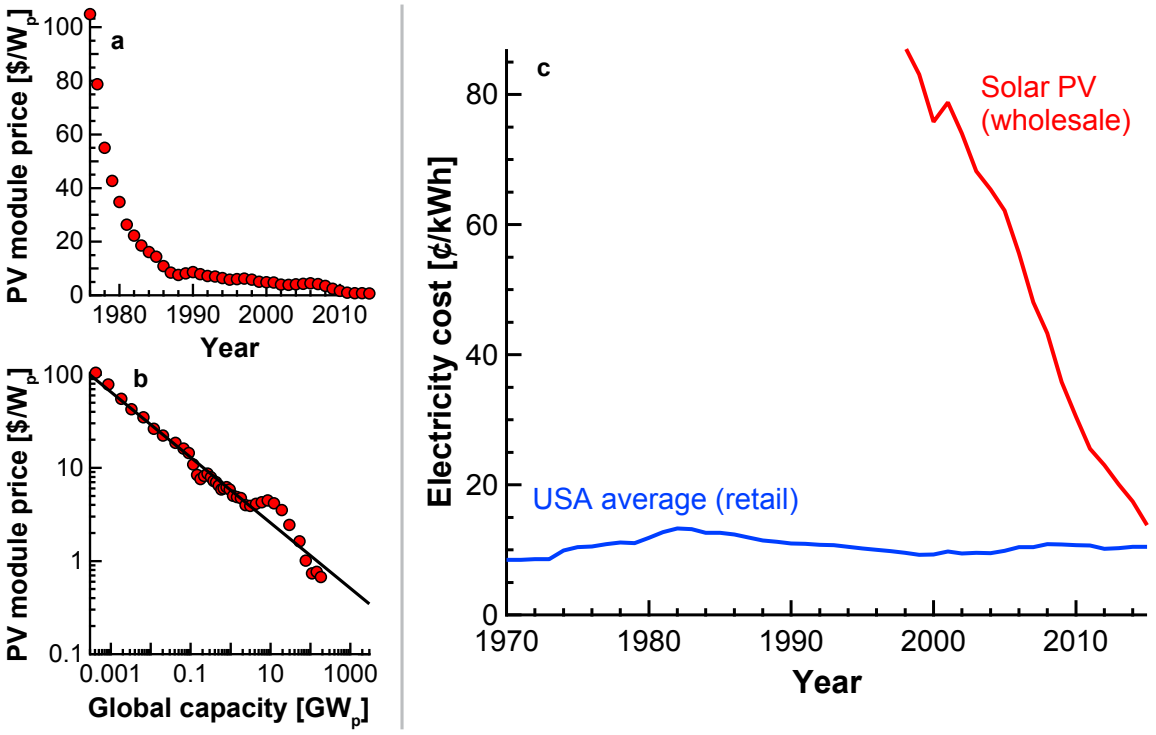

Figure 1-4: **a**,**b**, Global average PV module price in $\$/W_{DC}$ (2014 U.S. dollars) plotted over time (**a**) and against cumulative installed PV capacity (**b**). [9] The trend line in **b** is fit according to the equation $Price(t) = Price(t_0)Capacity^{-w}$ and indicates a learning rate of 21.6 %. **c**, U.S. levelized cost of PV electricity (wholesale) over time compared to U.S. grid electricity (retail). Solar LCOE data are from LBNL [10, 11] and MIT [12, 13]; residential electricity price data are from EIA. [14] Note that the retail electricity price includes both the wholesale price of electricity and the price of transmission and distribution, which contribute in roughly equal measure to the total price, so the wholesale cost of PV electricity would have to fall well below the retail price of electricity in order for PV to displace conventional generation on a cost basis alone. LCOE is in general an imperfect metric for comparing intermittent solar generation with other dispatchable technologies (a point explored in detail elsewhere [12]), particularly at high solar penetration levels, though it provides a general sense of economic competitiveness at today's relatively low level of solar penetration.

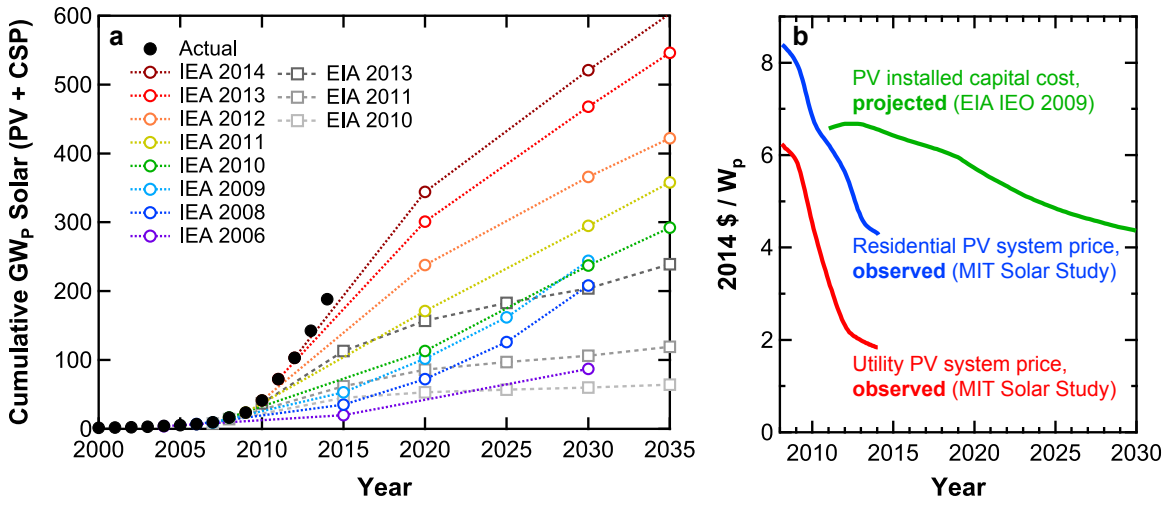

Figure 1-5: **Solar capacity growth and costs compared to projections. a**, International Energy Agency (IEA) and Energy Information Administration (EIA) projections for cumulative photovoltaic (PV) and concentrated solar power (CSP) installed capacity are represented by empty colored circles and squares; actual historical data for cumulative PV and CSP installed capacity are represented by filled black circles. Dotted lines are given as guides to the eye. Projections are from the IEA *World Energy Outlook* reports over the period from 2006 to 2014 [15, 16, 17, 18, 19, 20, 21, 22] and the EIA *International Energy Outlook* reports over the period from 2010 to 2013; [23, 24, 25] actual data from cumulative PV capacity are from EPIA [26] and IHS, Inc.; [27] actual data for cumulative CSP capacity are from REN21. [28] **b**, Observed PV system price (red and blue curves) from MIT [12] compared to projected PV capital cost from EIA [29] (red curve), given in 2014 US dollars per peak watt.

exponential growth of PV deployment and exponential decline in PV price indicate a learning rate of 21.6 %, meaning that price decreases by 21.6 % for every doubling in cumulative deployment; this learning rate is significantly higher than that observed for other energy generation technologies (particularly nuclear, which has demonstrated a negative learning rate in recent years due to rising planning and financing costs). [106, 107]

In the face of these rapid changes, the global expansion in the deployment of solar power has consistently outstripped projections. **Figure 1-5** shows a series of "reference scenario" projections from the International Energy Agency's (IEA's) World Energy Outlook reports for the worldwide cumulative electric generation capacity of solar power alongside actual historical capacity. [15, 16, 17, 18, 19, 20, 21, 22] IEA projections have been continuously revised upward to capture solar growth: the

2006 WEO projection for cumulative solar capacity in 2030 was surpassed in 2012 and the 2011 WEO projection for 2020 was surpassed in 2014. While the "reference scenario" projections do not capture the effect of the significant deployment policies that have driven wind and solar adoption, even the IEA's "New Policies" and "450 ppm" scenarios have had to be consistently revised upward to account for the previously unexpected growth in deployment of this technology. Projections from the U.S. Energy Information Administration (EIA) have been similarly low; the EIA's International Energy Outlook 2013 projection for cumulative solar capacity in 2025 was surpassed the year after the release of the report, in 2014. [23, 24, 25] The cost of PV installations has also fallen much more rapidly than projected. In 2014, prices for residential PV systems reached the level projected for installed PV capital costs in 2030 according to EIA's 2009 International Energy Outlook report, and utility PV system prices have fallen even faster. [29]

1.1.3 Why thin film?

The majority of photovoltaics installed today—over 90 % of the PV market—are based on crystalline silicon solar cells. Silicon solar cells are highly efficient, [53] are stable for more than 25 years, and are fabricated from earth-abundant materials (silicon is the second-most abundant element in the earth's crust). The rapid reduction in PV module costs noted in Section 1.1.2 has resulted from steady improvements in the manufacturing process for silicon solar cells, and has significant room for continuation before fundamental commodity cost floors are reached.

Yet while module costs have dropped precipitously and are expected to continue to drop, the solar module itself is no longer the largest cost component in a PV system. The "balance of system" (BOS)—everything from the wiring and racking to installation labor, permitting, and planning—accounts for roughly 65 % of the system price for utility-scale PV systems and 85 % of the system price for residential-scale systems. [12] The BOS cost—specifically the installation cost—is inherently tied to the form factor of the solar module. Silicon, as an indirect bandgap material, requires relatively thick wafers in order to absorb sufficient sunlight to reach its optimum efficiency. Such thick,

crystalline wafers are relatively brittle, and require the use of rigid, glass-encapsulated modules for protection. Economies of scale can be achieved by increasing the module size, but are limited by the size and weight that can be safely carried on a rooftop (for residential systems) or by the constraints of racking and mounting hardware sufficient to withstand wind loads corresponding to the highest-wind conditions expected in the location of installation throughout the >25 yr life of the system (for ground-mount utility-scale systems). Rigid glass modules can also lead to difficulties in transport for the construction of rural off-grid systems.

Thin film photovoltaic technologies could provide an alternative module form factor to the rigid glass modules required for silicon solar cells. Thin film technologies employing low-temperature manufacturing processes can be deposited on thin, flexible, lightweight substrates—thin enough to be wrapped around a human hair, [108] or floated on a soap bubble [109]—enabling a reimagining of the ways in which solar PV could be deployed. Modules with this form factor have the potential to access a lower regime of BOS and system costs than traditional silicon modules through high-throughput manufacturing, transportation, and installation processes—only, of course, if current limitations in efficiency, lifetime, and manufacturability can be addressed.

1.1.4 Why quantum dots?

Commercial thin film PV technologies primarily include cadmium telluride (CdTe) and copper indium gallium diselenide (CIGS) (and, to a smaller extent, amorphous silicon). CdTe competes with silicon solar cells at utility scale on cost today, and CIGS solar cells can be manufactured on thin, lightweight, flexible substrates. But at the terawatt scale—the scale that PV installation must reach in order to have a meaningful impact in addressing climate change—both of these technologies could encounter serious problems with resource scarcity.

Figure 1-6.a shows the extra time that would be needed between 2014 and 2050, at 2012 rates of production, for sufficient amounts of critical elements for different solar cell technologies to be produced in order to manufacture enough PV modules to

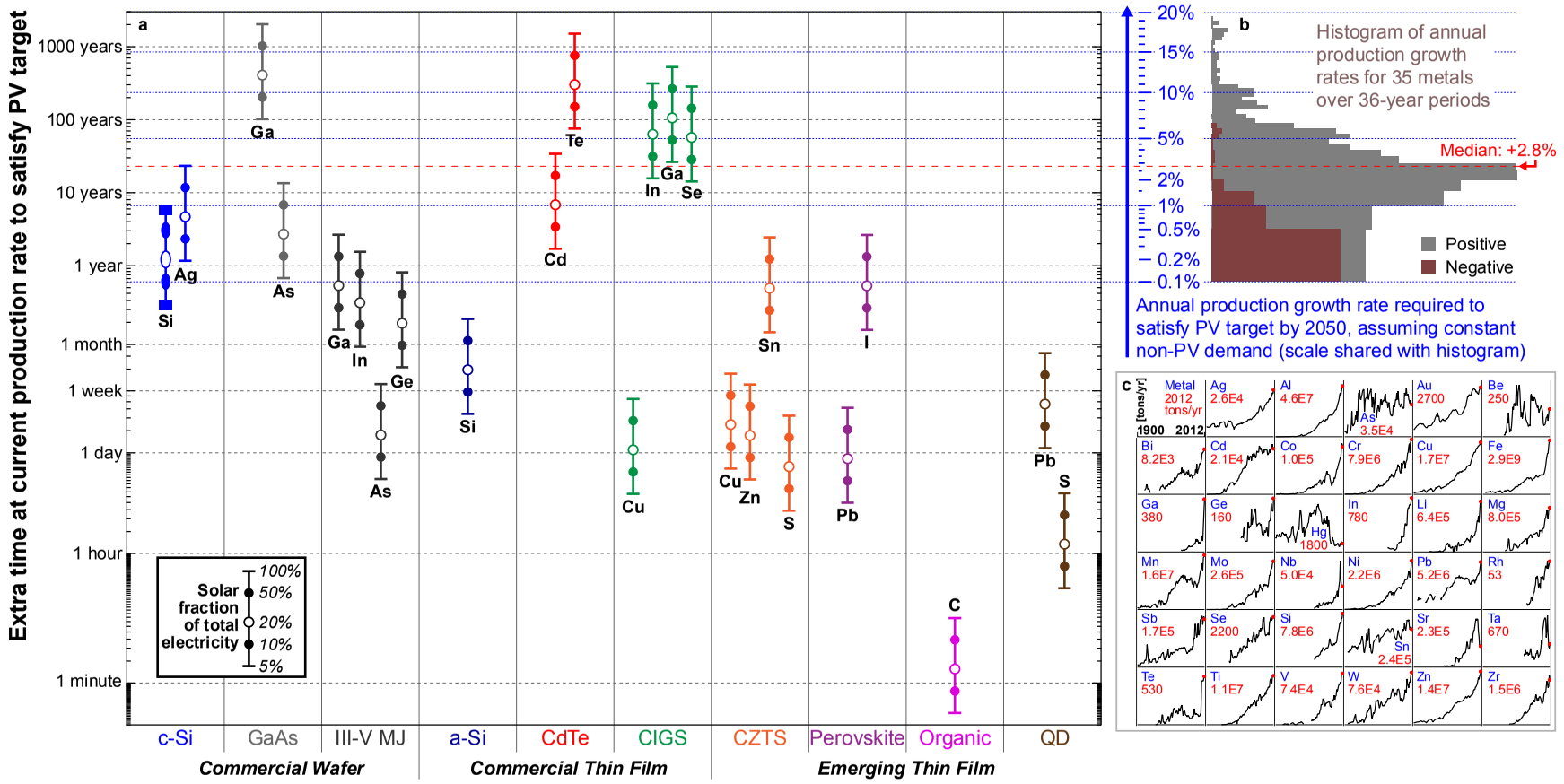

Figure 1-6: **Materials growth requirements for different PV technologies.** **a**, Time needed to produce sufficient amounts of critical elements for different PV technologies to satisfy 5–100 % of global electricity demand in 2050 from solar PV. Projected electricity demand is for a 2 °C scenario from IEA; [30] 100 % solar fraction of total electricity corresponds to 25 TW_{peak} of installed PV capacity. Material intensities are calculated for record-efficiency devices and standard layer thicknesses reported in the literature. [31] Joel Jean assisted with data collection and analysis for this figure. **b**, Histogram of annual production growth rates for 35 different metals over overlapping 36-year periods between 1900 and 2012 (for ranges where uninterrupted datasets are available). The median annual growth rate across all metals and periods is 2.8 %, marked by a red dotted line. The stretched y-axis and horizontal grid lines of panel **b** are scaled to match the logarithmic y-axis of panel **a**. **c**, Annual production data for the period 1900–2012 in tons/year for 35 different metals, used to produce the histogram in **b**. [32, 33] 2012 production levels for the different metals, which are used to generate the data shown in panel **a**, are listed in red and denoted by red dots. Note that the y-axis scale varies between subplots. [31]

satisfy 5–100 % of projected worldwide electricity demand in 2050 from solar PV.[ii] [31]

Stark differences can be seen between the different technologies. 1400 years of production at 2012 rates would be required to produce enough tellurium to meet 100 % of 2050 electricity demand with CdTe PV, while only 6 years of production would be required to produce enough silicon to meet the same target with crystalline silicon PV. The same target could be met with 23 days of lead production and 7 hours of sulfur production for lead sulfide quantum dot (PbS QD) solar cells, even at today's efficiency.

While PbS QD solar cells are not manufactured commercially today, PbS QDs demonstrate a number of properties beyond the high elemental abundance of their precursors that make them an attractive choice for further development. PbS QDs are fabricated via solution-phase chemical synthesis and can be deposited using a variety of scalable methods, including spray coating and dip coating. [111, 112, 113] Their room-temperature deposition makes them compatible with a variety of flexible plastic substrates, [114] and PbS QD photovoltaics are stable in air over hundreds to thousands of hours. [115, 69] Certified efficiencies of PbS QD solar cells have reached 10.6 %. [116, 53]

Yet perhaps more than any other metric, PbS QDs are distinguished from other solar cell materials by our ability to engineer their electronic properties through relatively simple chemical modifications. The bandgap of PbS QDs can be tuned over a range of more than 1.5 eV simply by changing the size of the QD cores, [74, 75] and the carrier mobility, density of states, and energy level positions of QD thin

[ii] Note that this "extra" production time would need to be added to the production required to meet growing demand from non-PV applications for the different metals. For comparison, a histogram of annual growth rates for 35 different metals over 36-year periods between 1900 and 2012 (Figure 1-6.b) is plotted such that the stretched y-axis scale of the histogram coincides with the y-axis scale of Figure 1-6.a, giving the growth rate in production that would be required between 2014 and 2050 to meet the extra demand from PV. For example, an annual growth rate of 2.8 %, the median observed across the 35 metals over the measured range, would correspond to 2.7 "extra" years of production between 2014 and 2050, on top of constant 2012 production. If non-PV demand for each metal grows at the median rate for all metals, 2.7 years would need to be added to the data points in Figure 1-6.a to represent the total (PV + non-PV) demand. If metal-specific historical growth rates are used instead of the the median historical growth rate of all 35 metals, the required growth rates for the 100 % PV cases are changed by no more than ±1 % in absolute terms for silicon, silver, tellurium, gallium, and selenium, and by +2.3 % in absolute terms for indium. [110] Joel Jean assisted with the data collection for Figure 1-6.a.

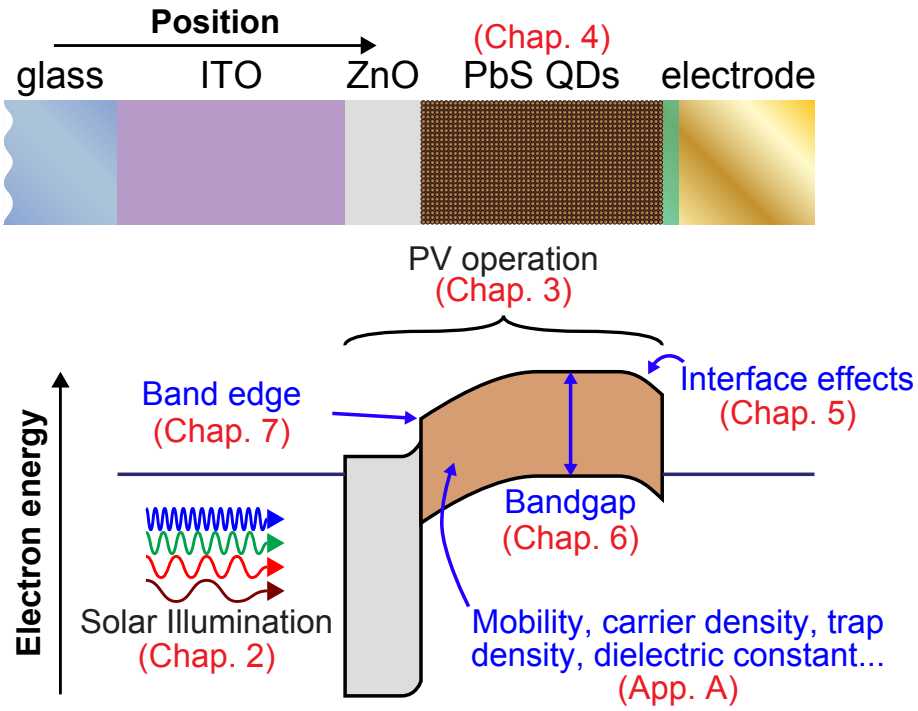

Figure 1-7: **Energy level engineering in colloidal quantum dot solar cells.** Physical cross section (top) and energy band diagram (bottom) of a prototypical PbS QD photovoltaic device. Components of the diagram, including details of the ability to control the phenomena in blue text, are described in the rest of the thesis in the sections noted in red text.

films can be predictably controlled through modification of the QD surface chemistry. [117, 118, 119] The physics behind this ability to engineer the energy level structure of PbS QD photovoltaics is the focus of this thesis.

1.2 Thesis organization

Figure 1-7 graphically outlines the content of this thesis. Chapter 2 describes the solar resource—its scale, spectral properties, geographic extent, and temporal characteristics—as context that is relevant for any solar cell technology. [120] Chapter 3 provides a general overview of photovoltaic devices, [121] and Chapter 4 describes the physical and chemical properties of colloidal lead sulfide quantum dots (PbS QDs), the primary focus of this thesis. The rest of the thesis describes three different approaches for modifying the energy level structure in PbS QD solar cells. Chapter 5 shows that a

Schottky barrier at the interface between PbS QDs and the hole-extracting electrode can be alleviated by inserting a thin layer of deep-work-function MoO_3 at the QD / electrode interface, thus improving carrier extraction from the film and increasing the power conversion efficiency of the device. [122] Chapter 6 shows how the tunable bandgap of PbS QDs can be used to elucidate charge- and exciton-transfer processes within QD PV devices—in particular, within singlet-fission-sensitized photovoltaics that have the potential to achieve efficiencies above the Shockley-Queisser limit. [83] Chapter 7 explores the influence of QD surface chemistry on the energy level structure of PbS QDs and identifies surface-chemistry-mediated energy level shifts as a versatile adjustable parameter in the performance optimization of QD optoelectronic devices. [119] Appendix A provides additional results on the influence of surface chemistry on the mobility and trap density of PbS QDs. [119]

Chapter 2

The Solar Resource

Portions of this chapter are reprinted with permission from MIT Energy Initiative, "Appendix A – The Solar Resource," in *The Future of Solar Energy*, [120] copyright 2015 Massachusetts Institute of Technology, and from Ref. [64] with permission from The Royal Society of Chemistry.

2.1 Introduction

The solar resource is significantly larger than every other energy source available on earth. [i] [123] Roughly 174 000 TW is continually delivered by solar radiation to the upper level of the earth's atmosphere. Given that global average power consumption totals roughly 17 TW, [25] the solar energy that strikes the earth in one hour is more than enough to supply all of humanity's current energy needs for one year. With the exception of nuclear, geothermal, and tidal energy, solar energy is the root source of all human energy resources—from the heat that drives the wind and the hydrologic cycle to the photosynthetically-derived chemical energy stored in fossil fuels (**Figure 2-1**). The solar resource is freely available and—compared to other energy resources—relatively evenly distributed across the globe.

Nevertheless, the solar resource is fundamentally distinguished from other energy

[i] Even utilizing every deuterium atom on earth for nuclear fusion would only generate $1/500^{\text{th}}$ of the energy that will be delivered to the earth by sunlight over the sun's remaining 5 billion years of life.

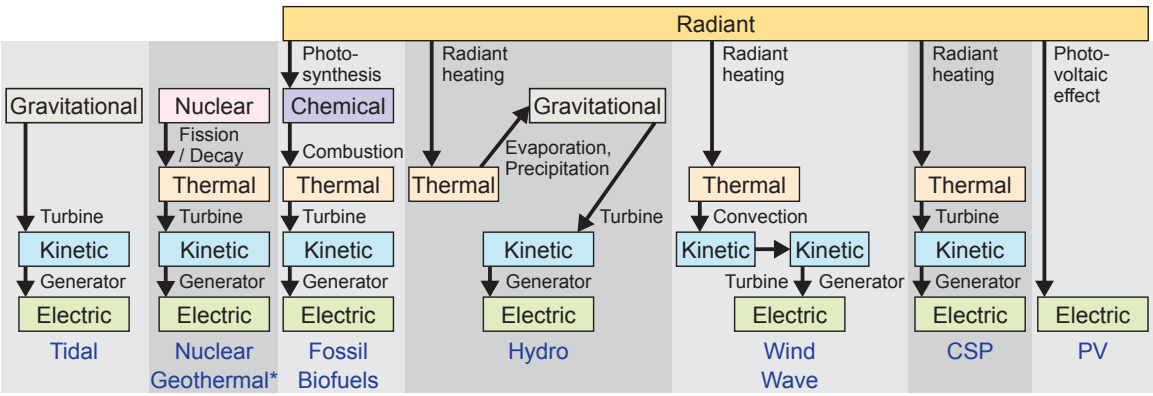

Figure 2-1: **Forms of energy and energy conversion processes.** Relevant forms of energy (colored boxes) and energy conversion processes (labeled arrows) for the production of electric power. Each energy conversion process involves the irreversible conversion of some portion of the energy input to low-grade thermal energy (i.e. waste heat). Note that gravitational, nuclear, and chemical energy all represent energy that can be stored for long periods of time with high efficiency; direct storage of thermal, kinetic, or electric energy is much less efficient. Radiant energy from the sun is the only external energy input to the earth system; photovoltaics are unique in their ability to directly convert radiant solar energy to electric energy. *The flow of geothermal energy from the earth's interior to its surface results in roughly equal measure from leftover energy still being dissipated from the earth's formation and from the nuclear decay of radioactive isotopes in the earth's interior. [34]

resources by its *intermittency*. At a given location on the earth's surface, the solar resource suffers from stochastic *unpredictability* (fluctuations over time spans of minutes to days resulting from cloud cover and weather systems) and deterministic *variability* (predictable fluctuations over time spans of days to months resulting from the earth's diurnal rotation and seasonal changes). Despite its large size, the solar resource is also dispersed. Hundreds of thousands of square kilometers of land would need to be covered by solar-energy-harvesting systems if solar power is to play a significant role in the transition to low- and zero-carbon energy sources that is necessary to avoid dangerous levels of anthropogenic climate change. [124, 125, 126, 127]

This chapter provides an introduction to the scope and limitations of the solar resource. Section 2.2 describes the physical nature of solar radiation and its interaction with the earth and its atmosphere. Section 2.3 describes the intrinsic intermittency of the solar resource, distinguishing between stochastic unpredictability and deterministic variability. Section 2.4 discusses variability in the solar resource over different geographic regions. Section 2.5 identifies the scale of electricity production that is

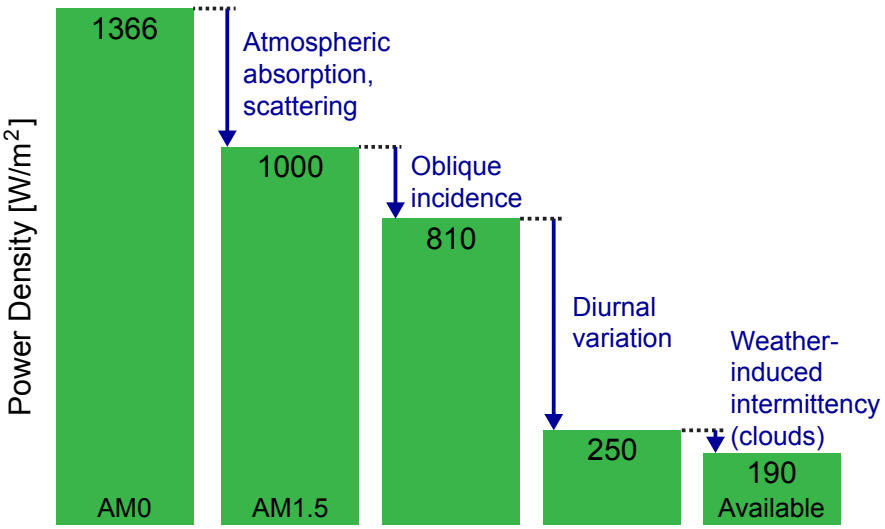

Figure 2-2: **Reduction in average solar power density from different factors.** Details of the different contributions are described in the text. [35, 36, 37, 38]

realistically attainable from the solar resource and estimates the land area required to meet a significant portion of U.S. electricity demand using solar power.

2.2 Nature of the solar resource

The vast majority of light that strikes the earth originates from the sun, which for the past 4.6 billion years has sustained a thermonuclear fusion reaction that produces the energy equivalent of roughly one trillion atomic bombs per second. [128] This reaction heats the sun's surface to approximately 6000 K and causes it to emit radiation via the same mechanism by which a heated tungsten filament produces visible light in an incandescent light bulb. [129]

Sunlight takes 8.3 minutes to travel the 1.5×10^8 km that separate the sun from the earth. [130] Because of this great propagation distance, rays of light spreading outward from the sun strike the upper level of the earth's atmosphere along mostly parallel paths. The sun can thus be considered a source of collinear light. Sunlight strikes the top of the earth's atmosphere with an average intensity of 1366 W m^{-2}; this quantity is known as the *solar constant* (**Figure 2-2**). [35] This intensity varies by ±3.3 % over the course of the year as the earth's slightly elliptical orbit takes it

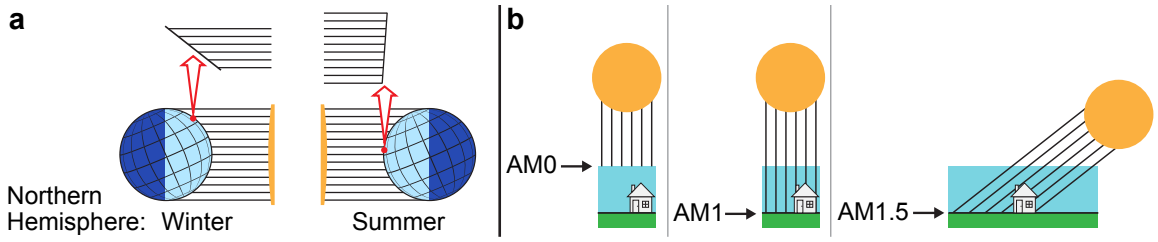

Figure 2-3: **Effects of seasonal variation (a) and atmospheric attenuation (b) on incident solar radiation.** The terms AM0, AM1, and AM1.5 are defined in the text.

closer to and further away from the sun. [131] There are also minor variations (less than $\pm 0.1\,\%$) over the course of the sun's 11-year sunspot cycle. [132]

Sunlight traveling from the top of the atmosphere to the earth's surface is both scattered and absorbed by air molecules, particulate matter, and clouds. Interaction with the atmosphere thus decreases the intensity of sunlight from the value measured at the outermost edge of the atmosphere. The effects of atmospheric attenuation are described by the air mass factor, where an air mass of 1 ("AM1") corresponds to the intensity of sunlight at the earth's surface when the sun is directly overhead (at the zenith) and the light has passed through a column of air equal in thickness to the atmosphere (**Figure 2-3**). The solar constant therefore corresponds to "AM0" conditions. An air mass of 1.5 corresponds to the intensity of sunlight when the sun is 48.2° from the zenith and the sunlight has passed through a column of air 1.5 times longer than the thickness of the atmosphere. Since the sun is rarely directly overhead, AM1.5 is used as a typical standard intensity in the testing and reporting of solar cell efficiencies. AM 1.5 conditions, representative of standard midday illumination across many of the world's major population centers, correspond to $1000\,\mathrm{W\,m^{-2}}$. [39]

While the earth's atmosphere is largely transparent to visible light, interactions with the atmosphere have important effects on the intensity, spectrum, and diffusivity of solar illumination at the earth's surface. Every surface emits thermal radiation, also known as blackbody radiation. The temperature of the surface determines the spectrum of this radiation, which is commonly reported as a function of the wavelength of light in nanometers. The spectrum of solar radiation at the top of the earth's

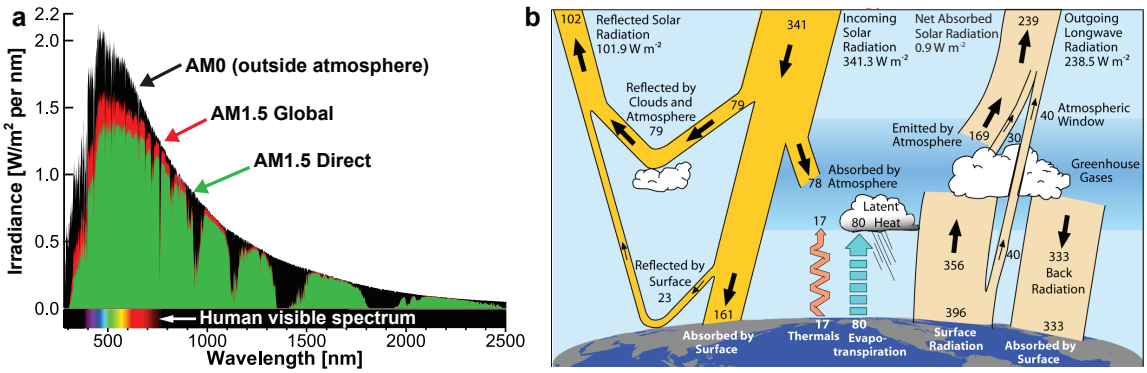

Figure 2-4: **The solar spectrum (a), and the influence of atmospheric effects on the earth's radiative energy balance (b)**. The data in **a** are from ASTM. [39] Panel **b** is reproduced from Trenberth. [40]

atmosphere closely matches the spectrum for a blackbody emitter at 5778 K, with a peak spectral irradiance in the visible portion of the spectrum between 400 and 750 nm in wavelength and a long tail extending deep into the infrared. During its transit through the atmosphere, sunlight interacts with air molecules (primarily water vapor, carbon dioxide, methane, nitrous oxide, and ozone) and portions of the light are absorbed or reflected. The absorption of light by air molecules occurs in distinct regions of the spectrum, giving rise to the sharp dips seen in the AM1.5 spectra in **Figure 2-4.a** and the greenhouse effect depicted schematically in **Figure 2-4.b**. Scattering most strongly affects shorter (bluer) wavelengths; hence, light scattered from the atmosphere to the earth's surface appears blue. The sun at sunrise and sunset appears red as a result of the increased atmospheric distance through which direct sunlight must travel at these times. The AM1.5 global spectrum includes the contribution of diffuse light scattered to the earth's surface from the atmosphere, and is thus higher at blue wavelengths than the AM1.5 direct spectrum, which excludes scattered light. Clouds are responsible for an additional amount of light absorption and scattering. These contributions are represented schematically in Figure 2-4.b.

The major sources of variation in solar intensity across time and geographic location arise from the varying obliquity of incoming solar radiation across different latitudes, the earth's revolution around the sun (seasonal variation), the earth's rotation about its own axis (diurnal variation), and changes in weather. In Section 2.3 we consider

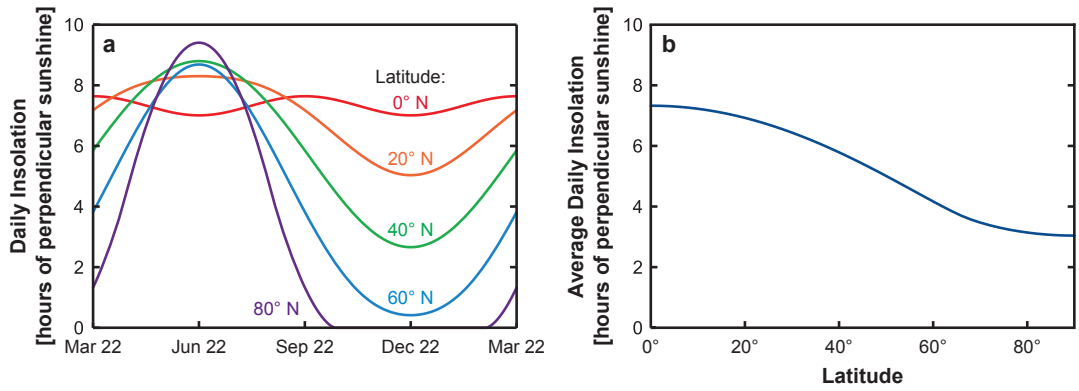

Figure 2-5: **Effects of latitude on daily (a) and yearly (b) insolation.** Both plots represent conditions at the top of the earth's atmosphere and thus neglect the influence of weather. Reproduced with permission from Jaffe and Taylor. [36]

the impact of the temporal variation induced by these phenomena. Here, we are concerned only with their impact on time-averaged illumination.

For a given location in the Northern Hemisphere, the sun's rays will generally strike the earth's surface at an oblique angle, as shown in Figure 2-3. Sunlight strikes the surface at a shallower angle in the winter than in the summer as a result of the earth's 23.4° axial tilt, giving rise to seasonal variations in insolation. In general, the amount of solar energy available to be harvested per unit area of the earth's surface decreases with increasing latitude, as shown in **Figure 2-5**. At 38° N, the average latitude for the United States, the tilt of the earth decreases the average daytime solar intensity (neglecting the influence of weather) to roughly $810\,\mathrm{W\,m^{-2}}$.

The earth's diurnal rotation further reduces the average solar intensity at a given point on the earth's surface. **Figure 2-6** shows three different metrics for solar intensity in Milford, Utah over the span of a cloudless day in June. [41] Global horizontal intensity reports the total amount of sunlight incident on a flat horizontal panel pointed directly overhead. Direct normal intensity reports the sunlight incident on a panel pointed directly at the sun using a continually adjusted two-axis tracking mount, excluding diffuse illumination scattered from clouds and from the atmosphere. Diffuse intensity reports solely the sunlight scattered from the atmosphere, with the direct normal component excluded. None of these metrics reports measurable solar

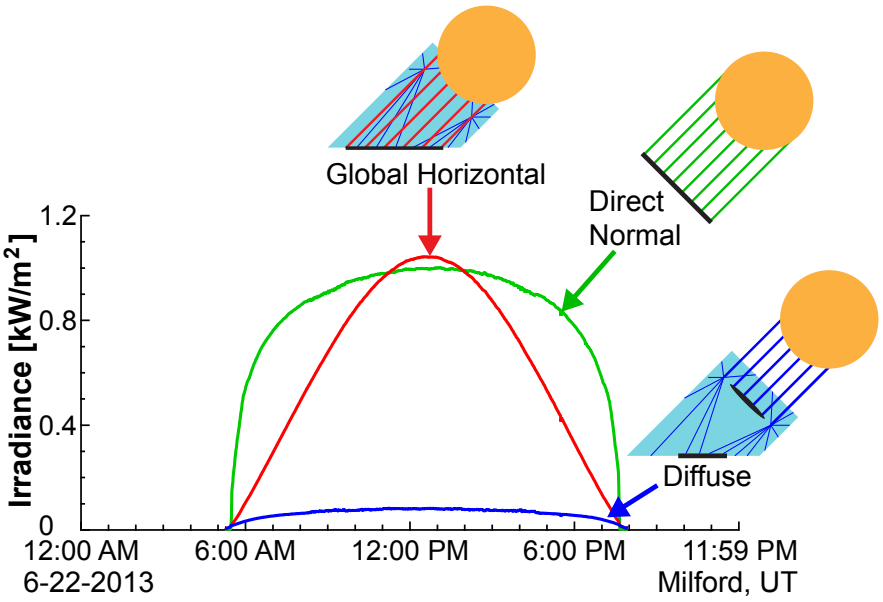

Figure 2-6: **Irradiance profiles at the earth's surface on a cloudless day.** Data are from NREL. [41]

intensity before dawn or after dusk. Integrating over a complete day at the average latitude of the United States, diurnal variation decreases the temporally averaged solar intensity over the course of a year to $250\,\mathrm{W\,m^{-2}}$.

The balance of direct and diffuse radiation impacts the relative effectiveness of different types of solar harvesting systems. Some solar harvesting systems focus, or concentrate, sunlight from a large collector area onto a smaller active area using mirrors or lenses. Concentration is employed in concentrating solar power (CSP) systems to heat a working fluid to much higher temperatures than would be attainable using non-concentrated sunlight. In PV systems, where concentration is used much less frequently, it enables the use of smaller, higher-efficiency solar cells. Simple geometric optics dictate that, as the concentration factor increases, the acceptance angle of incoming light decreases. In much the same way as a telescope must be precisely aligned with its target to achieve a highly magnified image, concentrating solar systems must employ active solar tracking to keep the collector aligned with the sun as the sun's position in the sky shifts throughout the day and the year (non-concentrating PV systems may also employ solar tracking to increase each PV panel's power output). As a result of their small acceptance angle, concentrating systems can only access the

collinear light rays of direct normal radiation. Diffuse radiation, which demonstrates no angular alignment, cannot be harvested by concentrating systems.

When the effects of cloud cover and weather-induced shading are factored in along with the effects noted above, the available global horizontal solar intensity averaged across the contiguous United States over the course of a year amounts to roughly $190\,\mathrm{W\,m^{-2}}$ or $4.5\,\mathrm{kW\,h\,m^{-2}\,d^{-1}}$. [37, 38] It bears emphasizing that this number represents an average over an entire year across a very large land area (roughly $8 \times 10^6\,\mathrm{km^2}$) and does not factor in the significant efficiency losses that are inevitably incurred when converting solar illumination to electricity or chemical energy. We address these considerations in the remainder of this chapter , starting with the issue of temporal intermittency.

2.3 Intermittency: Temporal unpredictability and variability

As illustrated by **Figure 2-7**, incident solar radiation at the earth's surface varies on many temporal scales over the course of a year. An unavoidable challenge inherent in utilizing solar power to meet a significant portion of humanity's energy needs lies in converting this highly intermittent resource, which is characterized by dramatic fluctuations in magnitude across wide temporal scales, into a steady and highly reliable source of electricity.

The most obvious temporal characteristic of the solar resource is its daily fluctuation. Longer variations are also seen over the course of the year: the length of the day as well as the peak and integrated irradiance increase moving into the summer and decrease moving into the winter. At the shortest timescales, shifting cloud cover can cause rapid variations in solar intensity: solar irradiance can drop by a factor of five or more in the span of minutes as a result of passing clouds. The difference between a completely sunny day and a completely overcast day can amount to a 15-fold difference in integrated irradiance, and weather systems that produce overcast

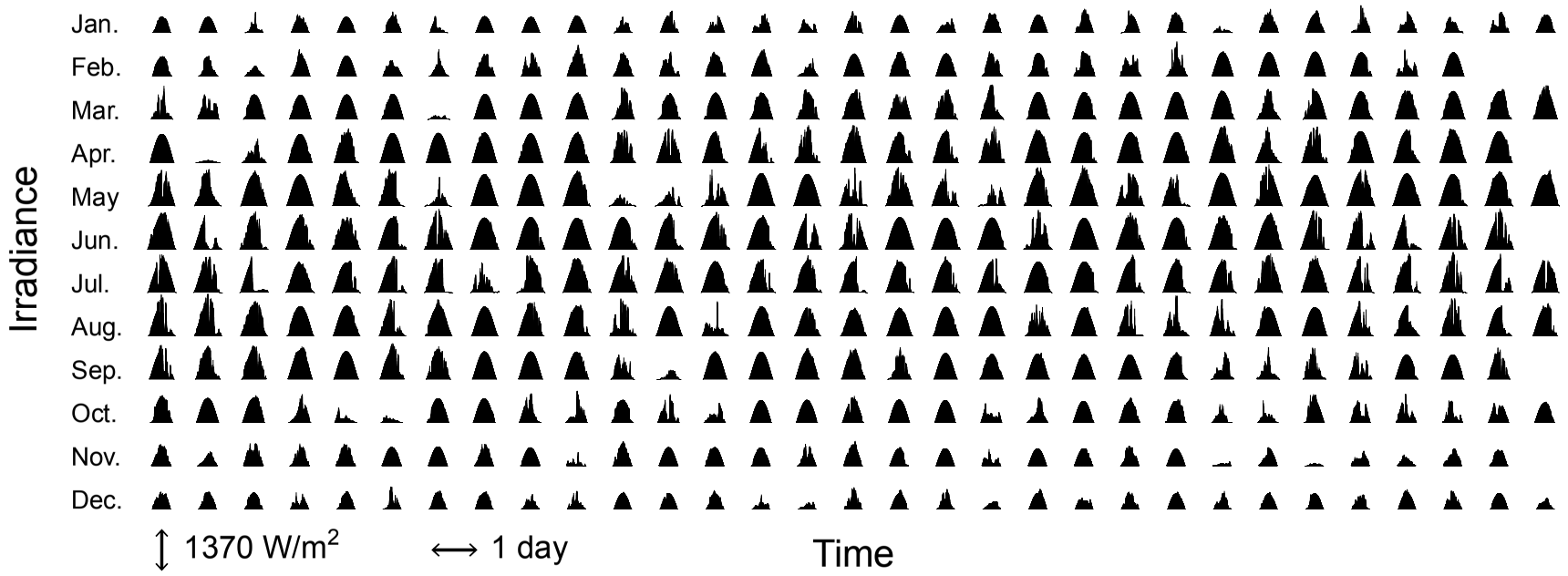

Figure 2-7: **Complete solar irradiance profile in Golden, Colorado for the year 2012.** The time axis is to scale (nights are included). Data are from NREL. [41]

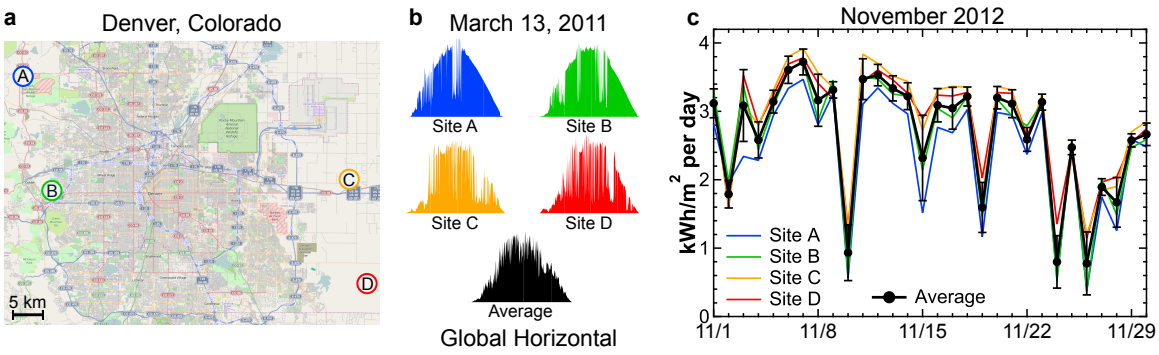

Figure 2-8: **Irradiance profiles at four separate measurement sites in the Denver area.** **a**, Map showing the location of the measurement sites; [42] **b**, the global horizontal irradiance profile at each of the sites and the four-site average on March 13, 2011, a day with many minute-to-minute variations; and **c**, daily average insolation for each site and for the four-site average over the month of November 2012, a month with many day-to-day variations. Data are from NREL. [41]

conditions sometimes persist for several days.

Some of these changes in intensity—including short, minute-to-minute changes as well as day-to-day fluctuations due to weather—are random and are labeled here as sources of unpredictability. Other fluctuations—including diurnal and seasonal variation—are broadly predictable and labeled here as sources of variability. We consider each of these features of the solar resource in turn, starting with unpredictability.

Figure 2-8 shows the solar intensity at four different measurement stations across the Denver, Colorado greater metropolitan area over two different time periods. [41, 42] On March 13, 2011, Denver experienced unpredictable cloud cover and steep changes in irradiance occurred on minute-to-minute timescales across the four measurement locations. Averaging the irradiance measured at the four different locations (Figure 2-8.b) reduces the scale of these rapid short-term fluctuations and smooths out the temporal profile. This observation suggests that small-scale grid interconnectivity, over distances greater than the typical size of a cloud, can to some extent mitigate the minute-to-minute unpredictability of the solar resource over the course of a day, even without relying on energy storage or non-solar sources of energy for backup.

Figure 2-8.c shows the daily insolation at each of the four Denver-area sites over the month of November 2012, as well as the daily insolation averaged across the four

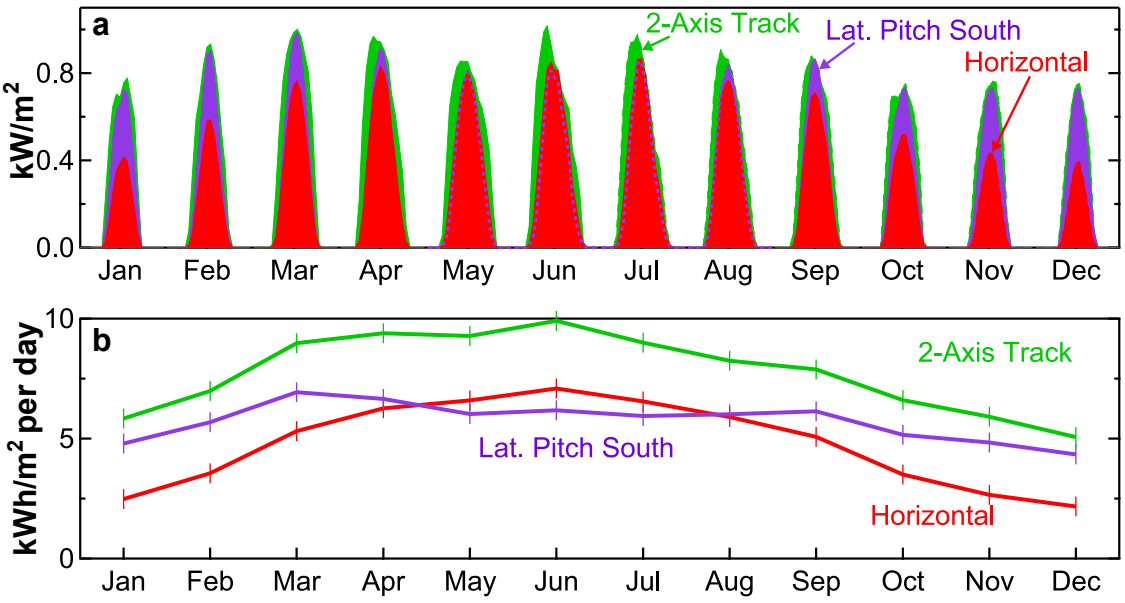

Figure 2-9: **Daily irradiance and monthly insolation profiles for different solar panel arrangements.** Solar intensity profiles are for a flat solar panel in horizontal, latitude pitch south, and two-axis tracking orientations in Golden, Colorado for each month of the year 2012, including **a**, daily irradiance profiles averaged over each month, and **b**, monthly average insolation. Data are from NREL. [41]

sites for the same month. In this case, small-scale grid interconnectivity does not significantly reduce fluctuations in resource availability: insolation still varies by over a factor of three from some days to the next. Larger-scale grid interconnectivity, similar in spatial extent to the size of weather systems, or suitable non-solar technologies (e.g. energy storage; complementary, curtailable, or dispatchable energy sources; or demand management) would be required to smooth out these day-to-day fluctuations.

While long-term weather and cloud patterns are unpredictable, some trends observed in Figure 2-7 are predictable far into the future. Diurnal variation is highly predictable, though smoothing out this source of variation in the absence of a globally integrated electric grid would require the use of non-solar technologies.

Seasonal variations are also somewhat predictable over the course of a year. **Figure 2-9.a** shows the average daily irradiance profile for each month of the year 2012 in Golden, Colorado, for three different solar panel arrangements: a panel pointed directly toward the zenith on a horizontal surface, a panel tilted south at a pitch equal to the latitude (40° for Golden), and a panel mounted on a two-axis tracking system

continually pointed toward the sun. Figure 2-9.b shows monthly average insolation over the course of the year.

The horizontal and two-axis tracking results follow expected seasonal trends. Average insolation is lowest in the winter (reaching a minimum in December) and highest in the summer (reaching its maximum in June). For both systems, there is more than a two-fold difference in average insolation between December and June. On the other hand, when the panel is tilted south at latitude pitch, these seasonal variations largely even out. [ii] At this angle, the orientation of the panel effectively splits the difference between the summer and winter locations of the noonday sun. This orientation results in a slight drop in insolation during the mid-summer months, but a smoother profile throughout the year and higher annual energy generation per panel. [iii]

It is worth noting that complete coverage of a given land area with horizontal panels results in the maximum possible harvest of solar energy. While a given area of panel can harvest more sunlight by being tilted toward the sun or by being placed on a tracking system, these architectures result in greater shading of the surrounding area, increasing the optimal spacing between panels. Relative to horizontal installations, tracking systems maximize power output per panel (a clear benefit for expensive panels), but reduce overall power output for a given area of occupied land. [48]

2.4 Geographic variability

We have noted that increasing the geographic extent of solar energy harvesting systems can smooth out some of the intrinsic unpredictability of the solar resource. However, insolation also varies predictably between different geographic locations. **Figure 2-10** illustrates geographic variation in average insolation across the United States;

[ii] PV panels installed in the Southern Hemisphere would be tilted north to achieve the same effect.

[iii] When location-specific diffuse irradiance profiles and seasonal shifts in cloud cover are taken into account, the optimal tilt for maximum annual energy generation per panel can vary from latitude pitch. If a location experiences cloudy winters and hazy summers, for example, a shallower tilt angle may be used to capture more diffuse light from the summer sky. Shallower tilt angles may also be used to minimize wind loading.

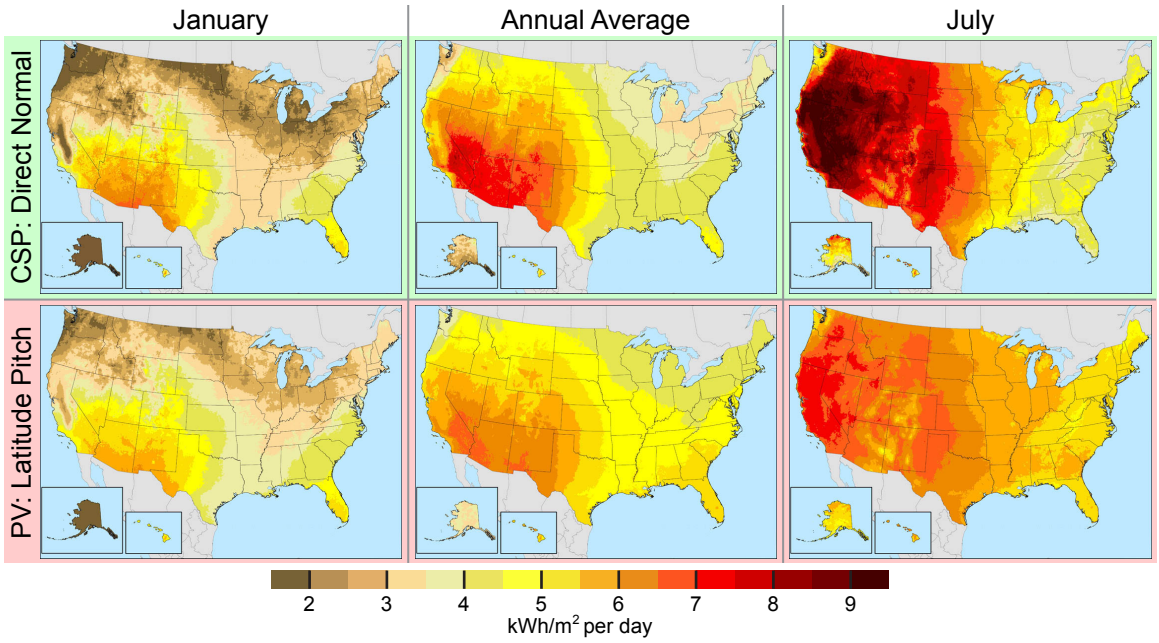

Figure 2-10: **Insolation maps for the United States.** The maps use data averaged over the period 1998–2005 and are reproduced from NREL. [37]

insolation values are shown for both direct normal and global latitude pitch and are averaged over three time periods (an entire year, the month of January, and the month of July). [37]

Figure 2-10 shows large seasonal and geographic differences in the magnitude and character of the solar resource in the United States. Clearly the American Southwest offers the most auspicious conditions for solar power, with nearly twice the average direct normal solar intensity of the Northwest and Northeast. It is also clear from these maps that different solar harvesting technologies are optimal for different locations. Concentrating systems primarily make use of direct normal illumination and therefore require tracking to operate efficiently, while non-concentrating systems can harness both direct and diffuse illumination. In areas characterized by frequent cloud cover (particularly the Northwest and Northeast) and diffuse sunlight, non-concentrating flat panels that capture global insolation will perform better than a concentrating system that employs two-axis tracking to capture direct normal insolation. On the other hand, concentrating systems offer a distinct advantage in hot, dry areas with little cloud cover.

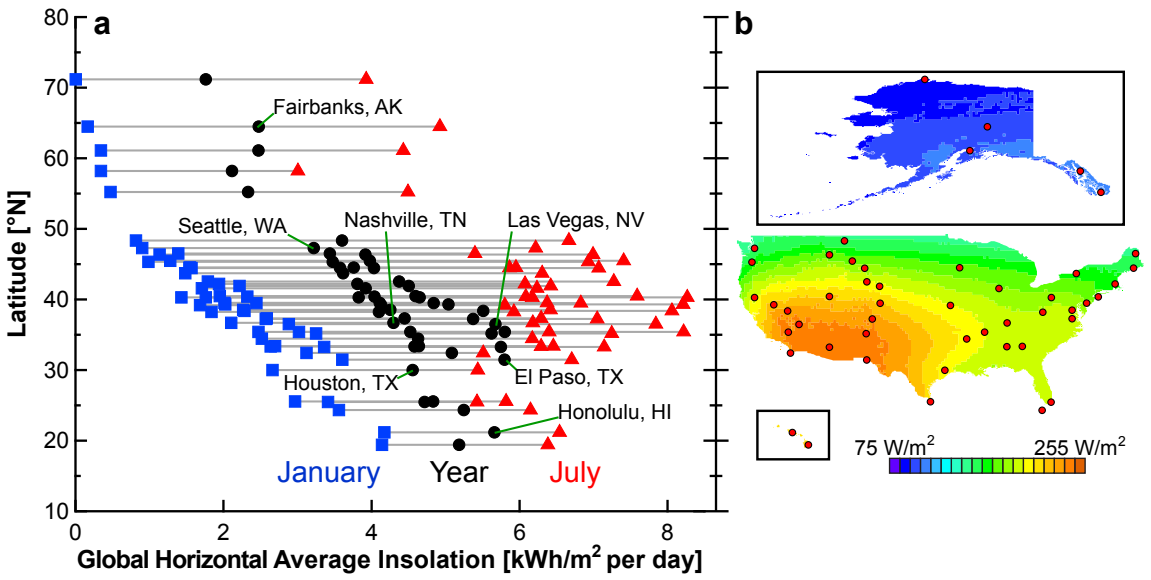

Figure 2-11: **Geographic and seasonal variability in insolation for specific U.S. cities.** In **a**, blue squares represent the average insolation for the month of January; red triangles represent the average insolation for July; black circles represent the yearly average insolation. Data are from NREL for the year 2010. [43] Each triplet of symbols connected by a gray line represents one city. Panel **b** shows the locations of the cities plotted in **a** on a solar irradiance map of the United States, using the same vertical (latitude) axis. Alaska and Hawaii are horizontally offset. Map adapted from Albuisson, Lefevre, and Wald. [44]

As noted in Figure 2-5, average insolation tends to increase with decreasing latitude. However, Figure 2-10 makes clear that latitude is not the only defining factor for solar insolation. Because of differences in weather patterns, global and direct normal solar intensities in the month of July vary more with longitude than they do with latitude.

Figure 2-11 summarizes geographic and temporal variations in the global horizontal solar resource for various cities across the United States. [43, 44] Average insolation values for the winter, summer, and year as a whole generally increase for decreasing latitude, but the range of values for a particular time interval at a given latitude is large. For example, the yearly average insolation for Las Vegas, Nevada is 30% higher than that for Nashville, Tennessee, despite the small (0.2°) difference in latitude between these two cities. The magnitude of seasonal variation in insolation also increases at higher latitudes. In Fairbanks, Alaska, for example, the average insolation in July is 30 times greater than the average insolation in January. In

Honolulu, Hawaii, by contrast, the average insolation for these two periods varies by only a factor of 1.6. However, as noted above, installing PV panels at latitude pitch would mitigate some of this seasonal variation. Across the contiguous United States, the average annual global insolation varies by roughly a factor of 1.8, between $3.2\,\mathrm{kW\,h\,m^{-2}\,d^{-1}}$ for Seattle, Washington and $5.8\,\mathrm{kW\,h\,m^{-2}\,d^{-1}}$ for El Paso, Texas.

This difference in annual average insolation across the United States is notable, as it implies that a solar installation providing 1 MWh of energy per day in Seattle would require nearly twice the number of solar panels and twice the land area of a 1 MWh-per-day solar installation in El Paso (or, equivalently, that a $1\,\mathrm{MW_p}$ PV array in El Paso would provide nearly twice the annual energy output of a $1\,\mathrm{MW_p}$ array in Seattle).

However, viewed on a global scale, sunlight is still one of the most uniformly distributed energy resources available. **Figure 2-12** shows a map of average solar intensity across the globe, with histograms of land area, population, and average irradiance as functions of latitude and longitude. [44, 45] The density of the solar resource varies by no more than a factor of three across heavily settled areas, and the vast majority of the human population has direct local access to the solar resource. [iv] These statements do not apply to fossil fuels and other extractive sources of energy. Access to the solar resource is also not highly correlated with wealth (here quantified in the conventional terms of GDP per capita), as shown in Figure 2-12.h. Average insolation varies across a much smaller range than GDP per capita, and the lack of a strong correlation between these two metrics implies that poorer nations are not fundamentally disadvantaged in their access to the solar resource. [v]

[iv] Areas in the Arctic and Antarctic Circles experience 24-hour periods without sunlight during the winter.

[v] Of course, there are large differences between rich and poor nations in terms of access to capital and infrastructure that could facilitate the manufacture, distribution, and incorporation of solar energy systems.

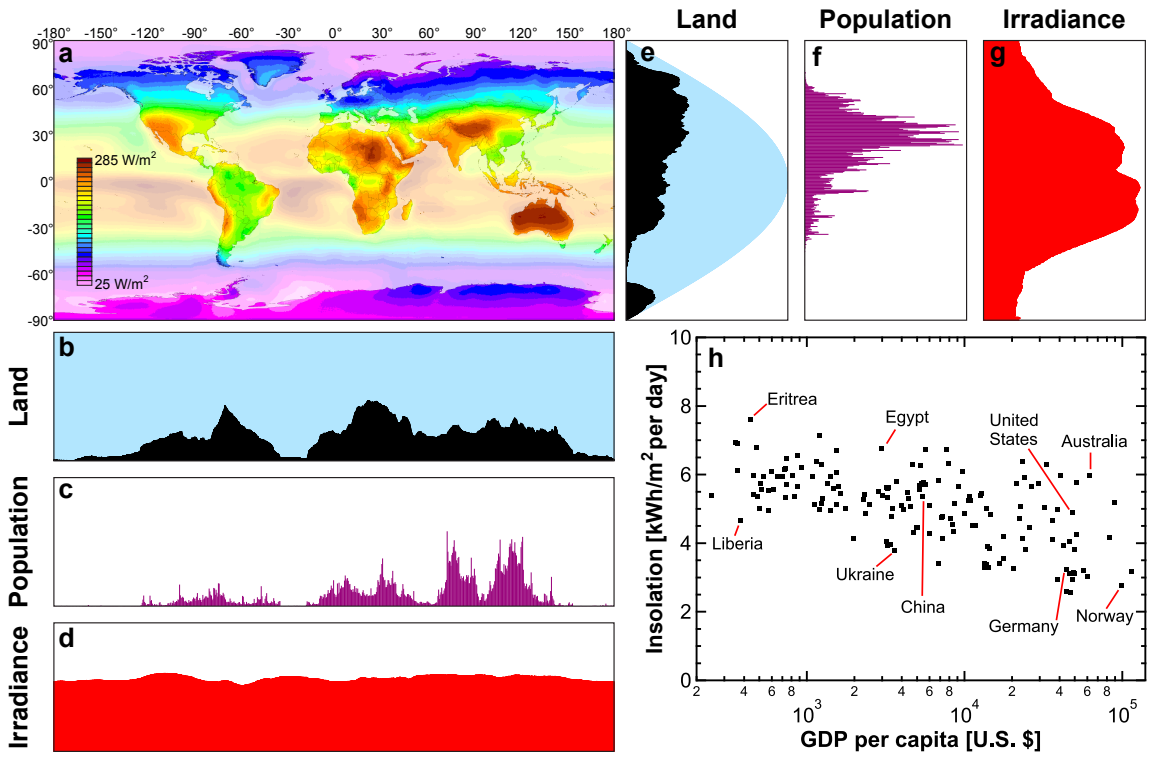

Figure 2-12: **Worldwide distribution of the solar resource.** **a**, Global map of solar irradiance averaged from 1990 to 2004 adapted from Albuisson, Lefevre, and Wald. [44] **b**–**g**, Histograms of world land area [$m^2/°$] (**b**), population [persons/°] (reproduced from Rankin [45]) (**c**), and average irradiance at the earth's surface [$W\,m^{-2}$] (**d**) as a function of longitude, and as a function of latitude (**e**–**g**). In **b** and **e**, land area is shown in black and water area in blue. **h**, Relationship between average insolation and GDP per capita for nations across the world for the year 2011. [46, 47] Each dot represents one nation.

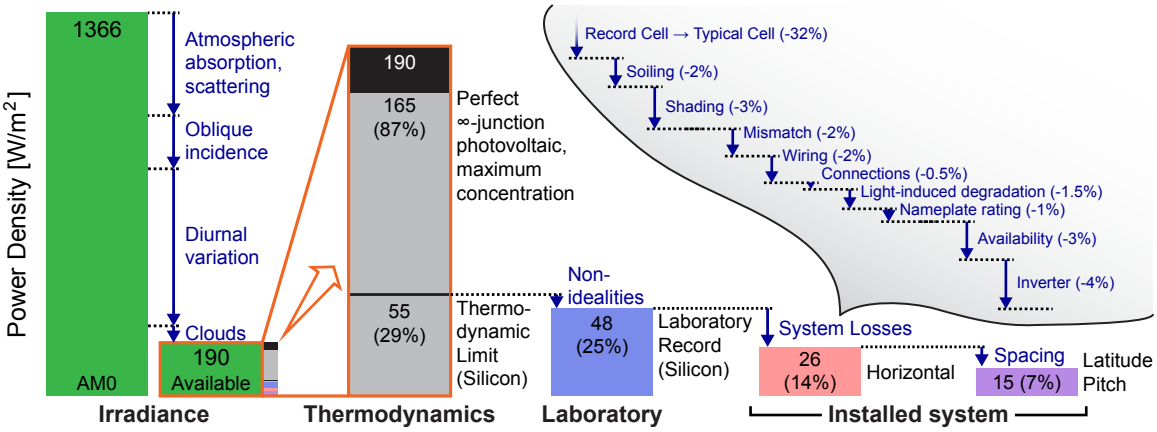

Figure 2-13: **Power conversion losses for solar PV.** Reductions in available power density for solar energy systems are summarized, including common losses incurred during the conversion of sunlight to electricity by photovoltaic cells. [48, 49, 50, 51, 52, 53, 54, 55, 56, 57]

2.5 Scale of the solar resource

Having described the nature of the solar resource, its intermittency, and its geographic variability, we now turn to the scale of the resource and consider the land area that would be required to supply 100 % of current U.S. electricity demand in 2050 using solar energy (an ambitious but illustrative example).

As noted in Section 2.2, the average power density of sunlight at a point on the earth's surface is attenuated relative to the solar constant by a combination of atmospheric absorption and scattering, the earth's tilt and rotation, and cloud cover. The time- and spatially-averaged solar power density over the land area of the contiguous United States is roughly $190\,\mathrm{W\,m^{-2}}$ or $4.5\,\mathrm{kW\,h\,m^{-2}\,d^{-1}}$. Converting this power to useful electrical or chemical energy engenders further power losses, as shown in **Figure 2-13**. This discussion takes a flat-panel silicon PV array, operating under the average solar intensity of the contiguous United States, as an example; observed power losses would be different for different PV or CSP systems.

The maximum efficiency allowed by the second law of thermodynamics for a fictional, perfect PV device that harvests the complete energy of each incident photon, under the maximum possible light concentration factor, [vi] is 86.8 %. [49] For a

[vi] The maximum possible concentration factor for sunlight is 45 900×, which corresponds to the

typical absorbing material such as silicon, which harnesses only a fixed amount of energy from each photon above a critical threshold of energy, the thermodynamic maximum efficiency is roughly 33 %. [50, 51, 52] Inherent inefficiencies and defects limit the maximum reported laboratory efficiency for silicon PV cells to ∼25 %. [53] Even greater losses are incurred for an installed array of PV modules: losses from manufacturing defects, panel soiling, interconnects, and the DC-to-AC inverter decrease the final installed system efficiency to roughly 14 % for horizontal panels with complete ground coverage. [vii] [54, 55] The greater inter-panel spacing required for latitude-tilt orientations decreases the efficiency per unit land area to roughly 7 % at the average latitude of the contiguous United States. This efficiency corresponds to a net power density under average U.S. illumination conditions of roughly $15\,\mathrm{W\,m^{-2}}$ or $0.36\,\mathrm{kW\,h\,m^{-2}\,d^{-1}}$. [viii] [48, 56, 57]

The average electric power consumption of the United States in the year 2050 is projected to total approximately 0.5 TW, which is equivalent to an average power consumption density of roughly $0.05\,\mathrm{W\,m^{-2}}$ over the land area of the United States. [30] Using the average net delivered solar power density of $15\,\mathrm{W\,m^{-2}}$ calculated above for panels at latitude tilt (and assuming that every kWh of energy produced by solar generators can be fully utilized to meet demand regardless of when it is generated), roughly $33\,000\,\mathrm{km^2}$ of land area (0.4 % of the land area of the United States, or roughly half the land area of West Virginia) would need to be covered with solar PV arrays to fully meet the nation's electricity needs. Note that this rough calculation assumes a uniform density of solar installations across the United States operating with the industry average multicrystalline silicon module efficiency. If solar arrays were instead only installed in areas with insolation of at least $5.5\,\mathrm{kW\,h\,m^{-2}\,d^{-1}}$ (the average

situation in which a flat cell "sees" the sun focused or reflected onto it from every possible direction. This concentration factor is equal to the reciprocal of the fraction of the sky occupied by the disk of the sun, viewed from the earth's surface.

[vii] We assume a module efficiency of 17.0 %, [54] combined system losses of 14 %, [55] and inverter efficiency of 96 %. [55]

[viii] At the average U.S. latitude of 38°N, the optimal ground coverage ratio to avoid panel shading is roughly 0.5. Lower ground coverage ratios would be optimal at higher latitudes and higher ratios at lower latitudes. The stated power density of $15\,\mathrm{W\,m^{-2}}$ takes into account the slightly higher average intensity available to panels at latitude pitch ($5.2\,\mathrm{kW\,h\,m^{-2}\,d^{-1}}$, versus $4.5\,\mathrm{kW\,h\,m^{-2}\,d^{-1}}$ for horizontal panels). [57]

global horizontal insolation in Arizona), using current industry-leading modules (21 % efficiency [133]) and horizontal installations with complete ground coverage, the land-use requirement for PV arrays drops to 12 000 km^2, or roughly the combined land area of the White Sands Missile Range and Dugway Proving Ground (neglecting resistive losses due to long-range transmission). [134, 135] **Figure 2-14** compares the land required to meet 100 % of projected U.S. electricity demand in 2050 using solar PV with the amount of land currently devoted to other distinct uses and shows that the land requirement, while large, is smaller than the amount of land currently dedicated to other energy industries and to national defense.

In conclusion, the global and national solar resource is both large and widely dispersed. Roughly 0.4 % of the land area of the United States, or 33 000 km^2, would need to host PV arrays to fully supply the projected U.S. electricity demand in 2050, an area that is comparable to the area currently devoted to other distinct uses. Despite the large scale and relatively even distribution of the solar resource, supplying a substantial portion of humanity's energy demand using solar would require some combination of energy storage, large-scale grid interconnectivity, and complementary, dispatchable, or curtailable energy technologies to overcome unavoidable variations in solar illumination.

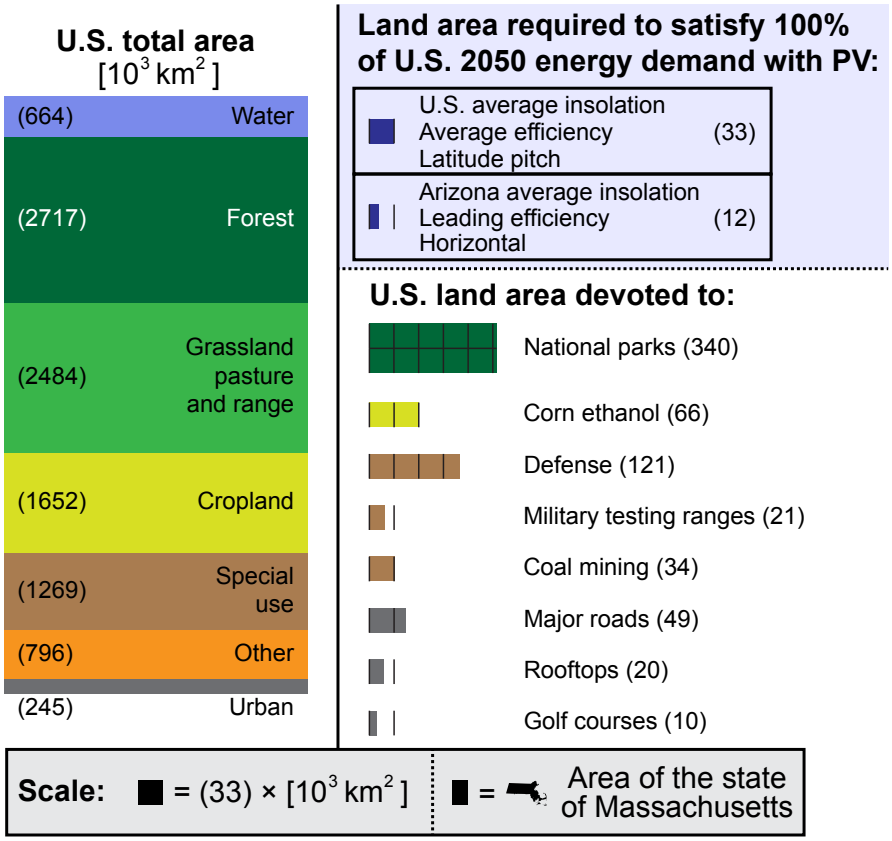

Figure 2-14: **Land requirements for large-scale PV deployment compared to existing land uses.** The solar land requirement is calculated assuming that solar PV generation is used to meet 100 % of projected 2050 U.S. electricity requirements (roughly 0.5 TW averaged over a year). Figures for other land areas represent actual current uses, and numbers in parentheses denote thousands of square kilometers of area. All elements of the figure are to scale. Land classes ("urban", etc.) are taken from U.S. Department of Agriculture. [58] "National parks" is from the National Park Service. [59] "Corn ethanol," "major roads," "rooftops," and "golf courses" are from Denholm and Margolis. [48] "Defense" is from the U.S. Department of Defense. [60] "Military testing ranges" corresponds to the sum of the net land area given by Wikipedia for four distinct U.S. testing ranges: Utah Test and Training Range (6930 km^2), White Sands Missile Range (8300 km^2), McGregor Range Complex (2400 km^2), and Yuma Proving Ground (3387 km^2). "Coal mining" corresponds to the net land area that has been disturbed by surface mining for coal and is taken from multiple sources. [61, 62, 63] This chart was developed in conjunction with MIT subject ESD.124, "Energy Systems and Climate Change Mitigation."

Chapter 3

Fundamentals of PV Operation

3.1 Introduction

This chapter describes, in simple terms, the principles that govern the conversion of light into electric power within photovoltaic (PV) devices. We introduce the concept of semiconductors and discuss the electric and optical properties that govern their interaction with light. We explain the concept of the diode as the fundamental functional unit of a PV device and review the characterization and standard performance metrics of solar cells. Finally, we explain how solar cells are combined to form PV modules and arrays.

This chapter describes, in simple terms, the principles that govern the conversion of light into electric power within photovoltaic (PV) devices. We discuss the electrical and optical properties of semiconductors and explain the concept of the p-n junction diode as the fundamental functional unit of a PV device. We review the characterization and standard performance metrics of solar cells and explain how solar cells are combined to form PV modules and arrays.

3.2 Electronic materials

A typical solid such as silicon contains roughly 7×10^{20} electrons per cubic millimeter of material. Electrons occupy states of well-defined energy within the solid; much like water filling up a bucket, electrons minimize their energy by filling up the lowest-energy states (the deepest part of the bucket, or the most tightly-bound atomic energy states) first. Electrons are one of two types of charge carriers within a typical solid; the other type of charge carrier is the hole, which is simply the absence of an electron in a state where an electron would normally be found. If electrons are compared to drops of water, holes can be compared to bubbles below the water's surface. By carrying an absence of negative charge within a surrounding sea of negatively charged electrons, [i] a hole can be treated as a carrier of positive charge, moving in the opposite direction from an electron under an applied electric field. The electrical conductivity σ of a material is proportional to the density (the number per unit volume) of mobile electrons and holes multiplied by the mobility (the ratio of a charge carrier's velocity to the magnitude of the electric field that drives its motion) of these charge carriers within the material and is given by

$$\sigma = \sigma_e + \sigma_h = e\left(n\mu_e + p\mu_h\right), \tag{3.1}$$

where σ_e and σ_h are the electron and hole conductivities, respectively; e is the charge of the electron; n and p are, respectively, the electron and hole densities; and μ_e and μ_h are, respectively, the electron and hole mobilities.

Electrons can be excited by the absorption of external energy in the form of photons or heat. A single excitation generates both an electron and hole; the excited electron, in its transition to a higher-energy state, leaves behind an empty hole in its previous state. As with vibrational modes on a vibrating guitar string, only certain electron energies are physically allowed within a material. In a single atom or molecule these energies exist as discrete, isolated energy states; in extended solids with large

[i] The negative charge of each electron is balanced by a positive charge in the nucleus of the atom from which the electron originates, such that the entire solid carries no net charge.

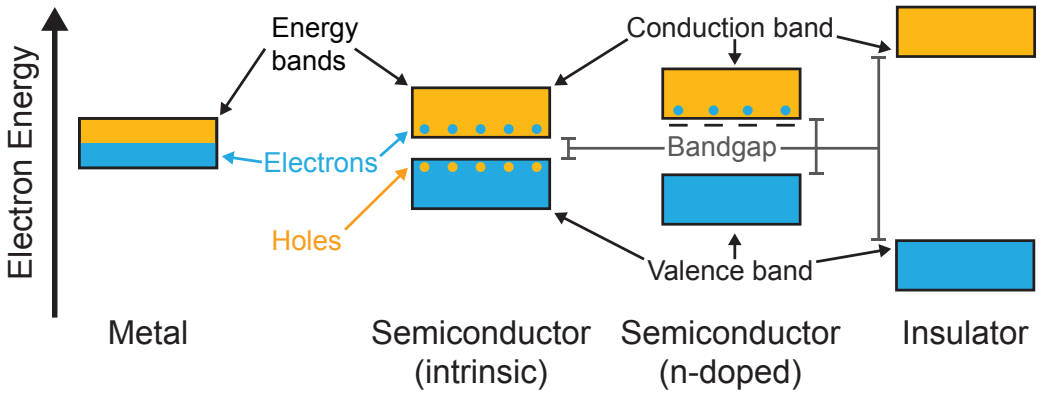

Figure 3-1: **Energy band structure of metals, semiconductors, and insulators.**

Table 3.1: **Bandgaps of various materials at room temperature.** [90, 91, 92, 93, 94]

Material	Bandgap [eV]
Metals	0
PbS (lead sulfide)	0.4
Si (silicon)	1.1
CdTe (cadmium telluride)	1.4
CIGS (copper indium gallium diselenide)	1.0–1.7
C (diamond)	5.5
SiO_2 (silica glass)	∼9
LiF (lithium fluoride)	13.6

numbers of atoms these discrete states are smeared out into broad energy bands. In pure materials, electrons can only reside at energies contained within these bands; they cannot occupy energies between bands, where there are no electronic states. The electronic properties of a given material are determined to a large extent by the profile of these energy bands and the extent to which they are filled with electrons. The highest-energy band that is completely filled with electrons is called the valence band; the next-higher band is called the conduction band.

As shown in **Figure 3-1**, the three major classes of electronic materials—metals, insulators, and semiconductors—are characterized by distinct energy band arrangements. Metals contain an incompletely filled energy band, allowing the collective motion of electrons at the energetic surface of the filled states (much like waves in a partially-filled container of water). Insulators contain completely filled bands separated

by a large bandgap. This bandgap in insulators is too wide to allow significant excitation of electrons across the gap by heat or visible photons. Since in most situations the valence band of insulators is filled with electrons (with no mobile holes) and the conduction band is empty of electrons, no charge carriers are available to flow under an applied electric field, making these materials electrically resistive. Semiconductors are intermediate between metals and insulators; they exhibit a bandgap between filled and empty bands, but the gap is small enough for electrons to be excited across it by heat or visible photons. Semiconductors can also be doped with minute quantities of impurity atoms that can easily donate excess electrons or holes to the rest of the solid, thereby increasing the density of free charge carriers and the conductivity of the semiconductor.

3.3 P-n junction diodes and solar cells

The fundamental functional unit of a solar cell is a p-n junction diode, which forms at the interface between two semiconductors, where one semiconductor is doped with an excess of electron-donating impurities (an n-type semiconductor, so named for the excess of free negatively-charged electrons) and the other semiconductor is doped with an excess of hole-donating impurities (a p-type semiconductor, so named for the excess of free positively-charged holes). **Figure 3-2** illustrates the fundamentals of the p-n junction diode. When an n-type and p-type material are put in contact, free electrons from the n-type side and free holes from the p-type side will diffuse across the interface, canceling each other out (the electrons "fill in" the holes). This "canceling out" of the free carriers in the region of the interface uncovers the fixed charges of the dopants that originally balanced the charge of the free electrons and holes, generating a built-in electric field in the "depleted" interface region that prevents further diffusion. This field corresponds to a built-in voltage gradient between the n-type and p-type sides of the junction.

The diode acts as a one-way valve for charge carriers, as shown in **Figure 3-3**. If a positive bias voltage is applied to the p-type side of the junction (the left side of

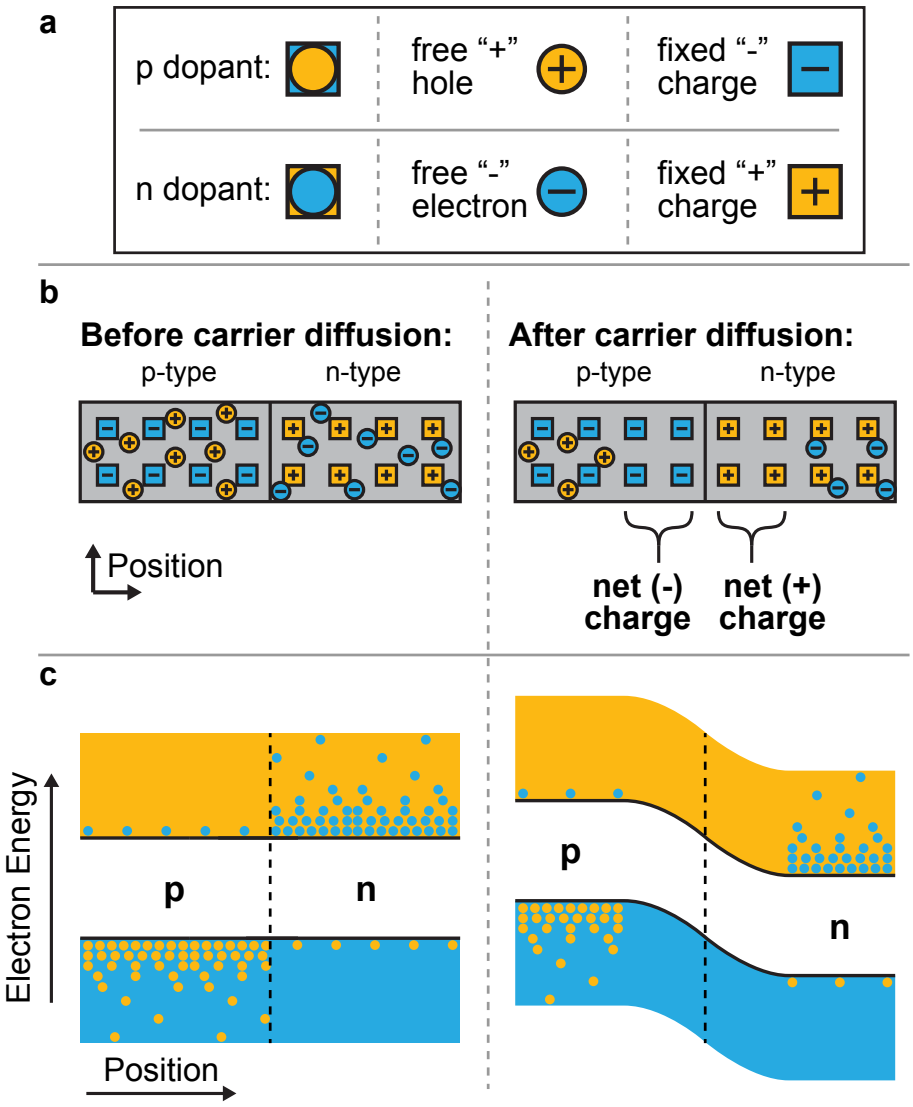

Figure 3-2: **Physical structure and electronic properties of a p-n junction diode.** The physical structure (**a,b**) and energy band structure (**c**) of a p-n junction diode without (left) and with (right) the diffusion of charge carriers across the junction interface. The orange and blue shaded regions in **c** represent the conduction and valence bands, respectively.

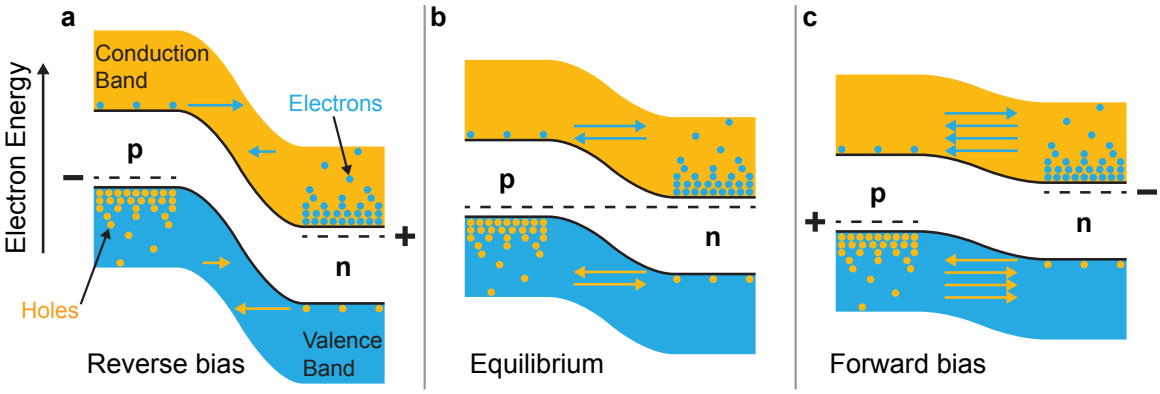

Figure 3-3: **Energy bands during operation of a p-n junction diode.** The energy bands shown correspond to reverse bias (negative voltage) (**a**), equilibrium (zero voltage) (**b**), and forward bias (positive voltage) (**c**) conditions. Blue and orange arrows represent electron flux and hole flux, respectively.

the junction as shown here) relative to the n-type side, the built-in field and width of the depleted region are reduced, and large numbers of carriers can diffuse across the interface, generating a large current. If a negative bias voltage is applied to the p-type side relative to the n-type side, the built-in field and width of the depleted region are increased and diffusion remains unfavorable. The current density output from a solar cell, J, as a function of voltage is given by

$$J = J_S \left(\exp \frac{eV}{k_B T} - 1 \right) - J_{SC}, \tag{3.2}$$

where J_S is the reverse saturation current density, e is the charge of the electron, V is the voltage applied to the solar cell, k_B is the Boltzmann constant, T is the temperature in kelvin, and J_{SC} is the short-circuit current density. With J_{SC} set to zero, this equation represents the current output of a simple diode. The curve labeled "dark" in **Figure 3-4.a** shows the current passed through a representative diode at different applied voltage levels; this current increases exponentially under positive voltage, but remains small under negative voltage.

A solar cell is simply a diode that can generate free electrons and holes through the absorption of light, as depicted in **Figure 3-5**. These free charge carriers are separated under the built-in electric field of the diode, generating photocurrent; the generation

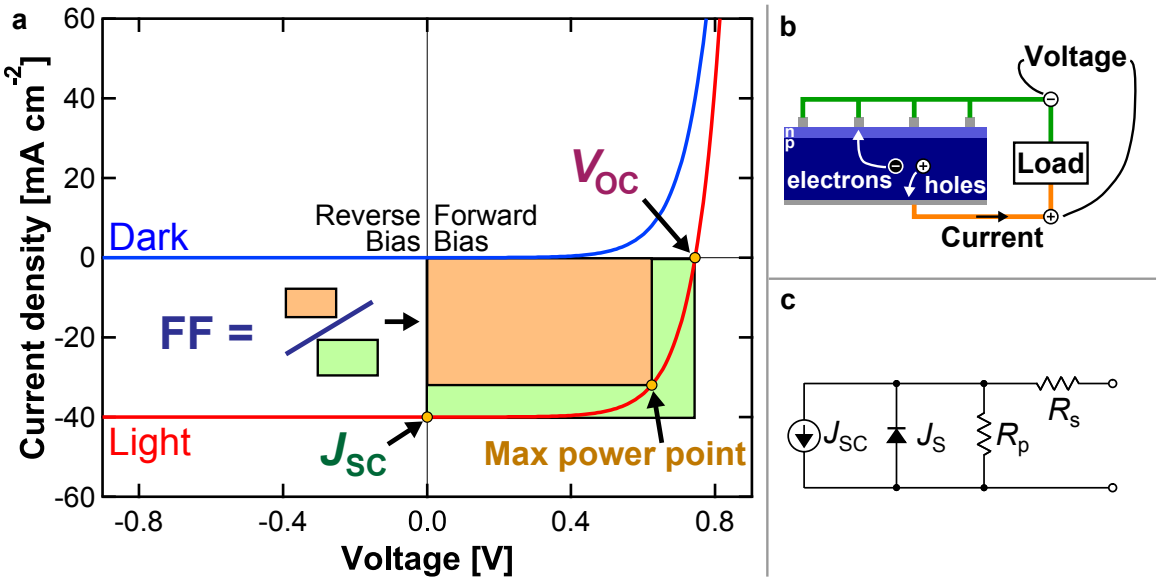

Figure 3-4: **Representative current-voltage characteristics of a solar cell. a**, Solar cell current-voltage characteristics in the dark (blue curve) and under illumination (red curve). The short-circuit current density (J_{SC}), open-circuit voltage (V_{OC}), and fill factor (FF) are indicated; the physical significance of these metrics is described in the text. The current output of an illuminated solar cell is proportional to its illuminated surface area, so current output is typically reported as *current density* (current divided by area) to normalize for different solar cell sizes. Voltage and current are measured between the positive and negative terminals of the solar cell (**b**). **c**, Circuit model for a solar cell, including the effects of series resistance (R_s) and shunt, or parallel, resistance (R_p).

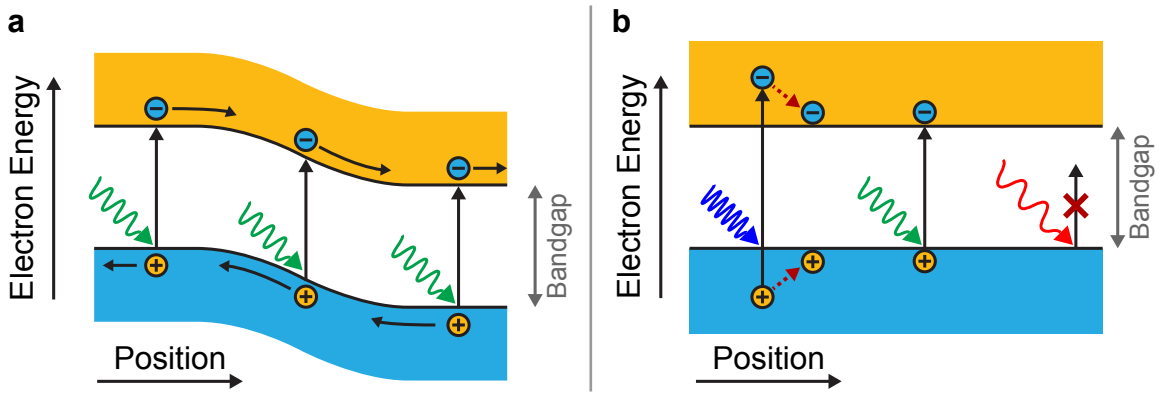

Figure 3-5: **Operation of a solar cell under illumination and interaction of light with a semiconductor. a**, Excitation of electrons and holes by photons in a solar cell, followed by charge carrier separation under the built-in electric field. The conduction band and holes are shown in orange; the valence band and electrons are shown in blue. **b**, Interaction of light of various wavelengths with a light-absorbing semiconductor. Short-wavelength photons of energy higher than the bandgap (here depicted as blue wavy lines) generate excited electron-hole pairs with net energy greater than the bandgap, but the electron and hole quickly lose their excess energy and "relax" to the bottom of the conduction band (for electrons) and top of the valence band (for holes). Long-wavelength photons of energy lower than the bandgap (here depicted as red wavy lines) are not absorbed and do not generate free electron-hole pairs.

of photocurrent is roughly independent of the voltage across the solar cell, so the "light" curve in Figure 3-4.a is vertically offset by a constant amount from the "dark" curve. The photocurrent is correlated with the number of carriers generated under illumination, which in turn depends on the absorption properties of the semiconductor and its efficiency in turning absorbed photons into extractable charge carriers (this efficiency, known as the external quantum efficiency, is described in more detail below). The voltage output is correlated with the strength of the built-in electric field of the diode.

Figure 3-4.a illustrates the current-voltage output of a representative solar cell, both in the dark (blue curve, acting as a simple diode) and under illumination (red curve), and identifies key operational parameters. The open-circuit voltage (V_{OC}) is the voltage measured between the two terminals of an illuminated solar cell when the terminals are left "open" (i.e. not connected to each other by a conductive path) and no current is allowed to flow. The short-circuit current density (J_{SC}) is the current density that flows through the solar cell when the two terminals are "shorted" together by a highly conductive pathway (like a copper wire) and held at the same voltage.

The voltage output of an operating solar cell will range between zero and the value of its V_{OC}; in the ideal case the current output stays roughly constant over much of this range, until the voltage approaches the V_{OC}. The power output at a given voltage is equal to the product of the voltage and the current at that voltage and will reach a maximum near the apparent "shoulder" in the current-voltage curve (as depicted by the orange rectangle in Figure 3-4.a). The fill factor of a solar cell, which corresponds to the perceived "squareness" of its illuminated current-voltage curve, is the ratio between its power output at the maximum power point and the product of its J_{SC} and V_{OC}. The power conversion efficiency is equal to the product of the J_{SC}, V_{OC}, and fill factor, divided by the intensity of the incident light (usually measured under standard illumination conditions of $1\,\mathrm{kW\,m^{-2}}$, as noted in Chapter 2).

In an actual solar cell, the simple ideal diode equation (3.2) does not fully describe the current-voltage response. The active material of the cell and the current-collecting electrodes have a finite series resistance R_s that can reduce the current output of

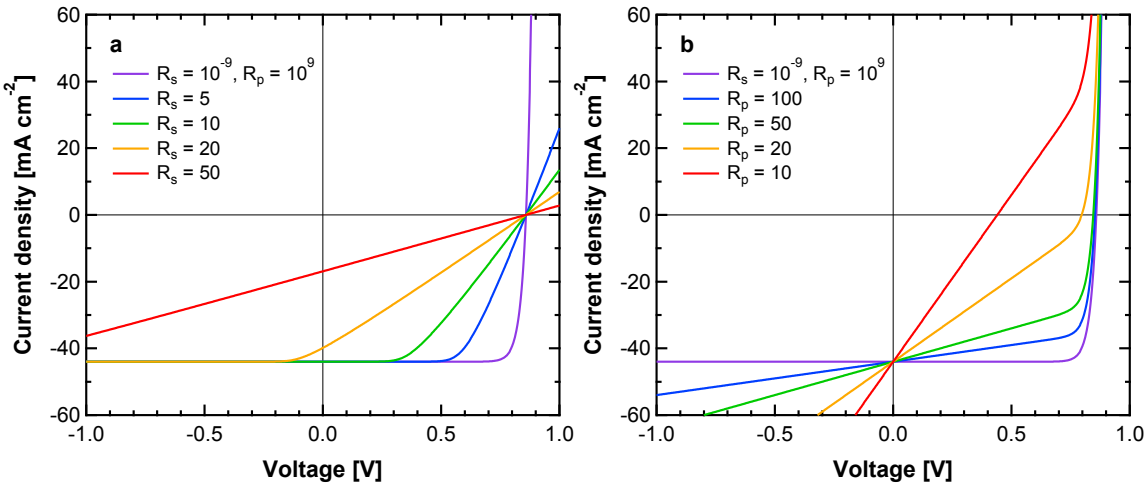

Figure 3-6: **Simulated performance of PV devices with different series resistance (a) and shunt resistance (b).** Resistances are given in ohms. Simulation parameters besides those listed in the figure are: $T = 300\,\mathrm{K}$; $n = 1$; $J_S = 1.7 \times 10^{-13}\,\mathrm{mA\,cm^{-2}}$; $J_{SC} = 44\,\mathrm{mA\,cm^{-2}}$.

the cell, and a finite shunt (or parallel) resistance R_p through the active layer that can reduce the voltage output. Taking into account these parasitic resistances, the current-voltage properties can be described by

$$J = \frac{R_p}{R_s + R_p}\left\{J_S\left[\exp\left(\frac{e\,(V - JR_s)}{nk_BT}\right) - 1\right] + \frac{V}{R_p}\right\}, \tag{3.3}$$

where n is the diode ideality factor. **Figure 3-6** shows simulated J-V curves for a solar cell with different values for the series (Figure 3-6.a) and shunt (Figure 3-6.b) resistance. Increasing the series resistance and decreasing the shunt resistance both result in a reduction in fill factor and efficiency; a high enough series resistance or low enough shunt resistance will also reduce the J_{SC} or V_{OC}, respectively.

Figure 3-7 shows how solar modules are built up from individually-manufactured solar cells in the case of wafer-based technologies or manufactured monolithically and scribed into individual cells in the case of thin-film technologies. Individual cells in both module designs are connected in series to increase the module output voltage. Modules may be connected in series to further increase the collective output voltage, or in parallel to increase the collective output current; such a collection of solar modules is often called a solar array. Additional components such as inverters

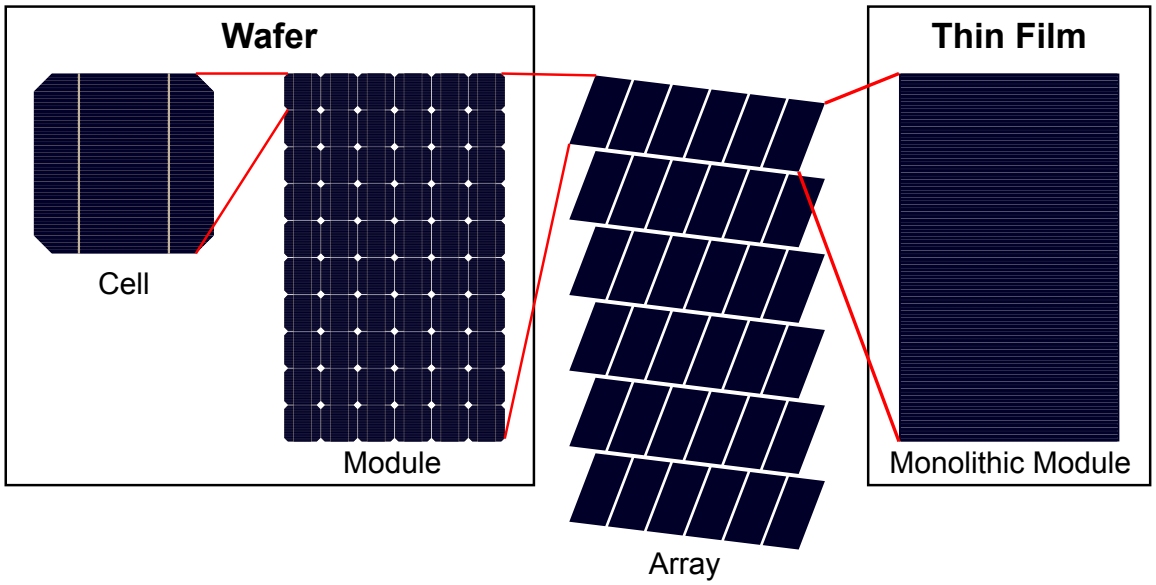

Figure 3-7: **Schematic representation of a solar cell, module, and array for wafer-based and thin film photovoltiacs.** Wafer-based technologies (such as crystalline silicon) combine multiple individually-fabricated cells into a larger module, while thin-film technologies (such as CdTe and amorphous silicon) employ active materials that are deposited over the complete module area and then scribed into individual cells. Modules of either type from the basis of larger solar arrays. Additional module components used for mechanical support and encapsulation and balance-of-system hardware components such as racking, wiring, inverters, and transformers are not shown here.

and transformers are necessary to convert the direct current (DC) output of a solar array into alternating current (AC) for incorporation into an electric grid; for off-grid applications, the DC output of a solar array may be utilized directly, or batteries and charge controllers may be incorporated to store the energy generated for later use.

3.4 Solar cell efficiency

The current and voltage output of a solar cell cannot be simultaneously maximized. Since a solar cell can only absorb photons with energy greater than the bandgap, reducing the bandgap will lead to larger currents. However, as depicted in Figure 3-5.b, electrons excited by photons with energy greater than the bandgap quickly dissipate their excess energy as wasted heat, ultimately coming to rest at an energy equal to the bandgap. The bandgap energy is thus the maximum energy that can be extracted as

electrical energy from each photon absorbed by the solar cell. Reducing the bandgap will lead to smaller voltages, eventually counteracting the benefit of increasing the current. The broad emission spectrum of the sun thus limits our ability to harvest both the maximum number of photons and the maximum energy from each photon. The theoretical maximum power conversion efficiency of a single-junction solar cell, under unconcentrated solar illumination and room-temperature operation, is roughly 33 %, a quantity known as the Shockley-Queisser Limit. [50, 51] This limit can be surpassed by multijunction solar cells that use a combination of materials of different bandgaps; these devices enable a greater fraction of the energy of each absorbed photon to be extracted as voltage and have a maximum theoretical efficiency of roughly 68 % under unconcentrated sunlight. [49] In an actual solar cell, the presence of defects and parasitic resistive losses will decrease the efficiency to values below these limits. The Shockley-Queisser Limit is discussed in more detail and derived in Section 6.2.

As mentioned above, the external quantum efficiency (EQE) of a solar cell is the efficiency with which individual photons of a given wavelength are converted to extracted charge carriers. **Figure 3-8** shows the EQE spectra of world-record solar cells of various types, compared with the solar spectrum observed at the earth's surface. Sharp cutoffs in EQE are observed on the high-wavelength (low-energy) side of each spectrum at the bandgap of the absorbing material, as photons with energy less than the bandgap cannot be absorbed. The multiplicative product of the EQE spectrum and the solar spectrum, integrated over all wavelengths, should give the J_{SC} produced by the solar cell. Many loss processes can reduce the EQE to levels below 100 %, including reflection of light from the surface of the solar cell, absorption of light by non-current-generating materials within the solar cell, or loss of current due to parasitic resistances. EQE and current-voltage analysis thus provide valuable information regarding the mechanism and efficiency of carrier generation and transport within photovoltaic devices, and are used throughout this thesis to analyze the operation of PbS QD solar cells.

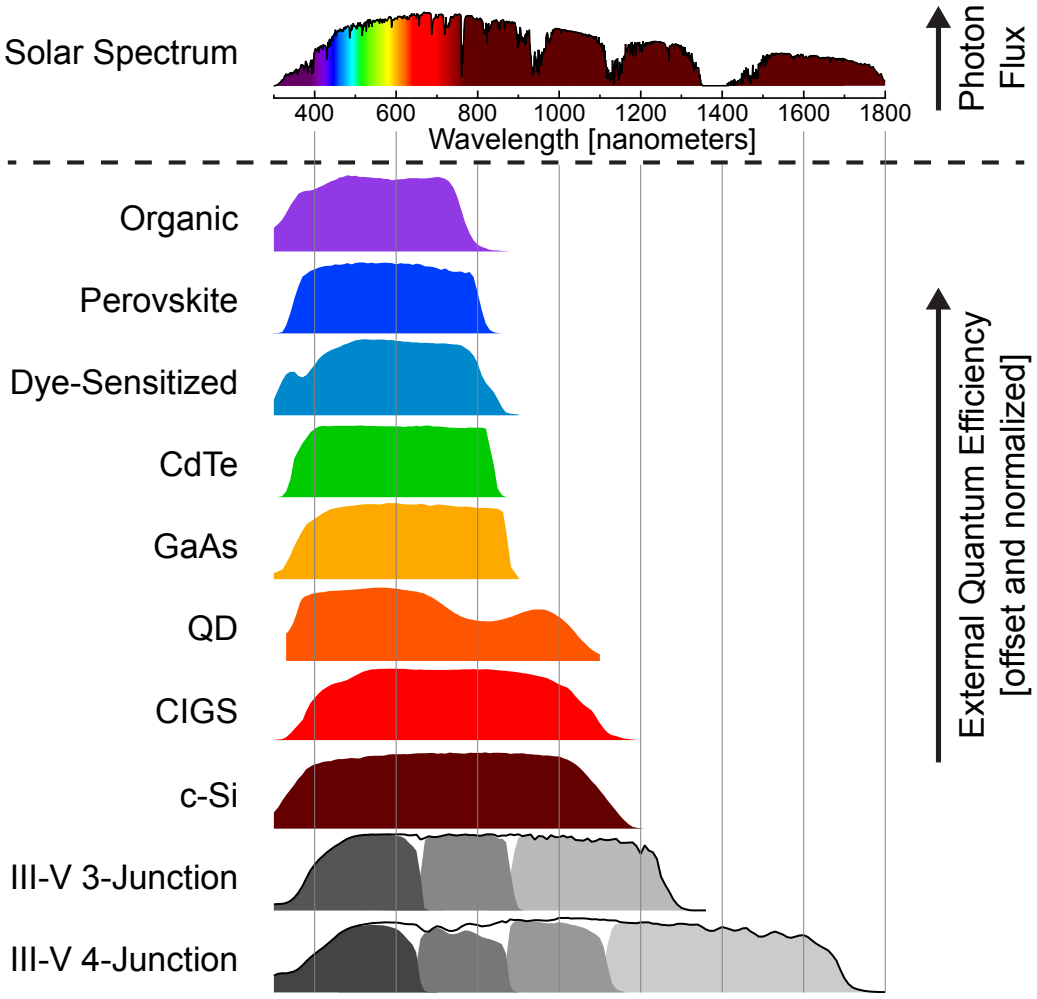

Figure 3-8: **Solar photon flux at the earth's surface and normalized EQE spectra for different types of solar cells.** The top part of the figure shows solar photon flux at the earth's surface as a function of wavelength. The types of solar cell technologies included in the bottom part of the figure are described in more detail by Jean et al. [64] EQE spectra are from Green et al. and Chuang et al. [65, 66, 67, 68, 69, 70]

Chapter 4

Colloidal Quantum Dots

We here provide a brief overview of the distinguishing characteristics of colloidal quantum dots (QDs), their synthesis in solution and deposition as bulk-like thin films, and their application in solar cells.

4.1 Colloidal quantum dots in solution

The term "quantum dot" (QD) typically refers to a system that can be approximated as a potential well that confines electrons and holes in three spatial dimensions, on a length scale smaller than the typical spatial extent of the electron and hole wavefunctions in the bulk QD parent material. In practice, quantum dots can be separated into two types: *epitaxial* quantum dots and *colloidal* quantum dots. Epitaxial QDs are heterostructures consisting of a semiconductor material grown on a parent substrate of a different material, where lattice mismatch between the QD material and parent substrate leads to dewetting of the QD material and island formation in the Stranski-Krastanow growth regime. [136] Colloidal QDs—the subject of this thesis—are nanocrystals of semiconductor material that are synthesized via chemical methods and can be dissolved in solution, typically with the assistance of chemical *ligands* physically adsorbed or chemically bonded to the nanocrystal surface. [137] Colloidal QDs have been synthesized from a wide range of materials, including CdS, CdSe, CdTe, PbS, PbSe, HgTe, InP, InAs, InSb, Si, Ge, and ZnO. [138] In this thesis

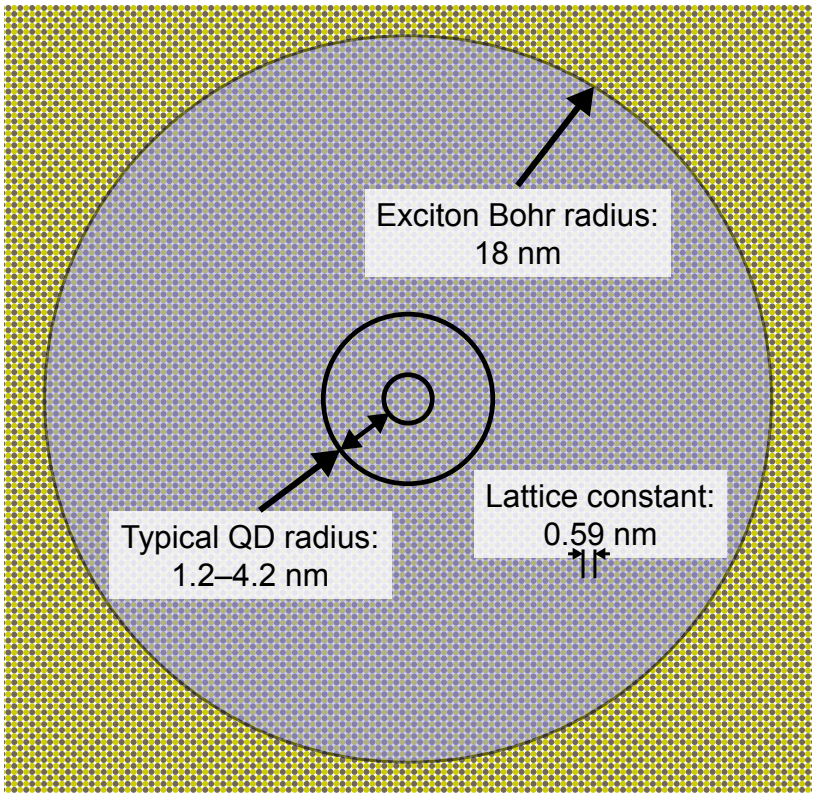

Figure 4-1: **PbS lattice spacing, exciton Bohr radius, and typical QD radius, displayed to scale.** Values are taken from the literature and described in the text. [71, 72, 73, 74, 75]

we confine ourselves primarily to lead sulfide (PbS), a semiconductor with a relatively low bandgap ($E_g = 0.41\,\text{eV}$ at $300\,\text{K}$) and a rock-salt crystal structure. [139, 140, 71]

Figure 4-1 gives an idea of the degree of quantum confinement that can be achieved in PbS QDs. The wavefunction of an excited electron-hole pair, when bound into a hydrogen-atom-like state referred to as an *exciton*, is delocalized in bulk semiconductors to a first approximation over a volume characterized by an exciton Bohr radius

$$r_B = \frac{\hbar^2 4\pi\varepsilon_0\varepsilon_{bulk}}{e^2}\left(\frac{1}{m_e^*} + \frac{1}{m_h^*}\right) \tag{4.1}$$

where $\hbar$ is Planck's constant, ε_0 is the permittivity of free space, e is the charge of the electron, ε_{bulk} is the dielectric constant of the semiconductor, and m_e^* and m_h^* are the effective masses of the electron and hole, respectively.

The bandgap of PbS occurs at the L point of the Brillouin zone, and to first order

the conduction and valence band can be approximated to be symmetric and parabolic. [141, 142] The electron and hole effective masses are given by

$$(m_e^*)^{-1} = \hbar^{-2} \frac{\partial^2 E_C}{\partial k_i \partial k_j} \tag{4.2}$$

$$(m_h^*)^{-1} = \hbar^{-2} \frac{\partial^2 E_V}{\partial k_i \partial k_j}, \tag{4.3}$$

where E_C is the conduction band and E_V is the valence band. The curvature of the conduction and valence bands at the L point is roughly the same, giving $m_e^* = m_h^* = 0.1\, m_e$, where m_e is the rest mass of the electron. [72] The high-frequency dielectric constant of PbS is 17.2, leading to an exciton Bohr radius in PbS of roughly 18 nm. [73] PbS QDs can be synthesized with radii between ∼1.2 nm and ∼4.2 nm, meaning that excitons in PbS QDs are very strongly confined.

As would be expected from a simple particle-in-a-box model (or, even more generally, from the Heisenberg uncertainty principle), confining the electron and hole wavefunctions to a volume smaller than their volume in the bulk material increases the energies of the electron and hole and increases the bandgap over its value in the bulk. As derived by Brus using the effective mass approximation (which is suitable as long as the lattice spacing is significantly less than the QD diameter) and the particle-in-a-sphere model, [137] the energy of the first excited state in a colloidal quantum dot can be approximated to first order by

$$E_g^{QD} \approx E_g^{bulk} + \frac{\hbar^2 \pi^2}{2R^2} \left(\frac{1}{m_e^*} + \frac{1}{m_h^*} \right) - \frac{1.8 e^2}{4\pi \varepsilon_0 \varepsilon_{bulk} R}, \tag{4.4}$$

where R is the radius of the QD. The dominant R^{-2} term represents the increase in energy arising from quantum confinement; the R^{-1} term represents the decrease in energy arising from the extra Coulombic stabilization of the electron and hole arising from their close mutual confinement. More detailed calculations of QD band structure can be made using a $\mathbf{k}\cdot\mathbf{p}$ Hamiltonian, [143, 144, 145] and reproduce the same general trend of increasing QD bandgap (including a shift in the conduction band to shallower energies and a shift in the valence band to deeper energies) with decreasing QD size.

Given their strong confinement, PbS QDs can be synthesized with bandgaps much greater than the bulk PbS bandgap, with reported QD bandgaps ranging from less than 0.7 eV to more than 2.1 eV. [74, 75]

Colloidal QDs are typically synthesized using a relatively simple one-pot batch-based method. [146, 147, 148, 149, 150] In the case of PbS, a lead-containing precursor (typically lead oxide or lead acetate) is dissolved in a solvent mixture including a coordinating solvent (oleic acid) and a non-coordinating solvent (1-octadecene) in a 3-neck flask connected to a nitrogen Schlenk line. As the mixture is heated under vacuum, the Pb^{2+} from lead oxide or lead acetate exchanges with the H^{+} from oleic acid, generating lead oleate. Dissolved oxygen and water boil off under continued heating under vacuum, and the rest of the synthesis is conducted under air- and water-free conditions. At a suitable temperature (90–150 °C), a room-temperature sulfur-containing precursor solution (typically hexamethyldisilathiane dissolved in 1-octadecene) is rapidly injected into the reaction flask, creating a supersaturated solution of Pb^{2+} and S^{2-} precursors. Oleic-acid-coated PbS clusters rapidly nucleate from the supersaturated solution and grow over time as remaining precursor ions add to the clusters. [151] In the ideal case, all of the nucleation sites are formed at the instant of injection and then continue to grow at the same rate, leading to highly monodisperse nanocrystal sizes (standard deviation $<5\,\%$). Further particle growth can occur after consumption of the precursors through Ostwald ripening, whereby small nanocrystals with high surface energy dissociate and transfer their precursors to large nanocrystals with lower surface energy. [146, 147, 152] Nanocrystal growth is quenched by cooling the reaction flask or injecting cold non-coordinating solvent (typically hexane) into the flask. The resulting QDs (dissolved in a mixture of hexane, 1-octadecene, and oleic acid) are then "washed" through a series of precipitation/dissolution cycles. In this process a non-solvent (typically acetone, ethanol, methanol, and/or butanol) is added to the reaction mixture, causing the QDs to precipitate out of the solution. The solution is centrifuged, and the supernatant (containing unreacted precursors, excess oleic acid, and other impurities) is discarded. The concentrated QD precipitate is then redissolved in a non-coordinating solvent (typically hexane or octane), and the washing

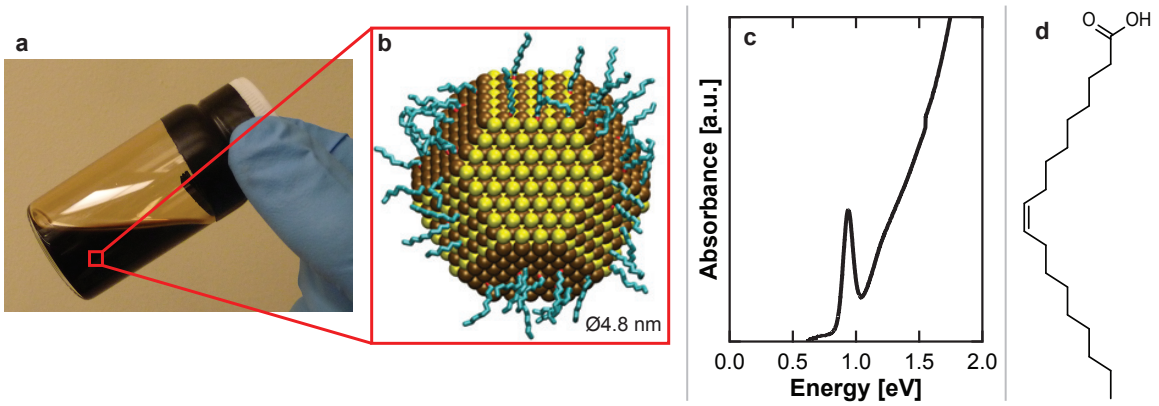

Figure 4-2: **Lead sulfide quantum dots.** **a**, Concentrated solution of PbS QDs with oleic acid ligands, dissolved in octane. **b**, Schematic of a single PbS QD with oleic acid ligands, reproduced from Thompson et al. [76] **c**, Absorption spectrum of colloidal QDs (∼4.7 nm in diameter, determined from a published sizing curve [75]) dissolved in hexane. **d**, Chemical structure of oleic acid.

process is repeated an additional 1–3 times. As large QDs are preferentially collected during the centrifugation step, the washing process can lead to further size-focusing and reduction in the polydispersity of QD diameters. The resulting QDs maintain their stabilizing oleic acid shell, and can be dissolved in a variety of nonpolar solvents. **Figure 4-2** shows a PbS QD solution, with a schematic of a PbS QD coated with oleic acid ligands and an absorption spectrum of PbS QDs in hexane. Note the strong excitonic peak at 0.94 eV (significantly higher in energy than the bulk bandgap of 0.41 eV) and increasingly strong absorption at higher energies.

The fact that PbS QDs synthesized through this process are coated with oleic acid (or negatively charged oleate), which binds to lead rather than sulfur, suggests that the QD surface would be lead-rich. Indeed, mass spectrometry shows that as-synthesized lead chalcogenide QDs are nonstoichiometric and enriched in lead. [153, 154] Deviation from balanced stoichiometry in a binary polar semiconductor leads to doping. In the case of PbS, where lead is in the +2 oxidation state and sulfur is in the −2 oxidation state, extra lead atoms would donate extra electrons to the solid and dope it n-type, while extra sulfur atoms would donate extra holes to the solid and dope it p-type. [155] The stoichiometry of the quantum dot can be tuned by adjusting the identity and density of chemical modifiers adsorbed to the QD surface, as discussed below.

4.2 Colloidal quantum dot solids

The discussion above applies to isolated colloidal QDs in solution. In the context of QD solar cells, we are concerned with colloidal QD solids, where the QDs are packed tightly enough to allow efficient conduction of electrons and holes between QDs.

Solid films of quantum dots can be deposited from a QD solution using a variety of methods including spin-coating, dip-coating, drop-casting, spray-coating, contact printing, and inkjet printing; [156, 113, 111, 112, 157, 158] in this work we use spin-coating. As long as the ligand on the QDs in a solid film remains the same as the ligand on the QDs in solution, the thickness of the film that can be deposited is limited, since adding further QD-containing solution to the film will redissolve QDs that have already been deposited. The original oleic acid ligands can be exchanged by treating a solid film of QDs with a new ligand dissolved in a polar solvent. The polar solvent will not dissolve the QD film, and the ligand—if it either binds more strongly to the QD surface than oleic acid (making exchange thermodynamically favorable), or is present in solution at very high concentration and binds with similar strength to oleic acid (making exchange kinetically favorable)—will displace the original oleic acid ligands on the QD surface. These QDs coated with polar ligands will not redissolve in the original nonpolar solvent, enabling thicker films to be built up in a layer-by-layer process involving sequential cycles of QD deposition followed by ligand exchange, as shown in **Figure 4-3**. One of the goals of ligand exchange, as noted in the next section, is frequently to decrease the inter-QD spacing and improve the conductivity. Replacing oleic acid with shorter ligands leads to volume contraction in the film, and can create islands of QDs separated by voids. [159] Depositing the film in a layer-by-layer process results in filling of inter-QD voids and generates smooth, glassy QD films that are uniform from the micron scale to the millimeter scale, as shown in Figure 4-3.b-d.

The discrete energy levels and sharp energy-level transitions predicted by the particle-in-a-sphere model for QDs can be observed using single-QD spectroscopy at low temperature, [160] but in a solution or a solid film consisting of an ensemble of QDs, polydispersity in the QD size leads to corresponding polydispersity in the

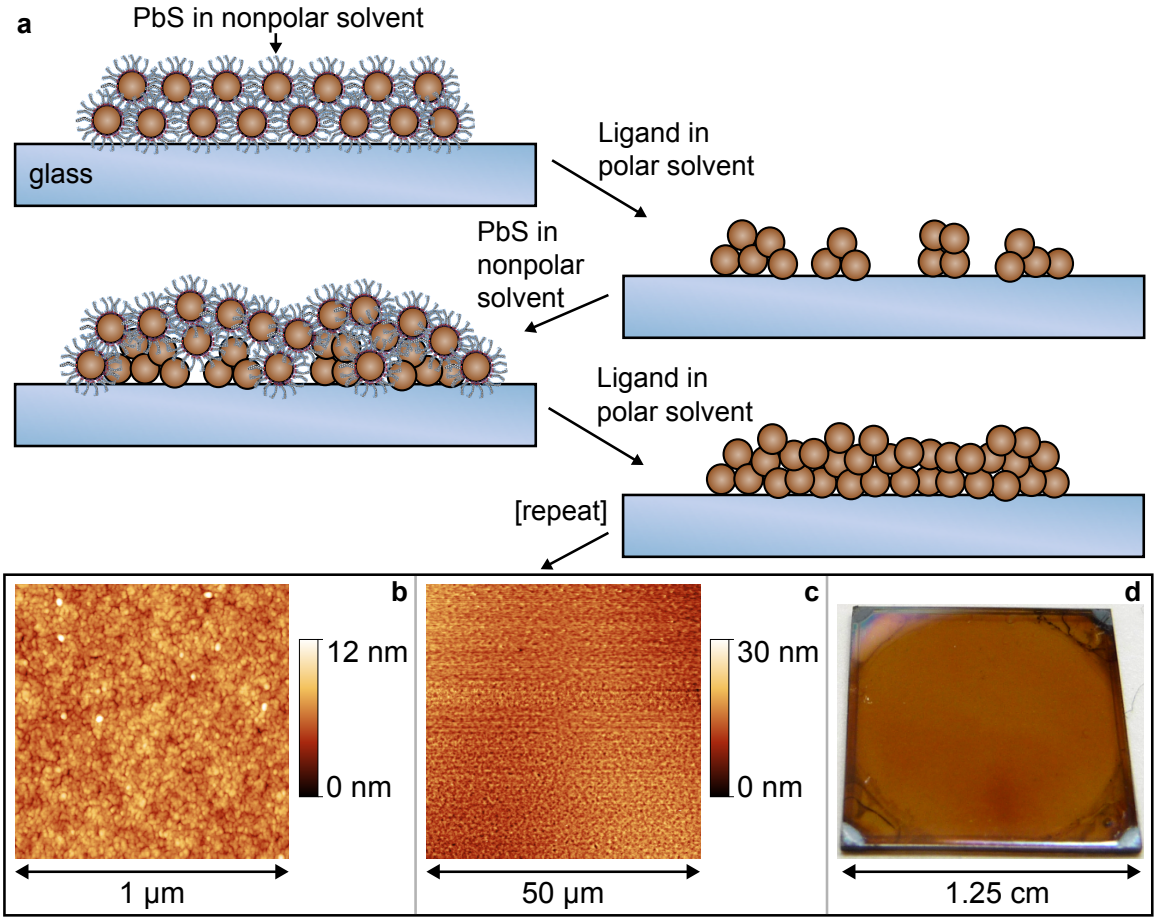

Figure 4-3: **Ligand exchange enables deposition of thick QD films.** **a**, Schematic of the layer-by-layer film deposition and ligand exchange process for PbS QD solids. **b**, **c**, Atomic force microscopy (AFM) images of ligand-exchanged PbS QD films deposited onto sputtered ITO / ZnO on glass, measured on an Agilent 5500 AFM in tapping mode. Both images are leveled by subtracting the line-by-line average and by fitting to a least-squares plane. The image in **c** is smoothed horizontally using a line-by-line second-order polynomial fit to correct for scanner nonlinearity. **d**, Photograph of a spin-coated PbS QD film after several QD/ligand deposition cycles.

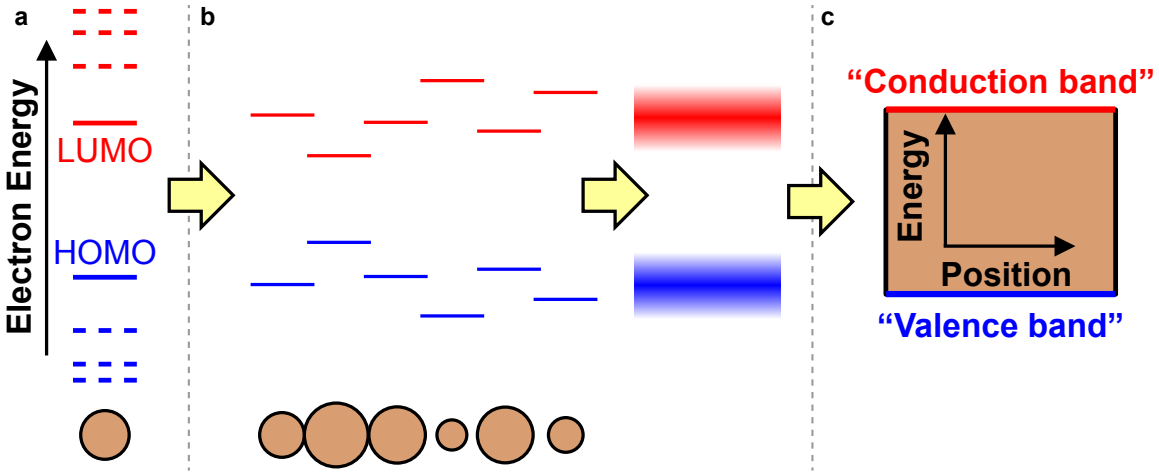

Figure 4-4: **Energy levels of an ensemble of QDs. a**, Energy levels of a single QD. The highest occupied molecular orbital (HOMO) and lowest unoccupied molecular orbital (LUMO) are designated by solid lines; higher excited states for the electron and hole are designated by dashed lines. States occupied by electrons in the ground state are blue; states unoccupied in the ground state are red. **b**, Energy levels for a collection of QDs of varying diameter. The dispersion in HOMO and LUMO levels is exaggerated. The energy levels of the ensemble as a whole are "smeared out" into Gaussian distributions, shown on the right. Note that higher excited states for the electron and hole are left out of this simple picture for clarity; in reality there will be significant density of states above the LUMO distribution and below the HOMO distribution, as suggested by the absorption spectrum in Figure 4-2.c. **c**, The nomenclature used in the rest of this thesis, where the "valence band" refers to the center of the Gaussian distribution of HOMO states and the "conduction band" refers to the center of the Gaussian distribution of LUMO states.

energetic landscape of the ensemble. **Figure 4-4** illustrates the conceptual progression from the discrete energy levels of a single QD (where the bandgap is given by the difference in energy between the highest occupied molecular orbital, or HOMO, and lowest unoccupied molecular orbital, or LUMO, of the QD) to the roughly Gaussian distribution of HOMO and LUMO states in a QD ensemble, the centers of which we term the "valence band" energy and "conduction band" energy, respectively.

While we use the terminology of energy bands, the carrier transport in a QD film is typically not band-like. [161] Given the lack of long-range order in films of randomly-packed QDs, carrier transport occurs via thermally-activated hopping of electrons and holes between individual QDs. The hopping rate between two sites ν_{ij}

can be approximated by the Miller-Abrahams model:

$$\nu_{ij} = \nu_0 \exp(-\beta d) \begin{cases} \exp\left[-\frac{E_j - E_i}{k_B T}\right] & \text{if } E_j > E_i \\ 1 & \text{if } E_j \leq E_i \end{cases}, \tag{4.5}$$

where ν_0 is an attempt frequency, E_i and E_j are the energies of the sites on QDs i and j (conduction band energies for electron transport, and valence band energies for hole transport), d is the distance between sites, k_B is the Boltzmann constant, and T is the temperature. [162, 163] The tunneling coefficient β is given by the WKB approximation:

$$\beta = \sqrt{\frac{2m^* \overline{E}_{barrier}}{\hbar^2}}, \tag{4.6}$$

where $\overline{E}_{barrier}$ is the average height of the barrier potential between sites (which can also be influenced by the identity of the ligand). [163] For randomly packed spherical QDs, the mobility can then be approximated as

$$\mu = \mu_0 \exp\left(-0.865\beta\overline{d}\right) \exp\left[-\frac{\Delta E}{k_B T}\right] \tag{4.7}$$

where $\overline{d}$ is the average inter-QD spacing. [163, 164]

Just as we use the bulk-like concepts of carrier mobility and conduction and valence bands to describe carrier transport in QD solids, the formation of electrical contacts and rectifying junctions between QD solids and other materials can be described using the bulk-like concepts of Ohmic and Schottky contacts. **Figure 4-5** illustrates a prototypical junction between a p-type solid QD film and an electrode. If the work function of the electrode is close to the Fermi level of the QDs, only a small buildup of charge within the QD layer (resulting from accumulation of holes, the majority carrier) is needed to bring the Fermi levels into alignment under equilibrium conditions, and holes can be injected or extracted relatively freely across the interface. If the electrode work function is much shallower than the QD Fermi level, a larger buildup of charge in the QD layer (negative charge in this case, resulting from depletion of the majority holes) is required to bring the Fermi levels into alignment, creating a built-in electric

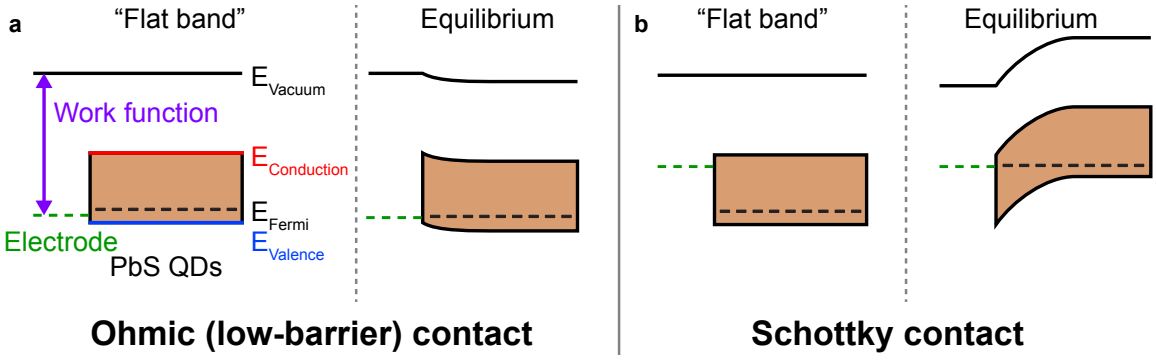

Figure 4-5: **Band diagrams for electrical contacts to QD films.** Flat-band and equilibrium energy levels for prototypical ohmic contact (**a**) and Schottky contact (**b**) to a p-type QD film. The Fermi levels of the electroe and QD film are shown as dashed lines.

field and a rectifying junction at the interface. The width of the depleted region w is given by

$$w = \sqrt{\frac{2\varepsilon\varepsilon_0 V_{bi}}{eN}}, \tag{4.8}$$

where ε is the dielectric constant of the QD solid, V_{bi} is the built-in voltage across the junction, and N is the majority carrier density in the QD film. The width of the depleted region is typically on the order of 100–200 nm for the QDs and electrodes used here.

4.3 Surface chemistry and ligand exchange

In complement to the control over the QD bandgap afforded by modification of the nanocrystal size, the electronic properties of coupled colloidal QD solids can also be tuned through modification of the QD surface chemistry via ligand exchange. [117] A wide variety of ligand chemistries have been utilized for PbS QDs, including bidentate aliphatic and aromatic thiols, [165] primary amines, [117] carboxylic acids, [166] thiocyanate ions, [167] and halide ions. [168] Earlier work in the field primarily focused on short bidentate ligands such as ethanedithiol and hydrazine; the more recent development of atomic halide ligands has led to significant increases in photovoltaic device performance. For a given ligand, the different facets of the rock-salt-structure

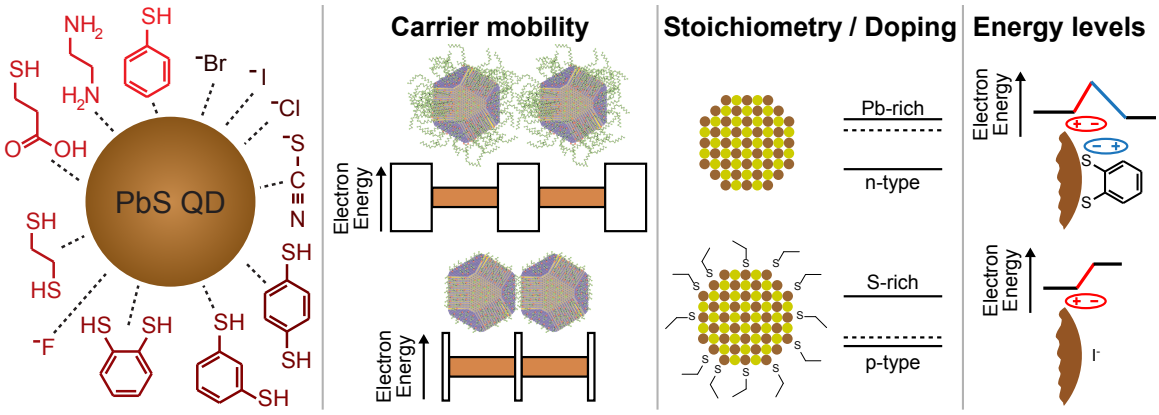

Figure 4-6: **Ligand exchange in colloidal quantum dot films.** QD illustrations in the "carrier mobility" panel are courtesy of Darcy Grinolds and Daniel Harris. Details of the effects shown in the figure are described in the text.

PbS nanocrystals present additional differences in steric opportunities and affinities for ligand binding. [169, 119]

Figure 4-6 illustrates some of the effects that ligand exchange can have on the electronic properties of QDs. We briefly describe these effects here, and explore certain effects in more detail in Chapter 7 and Appendix A.

- **Increased carrier mobility.** The oleic acid ligands originally present on the QD surface in solution are insulating and relatively long (∼1–2 nm). One of the primary motivations for performing ligand exchange is to increase the charge carrier mobility of the QD film by reducing the inter-QD spacing through exchange of the long oleic acid ligands with shorter ligands; Talapin and Murray showed that the conductivity of PbSe QD solids can be increased by 10 orders of magnitude by treating oleic-acid-coated PbS QDs with hydrazine. [117] As expected for a tunneling-mediated process, the carrier mobility increases exponentially with decreasing inter-QD spacing $\overline{d}$ (4.7). [163] Changing the ligand may also affect the energetic height of the tunneling barrier between QDs, further influencing the mobility.

- **Modified QD stoichiometry, doping, and trap density.** As noted above, as-synthesized PbS QDs are enriched with lead on the QD surface, primarily at the PbS(111) facets. [153, 154] In the absence of any ligand passivation, an

as-synthesized PbS QD film would therefore be doped n-type, with a significant density of trap states within the bandgap. [170] Passivation of the QD surface with an appropriate density of negatively-charged ligands balances the stoichiometry, passivates mid-gap trap states, and enables adjustment of the doping character and doping density of the QD film. [117, 171, 118, 170, 154] The QD stoichiometry can also be tuned directly through addition of elemental lead or sulfur. [172, 173]

- **Surface-dipole-induced energy level shifts.** Changing the identity of the chemical binding group and dipole moment of the ligand changes the strength of the QD-ligand surface dipole, shifting the vacuum energy and, in turn, the QD valence band and conduction band energies. [174, 175, 75, 176, 119] This effect is explored in depth in Chapter 7.

- **Dielectric constant.** The QD size, QD core material dielectric constant, and ligand dielectric constant all have an influence on the effective dielectric constant of the QD/ligand composite solid. The dielectric constant of PbS QD thin films has been found to deviate from the predictions of simple models such as volume-weighted effective medium theory, Maxwell-Garnett effective medium theory, and Bruggeman effective medium theory, [177, 178] perhaps due to surface effects or confinement effects within the QD. But in general, increasing the dielectric constant of the ligand (through the use of more polarizable atoms or molecules, such as conjugated aromatic hydrocarbons or large halide ions rather than aliphatic hydrocarbons) should increase the dielectric constant of the film. All else being equal, a higher dielectric constant results in a larger depletion width within the film (4.8), which can increase the probability of photogenerated carrier collection.

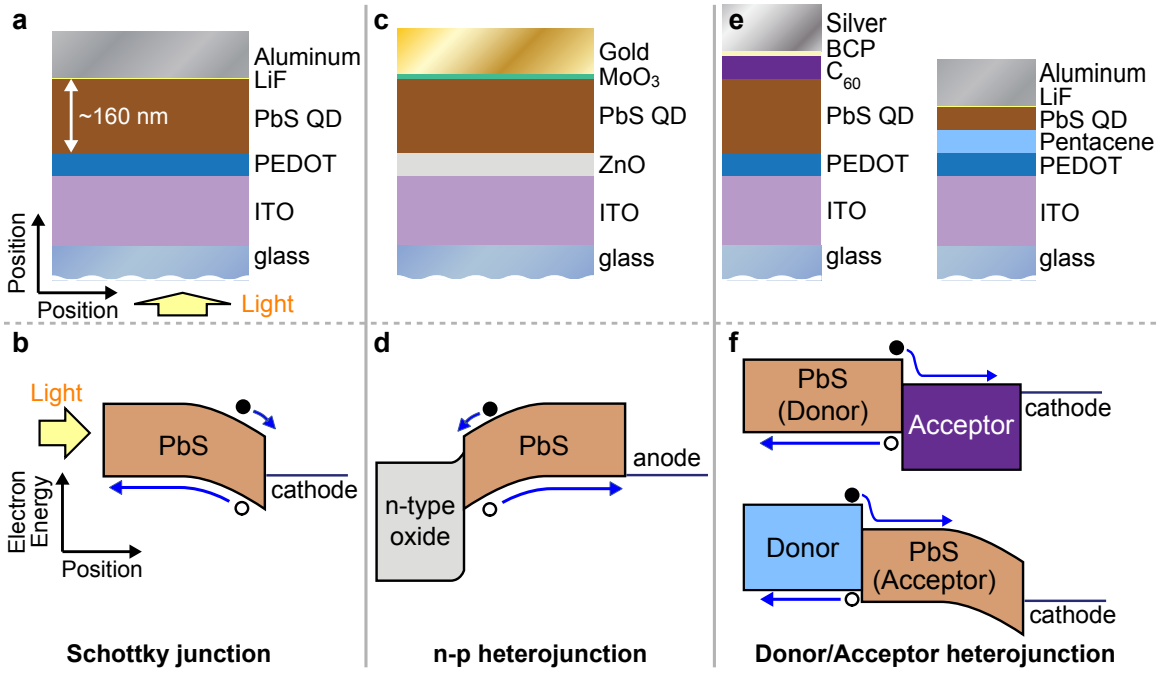

Figure 4-7: **PbS QD photovoltaic device architectures used in this thesis.** Illumination is incident from the bottom in panels **a**, **c**, and **e** and from the left in panels **b**, **d**, and **f**. Layer thicknesses in panels **a**, **c**, and **e** are shown to scale in the direction perpendicular to the substrate. Each device is drawn with a PbS QD layer thickness of 160 nm, corresponding to ~50 monolayers of QDs. Arrows in panels **b**, **d**, and **f** represent the motion of photogenerated electrons and holes under short circuit conditions.

4.4 Quantum dot solar cells

A number of photovoltaic device structures incorporating colloidal QDs have been reported, including QD Schottky diodes, [179, 180, 113, 181] oxide / QD n-p heterojunctions, [115, 87, 77, 166] QD-sensitized solar cells, [182, 183] QD / organic bilayers, [156, 184, 185, 186] and QD / organic bulk heterojunctions. [187, 188] Oxide / QD n-p heterojunctions have shown particular promise, with NREL-certified efficiencies of 10.6 % [189, 116, 53] and lifetimes in excess of 1000 hours [115] reported for ZnO / PbS. **Figure 4-7** shows the solar cell architectures used in this thesis.

Schottky junction devices (Figure 4-7.a-b) rely on the Fermi level offset between the QD layer and a low-work-function cathode to generate a depleted region within the QD film near the cathode interface. A drawback of this architecture is that the device is illuminated from the side of the quasi-neutral region of the QD film. Carrier

collection is less efficient for carriers generated in the quasi-neutral region than for carriers generated in the depleted region, since electrons must diffuse to the depleted region without the assistance of a built-in field and are susceptible to recombination with trapped or free holes during the relatively slow process of diffusion.

Recent work has primarily focused on the n-p heterojunction architecture (Figure 4-7.c-d), which relies on the Fermi level offset between a wide-bandgap n-type oxide (typically ZnO, which is used here, or TiO_2) and the QD layer to generate a depleted region near the oxide/QD interface. This structure has the advantage of being illuminated directly at the deleted side of the QD film, where carrier collection is most efficient. Current-record-efficiency QD PV devices use this architecture. [189, 116, 53]

A third architecture is the donor/acceptor heterojunction (Figure 4-7.e-f), which is similar to the architecture used in organic photovoltaics. The QDs can act either as an electron donor when paired with an organic acceptor such as buckminsterfullerene (C_{60}), or as an electron acceptor when paired with an electron donor such as pentacene. The operation of donor/acceptor heterojunction photovoltaics is primarily dictated by the energy level alignment at the donor/acceptor interface. These devices are not highly efficient, but are useful for characterizing shifts in the energy levels of the QD material. Note that excitons generated in the organic material are unlikely to dissociate on their own given the small dielectric constant and high exciton binding energy of the organic material. Excitons in the organic material must thus diffuse to the interface with the QD layer in order to dissociate into free electrons and holes, where dissociation is aided by the extra energy stabilization that can be gained by moving one carrier through the conduction band or valence band energy offset (a process discussed in more detail in Section 6.3.3). Excitons generated in PbS QD films, on the other hand, are believed to dissociate in the absence of an electric field or dissociating interface. [190, 191] Characterization of devices based on each of these structures can provide different pieces of information about the energy levels and other electronic properties of the QDs used in their fabrication and can lead to greater insight than devices of a single architecture would be able to provide.

Chapter 5

Improved Current Extraction from ZnO / PbS Quantum Dot Heterojunction Photovoltaics Using a MoO_3 Interfacial Layer

Portions of this chapter are reprinted with permission from Brown, P. R.; Lunt, R. R.; Zhao, N.; Osedach, T. P.; Wanger, D. D.; Chang, L.-Y.; Bawendi, M. G.; Bulović, V. *Nano Letters* **2011**, *11*, 2955–2961. [122] Copyright 2011 American Chemical Society.

5.1 Introduction

In Chapters 3 and 4 we described the formation of rectifying junctions between semiconductors (including QD solids) and other semiconductors or metals and how these junctions can be used to provide the driving force for solar cell operation. In particular, we discussed how a Schottky junction can form at the interface between PbS QDs and a low-work-function metal. Schottky junctions at QD-metal interfaces are sometimes desirable—in the case of the Schottky-junction photovoltaic architecture, decreasing the work function of the metal and increasing the magnitude of the Schottky barrier at the interface will increase the V_{OC} and overall performance of the

photovoltaic device. Yet in the case of the (typically more efficient and more stable) n-p heterojunction device architecture, a Schottky junction at the QD / electrode interface would act in opposition to the main n-p heterojunction diode and significantly decrease the efficiency of the device. A deep-work-function electrode (typically gold) is therefore desirable for the top contact in oxide / QD n-p heterojunction devices to avoid the formation of a Schottky barrier, which would impede the extraction of holes from the PbS active layer. [192, 74] However, Gao and Luther have shown that Fermi-level pinning can lead to the formation of a Schottky barrier even between PbS QDs and gold, despite the apparently close alignment between the Fermi level of gold and the valence band edge of PbS QDs. [113, 74] Similar back-contact Schottky barriers have also been noted in CdTe thin-film solar cells, [193] and lead to sizable reductions in the open circuit voltage, fill factor, and efficiency. Achieving high power-conversion efficiency in oxide / QD n-p heterojunction photovoltaics requires the formation of a low-barrier contact between the QD layer and the top-contact anode.

Here, it is demonstrated that the insertion of a thin film of molybdenum oxide (MoO_3) between the PbS photoactive layer and the anode contact inhibits the formation of a Schottky junction at the QD / anode interface. [122] Molybdenum oxide has previously been utilized as a hole-injection layer for organic thin films, [194, 78] as both an electron-blocking layer and a physical buffer layer in photovoltaics, [195, 196, 197, 198, 199, 200, 201] and as a charge-transfer dopant in organic field-effect transistors (FETs). [202] In the architecture described here, the MoO_3 layer, rather than the anode layer, determines the band-bending at the QD interface. The deep-work-function MoO_3 enables the formation of an ohmic contact to PbS and allows even low-work function metals to be used as the anode without forming a voltage-limiting Schottky contact. The MoO_3 thus allows the performance of the device to be effectively decoupled from the properties of the anode material, which enables the use of a transparent ITO anode to optically probe different interfaces within the device and potentially to facilitate the design of stacked multijunction devices. We demonstrate that the removal of this opposing Schottky diode barrier in ZnO / PbS heterojunctions leads to an enhancement in the short-circuit current (J_{SC}), open-circuit voltage (V_{OC}),

and fill factor (FF) of the device, resulting in a power conversion efficiency (η_P) of $(3.5 \pm 0.4)\,\%$ under AM1.5G illumination.

5.2 Methods

Oleic acid-capped PbS QDs with a mean diameter of 3.7 nm (corresponding to an optical energy gap, measured to the first excitonic peak, of $E_g = 1.3\,\text{eV}$) [79] are synthesized via standard literature methods. [186] All fabrication and testing are performed in nitrogen-atmosphere gloveboxes to avoid exposing the QDs to oxygen or water. Prior to device fabrication, the QDs undergo three rounds of precipitation and centrifugation with acetone and 1-butanol, and then are redissolved in octane at $25\,\text{mg}\,\text{mL}^{-1}$ and filtered (0.1 µm PTFE). The ZnO layer (50 nm thickness) is deposited at a rate of $0.05\,\text{nm}\,\text{s}^{-1}$ onto oxygen-plasma-cleaned patterned ITO substrates (obtained from Kintec) via rf-sputtering at 165 W in an atmosphere of 20 mtorr Ar, as described in Leschkies et al. [77] Adhesion of the QDs to plain glass / ITO substrates is increased by pretreating the glass with 12 mM (3-mercaptopropyl)trimethoxysilane in toluene for 12 h; no pretreatment is necessary for deposition onto ZnO. The QD films are deposited via sequential spin-casting, as described elsewhere. [87, 186] For each layer, ~15 µL of PbS solution is spin-cast at 1500 rpm for 60 s; the film is then dipped into a solution of 1.7 mM 1,3-benzenedithiol (BDT) in acetonitrile for 30 s, which is followed by a 3 s dip in pure acetonitrile to remove excess BDT. This process is repeated 2 to 10 times to generate QD films with thicknesses between 45 nm and 220 nm, with each iteration resulting in the deposition of approximately 20 nm of QDs. Unless otherwise noted, 8 spins are employed to generate a film 175 nm thick. The MoO_3 (Alfa, 99.9995%), Au, and Ag films are deposited via thermal evaporation at a rate of $\sim 0.1\,\text{nm}\,\text{s}^{-1}$ at a base pressure of 1×10^{-6} torr. The ITO (Plasmaterials) is deposited via rf-sputtering in a 3–5 mtorr Ar atmosphere, where the first 20 nm of the film thickness is deposited at a rate of $0.005\,\text{nm}\,\text{s}^{-1}$ using a low sputtering power of 7 W to minimize damage to the underlying PbS film; the remaining ~80 nm of ITO film is deposited at $0.05\,\text{nm}\,\text{s}^{-1}$ and 50 W. The device area is defined by the anode-cathode

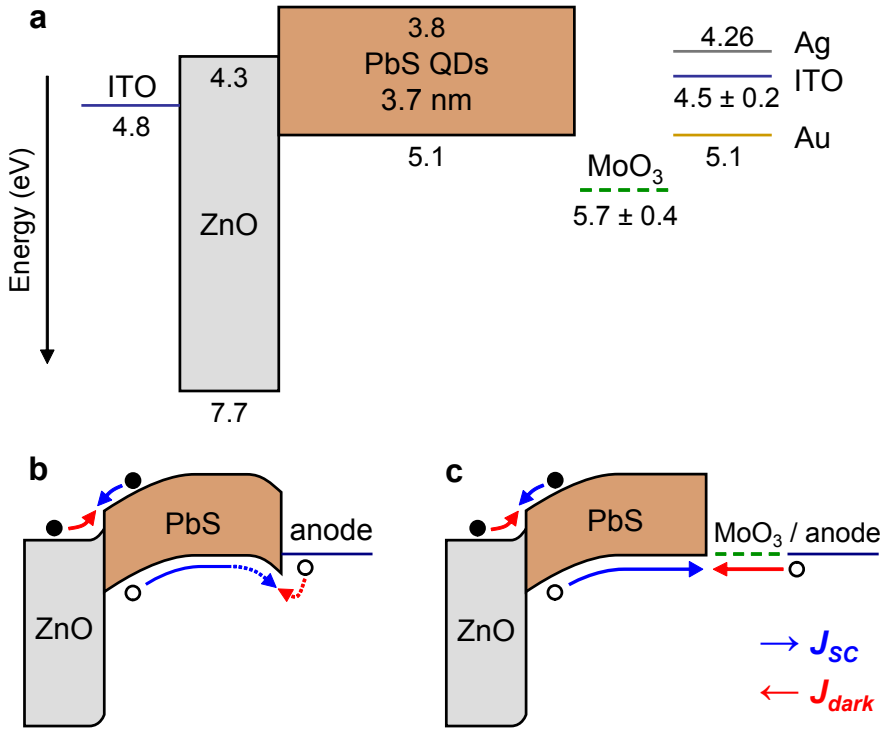

Figure 5-1: **Band diagrams of a ZnO / PbS n-p heterojunction photovoltaic device under different conditions.** **a**, Flat-band energy level alignment of the thin films constituting the ZnO / PbS heterojunction photovoltaic device. Band energies are given in eV and are taken from the literature. [77, 78, 79, 80] Illumination under normal operation is incident from the ZnO side. **b**, Proposed band-bending in the MoO_3-free device, showing the depleted n-p heterojunction at the ZnO / PbS interface and a hole-current-limiting Schottky contact at the PbS / anode interface, and **c**, the removal of the Schottky contact following the insertion of MoO_3 between PbS and the anode material.

overlap to be 1.24 mm^2. The current density-voltage (J-V) measurements are recorded by a Keithley 6487 picoammeter, the capacitance-voltage (C-V) measurements are recorded by a Solartron 1260 impedance analyzer, and $(100 \pm 10)\,mW\,cm^{-2}$ illumination is provided by a nitrogen-glovebox-integrated 150 W xenon arc-lamp (Newport 96000) equipped with an AM1.5G filter. The external quantum efficiencies (EQE) are measured without bias illumination or voltage.

5.3 ZnO / PbS heterojunction

Figure 5-1 shows the flat-band energy level diagram of the device, with energy values

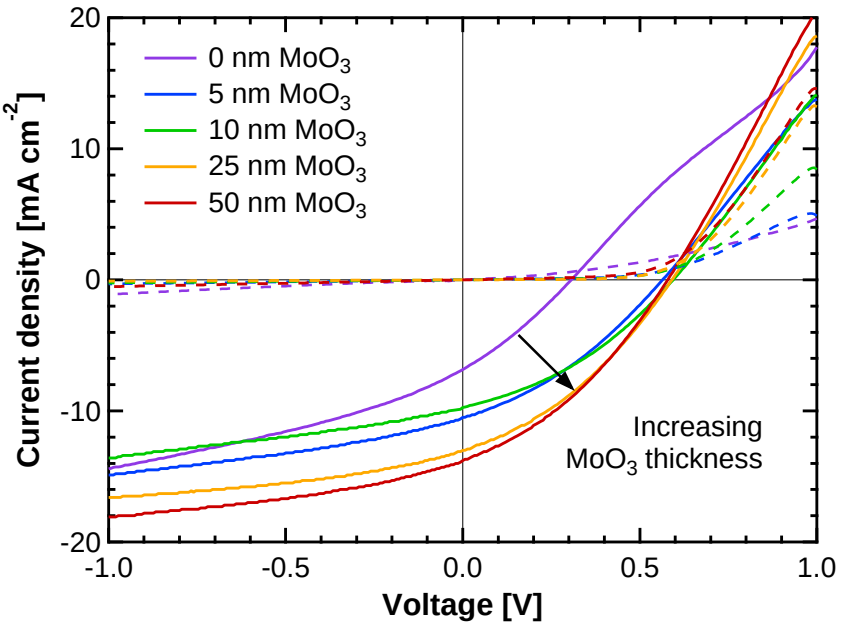

Figure 5-2: ***J-V* characteristics measured in the dark (dashed lines) and under $(100 \pm 10)\,\mathrm{mW\,cm^{-2}}$ AM1.5G illumination (solid lines) for ITO / ZnO / PbS / MoO_3 / ITO devices with varying thicknesses of MoO_3.** Each curve represents the average of seven to ten devices fabricated on the same substrate. The roll-over in light current observed at $+0.5\,\mathrm{V}$ for the device without MoO_3 is ascribed to the presence of a Schottky junction at the anode contact. The addition of MoO_3 alleviates this roll-over and simultaneously increases the J_{SC}, V_{OC}, FF, and η_P.

taken from the literature. [77, 78, 79, 80]. The inclusion of the MoO_3 interlayer in the device structure strongly influences the J-V characteristics, as shown in **Figure 5-2** for a series of devices with an ITO anode, all illuminated from the ZnO side. For the device without MoO_3, a "roll-over" in the forward-bias photocurrent at $V > 0.5\,\mathrm{V}$ is observed, similar to that reported by Gao et al. for ZnO / PbS heterojunction devices employing a silver anode [74] and by Lin et al. for CdS / CdTe / Ni devices. [203] The roll-over is consistent with the presence of a Schottky barrier at the PbS / anode contact in opposition to the n-p heterojunction diode formed at the ZnO / PbS interface. Such a Schottky barrier would impede the extraction of holes from the PbS active layer, limiting both the dark current and the photocurrent in forward bias and reducing the V_{OC}, as is observed in Figure 5-2. The incorporation of MoO_3 between the PbS and the top ITO contact reduces this roll-over effect, simultaneously increasing the J_{SC}, V_{OC}, and FF of the device and resulting in up to a 4.5-fold increase in the

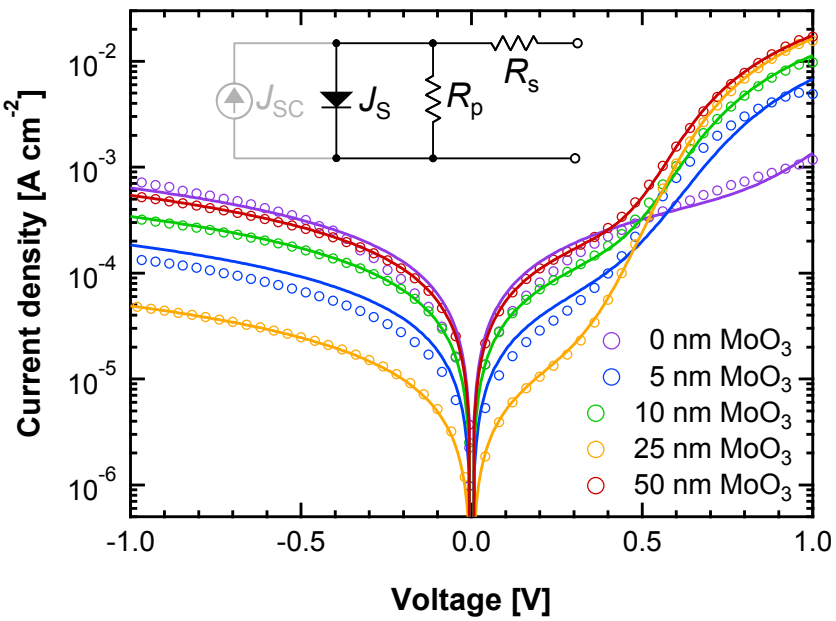

Figure 5-3: **Dark current for representative ITO / ZnO / PbS / MoO_3 / ITO devices with varying MoO_3 thickness (circles) and fit to the generalized Shockley equation (solid lines).** The diode fitting parameters R_p, R_s, J_S, and n defined in the text are reported in Table 5.1. The improved fit to the single-diode equation with increasing thickness of MoO_3 reflects the attenuation of the back Schottky diode, and a diode ideality factor of $n = 2.0 \pm 0.1$ for the device employing 50 nm of MoO_3 indicates that the behavior of this device is well-described by a single diode model.

power conversion efficiency, from $\eta_P = 0.64\%$ without MoO_3 ($J_{SC} = 7.2\,\mathrm{mA\,cm^{-2}}$, $V_{OC} = 0.31\,\mathrm{V}$, and FF = 0.29) to $\eta_P = 2.9\%$ with a MoO_3 thickness of 50 nm ($J_{SC} = 14.6\,\mathrm{mA\,cm^{-2}}$, $V_{OC} = 0.58\,\mathrm{V}$, and FF = 0.35).

The effects of the MoO_3 interlayer are also discernible in the dark J-V characteristics. In **Figure 5-3**, the dark current for a range of MoO_3 thicknesses is plotted along with its fit to the generalized single-diode Shockley equation: [204]

$$J = \frac{R_p}{R_s + R_p}\left\{J_S\left[\exp\left(\frac{e\,(V - JR_s)}{nk_BT}\right) - 1\right] + \frac{V}{R_p}\right\}, \tag{5.1}$$

where R_p is the shunt resistance, R_s is the series resistance, J_S is the reverse saturation current, and n is the diode ideality factor. Fitting parameters are given in **Table 5.1**. An improved fit to the measured J-V data is observed for increasing MoO_3 thickness,

Table 5.1: **Dark J-V fitting parameters for Figure 5-3.** The J-V data are fit to the single-diode Shockley equation (5.1).

MoO_3 thickness [nm]	R_p [Ω]	R_s [Ω]	J_S [$\mathrm{A\,cm^{-2}}$]	n
0	1500	34	2.1×10^{-8}	3.5
5	5400	29	1.6×10^{-7}	2.9
10	2900	23	3.9×10^{-8}	2.3
25	20 400	16	3.2×10^{-8}	2.2
50	1800	16	2.0×10^{-8}	2.0

corresponding to the removal of the Schottky diode at the PbS / anode interface, which is not accounted for by the single-diode equation. A diode ideality factor of $n = 2.0 \pm 0.1$ for a MoO_3 thickness of 50 nm indicates that the J-V behavior of this device is indeed consistent with the single-diode model. An increase in the forward-bias dark current is also observed, which reflects the increased hole extraction efficiency brought about by the reduction in the Schottky barrier height. This effect is consistent with reports of enhanced hole injection into organic hole-transport layers upon insertion of a MoO_3 interlayer between the active organic layer and an ITO anode. [194]

5.4 Semi-transparent Schottky device

The roll-over behavior and interfacial energy level alignment are further explored by removing the n-type ZnO layer. In this case, the characteristics of the PbS / anode and PbS / MoO_3 interfaces may be probed without interference from the n-p heterojunction diode at the ZnO / PbS interface. **Figure 5-4** compares the J-V characteristics of a glass / ITO_P / PbS / ITO device and a device employing a 5 nm thick interlayer of MoO_3 between PbS and the top ITO electrode (glass / ITO_P / PbS / MoO_3(5 nm) / ITO); ITO_P refers to annealed, O_2 plasma-cleaned ITO, which is expected to form a low-injection-barrier contact to PbS. [180] In-situ sputtered ITO is known to have a lower work function than O_2-plasma-cleaned ITO; [80, 205] thus, for a p-type PbS QD film, a Schottky junction with downward band-bending is expected to form at the top interface of the glass / ITO_P / PbS / ITO device. Without an n-p heterojunction

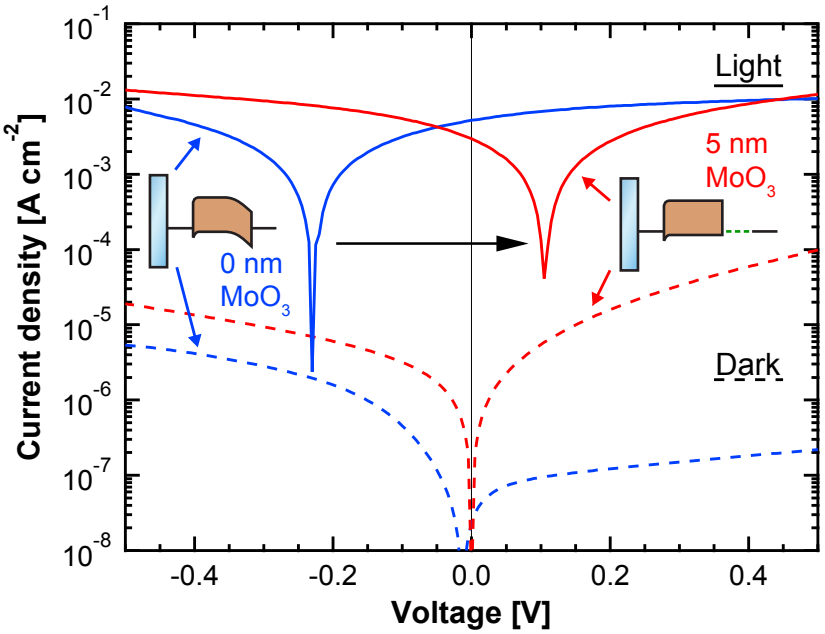

Figure 5-4: ***J-V* characteristics of $\mathbf{ITO_P}$ / PbS / ITO and $\mathbf{ITO_P}$ / PbS / $\mathbf{MoO_3}$(5 nm) / ITO devices in light (solid curves) and dark (dashed curves).** The insets represent the proposed band-bending in each device. A reversal of the diode rectification ratio in dark, and of the polarity of the V_{OC} and J_{SC} in light, indicates the attenuation of the top Schottky contact upon incorporation of MoO_3.

at the bottom interface, this Schottky junction dominates the device performance, explaining the reversal of the polarity and direction of rectification relative to the heterojunction devices shown in Figure 5-2. Upon insertion of MoO_3 between the PbS active layer and the top ITO electrode, a significant change in device operation is observed: the direction of rectification is reversed and the V_{OC} changes polarity from $-0.23\,V$ without MoO_3 to $+0.10\,V$ with MoO_3. The reversal of the direction of rectification and, correspondingly, of the built-in potential shows that the effect does not arise from an asymmetric blocking of photogenerated electrons by MoO_3 or a related exciton-blocking effect. The magnitude and direction of the change in V_{OC} in this Schottky device reflects the ~0.3 V increase in V_{OC} upon the inclusion of MoO_3 in the complete ZnO / PbS heterojunction device, providing further evidence for the role of MoO_3 in diminishing the top-contact Schottky barrier.

The use of transparent ITO as the top contact enables illumination of the device through either the bottom ITO_P / PbS interface or the top PbS / MoO_3 / ITO interface,

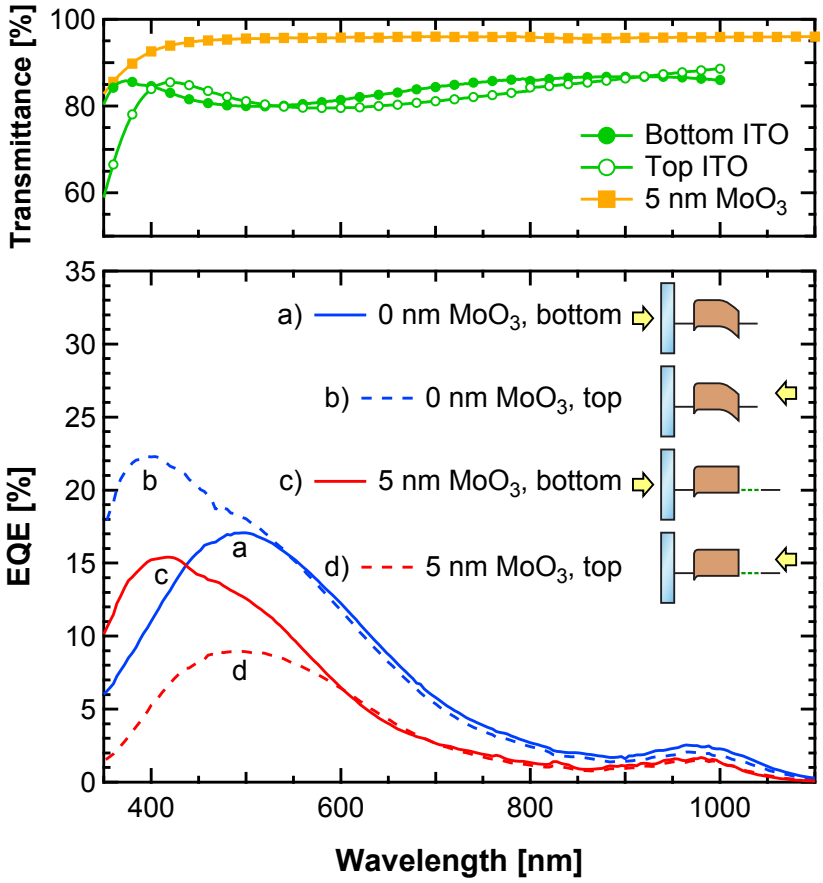

Figure 5-5: **EQE spectra of the ITO_P / PbS / ITO and ITO_P / PbS / MoO_3(5 nm) / ITO devices shown in Figure 5-4, measured with illumination from the bottom (solid lines), as in normal operation, and from the top (dashed lines).** Transmission spectra of the bottom ITO_P, top ITO, and 5 nm MoO_3 layer are included. The inset figures illustrate the proposed change in the spectral response resulting from attenuation of the top Schottky diode by incorporation of MoO_3.

which allows for further characterization of the interfacial energetics. In **Figure 5-5**, the external quantum efficiency (EQE) spectra of the glass / ITO_P / PbS / ITO and glass / ITO_P / PbS / MoO_3(5 nm) / ITO devices described above are displayed for both bottom-illumination (as in normal device operation) and top-illumination. The absorbance of PbS QDs is stronger in the blue region of the spectrum than in the red; for the 3.7 nm-diameter QDs used here, $\alpha^{-1} \approx 55$ nm for wavelength $\lambda = 400$ nm, as compared to $\alpha^{-1} \approx 400$ nm for $\lambda = 600$ nm, where α is the optical absorption constant. Thus, in a spectrally resolved measurement of the EQE, the blue region of the EQE primarily corresponds to the current resulting from carrier generation

near the illuminated interface, while the red region of the EQE corresponds to carrier generation throughout the bulk of the active layer. [113, 206] A close match between the transmission of the bottom ITO electrode and the top ITO electrode, as well as the high transmission of the 5 nm-thick MoO_3 film (>90% for $\lambda > 380$ nm), indicates that differences in the EQE spectra can primarily be ascribed to changes in device internal efficiencies rather than optical absorption.

For the device without a MoO_3 interlayer, the EQE peaks at a greater magnitude and lower wavelength for top-illumination ($\lambda_{max,top} = 392$ nm) than for bottom-illumination ($\lambda_{max,bottom} = 500$ nm). This trend supports a more strongly photoactive top section of the device, which is consistent with the identification of a Schottky junction at the top PbS / ITO interface that sweeps electrons to the top ITO electrode and holes to the bottom ITO_P electrode. This polarity is opposite from the intended operation of the complete ZnO / PbS device. In contrast, for the device incorporating a 5 nm MoO_3 interlayer, the EQE peaks at a lower wavelength for bottom-illumination ($\lambda_{max,bottom} = 420$ nm) than for top-illumination ($\lambda_{max,top} = 496$ nm). The 4-fold decrease in top-illuminated EQE at $\lambda = 400$ nm for the MoO_3-containing device relative to the MoO_3-free device, in conjunction with the polarity reversal of the photocurrent, directly corresponds to the attenuation of the Schottky-junction-induced depletion region at the PbS / anode interface. It also suggests that, while the work function of MoO_3 is greater than the ionization energy of PbS (Figure 5-1), the MoO_3 does not appear to induce significant upward band-bending at the interface, which would provide an additional driving force for exciton dissociation and hole collection at the top interface (although a later study by Gao et al., [207] which employs ultraviolet photoelectron spectroscopy to examine the energetics of the PbS / MoO_3 interface, suggests that there could be some degree of upward band-bending in the PbS layer at the interface). A weak downward band-bending at the bottom ITO_P / PbS interface would then explain the greater low-wavelength EQE in bottom illumination than in top illumination for the MoO_3-containing device. We note that in this particular experiment the EQE for the MoO_3-free device corresponds to photocurrent of polarity opposite to that generated at the ZnO / PbS heterojunction, representing a loss mech-

anism in the complete device. The inversion of polarity and overall decrease in EQE for the device incorporating MoO_3 indicate the attenuation of this loss pathway.

5.5 Electrode and thickness dependence

While the choice of ITO as the anode material allows optical characterization of the PbS / MoO_3 interfacial energetics and a direct demonstration of the effect of MoO_3 in attenuating the back-contact Schottky barrier, it also introduces transmissive losses for long-wavelength light. Capping the ITO anode with a reflective layer of silver allows for greater optical absorption in a thinner, and correspondingly less resistive, PbS active layer; optical simulations show that for the PbS active layer thicknesses used here, the incorporation of a silver back reflector results in a 30% increase in the integrated absorption. [122] In **Figure 5-6**, the *J-V* characteristics of a complete ITO_P / ZnO / PbS / MoO_3(10 nm) / ITO(100 nm) / Ag heterojunction device are displayed for a range of active layer thicknesses. A linear increase in J_{SC} is observed with increasing PbS thickness up to a PbS thickness of 175 nm. This result is consistent with Mott-Schottky measurements indicating a (200 ± 30) nm depleted region in PbS at the heterojunction interface (Figure 5-9 in Section 5.6). For an active layer thickness less than or equal to the depletion width, efficient carrier generation and transport is achieved throughout the entire active layer as a result of the built-in electric field. For PbS thicknesses greater than 175 nm, a rolloff in J_{SC} and a drop in FF is observed, corresponding to a widening of the quasi-neutral region at the rear of the device and a resulting increase in series resistance.

Alternatively, the sputtered ITO layer may be omitted, enabling a metallic anode to be evaporated directly onto the PbS / MoO_3 active layer. If MoO_3 does determine the band-bending at the top PbS interface, as suggested by the results described above using an ITO anode, then the V_{OC} would be expected to be independent of the anode work function for devices employing a MoO_3 interlayer. In **Figure 5-7**, the *J-V* characteristics of ZnO / PbS heterojunction photovoltaics employing ITO, Ag, and Au anodes with and without a MoO_3 interlayer are displayed. The device performance

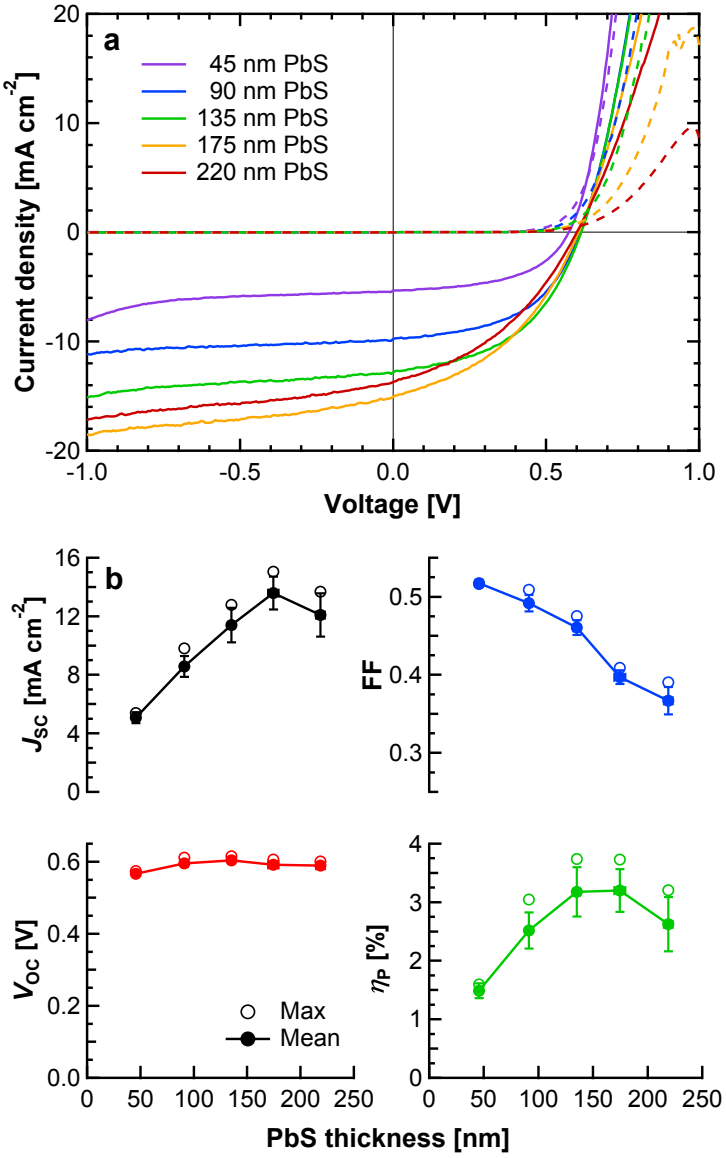

Figure 5-6: **Dependence of PV performance on PbS active layer thickness.** **a**, J-V characteristics of ITO / ZnO / PbS / MoO_3 / ITO / Ag devices employing a 10 nm layer of MoO_3, a 100 nm layer of ITO, and a PbS layer of varying thickness. **b**, Performance characteristics of the above devices. Filled circles and error bars correspond to the average and standard deviation across five to six devices on the same substrate, and empty circles represent the value for the best-performing device. Lines serve as guides to the eye. An efficiency maximum is achieved for a 175 nm-thick PbS layer, with $J_{SC} = (14 \pm 1)\,\mathrm{mA\,cm^{-2}}$, $V_{OC} = (0.59 \pm 0.01)\,\mathrm{V}$, FF $= 0.40 \pm 0.01$, and $\eta_P = (3.2 \pm 0.4)\,\%$.

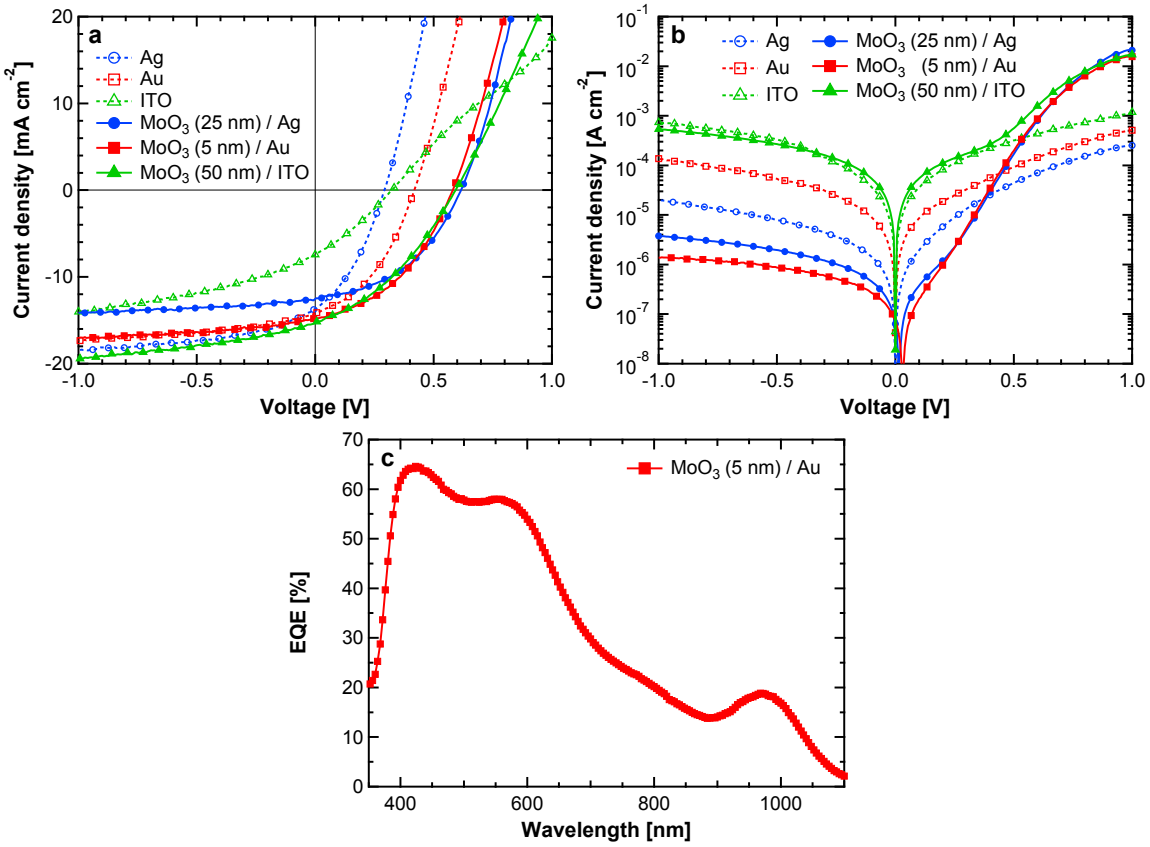

Figure 5-7: **PV performance with different electrode materials.** **a**, J-V characteristics under illumination of representative ITO / ZnO / PbS / MoO_3 / anode devices with varying thicknesses of MoO_3, where the anode is Ag (blue circles), Au (red squares), or ITO (green triangles). **b**, Dark J-V characteristics of the same devices, showing an increase in forward bias dark current corresponding to a reduction of the Schottky barrier for holes. **c**, EQE spectrum of a representative ITO / ZnO / PbS / MoO_3 / Au device employing a 5 nm-thick layer of MoO_3. Integrating the product of the EQE with the AM1.5G solar spectrum yields a J_{SC} of 14.4 mA cm^{-2}, in close agreement with the measured J_{SC} of 14.8 mA cm^{-2}.

parameters (J_{SC}, V_{OC}, η_P, FF, R_p, and R_s) are summarized in **Figure 5-8**, and complete J-V curves are included in Figure 5-10 in Section 5.6. A convergence of the V_{OC} with increasing MoO_3 thickness is indeed observed, irrespective of the anode material. For devices without a MoO_3 interlayer, the V_{OC} varies with the anode work function in a manner reflecting the presence of a Schottky contact between the p-type PbS active layer and the anode, with a lower V_{OC} obtained for lower-work function materials (V_{OC} = 0.29 V for Ag, 0.31 V for ITO, and 0.41 V for Au, which have work functions of 4.3, 4.5 ± 0.2, and 5.1 eV, respectively [80, 208]). However, for a sufficiently thick layer of MoO_3, the V_{OC} increases to (0.59 ± 0.01) V for each of the electrode materials, despite a difference of up to 0.8 eV in the electrode work functions. For all three electrodes, an increase in the forward-bias dark current upon the insertion of MoO_3 further reflects the transition from a Schottky contact to an ohmic contact at the PbS / anode interface. The 2.3-fold increase in η_P for the Ag-anode device (η_P = 1.4% without MoO_3 and 3.1% with 25 nm-thick MoO_3) and 1.5-fold increase for the Au-anode device (η_P = 2.3% without MoO_3 and 3.5% with 5 nm-thick MoO_3) demonstrate the dramatic effect of this improved contact on the device performance.

A different trend is observed in the variation of J_{SC} and R_s with MoO_3 thickness for the three anode materials. For Au, a maximum in the J_{SC} occurs at a MoO_3 thickness of 5 nm, while for Ag, the maximum J_{SC} is obtained for 25 nm-thick MoO_3. For ITO, however, the J_{SC} continues to increase with increasing MoO_3 thickness, reaching a maximum at 50 nm-thick MoO_3. Optical simulations show that this increase in J_{SC} is not due to an interference effect resulting from the addition of MoO_3 between the active layer and the anode. [122] An increase in R_s is seen with increasing MoO_3 thickness for Ag and Au, while for ITO the R_s is observed to decrease for thicker MoO_3 layers. These opposing trends are possibly explained by the reported observance of a "dead zone" at the interface between PbS and sputtered ITO, [206] resulting from damage to the underlying PbS layer induced by the high-energy reactive ions present during the ITO sputtering process. The MoO_3, which is thermally evaporated, is expected to act as a physical protective layer for the underlying PbS during sputtering of the ITO, with a thicker MoO_3 layer providing better protection and a correspondingly

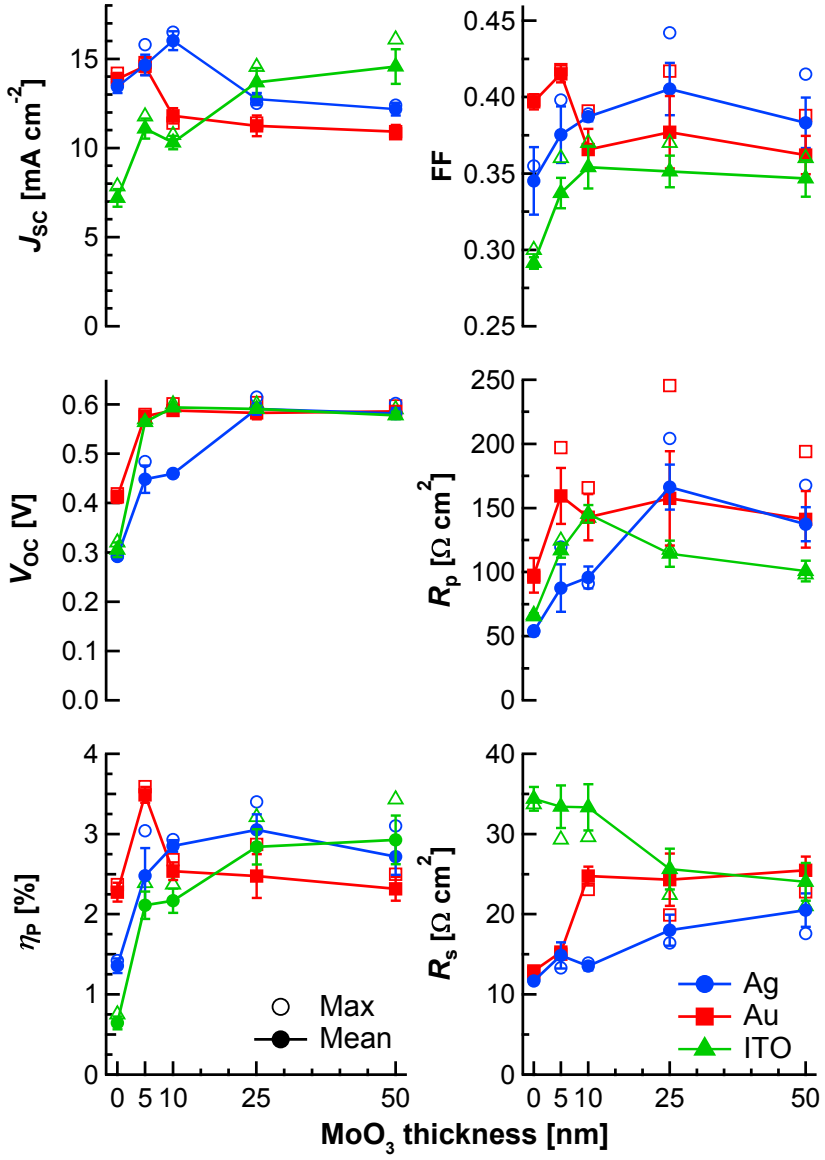

Figure 5-8: **Device parameters of ITO / ZnO / PbS / MoO_3 / anode devices as a function of MoO_3 thickness.** Filled circles and error bars correspond to the average and standard deviation across eight to ten devices on the same substrate, and empty circles represent the value for the best-performing device. Lines serve as guides to the eye. Complete J-V characteristics of the Ag- and Au-anode devices are included in Figure 5-10 in Section 5.6. R_p and R_s are obtained from the inverse of the slope of the light J-V curve at $V = 0$ and $V = V_{OC}$, respectively.

lower R_s and higher J_{SC}. The high V_{OC} and FF observed in Figure 5-8 for the device employing a thin 46 nm-thick layer of PbS suggests that MoO_3 is indeed effective in preventing damage to the PbS, although the low sputtering power used here (7 W, vs. 30 W used by Barkhouse et al. [206]) may also reduce the level of damage. Further work is necessary to characterize chemical or structural changes at the PbS / anode interface if sputtered top electrodes are to be widely employed.

We note that the work function and band energies of MoO_3 presented in Figure 5-1 have been subject to some debate, with reported values differing by ±1 eV for the work function and ±4 eV for the electron affinity and ionization energy. [194, 195, 209] Much of this disagreement may stem from differences in measurement conditions, as Irfan et al. [210] and Meyer et al. [211] have shown that the work function of thermally evaporated MoO_3 decreases from 6.8 eV in ultrahigh vacuum (UHV) to 5.7 eV after brief exposure to ambient conditions. The lower value for the work function is perhaps more representative of the MoO_3 employed here, as our devices are exposed to an ambient-pressure atmosphere of nitrogen inside a glovebox between UHV deposition of the MoO_3 and anode layers. The observation of electron-blocking characteristics reported in organic photovoltaics [197] suggests a p-type character for MoO_3, where the MoO_3 functions to transport holes and block back-electron transfer from PbS to the anode; however, an n-type character for MoO_3, involving electron injection from the anode into MoO_3 and subsequent recombination of photogenerated holes and injected electrons at the PbS / MoO_3 interface, is more consistent with ultraviolet photoemission spectroscopy results reported elsewhere. [194] In FET measurements performed within this study (not shown here), no field effect was observed for MoO_3, so an assignment of n-type or p-type character was unable to be made; nevertheless, a work function of ~5.7 eV, which is experimentally agreed upon for ambient-exposed MoO_3, would induce a similar change in the PbS energy levels regardless of the MoO_3 doping type.

Some previous reports on the incorporation of MoO_3 into photovoltaic devices have ascribed an increase in efficiency to a reduction in series resistance resulting from improved hole extraction from the p-type donor through the high-work function

MoO_3, [196, 203] while others have attributed it to a decrease in dark current and concomitant increase in shunt resistance, identifying an electron-blocking character as the primary contribution of MoO_3. [197, 199] Both effects are observed in the present study, although the improvement in hole extraction resulting from removal of the top Schottky barrier plays the dominant role. For each of the three electrode materials, the shunt resistance is increased upon incorporation of MoO_3 (Figure 5-8), although the increase is not monotonic with MoO_3 thickness. This increase in shunt resistance reflects a general reduction in reverse-bias leakage current in the dark (Figure 5-7.b), although the dark leakage current has also been observed to vary significantly without a strong effect on the light J-V characteristics (Figure 5-11 in Section 5.6). The key distinction between the devices described here without MoO_3 and those described by Li et al. [197] is a more pronounced crossover between the light and dark current in forward bias in our devices (Figure 5-2.a). This deviation from ideal single-diode behavior indicates that a low forward bias current in the dark does not necessarily translate into a high V_{OC} in the light. Instead, the forward-bias dark current and the V_{OC} increase simultaneously upon incorporation of MoO_3 (Figure 5-7.a-b). While an electron-blocking character for MoO_3 may still play a role, the polarity reversal and spectral shift of the ITO_P / PbS / ITO device in Figures 5-4 and 5-5 suggest that the primary impact of MoO_3 on the device performance is due to the attenuation of the top-contact Schottky barrier. The crossover effect has been observed to varying degrees in organic, [212] QD, [74] CdS / Cu_2S, [213] and CdS / CdTe [214] photovoltaics, and has been attributed to a variety of factors. A more complete understanding of the determinants of this effect could lead to further improvements in V_{OC} and FF for QD photovoltaics.

In summary, the performance of ZnO / PbS QD heterojunction photovoltaics is significantly enhanced through engineering of the charge extraction barrier at the anode contact. The insertion of a MoO_3 thin film between the PbS active layer and the top-contacted anode improves the J_{SC}, V_{OC}, FF, and η_P simultaneously for a variety of anode materials. The high-work-function MoO_3 film prevents the formation of a Schottky junction at the anode contact, which could impede the extraction of

holes from PbS. Similar results were later reported by Gao et al. [207] We show that this device structure effectively decouples the device performance from the work function of the anode, which allows for the use of a transparent ITO top electrode to optically probe the different device interfaces during operation and which could aid in the future design of stacked tandem QD photovoltaics.

5.6 Supplementary results and discussion

Here we provide a calculation of the depletion width in ZnO / PbS QD photovoltaics, capacitance-voltage measurements on PbS Schottky junction devices, and complete J-V curves for devices in Figure 5-8.

5.6.1 Depletion width calculation

The ZnO / PbS QD interface can be characterized as an abrupt n-p heterojunction, where N_D is the doping density in the n-type ZnO and N_A is the doping density in the p-type PbS QDs. In this case the total depletion width is given by $w = w_n + w_p$, where w_n is the depletion width in ZnO and w_p is the depletion width in the PbS QDs. The depletion widths w_n and w_p are given by

$$w_n = \sqrt{\frac{2\varepsilon_{ZnO}\varepsilon_0 V_{bi}^n}{eN_D}} \tag{5.2}$$

and

$$w_p = \sqrt{\frac{2\varepsilon_{QD}\varepsilon_0 V_{bi}^p}{eN_A}}, \tag{5.3}$$

where ε_{ZnO} is the dielectric constant of the ZnO, ε_{QD} is the dielectric constant of the PbS QD film, ε_0 is the permittivity of free space, e is the charge of the electron, V_{bi}^n is the built-in potential drop in the ZnO, and V_{bi}^p is the built-in potential drop in the PbS QDs. [215] The total built-in potential V_{bi} is given by

$$V_{bi} = V_{bi}^n + V_{bi}^p, \tag{5.4}$$

where

$$N_D V_{bi}^n = N_A V_{bi}^p. \tag{5.5}$$

To calculate w_p, it is thus necessary to obtain V_{bi}, N_D, N_A, and ε_{QD}. The built-in potential V_{bi} is approximated by the crossover point between the light and dark J-V curves, [216] and is found from Figure 5-6.a in Section 5.5 to occur at (0.63 ± 0.02) V. The doping density N_D of Ar-sputtered ZnO is reported to be $1.4 \times 10^{16}\,\mathrm{cm}^{-3}$ for the same growth conditions as in the present work. [77]

The doping density N_A and dielectric constant ε_{QD} of the PbS QD film may be determined from the capacitance-voltage (C-V) characteristics of a Schottky device:

$$N = 2\left[A^2 e \varepsilon_{QD} \varepsilon_0 \frac{d}{dV}\left(\frac{1}{C^2}\right)\right]^{-1} \tag{5.6}$$

where A is the area of the device. [215] **Figure 5-9** shows the J-V and C-V characteristics of an ITO / PbS (190 nm) / LiF (0.9 nm) / Al (100 nm) Schottky device fabricated for the purpose of this study. The C-V characteristics are well-described by a model employing a single capacitor and resistor connected in parallel. Given the low leakage current ($J < 3 \times 10^{-7}\,\mathrm{A\,cm}^{-2}$ in reverse bias), ε_{QD} may be calculated from the average capacitance of the fully-depleted film in reverse bias with knowledge of the film thickness and device area. It is found that $\varepsilon_{QD} = 14 \pm 2$, in reasonable agreement with values reported elsewhere for dithiol-treated PbS QD films. [217] The slope of the Mott-Schottky plot in the linear regime may then be used to calculate the hole density in the PbS QDs, giving $N_A = (1.3 \pm 0.2) \times 10^{16}\,\mathrm{cm}^{-3}$. By (5.3), (5.4), and (5.5), the depletion width in the PbS QDs is found to be $w_p = (200 \pm 30)$ nm.

5.6.2 Supplementary figures

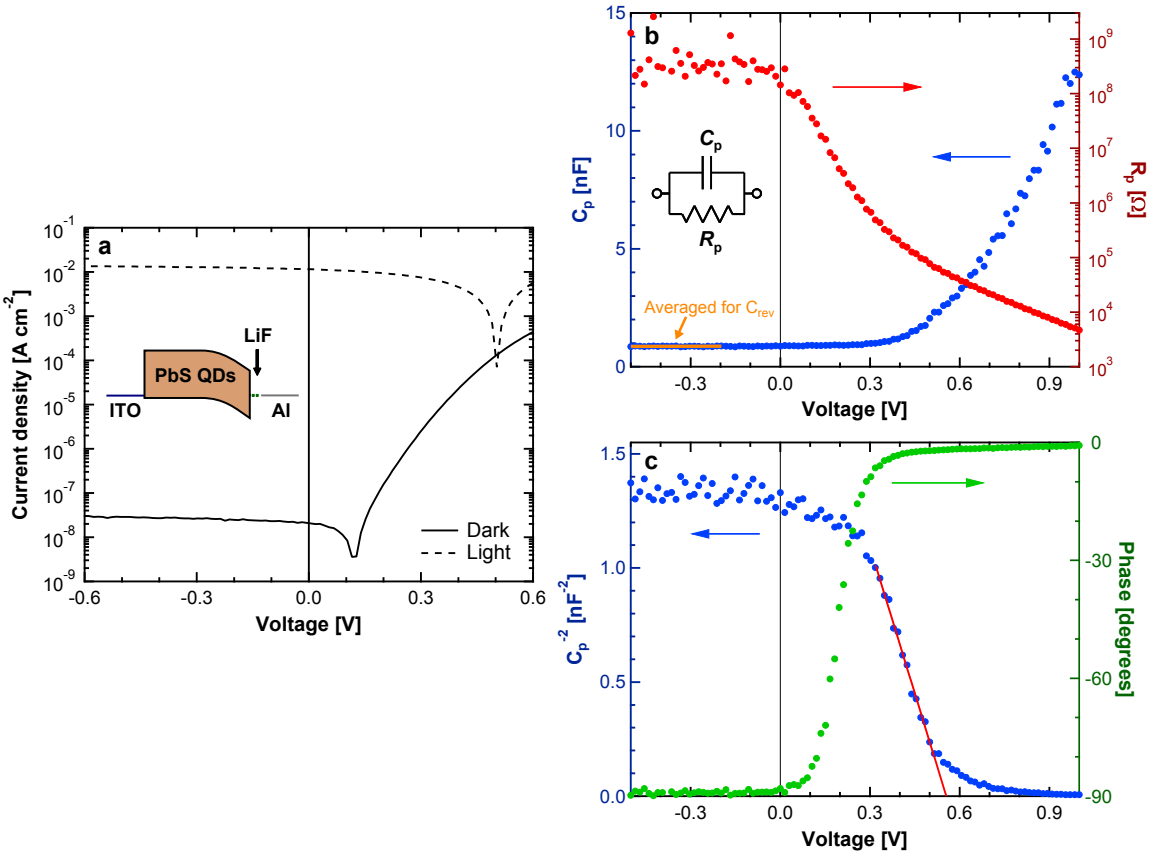

Figure 5-9: **Impedance analysis of a PbS QD Schottky device.** **a**, Device structure and J-V characteristics of an ITO / PbS(190 nm) / LiF(0.7 nm) / Al Schottky device. **b**, C_p-V and **c**, Mott-Schottky plots of the same device. C_p and R_p values are extracted by modeling the device as a single capacitor and resistor in parallel, and the impedance magnitude and phase are measured directly. The capacitance in reverse bias is used to calculate ε_{QD}, and the slope of the Mott-Schottky plot in the linear regime is used to calculate N_A using (5.6).

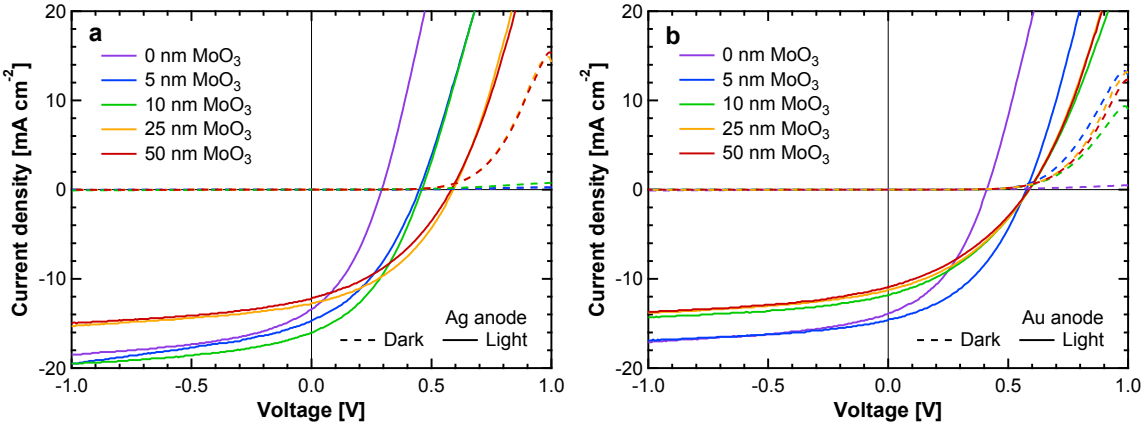

Figure 5-10: **Electrode dependence of photovoltaic performance.** J-V characteristics of ITO / ZnO / PbS / MoO_3 / anode devices with Ag (**a**) and Au (**b**) anodes. Each trace represents the average across 6–10 working devices. The performance parameters are reported in Figure 5-8 in Section 5.5.

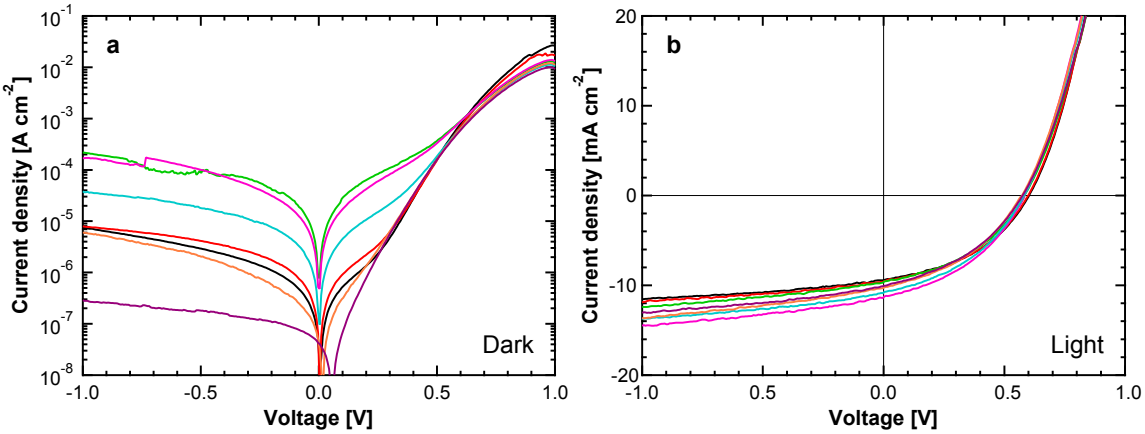

Figure 5-11: **Variability of dark current.** **a**, Dark and **b**, light J-V characteristics of seven ITO / ZnO / PbS / MoO_3 / Au devices fabricated on the same substrate. The large variation in dark leakage current (nearly 3 orders of magnitude) does not significantly impact the device operation in light, showing that a simple reduction in dark current upon inclusion of MoO_3 does not explain the V_{OC} increase reported here.

Chapter 6

Triplet Exciton Dissociation in Singlet Exciton Fission Photovoltaics Probed Using Quantum Dot Bandgap Modification

6.1 Introduction

As noted in Chapter 3, the power conversion efficiency of a conventional single-junction photovoltaic device—one based upon a single light-absorbing semiconductor material under one-sun illumination at room temperature that generates one electron-hole pair for each absorbed photon—is limited to roughly 33 %, a quantity known as the single-junction Shockley-Queisser limit. [50, 51] Yet the Shockley-Queisser limit is not an absolute thermodynamic limit for the conversion of sunlight into electrical energy, and

[i]* These authors contributed equally to the cited work.

a number of strategies have been demonstrated and proposed for achieving efficiencies higher than the Shockley-Queisser limit. Multijunction photovoltaics employ multiple p-n junctions fabricated from semiconductor light absorbers of varying bandgap, with different subcells matched to different parts of the solar spectrum (Figure 3-8). Multijunction photovoltaics are the only devices to have actually demonstrated efficiencies above the single-junction Shockley-Queisser limit, [53] but other phenomena also have the potential to enable access to this efficiency regime. Multiple exciton generation (MEG), which has been observed in some nanocrystalline systems, is a process whereby photons with energy greater than the bandgap generate multiple electron-hole pairs instead of wasting their excess energy as heat, [218, 219] and has been shown to lead to external quantum efficiencies above 100 % in MEG-enhanced solar cells. [220, 221] Hot-carrier solar cells could directly capture the energy of electron-hole pairs excited by photons with energy greater than the bandgap, before the carriers can lose their excess energy as heat, [222] and intermediate-band solar cells could allow the absorption of photons with energy below the bandgap through a two-photon process mediated by an optically active mid-gap state; [223] both architectures would enable greater utilization of photon energy across the broad solar spectrum.

Here, we explore the pairing of lead sulfide colloidal quantum dots (PbS QDs) with an organic material that undergoes *singlet exciton fission*, a form of multiple exciton generation (though we label MEG and singlet fission separately in this chapter). Singlet fission refers to the process whereby an optically excited singlet exciton splits into two lower-energy triplet excitons, thus generating two electron-hole pairs per absorbed photon. [224] The incorporation of singlet-fission-sensitized materials into solar cells has the potential to unlock efficiencies beyond the Shockley-Queisser limit, but only if the triplets generated by singlet fission can be efficiently dissociated and the singlet fission material is paired with a complementary lower-bandgap light-absorbing material. [51] We demonstrate that PbS QDs are an attractive material candidate for singlet fission photovoltaics—not as a singlet fission material themselves, but as an electron acceptor and low-bandgap absorber paired with a higher-bandgap singlet-fission-sensitized electron donor. [83, 225, 226] We find that PbS QDs can

accept electrons from triplets generated by singlet fission in pentacene, and explore the dependence of the triplet dissociation process on the energy levels of the QDs. The small bandgap of large-diameter PbS QDs makes them well-suited to act as complementary absorbers for large-bandgap singlet fission materials, and the ability to tune the conduction band energy of QDs enables precise probing and optimization of the triplet dissociation process, which depends on the energy level alignment at the donor-acceptor interface.

We first introduce the theory behind the Shockley-Queisser limit and describe how different solar cell architectures can move beyond this limit. We then provide a brief overview of the singlet fission process and describe the architecture and operation of our pentacene / PbS QD photovoltaic devices. We show how the external quantum efficiency spectrum of these devices can provide information on the efficiency of triplet dissociation at the pentacene / PbS QD interface, and we demonstrate that triplet dissociation occurs only when the energy offset between the pentacene highest occupied molecular orbital (HOMO) and the PbS QD conduction band is less than the pentacene triplet energy. While the power conversion efficiency attained by these pentacene / PbS QD photovoltaics is not high, characterization of this architecture provides valuable insights into the processes of singlet fission and triplet dissociation in singlet-fission-sensitized photovoltaics and identifies numerous avenues for further study and optimization.

6.2 The Shockley-Queisser limit

The solar cell efficiency limit derived by Shockley and Queisser applies to a single-junction semiconductor absorber at temperature $T_{earth} = 300\,\mathrm{K}$ at the earth's surface under illumination from the sun (which is approximated by a blackbody at $T_{sun} = 6000\,\mathrm{K}$). [50] It has since been recalculated using the NREL AM1.5G reference spectrum (shown in Figure 2-4 [39]) by Hanna and Nozik. [51] **Figure 6-1.a** provides a schematic representation of the current/voltage tradeoff inherent in using a typical single-bandgap semiconductor to capture energy from the broad spectrum of solar

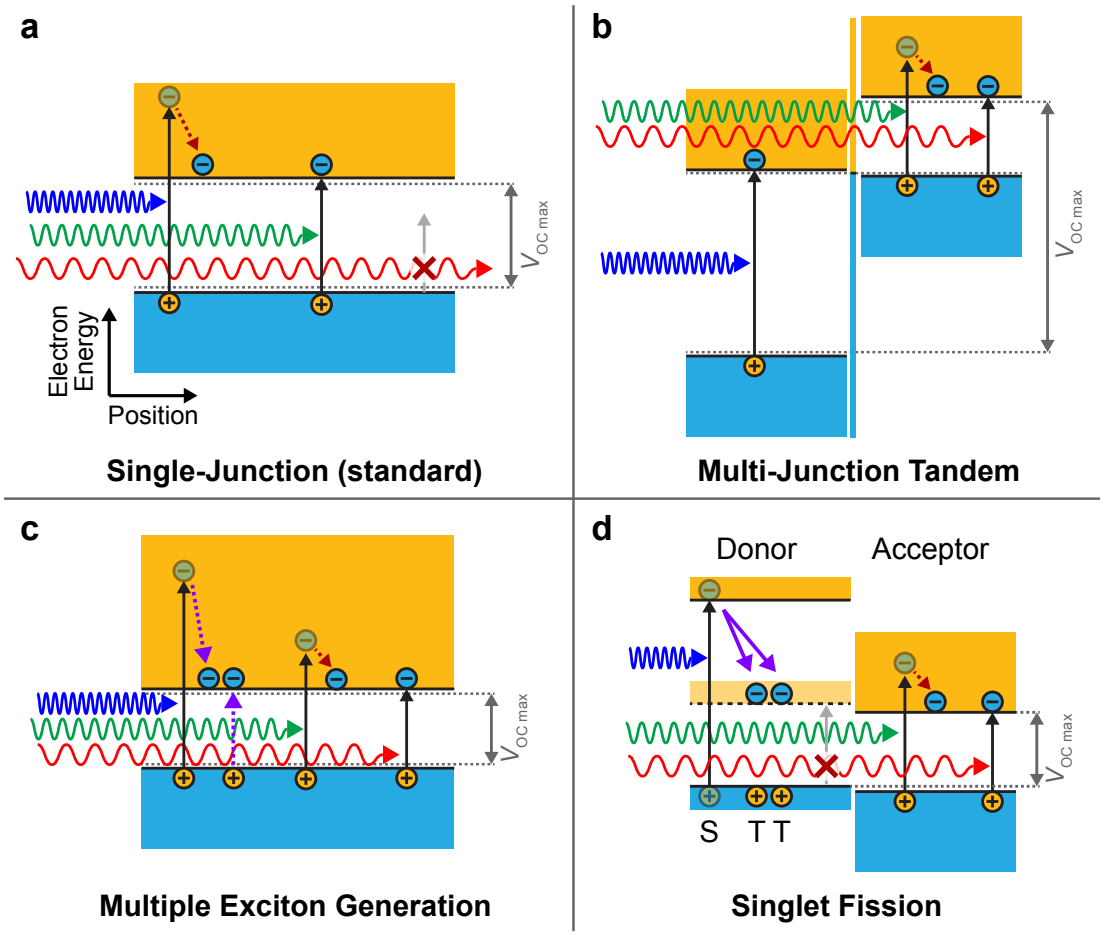

Figure 6-1: **High-efficiency photovoltaic device architectures.** Electronic energy band structures for photovoltaics employing: **a**, a single p-n junction made of a light-absorbing semiconductor that does not demonstrate carrier multiplication; **b**, two p-n junctions connected in series, without carrier multiplication; **c**, a p-n junction made of a semiconductor that exhibits multiple exciton generation; and **d**, a donor-acceptor heterojunction between an electron donor that demonstrates singlet exciton fission and an electron acceptor that demonstrates no carrier multiplication. All devices are shown under flat band conditions for simplicity. Orange areas represent empty electronic states; light blue areas represent filled electronic states. Colored wavy arrows represent photons of varying wavelength; black solid arrows represent electronic transitions resulting from photon absorption; maroon dotted arrows represent intra-band phonon-mediated carrier relaxation; purple arrows represent carrier multiplication processes; red × symbols represent forbidden transitions. Gray dotted lines represent the electron and hole quasi-Fermi levels under illumination, such that the difference in energy between the quasi-Fermi levels denotes the maximum attainable V_{OC}. In panel **d**, singlet excitons in the donor are labeled by "S", triplet excitons are labeled by "T", and the triplet state energy is denoted by the light orange band.

radiation: electrons and holes excited by photons with energy greater than the bandgap (here denoted by the blue wavy arrow) quickly relax in energy to the edges of the conduction and valence bands, while photons with energy less than the bandgap (red wavy arrow) pass through the semiconductor without being absorbed. The short-circuit current (J_{SC}) produced by this prototypical solar cell should thus decrease monotonically as the bandgap (E_g) increases, while the open-circuit voltage (V_{OC}) should increase. [ii] Electric power is given by the product of current and voltage, so a maximum in power conversion efficiency is observed for a bandgap that falls within the range of the solar spectrum.

Quantitatively, for an ideal semiconductor of bandgap E_g that is perfectly absorptive above the bandgap and perfectly transparent below the bandgap, with no losses due to series resistance or shunt resistance, the external quantum efficiency (η_{EQE}) for the conversion of incident photons of energy E to extracted electron-hole pairs is given by

$$\eta_{EQE}(E) = \begin{cases} 0 & \text{if } E < E_g \\ 1 & \text{if } E_g \leq E \end{cases} . \tag{6.1}$$

The external quantum efficiency for this perfect single-junction absorber is represented graphically by the curve labeled "Normal" in **Figure 6-2.a**. Integrating over the spectrum of incident radiation $S(E)$ (here taken as the AM1.5G spectrum [39]) as a function of energy, the short-circuit current is given by

$$J_{SC} = \int_0^\infty S(E)\, \eta_{EQE}(E)\, \mathrm{d}E, \tag{6.2}$$

plotted in Figure 6-2.b as a function of E_g.

The Shockley-Queisser calculation considers a semiconductor junction under detailed-balanced conditions, where carriers recombine only radiatively (i.e. without any nonradiative recombination) and have infinite mobility. In this case, for a junction

[ii] For bandgaps above ~4.1 eV, the V_{OC} of a solar cell under AM1.5G illumination begins to decrease with increasing bandgap, as the flux of absorbable solar photons rapidly vanishes above this energy. The J_{SC} and achievable power conversion efficiency of such high-bandgap solar cells would already be minuscule, so such devices are not of technical interest.

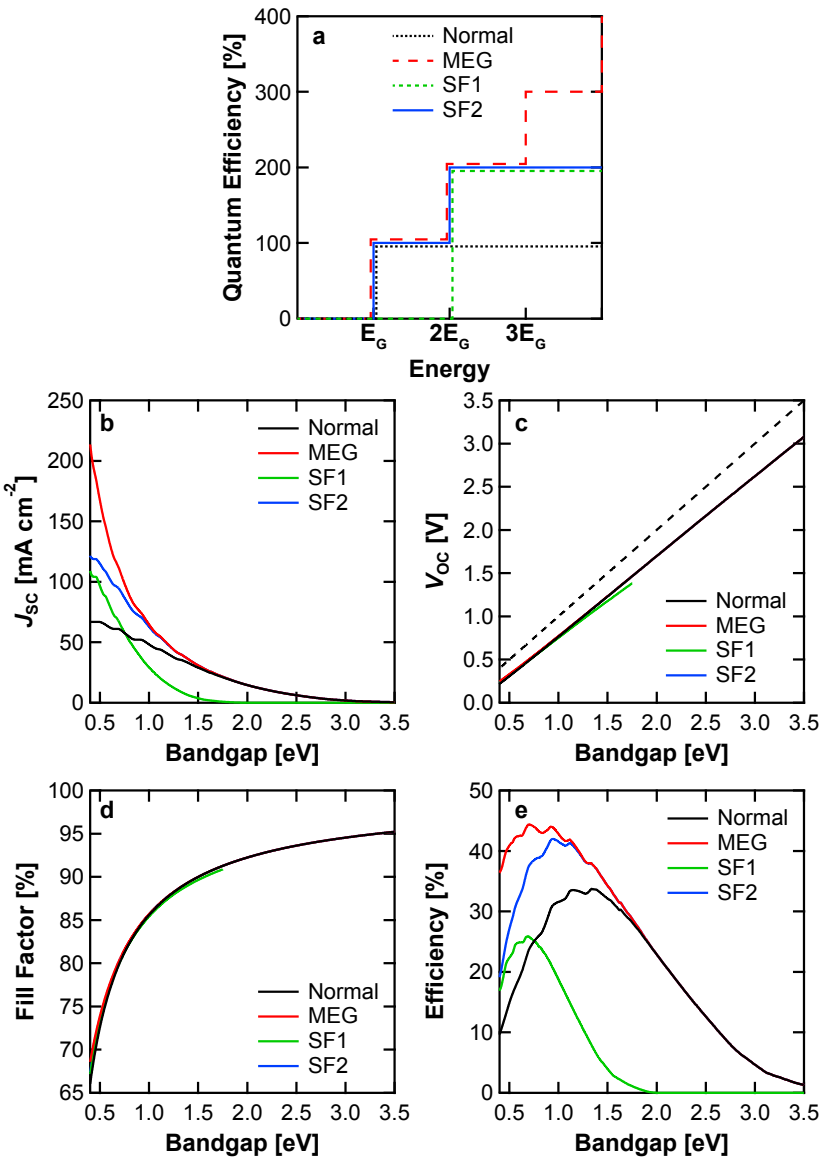

Figure 6-2: **Thermodynamic limits to photovoltaic device performance parameters as functions of bandgap and quantum efficiency.** **a**, Quantum efficiency of photon-to-electron conversion as a function of photon energy for the four different photovoltaic materials of bandgap E_g considered here: a material that does not demonstrate carrier multiplication ("Normal"); a material that demonstrates the highest possible efficiency of multiple exciton generation ("MEG"); a material that undergoes singlet fission without a paired complementary absorber at the triplet energy ("SF1"); and a material that undergoes singlet fission with a paired complementary absorber at the triplet energy ("SF2"). For SF1 and SF2, the bandgap is defined as the energy of the triplet state, and the energy of the singlet state is taken to be exactly twice the energy of the triplet state. Curves are slightly offset for clarity. **b-e**, Thermodynamic limit for short-circuit current density (J_{SC}) (**b**), open-circuit voltage (V_{OC}) (**c**), fill factor (**d**), and power conversion efficiency (**e**) as a function of the bandgap E_g of the photovoltaic material. The dotted line in **c** represents $V_{OC} = E_g$.

under open-circuit (zero bias) conditions in the dark, this radiative recombination is described by the Planck equation for blackbody radiation. The recombination current density leading to this radiation flux (here denoted by J_S) is equal to the photon flux from blackbody radiation times the charge of the electron, for the case of a material that acts as a perfect blackbody above the bandgap and as a transparent body below the bandgap:

$$J_S = \frac{2\pi e}{c^2 h^3} \int_{E_g}^{\infty} \frac{E^2}{\exp\left(E/k_B T\right) - 1} \, \mathrm{d}E, \tag{6.3}$$

where e is the charge of the electron, c is the speed of light in vacuum, h is Planck's constant, k_B is the Boltzmann constant, and T is the temperature of the cell ($T = 300\,\mathrm{K}$). Under zero bias in the dark, the recombination and (thermal) generation current densities are in equilibrium, such that $J_S = J_{recom}(V = 0) = -J_{gen}$ and the net current ($J(0) = J_{recom}(0) + J_{gen}$) is zero.

The application of a bias voltage V across the junction splits the electron quasi-Fermi level on the n side of the junction and hole quasi-Fermi level on the p side of the junction by an energy $\Delta E_{QFL} = \Delta E^e_{QFL}(n) - \Delta E^h_{QFL}(p) = e\,V$, thus changing the density of free electrons and holes throughout the junction. [iii] The generation current is unaffected by the applied bias, but the change in carrier density leads to a change in the recombination current (positive voltages increase the free carrier density in the depleted region and correspondingly increase the recombination current, while negative voltages lead to a decrease in carrier density and current), which is manifested by factoring the quasi-Fermi level splitting $e\,V$ into the Boltzmann term

[iii] The use of quasi-Fermi levels reflects the fact that under applied bias (or illumination) and current flow the junction as a whole is no longer under equilibrium. Yet the distribution of carriers within each band (electrons in the conduction band and holes in the valence band) does stay in independent thermal equilibrium, with the electrons and holes each obeying their own Fermi-Dirac distributions, so we speak of a quasi-Fermi level for electrons in the conduction band and a quasi-Fermi level for holes in the valence band. Each of these quasi-Fermi levels can vary across the junction. Under equilibrium (zero applied bias and no illumination) the quasi-Fermi levels are each equal to the Fermi level throughout the junction. A deviation in the electron or hole quasi-Fermi level indicates a change in carrier density at that position compared to equilibrium conditions.

of the recombination current, giving a total current of

$$\begin{aligned} J(V) &= J_{recom}(V) - J_{gen} \\ &= \frac{2\pi e}{c^2 h^3} \int_{E_g}^{\infty} \frac{E^2}{\exp\left(\left(E - eV\right)/k_B T\right) - 1} \, \mathrm{d}E - \frac{2\pi e}{c^2 h^3} \int_{E_g}^{\infty} \frac{E^2}{\exp\left(E/k_B T\right) - 1} \, \mathrm{d}E. \end{aligned} \tag{6.4}$$

For $(E - eV) \gg k_B T$, as is the case for the bandgaps considered here at room temperature at biases of interest for solar cell operation, the Boltzmann term involving the quasi-Fermi level splitting eV can be brought outside the integral, yielding the familiar equation for current flow through a diode as a function of applied bias:

$$J(V) = J_S \left[\exp\left(\frac{eV}{k_B T}\right) - 1\right]. \tag{6.5}$$

Under detailed balance conditions the short-circuit current under illumination is independent of applied voltage and opposite in sign to the diode current, yielding

$$J(V) = J_S \left[\exp\left(\frac{eV}{k_B T}\right) - 1\right] - J_{SC}. \tag{6.6}$$

The open-circuit voltage is then obtained by setting $J = 0$ and solving for V:

$$V_{OC} = \frac{k_B T}{e} \ln\left(\frac{J_{SC}}{J_S} + 1\right), \tag{6.7}$$

shown as a function of bandgap in Figure 6-2.c.

The power conversion efficiency η_P is obtained by dividing the maximum negative product of the current density and voltage by the incident radiation intensity,

$$\eta_P = \frac{\left(-J(V) \cdot V\right)_{max}}{1000\,\mathrm{W\,m^{-2}}}, \tag{6.8}$$

and the fill factor (FF) is given by the ratio between the maximum power produced

and the product of the J_{SC} and V_{OC}:

$$\mathrm{FF} = \frac{(-J(V) \cdot V)_{max}}{J_{SC} \cdot V_{OC}}. \tag{6.9}$$

The maximum attainable η_P and FF are shown as a function of E_g in Figure 6-2.c-d, with the maximum efficiency of $\sim$33 % attained at a bandgap of $\sim$1.3 eV.

6.3 Beyond the single-junction Shockley-Queisser limit

Multiple strategies have been demonstrated and proposed for moving beyond the single-junction Shockley-Queisser limit. In a general sense, these strategies are designed to make more efficient use of the broad solar spectrum by reducing the energy lost during absorption of photons with energy greater than the bandgap and/or enabling the absorption of photons with energy less than the bandgap. These strategies result either in the enhancement of the V_{OC} of the solar cell (in the case of multijunction or hot-carrier solar cells) or in the enhancement of the J_{SC} (in the case of multiple exciton generation, singlet fission, and intermediate-band architectures). We here give a brief overview of the operation and design considerations of a selection of these solar cell architectures.

6.3.1 Multijunctions

In a multijunction solar cell, two or more single-junction solar cells, in almost all cases utilizing semiconductors of different bandgaps, are stacked on top of each other, with incident light passing sequentially through the subcells. These subcells are typically connected in series, with recombination layers or tunnel junctions between the component subcells, such that the entire multijunction stack is electrically accessed using two electrodes. When subcells are connected in series, the voltage across the stack is equal to the sum of the voltages produced by each subcell. The current passing through each subcell must in such case be equal, and the total current produced from the multijunction stack under illumination is limited by the lowest-current subcell.

The thickness and bandgap of each subcell must therefore be carefully tuned in order to ensure that each subcell is biased as closely as possible to its maximum power point under typical insolation conditions. [iv]

Figure 6-1.b shows a schematic representation of a two-junction solar cell under illumination. The cell is illuminated from the side of the larger-bandgap subcell, allowing light that is not absorbed by the first subcell to pass through and be absorbed by the second, lower-bandgap subcell. Similar arrangements are used for multijunction devices with three or more subcells. Two-, three-, and four-junction solar cells have been reported with certified efficiencies of 31.6 %, 37.9 %, and 38.8 %, respectively, under 1-sun illumination (34.1 %, 44.4 %, and 46.0 %, respectively, under concentration). [53] The maximum theoretical efficiencies of two-, three-, and four-junction solar cells are 42 %, 49 %, and 53 % under 1-sun illumination and 55 %, 63 %, and 68 % under the maximum possible solar concentration. [49]

High-efficiency multijunction devices are primarily fabricated from lattice-matched epitaxially-grown stacks of single-crystal inorganic semiconductors, typically at very high cost per unit area relative to other solar cell technologies. Such high-cost, high-efficiency devices are useful in space-based applications (where power production per unit weight is at a premium) and in concentrating photovoltaics (where sunlight is focused onto a small active area, enabling the substitution of lower-cost mirrors and lenses for higher-cost active cell area), but are too expensive for use in large-area fixed-tilt or single-axis-tracking arrays. Alternative multijunction strategies include the use of thin-film subcells (amorphous silicon, CIGS, perovskite, quantum dot, or organic materials) matched with other thin-film subcells or with crystalline silicon subcells. [227, 228, 229, 230, 231, 232, 233]

[iv] It is also possible to make electrical contact to each subcell individually, such that an n-junction solar cell would utilize $2n$ electrodes (rather than 2 electrodes in the series-connected case). Such independently-contacted architectures are useful for prototyping and remove the requirement to match the current of the subcells, but would significantly complicate the design and interconnection of commercial modules.

6.3.2 Multiple exciton generation

Multiple exciton generation (MEG)—also known as impact ionization, inverse Auger recombination, or more broadly as carrier multiplication—refers to the production of multiple electron-hole pairs from a single absorbed photon. The operation of a MEG-sensitized solar cell is represented graphically in Figure 6-1.c, where a blue photon creates two electron-hole pairs and a green and red photon each create a single electron-hole pair. The η_{EQE} of a MEG absorber in the ideal case, where the number of carriers generated increases stepwise as the photon energy E reaches increasing multiples of the bandgap E_g, is given by

$$\eta_{EQE}(E) = \begin{cases} 0 & \text{if } E < E_g \\ 1 & \text{if } E_g \leq E \leq 2E_g \\ 2 & \text{if } 2E_g \leq E \leq 3E_g \\ 3 & \text{if } 3E_g \leq E \leq 4E_g \\ \dots & \end{cases} \qquad \text{“MEG”} \qquad (6.10)$$

and represented graphically in Figure 6-2.a as a function of the bandgap of the MEG material. The corresponding thermodynamic maxima for J_{SC}, V_{OC}, fill factor, and η_P are shown in Figure 6-2.b-e. A solar cell employing a perfect MEG material could reach a maximum efficiency of 44.4 % under 1-sun illumination and 86 % under the maximum possible solar concentration. [51]

MEG has long been known to occur in bulk semiconductors such as silicon and PbSe, but it appears to occur more efficiently in nanocrystalline systems. [218, 219, 234, 235] It has been hypothesized that the reduced density of phonon states in low-dimensional systems could create a “phonon bottleneck” that slows intraband thermal relaxation of hot carriers and makes the inverse-Auger process of MEG more likely, but disagreement remains over this interpretation (particularly given the addition of vibrational degrees of freedom from chemical ligands and the mechanical “softness” of the nanocrystal surface) . [236, 237, 238, 239] A peak external quantum efficiency over 100 % has been

reported for a ZnO / PbSe QD solar cell, [220] but the power conversion efficiency of such devices remains low (<2.5 %) because of the low V_{OC} of PbSe QD-based devices and the relatively low efficiency of MEG in these systems compared to the theoretical maximum.

6.3.3 Singlet fission

Before describing the details of singlet fission and its application to solar cells, we first review the fundamentals of electronic excitations in organic materials. [240] Molecular organic materials are differentiated from crystalline materials by their low dielectric constant and their combination of strong intramolecular covalent bonds and weak intermolecular van der Waals interactions. In extended inorganic crystals such as gallium arsenide, bound electronic excitations are typically delocalized over many unit cells and are referred to as *Wannier-Mott excitons*. In most inorganic materials relevant for solar cells, the dielectric constant is sufficiently high and the exciton binding energy is sufficiently low that the thermal energy k_BT at room temperature is sufficient to overcome the exciton binding energy and separate the constituent electron and hole, meaning that such excitons can only be observed at low temperature. In molecular organic materials, the dielectric constant is typically quite low ($\varepsilon \approx 2$–3), resulting in significant Coulomb attraction between electrons and holes. Electronic excitations in molecular materials are thus strongly confined to a single molecule or a small number of molecules, where they are referred to as *Frenkel excitons*. Frenkel excitons typically have binding energies in the range of a few hundred meV, and as such are unlikely to spontaneously separate at room temperature.

Because of the close confinement of Frenkel excitons, the electron-electron interaction plays a larger role in determining the excitonic properties of molecular materials than it does in bulk inorganic materials, and the spin state of a Frenkel exciton has a large impact on the exciton energy. The electronic ground state of a molecule with two electrons in the highest occupied molecular orbital (HOMO) is a singlet state

with $|s, m\rangle = |0, 0\rangle$ and

$$|0, 0\rangle = \frac{1}{\sqrt{2}} \left(|\uparrow\rangle |\downarrow\rangle - |\downarrow\rangle |\uparrow\rangle \right). \tag{6.11}$$

The absorption of a photon will leave the spin state unchanged, but will promote one of the electrons to the energy state that was formerly the lowest unoccupied molecular orbital (LUMO).

While it cannot be generated optically, another excited state with symmetric electron spins is also possible. In the absence of an external magnetic field, the three triplet states with $s = 1$ and $m = (-1, 0, 1)$ will be degenerate in energy:

$$|1, 1\rangle = |\uparrow\rangle |\uparrow\rangle \tag{6.12}$$

$$|1, 0\rangle = \frac{1}{\sqrt{2}} \left(|\uparrow\rangle |\downarrow\rangle + |\downarrow\rangle |\uparrow\rangle \right) \tag{6.13}$$

$$|1, -1\rangle = |\downarrow\rangle |\downarrow\rangle . \tag{6.14}$$

Triplet excited states can be generated through intersystem crossing in molecules with large spin-orbit coupling, through the coalescence of a free electron and hole with symmetric spin onto the same molecule, or through singlet fission. The symmetric spins of the triplet exciton necessitate an antisymmetric spatial wavefunction. As such, the energy of the triplet excited state of a given molecule will always be lower than the energy of the singlet excited state, as the increased separation between the two electrons will reduce the electron-electron repulsion and stabilize the state.

Electronic relaxation of the singlet excited state is spin-allowed and therefore takes place relatively rapidly, on the timescale of a few nanoseconds, through a radiative (fluorescent) or nonradiative transition. Relaxation of the triplet excited state, on the other hand, is spin-forbidden, since the ground state is a singlet state. Triplet excited states thus demonstrate lifetimes many orders of magnitude larger than singlet excited states, on the scale of microseconds or even milliseconds, before decaying radiatively (phosphorescently) or nonradiatively through intersystem crossing.

For molecules in which the energy of the triplet state is less than or equal to

(or no more than $\sim k_B T/2$ greater than) half of the energy of the singlet state, a singlet exciton on one molecule can transfer part of its energy to an adjacent ground-state molecule, leaving both molecules in lower-energy triplet states through the spin-allowed process of singlet fission. Singlet fission is primarily observed in acenes, of which tetracene and pentacene are the best-known and best-characterized examples, but has also been observed in carotenoids, polydiacetylenes, and other materials. [224, 241, 242, 243, 244] The molecules involved are typically nearest neighbors in a solid molecular crystal, though singlet fission has also been observed in disordered thin films and in solution. [245, 246]

Singlet fission can be described by the simple rate equation

$$\mathrm{S_0} + \mathrm{S_1} \underset{k_{-1}}{\overset{k_1}{\rightleftharpoons}} {}^1(\mathrm{TT}) \underset{k_{-2}}{\overset{k_2}{\rightleftharpoons}} \mathrm{T_1} + \mathrm{T_1} \tag{6.15}$$

where $\mathrm{S_0}$ is a molecule in the ground state, $\mathrm{S_1}$ is a molecule in the lowest singlet excited state, ${}^1(\mathrm{TT})$ is a correlated multiexciton state with net singlet character between the two molecules, and $\mathrm{T_1}$ is a molecule in the (uncorrelated) lowest triplet excited state. [247, 248, 249, 244] Chan et al. have shown that in the case of crystalline pentacene, the $\mathrm{S_1}$ and ${}^1(\mathrm{TT})$ states are created together in a coherent superposition upon the absorption of a photon. [250] This observation suggests a modified version of (6.15):

$$[(\mathrm{S_0} + \mathrm{S_1}) \Leftrightarrow {}^1(\mathrm{TT})] \underset{k_{-1}}{\overset{k_1}{\rightleftharpoons}} {}^1(\mathrm{TT})' \underset{k_{-2}}{\overset{k_2}{\rightleftharpoons}} \mathrm{T_1} + \mathrm{T_1}, \tag{6.16}$$

where ${}^1(\mathrm{TT})'$ is the multiexciton state after dephasing and decoupling from $\mathrm{S_1}$. The entire singlet fission process is reversible, where it is referred to as *triplet exciton fusion*; indeed, the process was first observed in the form of triplet fusion in tetracene crystals. [247] For our purposes, the equation can be simplified to

$$\mathrm{S_0} + \mathrm{S_1} \underset{k_{-F}}{\overset{k_F}{\rightleftharpoons}} \mathrm{T_1} + \mathrm{T_1}, \tag{6.17}$$

where k_F is the rate of singlet fission and k_{-F} is the rate of triplet fusion. In crystalline pentacene, singlet fission has been observed to occur within $\sim$100 fs with a quantum

efficiency (photons absorbed to triplets generated) of well over 100 %. [251, 252, 250]

We now return to our discussion of the impact of singlet fission on ideal solar cell performance. For a solar cell in which a singlet fission material is the only current-generating element, the external quantum efficiency as a function of photon energy E is given by

$$\eta_{EQE}(E) = \begin{cases} 0 & \text{if } E < 2E_g \\ 2 & \text{if } 2E_g \leq E \end{cases} \qquad \text{“SF1”} \tag{6.18}$$

where E_g is defined as the energy of the triplet state and the triplet energy is exactly half the singlet energy (note that this ideal energetic arrangement is not necessarily observed in most singlet fission materials). Since the triplet state itself is not optically active, light incident upon a singlet fission material at the triplet state energy is not absorbed and does not generate photocurrent. The ideal performance parameters of a solar cell operating in this arrangement are indicated by the curves labeled “SF1” in Figure 6-2. As is evident from the figure, the use of a singlet fission material as the only light-absorbing element in a solar cell actually results in a decrease in the maximum attainable efficiency, as the extra energy collected from photons with energy greater than $2E_g$ does not make up for the energy that is wasted from photons with energy between E_g and $2E_g$. [52]

Figure 6-1.d shows an alternative device architecture, where the singlet fission material (here taken to be the electron donor) is paired with another optically active, singlet-fission-free material (here the electron acceptor) with a bandgap on the order of the triplet energy in the singlet fission material. The external quantum efficiency as a function of photon energy E in this case is given by

$$\eta_{EQE}(E) = \begin{cases} 0 & \text{if } E < E_g \\ 1 & \text{if } E_g \leq E \leq 2E_g \\ 2 & \text{if } 2E_g \leq E \end{cases} \qquad \text{“SF2”} \tag{6.19}$$

assuming that the triplet energy of the singlet fission material (here defined as E_g) is again exactly half the singlet energy, and that the bandgap of the complementary material is equal to the triplet energy of the singlet fission material. The ideal performance parameters of a solar cell with this architecture are given by the curves labeled "SF2" in Figure 6-2. The combination of a singlet fission material and a complementary absorber ("SF2") results in a maximum efficiency that is significantly greater than that of both the standard single-junction case ("Normal") and the single-material singlet fission case ("SF1"), reaching a maximum of 42 % for a triplet energy of 0.95 eV.

The singlet fission solar cell architecture described here can be thought of as a hybrid between a multijunction architecture and a MEG architecture, yet has advantages over each. Unlike a traditional multijunction architecture, there is no requirement for current matching between the singlet fission material and the complementary absorber, since there is only a single junction; the currents produced by the singlet fission material and the complementary absorber are simply additive. In comparison with MEG, singlet fission from the higher-energy singlet exciton state does not face competition from intraband relaxation, while MEG must compete with rapid intraband cooling of hot carriers. Singlet excitons have lifetimes of nanoseconds, while vibrational excited states have lifetimes of picoseconds (and singlet fission in pentacene, which occurs within ∼100 fs, would outrun vibrational relaxation even if it were possible). As such, the experimentally observed quantum efficiency of singlet fission is significantly higher than that of MEG for photon energies close to the $2E_g$ multiplication threshold. [253, 221] The triplet excitons that are produced as a result of singlet fission also have significantly longer lifetime than the singlet excitons that are produced as a result of MEG, increasing their chances of being successfully converted into separated electrons and holes. And the maximum efficiency of a singlet-fission-enhanced "SF2" device under AM1.5G illumination (42 %) approaches that of the perfect MEG device (44.4 %), suggesting that most of the benefit from carrier multiplication is already achieved with the production of a single extra electron-hole pair for photon energies greater than twice the bandgap. The production of a third or fourth electron-hole pair from

photons of energy three or four times the bandgap (and so on up to higher energies) generates significantly diminishing returns for the maximum solar cell efficiency.

6.4 Pentacene-PbS QD singlet fission photovoltaic device design

Figure 6-3 outlines the energetic and spatial design requirements for a singlet fission photovoltaic device. The singlet fission material may in principle act either as the electron donor or the electron acceptor in a donor-acceptor heterojunction device, but pentacene (the best-studied and highest-efficiency singlet fission material, and the focus of our study) is typically used as an electron donor in singlet-fission photovoltaics and photodetectors [254, 255, 221, 256] given its relatively shallow LUMO and its much higher hole mobility than electron mobility. [257, 258] As noted earlier, excitons (either singlet or triplet) are unlikely to separate into free charge carriers in a pure molecular organic material given their large exciton binding energy. The energy of the final charge-separated state, with the electron on the electron acceptor and the hole on the electron donor, is given by the difference in energy between the LUMO of the acceptor and the HOMO of the donor, here referred to as ΔE_{DA}. If ΔE_{DA} is lower than (or within $\sim k_B T$ of) the energy of the triplet exciton state, the triplet can spontaneously separate at the donor-acceptor interface, generating a photocurrent. If ΔE_{DA} is between that of the triplet and singlet exciton states, only the singlet exciton can generate free charge carriers, and singlet fission will reduce, rather than increase, the total photocurrent (by acting as a loss pathway for singlet excitons). Note also that the ΔE_{DA} represents the maximum energy that can be harvested from a single photon; a larger ΔE_{DA} thus typically leads to a larger V_{OC}.

An efficient singlet fission photovoltaic device thus requires: a high singlet fission rate and yield in the singlet fission material; efficient triplet diffusion and/or strong light absorption in the singlet fission material; a ΔE_{DA} that is just low enough to facilitate triplet dissociation without unnecessarily limiting V_{OC}; and a complementary

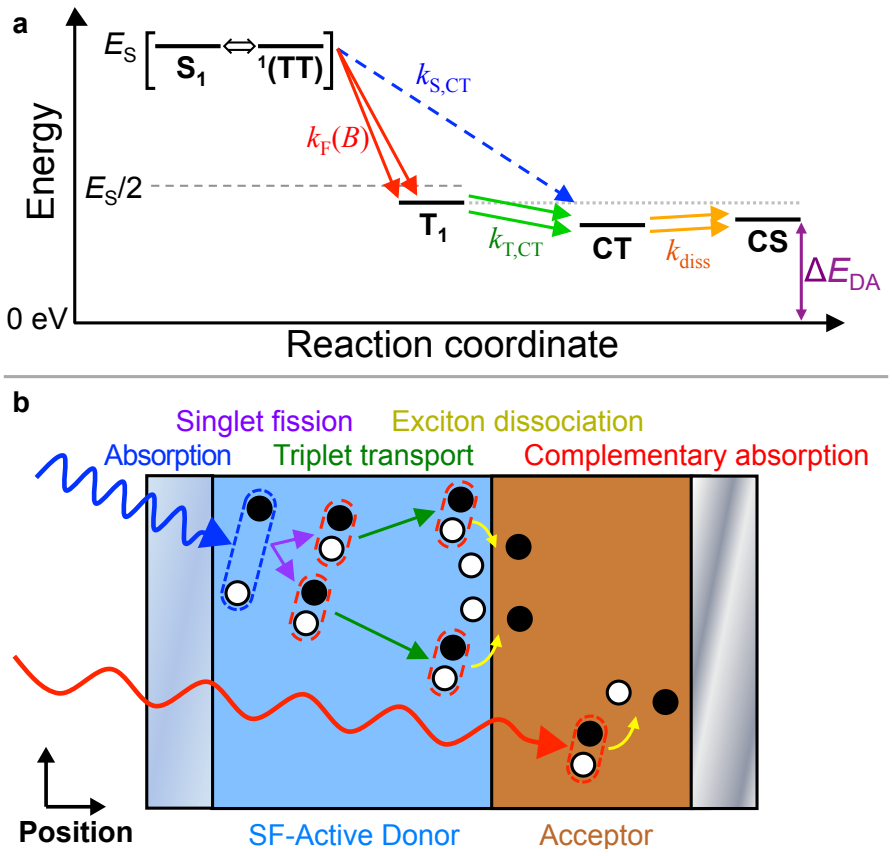

Figure 6-3: **Electronic processes in a singlet fission photovoltaic device. a**, Energy state diagram for a singlet fission photovoltaic device with the architecture depicted in Figure 6-1.d. $\mathbf{S_1}$ represents the first singlet exciton state; $\mathbf{^1(TT)}$ represents the coherent multiexciton state; $\mathbf{T_1}$ represents the triplet exciton state; **CT** represents the bound charge-transfer state at the donor-acceptor interface, with the electron in the acceptor and the hole in the donor; **CS** represents the charge-separated state, with the unbound electron in the conduction band of the acceptor and the unbound hole in the valence band of the donor. ΔE_{DA} represents the difference in energy between the valence band of the donor and the conduction band of the acceptor. Rate constants for transitions are denoted by k. **b**, Schematic of electronic processes in the solar cell architecture used here, where pentacene is the singlet-fission-sensitized donor and PbS QDs are the acceptor.

absorber with a bandgap close to the triplet energy of the singlet fission material. Given these considerations, the combination of pentacene as electron donor and PbS QDs as electron acceptor presents an attractive device design for singlet fission photovoltaics. The triplet and singlet energies of pentacene are 0.86 eV and 1.83 eV, respectively, [259, 260, 261, 244] meaning that singlet fission is energetically allowed and occurs with an energy loss of only 0.11 eV per photon. And as noted above, singlet fission occurs in pentacene within ∼100 fs with a photon-to-triplet quantum efficiency of at least 160 %. [251, 252, 250, 221] The relatively deep energy levels of PbS QDs relative to pentacene makes PbS QDs well-suited to act as an electron acceptor, with pentacene acting as the electron donor. The ability to tune the conduction band energy of PbS QDs by controlling the size of the QDs (along with the ability to tune the absolute energy levels of the QDs through ligand exchange, as discussed in Chapter 7) should enable precise tuning of ΔE_{DA} to allow triplet dissociation without significantly sacrificing V_{OC}. And the low and tunable bandgap of large PbS QDs enables this material to act as a complementary absorber to pentacene, absorbing photons below the relatively high 1.83 eV pentacene singlet energy.

Here, we use a hybrid donor-acceptor / Schottky junction architecture to explore the operation of pentacene / PbS QD singlet fission photovoltaics. In particular, we seek to explore the process of triplet dissociation at the pentacene / QD interface by tuning the interfacial energetics through modification of the QD bandgap. Photovoltaic devices used in this study utilize the architecture glass / ITO / PEDOT:PSS / pentacene (40 nm) / PbS QD (40 nm) / LiF (0.7 nm) / Al (100 nm) unless otherwise noted. PEDOT:PSS acts as a hole-extraction layer, and the low-work-function LiF / Al electrode forms a Schottky contact to the PbS QDs, generating a built-in electric field that drives electron collection through the LiF / Al contact and hole collection through the ITO / PEDOT:PSS contact (the mechanics of PbS QD Schottky junction PV operation are described in more detail in Section 7.4). The devices are illuminated through the glass / ITO electrode, such that short-wavelength light is preferentially absorbed in the pentacene rather than in the PbS QDs (as depicted in Figure 6-1.d and Figure 6-3.b) in order to derive the greatest benefit from singlet fission in pentacene.

6.5 Methods

ITO-coated glass substrates were purchased from Thin Film Devices and cleaned by sequential ultrasonication in micro-90 soap solution, deionized water, acetone, and isopropanol (5 min each), followed by treatment with ozone plasma (1 min). Polyethylenedioxythiophene-polystyrene sulfonate (PEDOT:PSS, conductive grade, Sigma-Aldrich) was deposited onto glass / ITO substrates by spin-coating (4000 rpm, 60 s duration, 1000 rpm/s ramp rate) and annealed in nitrogen at 150 °C for 15 min. All subsequent fabrication and testing steps were performed in oxygen- and water-free conditions. Pentacene, lithium fluoride (LiF, 99.99 %), and aluminum were deposited by thermal evaporation at a base pressure of 3×10^{-6} torr. PbS QDs were synthesized by standard literature methods [186]; the QD diameter was controlled by adjusting the injection temperature, growth duration, and 1-octadecene / oleic acid ratio. PbS QD films were deposited by sequential spin-coating and ligand exchange as described in Section 5.2, including ligand exchange with 1,3-benzenedithiol (1,3-BDT, Sigma Aldrich, 99 %). The device active area was defined by the ITO / Al overlap to be 1.24 mm^2.

Current-voltage measurements were performed using a Keithley 6487 picoammeter, and 100 mW cm^{-2} illumination was provided by a Newport 96000 solar simulator with an AM1.5G spectral filter. External quantum efficiency (EQE) spectra were collected without bias voltage or bias illumination; monochromatic illumination was provided by passing white light from a Thermo Oriel 66921 xenon lamp through a monochromator and optical chopper, and the device current was measured using a Stanford Research Systems SR830 lock-in amplifier. The pentacene absorption spectrum was measured using an Aquila nkd-8000.

6.6 Singlet fission device operation

6.6.1 Triplet dissociation at the donor-acceptor interface

Figure 6-4.a shows the absorption constant α of a thin film of evaporated pentacene.

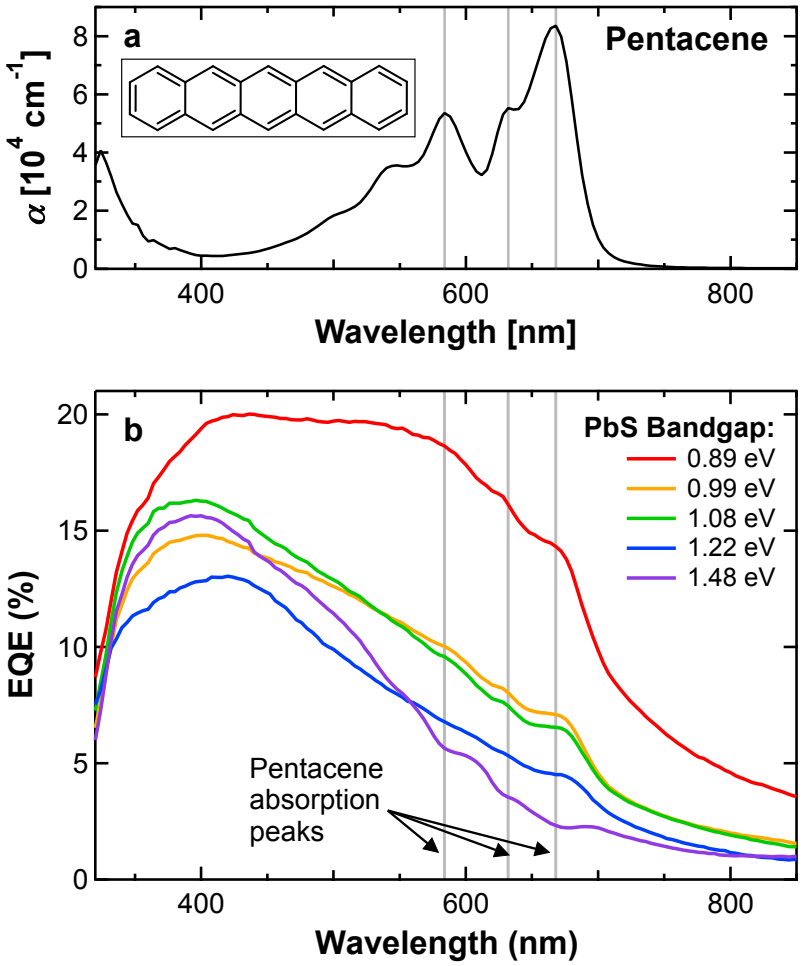

Figure 6-4: **Spectral signature of singlet fission in pentacene / PbS QD photovoltaic performance.** **a**, Absorption constant of thin-film polycrystalline pentacene. Peak positions are denoted by gray vertical lines. The boxed inset shows the chemical structure of pentacene. The absorption spectrum was measured by Priya Jadhav. **b**, External quantum efficiency (EQE) of pentacene / PbS QD photovoltaics employing different QD bandgaps. PbS QD bandgaps are taken from the peak of the first excitonic absorption feature in solution. Positive peaks in the EQE spectrum are noted at pentacene absorption maxima for QD bandgaps between 0.89 eV and 1.22 eV; negative dips in the EQE spectrum are noted for a QD bandgap of 1.48 eV.

Note in particular the strong absorption peaks at wavelengths of 584 nm, 632 nm, and 668 nm. These peaks present a useful spectral signature for determining the contribution of pentacene to the device photocurrent. Given the exceedingly rapid rate of singlet fission in pentacene compared to the relatively slow rate of exciton diffusion, [251, 262] the relatively large pentacene thickness (40 nm, or roughly 25 pentacene monolayers), the fact that the pentacene is illuminated at the PEDOT:PSS / pentacene interface rather than at the pentacene / PbS QD interface (thus giving ample time for singlet fission to occur before excitons reach the dissociating pentacene / PbS QD interface), and the fact that even submonolayer pentacene has been observed to transfer two excitons to an adjacent C_{60} layer per absorbed photon (either directly from the $^1(TT)/^1(TT)'$ state within ~900 fs, or from the separated $T_1 + T_1$ state within ~5 ps [250, 254]), it is safe to assume that any photocurrent signature from pentacene arises from triplets rather than from singlets. A spectrally resolved measurement of the external quantum efficiency (EQE) of the device thus has the capacity to determine whether singlet-fission-generated triplets are dissociating and generating current. If positive peaks are observed in the EQE spectrum at wavelengths corresponding to the pentacene absorption peaks, it can be concluded that triplets are dissociating and contributing to the device current; if dips are observed, the absorption of light in pentacene and generation of triplets is detracting from the total device current rather than adding to it, and triplet dissociation is unlikely (or, at least, less efficient than current generation at the corresponding wavelengths within the PbS QD layer).

Figure 6-4.b shows the EQE spectra of pentacene / PbS QD devices fabricated using PbS QDs of five different bandgaps and sizes (0.89 eV, 0.99 eV, 1.08 eV, 1.22 eV, and 1.48 eV as measured from the peak of the first excitonic absorption feature in solution, corresponding to QD diameters of 5.1 nm, 4.4 nm, 4.0 nm, 3.5 nm, and 2.8 nm, respectively, as determined from a published sizing curve [75]). For each device, the EQE response above ~700 nm and below ~500 nm in wavelength shows that PbS QDs are contributing to the photocurrent. At the wavelengths of peak pentacene absorption, a notable difference can be observed in the EQE spectra of the different devices. For PbS QD bandgaps of 1.22 eV and below, positive peaks are observed in

the EQE spectra at the wavelengths of peak pentacene absorption, confirming that singlet fission contributes to the photocurrent of these devices. Similar results were reported by Ehrler et al. [226] during the course of our investigations, though the two bodies of work were developed independently. Note that photocurrent from pentacene is observed even when the PbS QD bandgap is significantly greater than the pentacene triplet energy—up to 0.36 eV greater in the case of the 1.22 eV-bandgap QDs, which is much too high for thermal activation at room temperature. Pentacene photocurrent in these devices must therefore result from direct triplet dissociation at the pentacene / QD interface (i.e. transfer of the triplet electron to a QD, leaving a hole behind in the pentacene), rather than from energy transfer of a complete pentacene exciton (electron and hole) into a QD followed by dissociation. For the device with a PbS QD bandgap of 1.48 eV, on the other hand, dips are observed in the EQE spectra at the wavelengths of peak pentacene absorption, suggesting that triplets are unable to dissociate at the pentacene / PbS QD interface in this device.

The transition from peaks to dips in the EQE spectrum at the wavelengths of the pentacene absorption peaks can be explained by examining the energy levels at the pentacene / QD interface. **Figure 6-5.a** shows the energy levels of pentacene (taken from the literature [81, 82]) and of the different PbS QD sizes used in Figure 6-4.b. PbS QD valence band energies were determined from published data for oleic-acid-capped PbS QDs, [75] but shifted by the observed difference between the published valence band energy for 1.29 eV-bandgap PbS QDs and our measured valence band energy for 1.29 eV-bandgap PbS QDs ligand-exchanged with 1,3-BDT (determined from ultraviolet photoelectron spectroscopy, described in detail in Section 7.2.2). The ΔE_{DA} for each pentacene / PbS QD pair is given by the difference in energy between the pentacene HOMO and the QD conduction band. Figure 6-5.b summarizes the observations from Figure 6-4 and Figure 6-5.a by comparing the ΔE_{DA} for each of the tested pentacene / PbS QD pairs to the pentacene triplet energy, with blue circles symbolizing pairs which demonstrate photocurrent from pentacene and red circles symbolizing pairs which do not. As expected from Figure 6-3.a, photocurrent from pentacene triplets is observed when ΔE_{DA} is less than the triplet energy, and is not

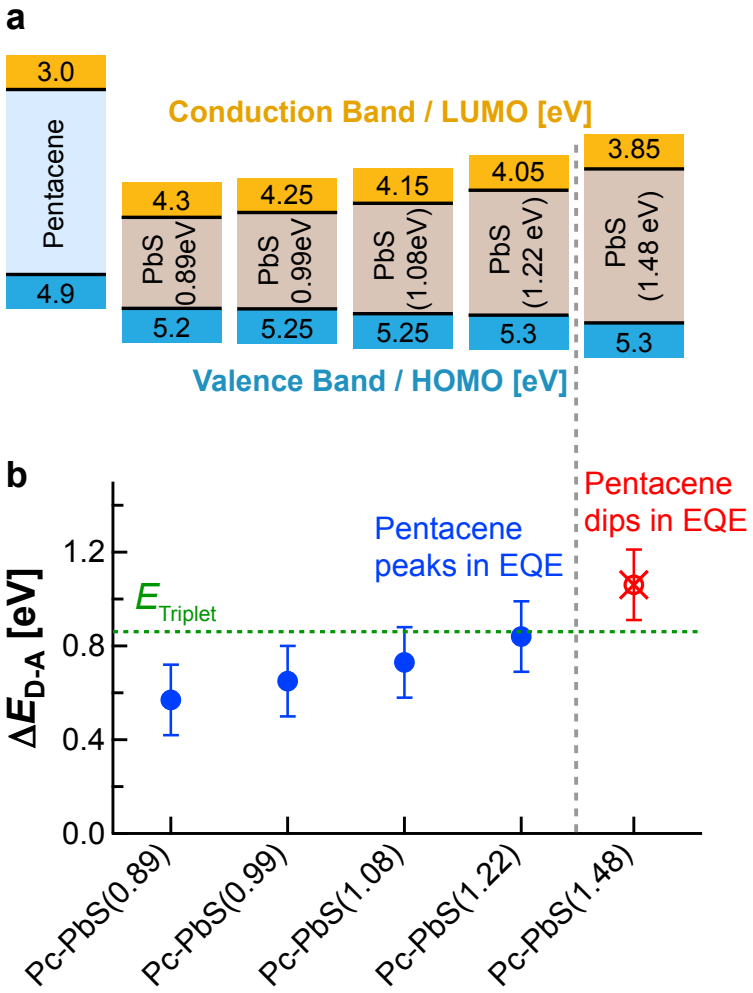

Figure 6-5: **Triplet dissociation at the donor-acceptor interface.** **a**, Energy level alignment between pentacene and PbS QDs of different bandgap, matching the bandgaps used in Figure 6-4.b. Pentacene energy levels are taken from the literature; [81, 82] PbS QD energy levels are determined as described in the text. [75] ΔE_{DA} is defined as the difference in energy between the pentacene HOMO and the QD conduction band. **b**, ΔE_{DA} for the different pentacene (abbreviated Pc) / PbS QD pairs as a function of QD bandgap. Blue symbols indicate pairs for which pentacene peaks are observed in the EQE spectrum; red symbols indicate pairs for which dips are observed. Note that the crossover from peaks to dips occurs when ΔE_{DA} crosses the pentacene triplet energy $E_{triplet}$, denoted by the green dotted line.

observed when ΔE_{DA} is greater than the triplet energy. These results verify the model for device operation explained above and highlight the utility of the tunable energy levels of PbS QDs in exploring the operational principles of nanostructured photovoltaic devices. Similar results were reported by Ehrler et al. [225] after acceptance for publication, but before publication, of our results; [83] these two bodies of work were developed independently.

We note the importance of accounting for ligand-induced energy level shifts in the determination of QD energy levels (a point explored in greater depth in Chapter 7). The energy levels measured in this study for 1,3-BDT-exchanged PbS QDs are shifted by $\sim$0.3 eV from values reported in the literature for oleic-acid-coated PbS QDs. [75] Using the energy levels from oleic-acid-coated QDs in the determination of ΔE_{DA} in Figure 6-5 would have shifted the expected ΔE_{DA} for all of the pentacene / QD pairs above the triplet energy of pentacene, suggesting that none of the devices tested here should demonstrate photocurrent from triplets in pentacene. The consistency of the results reported in Figures 6-4 and 6-5 highlights the importance of ligand-induced energy level shifts in the operation of PbS QD electronic devices.

It is also notable that the trends observed here are not confined to pentacene / PbS QD singlet fission photovoltaics. Jadhav and Brown et al. [83] explored a broad range of donor-acceptor material pairings for singlet fission photovoltaics, including pentacene and diphenylpentacene (DPP) as singlet-fission-active donors, and different small molecules (PDIF-CN2, PDI-CN2, C_{60}) and nanocrystals (PbSe QDs and the PbS QDs already discussed) as acceptors. These results, reproduced in **Figure 6-6**, match the trend shown in Figure 6-5: donor-acceptor pairings with ΔE_{DA} below the triplet energy demonstrate positive peaks in EQE at the wavelengths of peak pentacene or DPP absorption, indicating photocurrent contribution from singlet fission, while pairings with ΔE_{DA} above the triplet energy do not demonstrate photocurrent from singlet fission.

6.6.2 Other observations on device performance

Figure 6-7 shows the EQE spectra of ITO / PEDOT:PSS / PbS QD (0.99 eV bandgap)

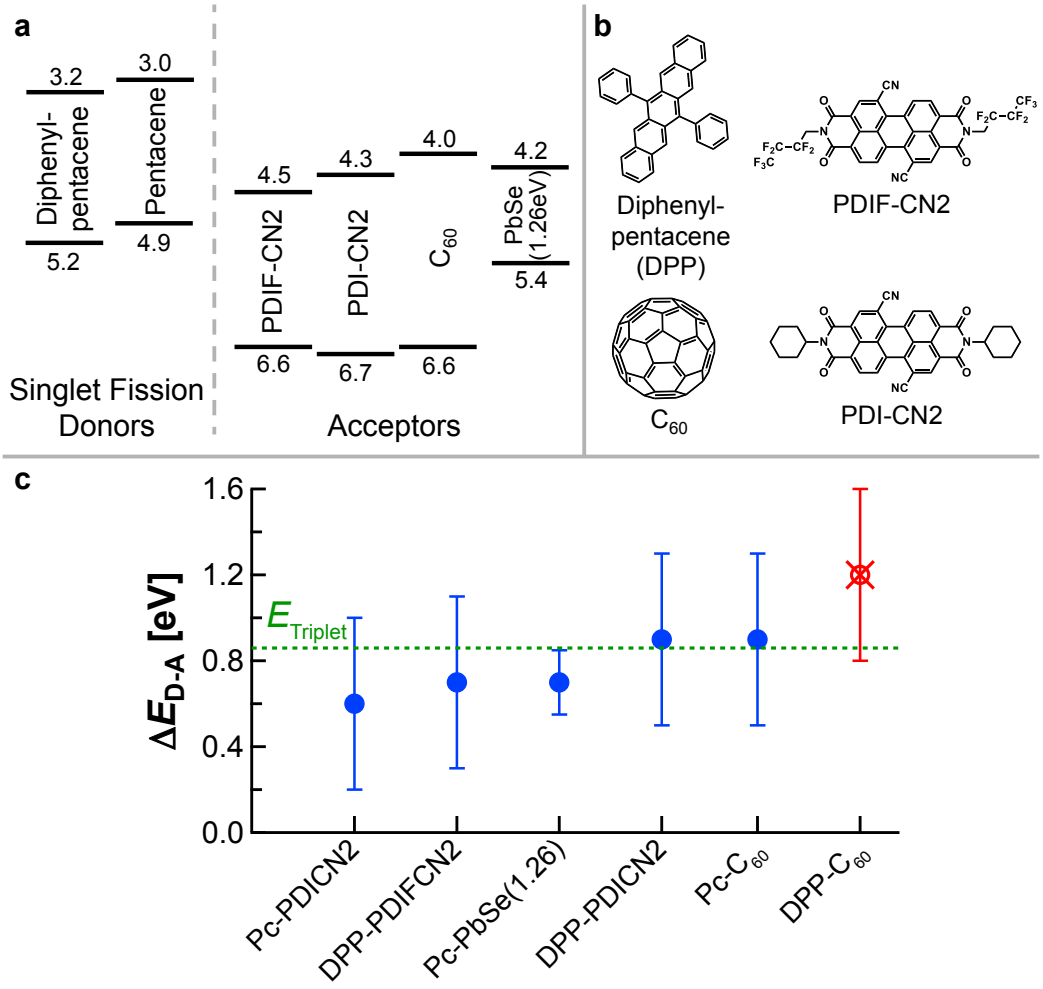

Figure 6-6: **Singlet fission photovoltaics using a range of materials pairings.** **a**, Energy levels and **b**, molecular structures of donor and acceptor materials used in Jadhav and Brown et al. [83] Energy levels are taken from the literature. [84, 85, 81, 82, 86, 75, 87, 88] Diphenylpentacene (DPP), N,N0-1H,1H-perfluorobutyl dicyanoperylenecarboxydiimide (PDIF-CN2), N,N'-dioctyl-6,12-dicyano-3,4,9,10-tetracarboxyperylene diimide (PDI-CN2) and buckminsterfullerene (C_{60}) are deposited by thermal evaporation; PbSe QDs are deposited by spin-coating with 1,3-BDT ligand exchange as described for PbS QDs. **c**, ΔE_{DA} of donor-acceptor pairs compared to the triplet energy of pentacene (abbreviated Pc) or diphenylpentacene (abbreviated DPP). Blue circles represent pairings that display photocurrent from the singlet fission material; red circles represent pairings that do not demonstrate photocurrent from the singlet fission material (measured by spectrally-resolved EQE as in Figure 6-4). The triplet energy $E_{triplet}$ is denoted by the green dotted line.

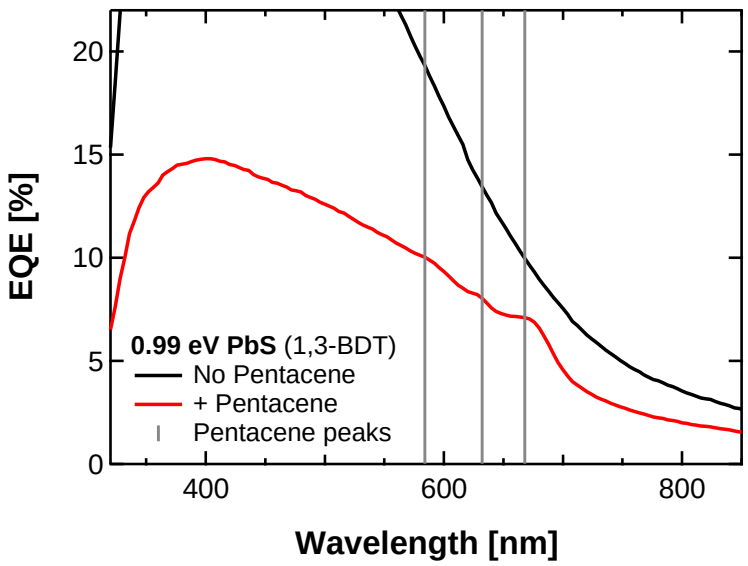

Figure 6-7: **External quantum efficiency of PbS QD photovoltaics with and without pentacene.** ITO / PEDOT:PSS / PbS QD / LiF / Al devices without (black) and with (red) the inclusion of a 60 nm-thick layer of pentacene between the PEDOT:PSS and PbS QD (0.99 eV bandgap, measured from the peak of the first excitonic absorption feature in solution) layers. Peaks in EQE are observed for the pentacene-containing device at the wavelengths of peak absorption of pentacene; the EQE of the device without pentacene is smooth and featureless in this region.

/ LiF / Al photovoltaic devices with and without the inclusion of pentacene between the PEDOT:PSS and PbS QD layers. The EQE of the pentacene-free device is smooth and featureless in the region of the pentacene absorption peaks, indicating that the EQE features discussed in the rest of this chapter result from the influence of pentacene rather than from the PbS QDs alone.

Figure 6-8 shows the current-voltage characteristics of the pentacene / PbS QD solar cells from Figure 6-4. The J_{SC} and V_{OC} follow the expected trends as a function of QD bandgap: J_{SC} increases as the QD bandgap decreases, as the absorption of the QDs extends further into the infrared and captures more of the broad solar spectrum, and V_{OC} decreases as the QD bandgap decreases, given the decreasing capacity for quasi-Fermi level splitting within the device.

Figure 6-9 shows the EQE of pentacene / PbS QD photovoltaics fabricated with a selection of the QD bandgaps reported in Figure 6-4.b, but where the PbS QDs have been ligand-exchanged with 1,2-BDT instead of 1,3-BDT (see Figure 7-1.d for the

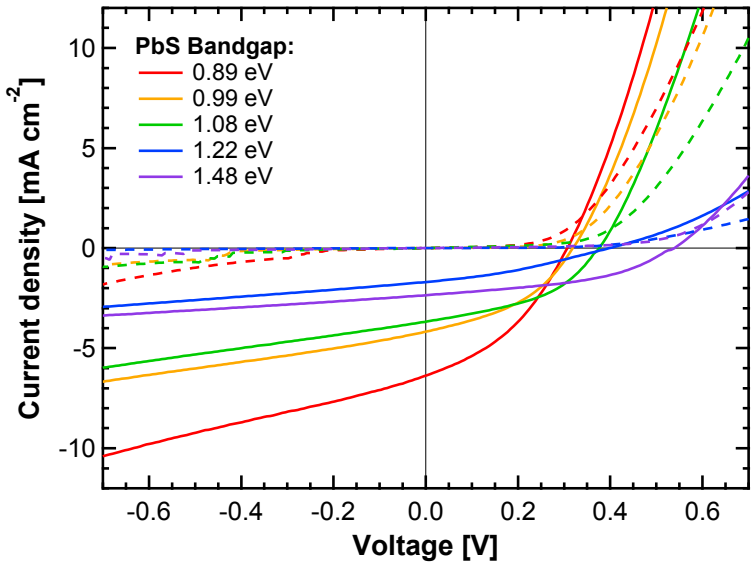

Figure 6-8: **Current-voltage characteristics of pentacene / PbS QD photovoltaics.** Dashed lines denote measurements taken in the dark; solid lines denote measurements taken under 100 mW cm^{-2} illumination. Data shown here represent averages taken over seven or more working devices from the same experimental run as the devices shown in Figure 6-4.

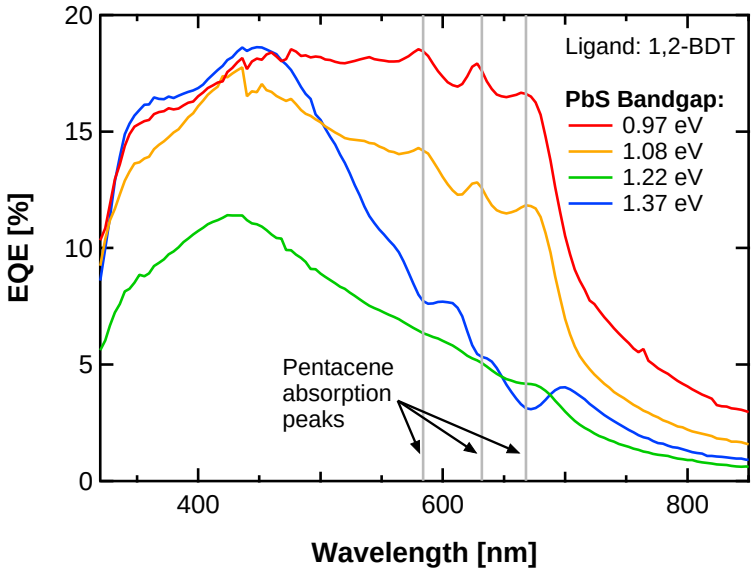

Figure 6-9: **External quantum efficiency of pentacene / PbS QD photovoltaics with 1,2-BDT ligand exchange.** PbS QDs for these devices are ligand-exchanged with 1,2-BDT instead of 1,3-BDT; all other fabrication details remain the same as in Figure 6-4.

chemical structures of 1,2-BDT and 1,3-BDT). The trend observed in Figure 6-9 is the same as in Figure 6-4.b—PbS QDs with small bandgaps and deep conduction band energies can dissociate triplets at the pentacene / QD interface, leading to positive peaks in the EQE spectrum at the peak absorption wavelengths of pentacene, while the PbS QDs with larger bandgap and shallower conduction band energy cannot dissociate triplets and thus demonstrate dips in EQE at the pentacene peak absorption wavelengths.

Figure 6-10.a shows the current-voltage characteristics of a 0.70 eV-bandgap PbS QD Schottky device with and without the inclusion of a layer of pentacene between the ITO / PEDOT:PSS electrode and the PbS QD layer. The incorporation of pentacene leads to a significant increase in shunt resistance and decrease in dark current, resulting in an increase in the V_{OC} of the device. Figure 6-10.b shows a possible explanation for this improvement: the pentacene and PbS QD bands are arranged such that pentacene could act as an electron blocking layer, decreasing electron leakage through the ITO / PbS interface. This effect has also been noted in small-molecule organic photovoltaics [197] and represents an additional benefit of the inclusion of pentacene in thin PbS Schottky junction devices, irrespective of the contribution of singlet fission. It should be noted, though, that similar performance enhancements could also be observed simply by increasing the thickness of the PbS QD layer.

6.7 Conclusion

In summary, the low and tunable bandgap and relatively deep energy levels of PbS QDs make this material an attractive candidate for the electron acceptor in singlet fission photovoltaics. The precisely tunable conduction band in particular enables a detailed exploration of the physics of charge and energy transfer at the interface between QDs and other materials—a characteristic that could be used to improve the understanding of many devices, even those that do not employ singlet fission.

At the same time, it is important to note that the power conversion efficiencies of the devices reported here are not high—less than 1 % in all cases, as shown in Figure 6-8.

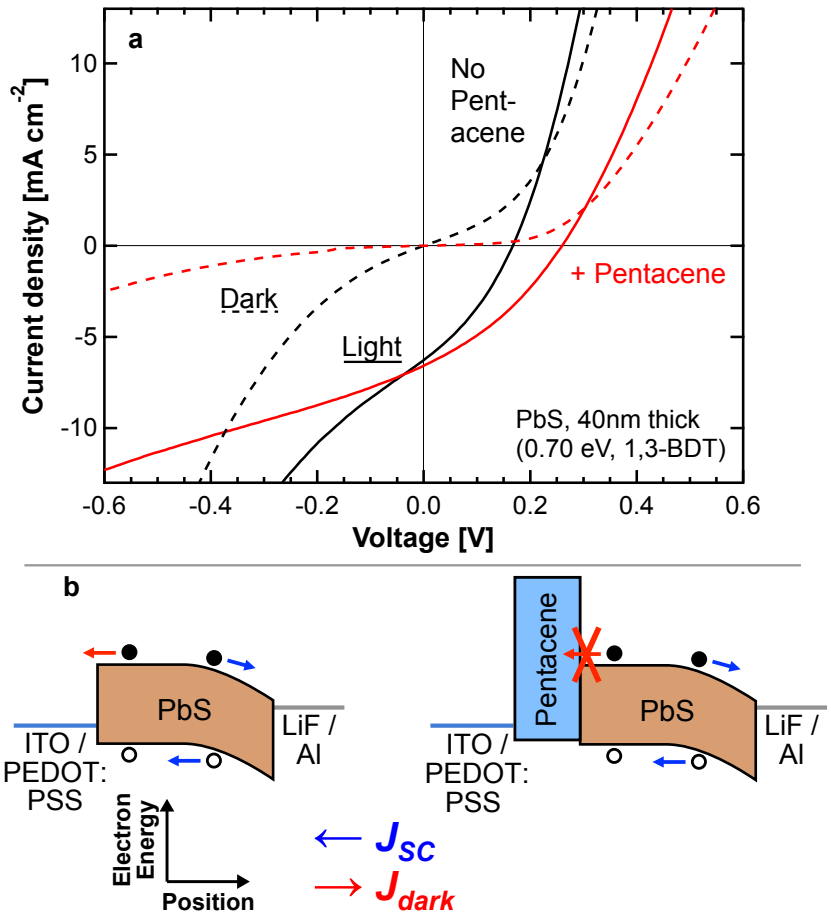

Figure 6-10: **Pentacene as an electron-blocking layer in thin PbS photovoltaics.** **a**, J-V curve of thin-film (∼40 nm) PbS QD photovoltaics in the dark (dashed line) and under illumination (solid line), with (red) and without (black) the inclusion of a 60 nm-thick layer of pentacene between the hole-transporting electrode and the PbS QD layer. The device with pentacene demonstrates a markedly higher shunt resistance and V_{OC}. **b**, Proposed energy band diagram for the PbS QD photovoltaic device with and without the inclusion of pentacene, suggesting that pentacene may increase the shunt resistance and V_{OC} by blocking the transfer of electrons from PbS to the hole-transporting electrode.

With thicker PbS layers, the QD photocurrent overwhelms the extra current generated from pentacene, suggesting that in the current device architecture, the pentacene does not significantly improve the device efficiency. Indeed, as shown in Figure 5-9.a, Figure 7-2, and Figure 7-3, higher efficiencies can be realized by fabricating PbS QD Schottky junction devices without a pentacene layer and with a higher PbS QD thickness. Nevertheless, the present study identifies important design parameters that apply to any singlet fission device and uncovers the physics of charge separation at the pentacene / PbS QD interface in a well-controlled way. Further studies exploring alternate device designs and ligand chemistries—particularly alternate chemistries at the pentacene / QD interface, or bulk heterojunction architectures mixing solution-processable singlet fission materials such as DPP with PbS QDs—may improve upon the architectures described here and realize higher efficiencies, making more complete use of the advantages that singlet fission provides.

Chapter 7

Energy Level Modification in Lead Sulfide Quantum Dot Thin Films Through Ligand Exchange

Portions of this chapter are reprinted with permission from Brown, P. R.;* Kim, D.;* Lunt, R. R.; Zhao, N.; Bawendi, M. G.; Grossman, J. C.; Bulović, V. *ACS Nano* **2014**, *8*, 5863–5872. [119] Copyright 2014 American Chemical Society.[i]

7.1 Introduction

As described in Chapter 4, the ability to tune the bandgap of colloidal QDs through control of the QD size is complemented by the ability to tune the charge carrier mobility, doping density, trap density, dielectric constant, and energy levels of QD solids through control of the QD surface chemistry via ligand exchange. Many studies have described the influence of ligand exchange on carrier transport processes within QD solids; relatively fewer have examined the effects of ligand exchange on energy level structure. Soreni-Harari et al. examined the energy levels of InAs QDs exchanged with five different ligands using scanning tunneling microscopy (STM); [174] Timp et al. examined PbSe QDs exchanged with two different ligands via ultraviolet photoelecron

[i]* These authors contributed equally to the cited work.

spectroscopy (UPS); [175] and Munro et al. and Jasieniak et al. examined CdSe QDs exchanged with a number of different ligands by UPS and photoemission spectroscopy in air (PESA). [176, 75] These studies identified energy level shifts of up to 0.35 eV across different ligand treatments. For PbS QDs, currently the highest-efficiency QD solar cell material, previous energy level measurements were primarily performed on QDs with the original oleic acid ligands, and were measured either in air or via cyclic voltammetry (CV) in solution. [79, 75] Later studies examined PbS QDs with a narrow subset of other ligands. [207, 263, 264] Considering the notable shifts in energy levels observed for CdSe QDs following ligand exchange and the large array of surface chemistries used in the literature for PbS QD photovoltaics, it is unlikely that the energy levels of oleic-acid-capped PbS QDs are representative of the energy levels of the ligand-exchanged films used in PbS QD solar cells. Given the significant impact that energy level offsets have on device performance (Chapters 5 and 6), a greater understanding of the energy level structure of PbS QDs exchanged with device-relevant ligands is necessary to enable further understanding and optimization of the performance of PbS QD photovoltaics.

Here, the energy levels of PbS QDs treated with twelve different ligands are measured using UPS. [119] These ligands were chosen for their relevance to QD PV devices and their similar procedures for ligand exchange; each class of ligands tested here has been used in the literature in QD photovoltaics, photodetectors, or transistors, [265, 186, 166, 191, 167, 266] and each can be substituted for the native oleic acid ligands on the QD surface using the layer-by-layer sequential spin-coating process described in Section 4.2. The measured valence band maxima of a single size of PbS QDs exchanged with these ligands span a range of 0.9 eV. Atomistic simulations of the vacuum energy shift induced by the binding of five of these different ligands to pristine PbS slabs reproduce the observed trend in energy level modification. The impact of these energy level shifts on photovoltaic performance is determined through studies on devices employing 1,2-ethanedithiol (EDT), 1,2-benzenedithiol (1,2-BDT), and 1,3-benzenedithiol (1,3-BDT) ligands. Even between these chemically similar ligands, shifts in the valence band energy of more than 0.2 eV necessitate

ligand-dependent adjustments of the electron- and hole-extracting contacts to achieve optimal performance. These results have recently guided the design and understanding of a certified 8.55% efficient PbS QD solar cell, a record at the time of fabrication for this class of devices. [69] These findings complement the known tunability of QD bandgap and highlight an important mechanism of control over the electronic properties of colloidal QDs.

7.2 Methods

7.2.1 PbS QD synthesis and film preparation

All synthesis, fabrication, and testing is performed under oxygen- and water-free conditions unless otherwise stated. Oleic-acid-capped PbS QDs are synthesized via standard literature methods [267] and purified three times by precipitation and centrifugation in a mixture of acetone and 1-butanol, followed by resuspension in hexane. After the final round of purification, the QDs are dissolved in octane at a concentration of $25\,\mathrm{mg\,mL^{-1}}$. All solid QD films are prepared by sequential spin-casting. For each layer, roughly 15 µL of QD solution is dispensed through a 0.02 µm filter (Anotop) onto a 12.5 mm × 12.5 mm substrate and spin-cast at 1500 rpm for 15 s. Roughly 200 µL of ligand solution is then dispensed through a 0.1 µm filter (PTFE) onto the substrate, allowed to sit for 30 s, and spun dry. The substrate is then flooded with the solvent used for ligand exchange and spun dry three times to remove unbound ligand, and the entire process is repeated; each complete iteration results in the deposition of roughly 20 nm of QDs. The ligand concentrations and solvents used in this study are representative of well-characterized ligand exchange conditions from the literature: benzenethiol and 1,2-, 1,3-, and 1,4-benzenedithiol, 1.7 mM in acetonitrile (ACN); [265] 1,2-ethanedithiol, 1.7 mM in ACN; [186] 3-mercaptopropionic acid, 115 mM in methanol (MeOH); [166] ethylenediamine, 1 M in MeOH; [191] ammonium thiocyanate, 30 mM in MeOH; [167] and tetrabutylammonium fluoride, chloride, bromide, and iodide, 30 mM in MeOH. [266] All chemicals are purchased from Sigma Aldrich at the

highest purity available.

7.2.2 Ultraviolet photoelectron spectroscopy

UPS spectra are collected using an Omicron ultrahigh vacuum system with a base pressure of 1×10^{-10} mbar. The substrates for the UPS measurement are 12.5 mm $\times$ 12.5 mm glass slides coated with Cr(10 nm) / Au(100 nm) anodes by thermal evaporation and stored in air-free conditions without further surface treatment. Five sequential spin casting cycles of PbS QDs with various ligand treatments, performed as described above, result in a QD film thickness of roughly 100 nm. Electrical contact from the steel sample plate to the Cr / Au anode is made using carbon tape. Samples for UPS are transported from an inert-atmosphere glovebox (<1 ppm O_2, <10 ppm H_2O) to the UPS system without exposure to air using a load-locked transfer system. During the UPS measurement, illumination at 21.22 eV is provided by the He(I) emission line from a Helium discharge lamp, and the chamber pressure increases to 1×10^{-7} mbar. The samples are biased at -5.0 V to ensure accurate determination of the low-kinetic-energy cutoff, and electron emission is collected at 0° from normal. Single kinetic energy scans are completed in <45 s to minimize charging. Cutoff energies are determined from the intersection of a linear extrapolation of the cutoff region to a linear extrapolation of the baseline.

7.2.3 Photovoltaic device fabrication

Photovoltaic devices are deposited onto ITO-coated glass substrates (Thin Film Devices) that have been cleaned by ultrasonication in micro-90 soap solution, deionized water, acetone, and isopropanol, followed by treatment with ozone plasma. The device area is defined by the anode-cathode overlap to be 1.24 mm^2. Zinc oxide (Plasmaterials) is deposited by rf-sputtering as described in Section 5.2. Molybdenum oxide (MoO_3, 99.9995%), lithium fluoride (LiF, 99.99%), buckminsterfullerene (C_{60}), 3,4,9,10-perylenetetracarboxylic bisbenzimidazole (PTCBI), bathocuproine (BCP), aluminum, silver, and gold are deposited by thermal evaporation at 0.5–1 Å s^{-1} at

a base pressure of 1×10^{-6} torr. Polyethylenedioxythiophene-polystyrene sulfonate (PEDOT:PSS, conductive grade, Sigma-Aldrich) is deposited by spin-casting in air at 4000 rpm for 60 s, then annealed at 150 °C inside a nitrogen-atmosphere glovebox for 30 min. Where noted in the text, the ITO-coated glass substrates are soaked overnight in a solution of 12 mM (3-mercaptopropyl)trimethoxysilane (3-MPTMS) in toluene to increase QD adhesion to the substrate, then sonicated for 1 min in isopropanol to remove unbound 3-MPTMS. N-p heterojunction (np-HJ) photovoltaic devices utilize the architecture ITO / ZnO (50 nm) / PbS QD (160 nm) / MoO_3 (10 nm) / Au (100 nm). Schottky junction photovoltaic devices utilize the architecture ITO / PEDOT:PSS / PbS QD (160 nm) / LiF (0.7 nm) / Al (100 nm) unless otherwise noted. Donor-acceptor photovoltaic devices utilize the architecture ITO / PEDOT:PSS / PbS QD (160 nm) / (C_{60} or PTCBI) (40 nm) / BCP (10 nm) / Ag (100 nm).

7.2.4 Electrical characterization

Current density-voltage (J-V) curves of photovoltaic devices are recorded using a Keithley 6487 picoammeter, and 100 mW cm^{-2} illumination is provided by a xenon lamp (Newport 96000) equipped with an AM1.5G filter. Spectral mismatch and additional electrical characterization details are given in Section 7.7.3.

7.3 Ligand-dependence of QD energy levels measured by UPS

Figure 7-1.a shows a representative UPS spectrum of a 100 nm-thick PbS QD film treated with 1,3-BDT without exposure to air. UPS measures occupied electronic states and thus provides information on the Fermi level (determined from the low-binding-energy cutoff) and valence band maximum (VBM, determined from the high-binding-energy-cutoff) of a material. The energy E_C of the conduction band minimum (CBM) can be approximated by subtracting the electronic transport gap E_g of the material from the energy E_V of the VBM, where E_g is determined from the sum

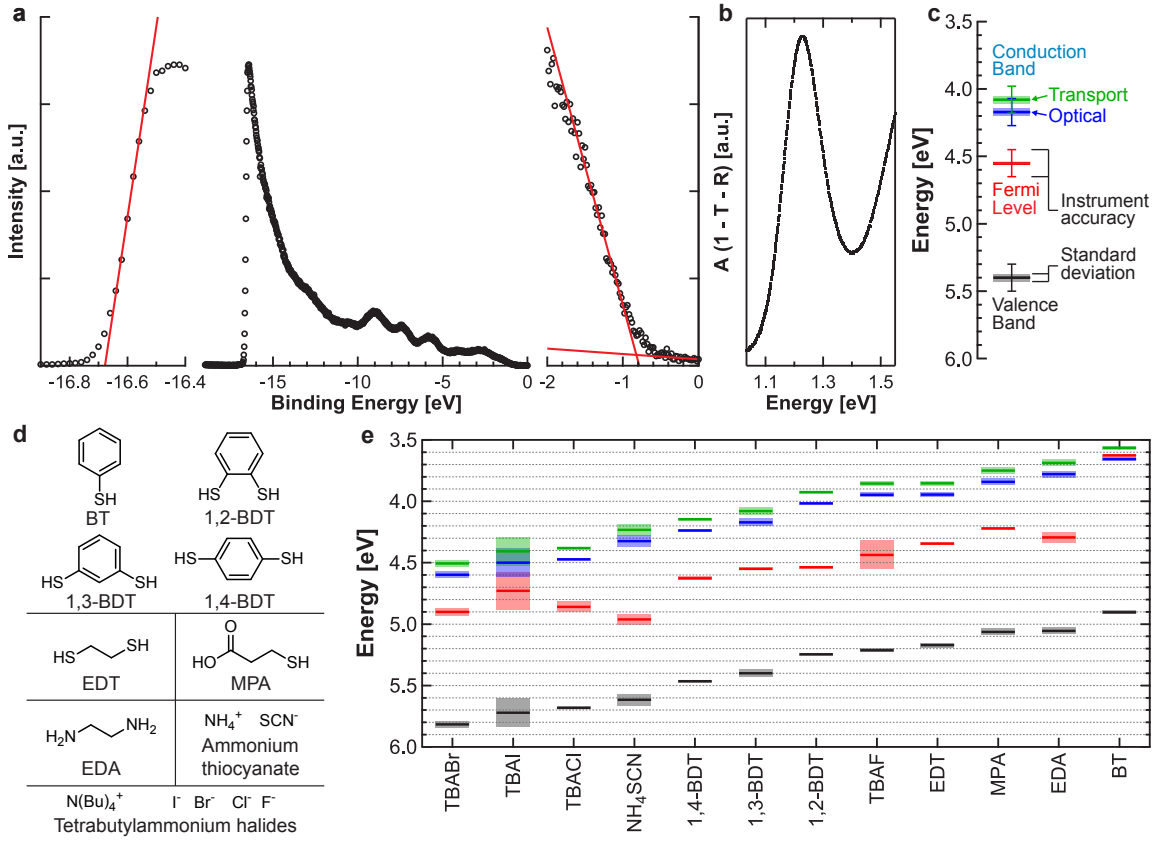

Figure 7-1: **Ligand-dependent energy levels measured by UPS. a**, Complete ultraviolet photoelectron spectrum of 100 nm-thick 1,3-BDT-exchanged PbS QD film on gold. The left and right side panels display magnified views of the high-binding-energy cutoff (Fermi level) and low-binding-energy cutoff (valence band edge binding energy) regions, respectively, where the band energies are determined from the intersection of a linear extrapolation from the cutoff region to the baseline. **b**, Optical absorption spectrum ($absorption = 1 - transmission - reflection$) of the first excitonic peak of 1,3-BDT-exchanged PbS QDs. The peak absorption at $E = 1.23\,\text{eV}$ is taken as the optical bandgap. **c**, Energy level diagram of 1,3-BDT-exchanged PbS QDs determined from the spectra in **a** and **b** and (7.1). Distinction is made between the instrumental accuracy (0.1 eV) and the standard deviation across multiple measurements (0.02 eV). **d**, Chemical structures of the ligands employed in this study. **e**, Complete energy level diagrams of PbS QDs exchanged with the ligands shown in **d**. All PbS QDs used in this figure have a first excitonic absorption peak at $\lambda = 963\,\text{nm}$ in solution with native oleic acid ligands. Each data point represents the average of 2–4 measurements across different samples; shaded bars indicate one standard deviation, and error bars for instrument accuracy are omitted for clarity.

of the optical bandgap E_g^{opt} and the Coulombic stabilization energy of the confined electron and hole, first derived by Brus using the particle-in-a-box model, such that

$$\begin{aligned} E_C &= E_V - E_g \\ &= E_V - {E_g}^{opt} - 1.786\frac{e^2}{4\pi\varepsilon_0\varepsilon_{QD}R}, \end{aligned} \tag{7.1}$$

where e is the charge of the electron, ε_0 is the permittivity of free space, ε_{QD} is the optical dielectric constant of the QD core material, and R is the quantum dot radius (determined by matching the first excitonic absorption peak in solution to a published sizing curve). [75, 268] [ii] The PbS QDs used in this study are highly confined, with quantum-confined bandgaps 0.6–1.1 eV larger than the bulk bandgap of PbS. The confined electrons and holes therefore have a high kinetic energy, and the optical dielectric constant (${\varepsilon_\infty}^{PbS} = 17.2$) is a more suitable choice than the static dielectric constant (${\varepsilon_0}^{PbS} = 169$). [269]

Figure 7-1.b shows a representative absorption spectrum of 1,3-BDT-treated PbS QDs on glass. The first excitonic absorption peak of the solid-state ligand-exchanged QDs is at energy $E_g^{opt} = 1.23\,\text{eV}$, corresponding to a transport bandgap of $E_g = 1.32\,\text{eV}$. Figure 7-1.c summarizes the energies of the VBM, Fermi level, and CBM determined from the measurements in Figure 7-1.a,b for 1,3-BDT-treated PbS QDs. While the instrumental accuracy of UPS is roughly 0.1 eV, [89] the standard deviation of our measurement (here across 4 different samples) is much smaller, in the range of 0.02 eV.

Figure 7-1.d shows the chemical structure of the twelve ligands employed in this study, including thiols [benzenethiol (BT), 1,2-, 1,3-, and 1,4-benzenedithiol (1,2-BDT, 1,3-BDT, and 1,4-BDT), 1,2-ethanedithiol (EDT), and 3-mercaptopropionic acid (MPA)], a primary amine [1,2-ethylenediamine (EDA)], ammonium thiocyanate (SCN), and halides [tetrabutylammonium iodide (TBAI), bromide (TBABr), chloride (TBACl), and fluoride (TBAF)]. Figure 7-1.e shows the measured energy levels of

[ii] Energy levels are reported in terms of their energy relative to the vacuum energy. Both the VBM and CBM are deeper in energy than vacuum; the statement "$E_V = 5\,\text{eV}$" means "An electron at the VBM is 5 eV lower in energy than an electron in vacuum."

a single batch of PbS QDs ($\lambda = 963\,\text{nm}$ first excitonic absorption peak in solution) exchanged with these different ligands, sorted by decreasing VBM binding energy (complete photoemission and absorption spectra for QDs exchanged with each ligand are given in Figures 7-7 and 7-11 in Section 7.7).

A maximum shift of 0.9 eV in the VBM is observed between QDs treated with TBABr and BT. Even among the chemically similar bidentate thiols, a shift of 0.3 eV is observed between PbS QDs treated with EDT and 1,4-BDT. Similarly large shifts in energy levels have been observed for conductors treated with thin layers of amine-containing polymers. [270] Such large shifts are expected to have considerable influence on the operation of electronic devices fabricated using PbS QDs. We note that these energy levels are characteristic only of the specific size of PbS QDs studied here, and only under air-free fabrication and storage conditions; UPS measurements performed on PbS QD films fabricated in air indicate different values for the Fermi level and VBM. [69] It is also notable that the majority of ligands tested in this study give rise to VBMs significantly deeper than those reported for oleic-acid-capped PbS QDs in the literature (oleic acid ligands are too insulating to be employed in UPS, which requires adequate grounding of the emissive surface to prevent charging-induced shifts in the observed energy levels). [75, 79] This result highlights the importance of performing energy level measurements on QDs in a chemical environment that is as close as possible to the environment present in an operating device, taking into account both the solid-state ligand environment and the history of environmental exposure.

7.4 Ligand-dependent PV performance

To determine the importance of these shifts in QD energy levels for photovoltaic devices, PbS QDs exchanged with EDT, 1,2-BDT, and 1,3-BDT are incorporated into ZnO / PbS QD n-p heterojunction, [77] Schottky junction, [180] and donor-acceptor heterojunction [186] photovoltaics, the operation and design of which are described in Section 4.4. These ligands have been well studied in PbS QD optoelectronic devices to date [165, 122, 271] and employ identical, reproducible ligand-exchange procedures,

so they provide an ideal platform for comparison. All QD film preparation for the photovoltaics studied here is performed under the same air- and water-free conditions as the film preparation for the UPS studies described above.

Figure 7-2 shows the dark and light J-V characteristics of indium tin oxide (ITO) / ZnO / PbS QD / MoO_3 / Au n-p heterojunction (np-HJ) photovoltaics (Figure 7-2.a) and ITO / PEDOT:PSS / PbS QD / LiF / Al Schottky junction (SJ) photovoltaics (Figure 7-2.b) fabricated with EDT-, 1,2-BDT, and 1,3-BDT-exchanged PbS QD (λ = 905 nm first excitonic absorption peak in solution) films. Two general performance trends are apparent. First, EDT treatment results in a lower open-circuit voltage (V_{OC}) than 1,2-BDT and 1,3-BDT treatments in both the np-HJ and SJ architectures. Second, the relative performance of 1,2-BDT and 1,3-BDT-exchanged QDs is reversed between the np-HJ and SJ architectures: 1,3-BDT exchange results in the best performance for the np-HJ architecture, while 1,2-BDT exchange results in the best performance for the SJ architecture. A straightforward comparison of trap distributions, carrier mobilities, and recombination rates could explain the lower performance of EDT in both structures, but not the switch in performance between 1,2-BDT and 1,3-BDT. As described in detail in Appendix A, while EDT treatment leads to the highest carrier mobility of the three ligands studied, the high recombination rate and high trap density of EDT-exchanged PbS QD films lead to a lower V_{OC} and power conversion efficiency (η_P) than BDT-exchanged films. However, changes in these properties do not explain the architecture-dependent performance of 1,2-BDT and 1,3-BDT-exchanged QDs. The difference in the energetic environment of the QD film between the np-HJ and SJ architectures suggests that a shift in the energy levels of the PbS QDs between the two different ligand treatments could explain this difference in performance.

By focusing on the SJ architecture, the interfacial energetics can be tuned in a controlled manner through modification of the electron- and hole-extracting contacts. A common modification to the simple ITO / PbS / cathode structure is to insert a layer of PEDOT:PSS as a hole-extracting layer between the ITO and the PbS QDs. [272, 87] PEDOT:PSS is known to aid in hole injection into, and hole extraction out of, organic semiconductors with deep highest occupied molecular orbitals (HOMOs) as a result of

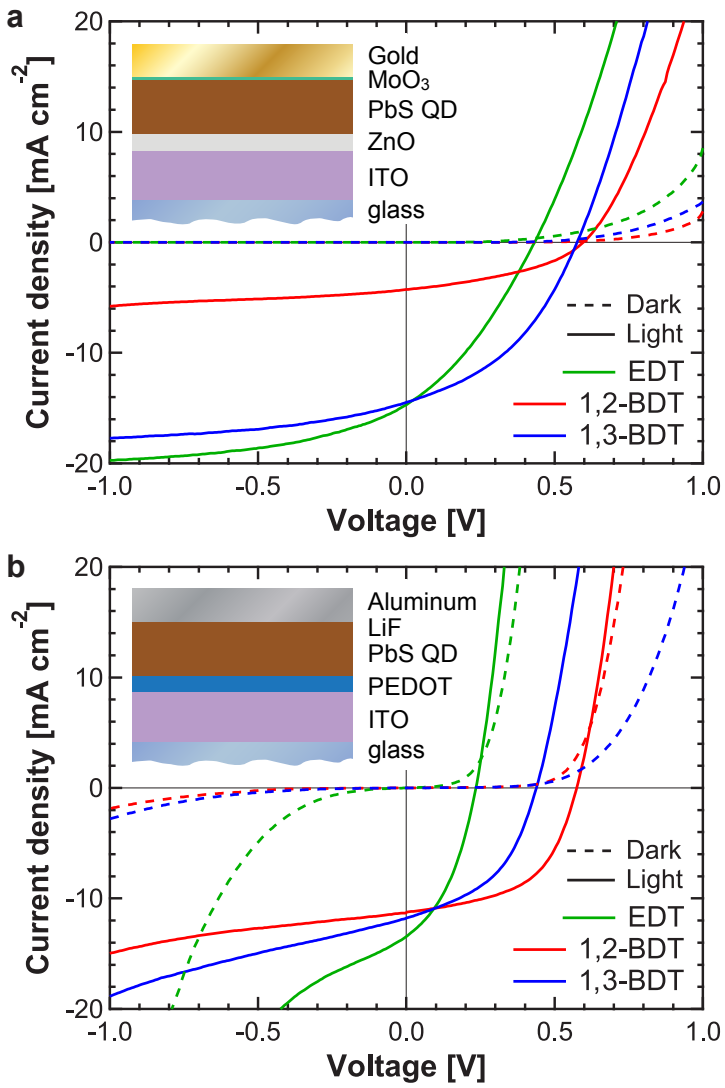

Figure 7-2: **Architecture-dependent photovoltaic performance.** Current-voltage characteristics measured in the dark (dashed lines) and under 100 mW cm^{-2} AM1.5 illumination (solid lines) for EDT-, 1,2-BDT-, and 1,3-BDT-exchanged PbS QDs (λ = 905 nm first excitonic absorption peak in solution) in **a**, ZnO / PbS n-p heterojunction and **b**, Schottky junction architectures. The devices in **a** and **b** have opposite polarities, but are plotted in the same polarity to facilitate comparison.

its deep work function ($E_F = 5.0\,\text{eV}$ for PEDOT:PSS, vs. $4.7\,\text{eV}$ for ITO). [273, 205] In **Figure 7-3.a**, it is observed that the inclusion of a PEDOT:PSS hole-extracting layer results in a 3.2-fold improvement in η_P for a SJ photovoltaic fabricated with 1,3-BDT-exchanged PbS QDs, while it has a negligible effect on a 1,2-BDT-exchanged SJ photovoltaic. This observation matches what would be expected from the energy levels reported in Figure 7-1.e: 1,3-BDT-treated QDs, with their deeper VBM, benefit more from the high-work-function PEDOT:PSS hole transport layer than do the 1,2-BDT-treated QDs.

Similarly, a thin layer of LiF is commonly inserted between the cathode and the electron transport layer in organic LEDs and solar cells, where it has been shown to increase the efficiency of electron injection and extraction. [274, 275] This effect is commonly attributed to a lowering of the effective cathode work function as a result of a strong interface dipole induced by the LiF, resulting in a reduced barrier height for electron injection. [276] In the PbS QD SJ architecture described here, a reduction in the cathode work function should result in a greater benefit for PbS QDs with a shallower VBM and CBM by strengthening the Schottky junction at the interface and increasing the driving force for electron extraction. Indeed, it is observed in Figure 7-3.b that the insertion of LiF results in a 2.2-fold improvement in η_P for 1,2-BDT-treated QDs while having a negligible effect on the η_P of 1,3-BDT-treated QDs, which is consistent with the shallower energy levels reported in Figure 7-1.e for 1,2-BDT-treated PbS QDs.

The donor-acceptor heterojunction (DA-HJ) is an alternative to the SJ architecture that relies directly on the band offsets at the D-A interface (rather than on Schottky barrier formation, which is known to be sensitive to surface traps and other complications) [113] to separate charge carriers, thus providing an architecture wherein the interfacial energy level alignment can be probed more directly. **Figure 7-4.a** displays a DA-HJ device architecture in which PbS QDs act as the electron donor and either buckminsterfullerene (C_{60}) or 3,4,9,10-perylenetetracarboxylic bisbenzimidazole (PTCBI) act as the electron acceptor.

Figure 7-4.b displays an outline of the energy level structure in a DA-HJ photo-

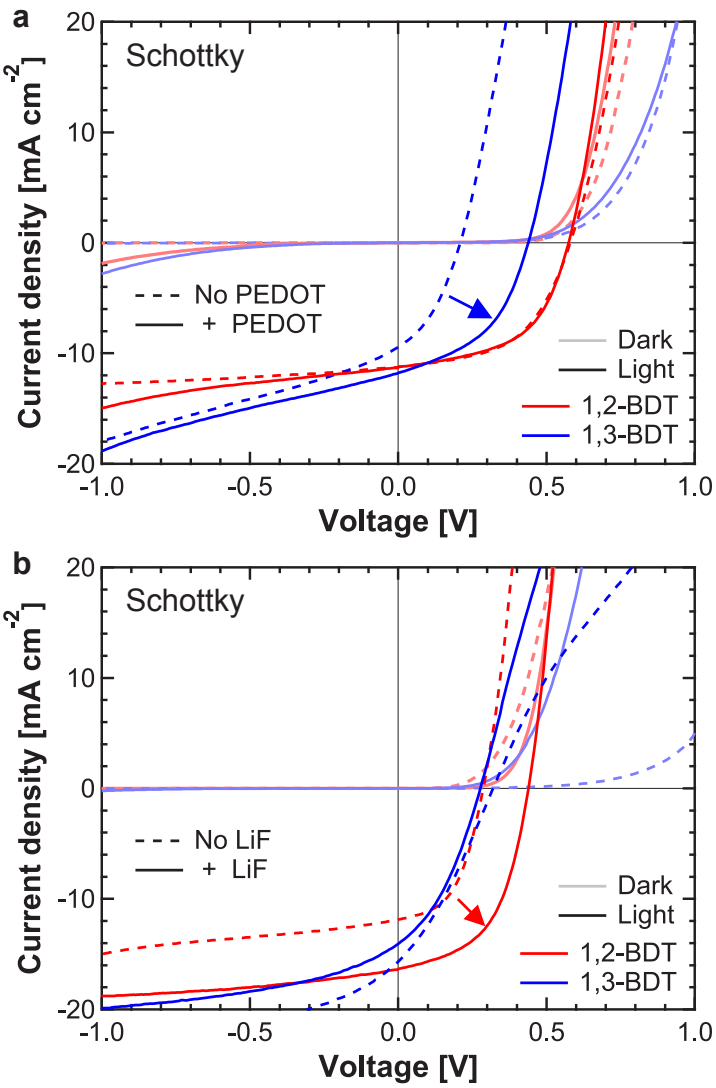

Figure 7-3: **Ligand-induced changes in Schottky photovoltaic performance.** Current-voltage characteristics of Schottky junction photovoltaics employing 1,2-BDT (red traces) and 1,3-BDT (blue traces) showing the influence of a PEDOT:PSS hole transport layer (**a**) and a LiF cathode interlayer (**b**). In each case the interlayer significantly improves the performance for only one of the two ligand-exchange methods, in a manner in keeping with the results of Figure 7-1.

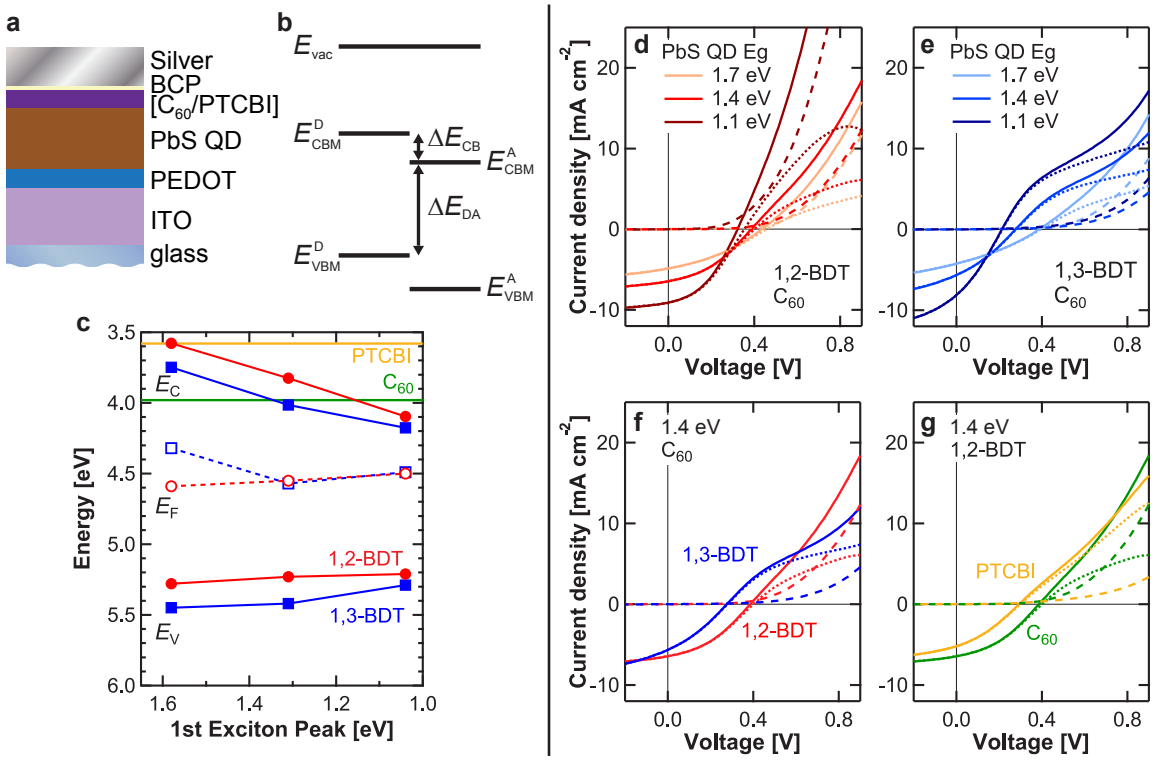

Figure 7-4: **Ligand- and QD-size-induced changes in DA-HJ photovoltaic performance.** **a**, Device structure of the donor-acceptor heterojunction and **b**, schematic band diagram of the donor-acceptor pair, showing a conduction band offset ΔE_{CB} that is favorable for photocurrent extraction. **c**, Measured energy levels of three different sizes of PbS QDs, with LUMO energies of C_{60} and PTCBI from the literature. The conduction band energy E_C corresponds to the transport gap; the optical gap is omitted here for clarity. The experimental uncertainty of the QD energy levels determined by UPS is 0.1 eV; the uncertainty of the LUMOs of the organic materials determined by inverse photoelectron spectroscopy in the literature is 0.5 eV. [89] **d-g**, Dark current (dashed curves), light current (solid curves), and photocurrent (dotted curves) of DA-HJ photovoltaics, comparing 1,2-BDT-treated QDs of different size paired with C_{60} (**d**), 1,3-BDT-treated QDs of different sizes paired with C_{60} (**e**), 1,2-BDT and 1,3-BDT-treated QDs of a given size paired with C_{60} (**f**), and 1,2-BDT-treated QDs paired with PTCBI and C_{60} (**g**).

voltaic device. An important design criterion for the DA-HJ is that the conduction band offset of the donor and acceptor, given by $\Delta E_{CB} = {E_{CBM}}^{D} - {E_{CBM}}^{A}$, must allow energetically favorable transfer of photogenerated electrons from the CBM of the donor to the lowest unoccupied molecular orbital (LUMO) of the acceptor. A large ΔE_{CB} should also prevent unwanted back-transfer of photogenerated electrons from the acceptor to the donor. Thus, by modifying ΔE_{CB} and observing the performance of the resultant DA-HJ photovoltaic device, shifts in the energy levels of the PbS QDs can be inferred and compared to those determined by UPS.

Figure 7-4.c shows the measured energy levels of three different sizes of PbS QDs (λ = 725 nm, 905 nm, and 1153 nm first excitonic absorption peaks in solution) after ligand exchange with 1,2-BDT or 1,3-BDT. The CBM is found to change more with QD size than the VBM, as has been noted previously in the literature. [75, 79] The LUMOs of C_{60} and PTCBI are taken from inverse photoelectron spectroscopy measurements reported in the literature to be 4.0 $\pm$ 0.5 eV and 3.6 $\pm$ 0.5 eV, respectively. [89] Figure 7-4.d-g shows the dark current, light current, and photocurrent J-V response (J_{dark}, J_{light}, and J_{pc}, respectively, where $J_{pc} = J_{light} - J_{dark}$) of DA-HJ photovoltaics pairing these three different sizes of 1,2-BDT- and 1,3-BDT-exchanged PbS QDs with C_{60} and PTCBI.

As the bandgap of the 1,2-BDT-exchanged QDs is reduced, the reduced capacity for quasi-Fermi level splitting leads to a smaller V_{OC}, but the increased absorption at longer wavelengths leads to a higher J_{SC} (Figure 7-4.d). This same trend is observed for 1,3-BDT-exchanged QDs (Figure 7-4.e), but the diode properties for 1,3-BDT deviate substantially from ideal behavior. As the bandgap decreases and the CBM moves to deeper energies, J_{light} crosses J_{dark} at smaller voltages and a "kink" in the forward-bias J_{light} becomes more pronounced, corresponding to a reversal in the polarity of J_{pc} as the short circuit current (negative polarity) is subsumed by an increased photoconductivity (positive polarity). This increase in photoconductivity in forward bias is expected if the ΔE_{CB} at the donor-acceptor interface is decreased, corresponding to a deepening of the donor (QD) CBM, as the barrier to electron back-transfer from acceptor to donor is reduced.

Similar trends are observed in Figure 7-4.f,g when comparing the performance of PTCBI and C_{60} as acceptors and the performance of 1,2-BDT-exchanged QDs and 1,3-BDT-exchanged QDs as donors. The LUMO of PTCBI is roughly 0.4 eV shallower in energy than that of C_{60}, leading to a reduction in ΔE_{CB}; correspondingly, the DA-HJ employing PTCBI demonstrates a greater contribution from photoconductive electron back-transfer in the form of a lower-voltage J_{light}-J_{dark} crossover. Similarly, from Figure 7-4.c, the measured CBM of 1,3-BDT-exchanged 1.4 eV-bandgap PbS QDs is 0.2 eV deeper than that of 1,2-BDT-exchanged PbS QDs of the same size, which also leads to a reduction in ΔE_{CB}; as such, J_{light} for 1,3-BDT demonstrates a stronger forward-bias "kink" and a lower-voltage crossover with J_{dark}.

Taken together, Figure 7-4.d-g shows that the substitution of 1,3-BDT for 1,2-BDT (which, from the energy level measurements reported here, results in a 0.1–0.2 eV deeper CBM) induces changes in DA-HJ photovoltaic performance that are qualitatively similar to those induced by reducing the bandgap of the QD or by substituting PTCBI for C_{60}, both of which are known from energy level measurements reported in the literature to result in a reduction in ΔE_{CB}. This observation provides support for the method of energy level measurement reported here and for the use of these energy levels in describing the performance of PbS QD optoelectronic devices.

7.5 Ligand binding simulations by density functional theory

We describe here the density functional theory (DFT) calculations performed by Donghun Kim in Brown and Kim et al. [119], which provide insight into the electric field profile at the QD/ligand interface and explain some of the band energy shifts observed in Figure 7-1.

DFT calculations are widely used to simulate energy level shifts at interfaces between inorganic materials and organic molecules. [169, 118, 170, 277, 278] As shown in **Figure 7-5.a**, the surface of a PbS QD is here approximated as a semi-infinite

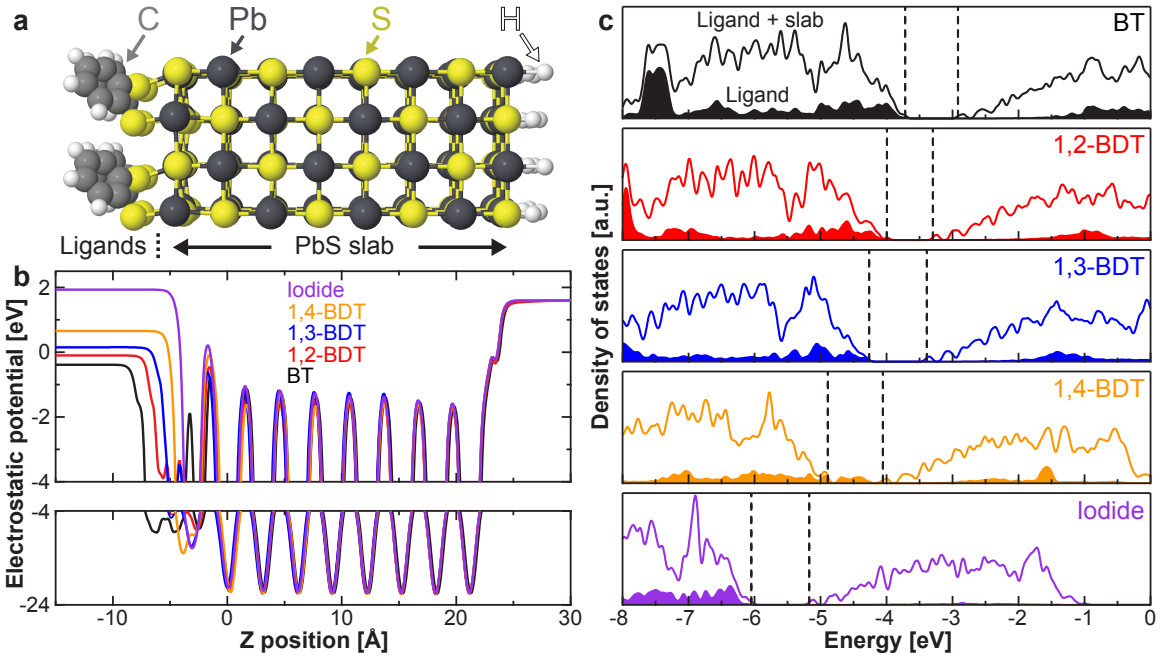

Figure 7-5: **DFT calculations of ligand-induced energy shifts for PbS slabs.** **a**, Schematic diagram of modeled PbS slab. The left side of the slab is passivated by adsorbed ligands (1,2-BDT is shown here as an example) and the right side is passivated by appropriate pseudo-hydrogen atoms to ensure charge balance. Monodentate (BT, iodide) and bidentate (1,2-, 1,3-, and 1,4-BDT) ligands are employed here, with ligand density set at one binding atom per surface Pb atom (hence bidentate ligands have half the areal density of monodentate ligands). **b**, Plane-averaged electrostatic potentials of PbS slabs with different ligands. The potential in the vacuum region far to the left of an unpassivated PbS slab is set to zero. **c**, Density of states of the ligand (filled curve) and ligand-slab system (unfilled curve) for each of the five ligands considered. The vacuum level above each passivated PbS slab is set to zero. The vertical dashed lines signify the valence and conduction band edge energies. DFT calculations performed by Donghun Kim.

PbS (100) slab, as the (100) and (111) facets are known to be dominant for PbS QDs (similar trends in DFT results are obtained for binding to Pb-rich (111) facets, as shown in Figure 7-14 in Section 7.7.2). [169, 279, 280] Modeling the QD surface as a semi-infinite quasi-two-dimensional slab is much more computationally efficient than modeling the entire three-dimensional QD/ligand system, and the electrostatic environment encountered by the electron or hole during transfer across the QD/ligand interface should be similar in both cases. A small dependence of the magnitude of the ligand-induced shift on QD size has been observed elsewhere for InAs QDs, [174] but the direction of the trend in energy levels for different ligands is expected to be independent of QD size. As shown in Figure 7-5.a, one side of the slab is passivated by ligands and one side by pseudo-hydrogen atoms for charge balance. Similar results are obtained when both sides of the slab are passivated by ligands (Figure 7-16 in Section 7.7.2).

Five of the ligands employed in Section 7.3 are simulated by DFT (BT, 1,2-BDT, 1,3-BDT, 1,4-BDT, and iodide), with the ligand coverage held constant at one ligand binding group per surface Pb atom (thus BT and iodide have twice the density of the benzenedithiols). The ligands tested here are known to efficiently displace the original oleic acid ligands, [168, 159, 217, 114, 281] but it is possible that some oleic acid remains bound to the QD surface, perhaps as a result of variations in binding affinity between the (100) and (111) facets. [169, 282, 283] To facilitate comparison between the different ligands and simplify the DFT simulations, complete exchange of oleic acid is assumed.

Figure 7-5.b shows the plane-averaged electrostatic potentials for these five ligands bound to PbS (100) slabs. Large shifts in vacuum energy (ΔE_{vac}) compared to the unpassivated PbS slab are observed. Figure 7-5.c shows the electronic density of states of the ligand (filled curve) and ligand-slab system (unfilled curve) for each of the five ligands. The PbS bandgap remains relatively unchanged upon ligand adsorption, while the VBM and CBM shifts match the ΔE_{vac} observed in Figure 7-5.b, indicating that the band edge shifts are electrostatic in origin. There is excellent agreement in the direction and ordering of band edge shifts observed by UPS (Figure 7-1.e) and

DFT (Figure 7-5), although the magnitude of the shifts is overestimated by DFT.

Shifts in the energy levels of QDs upon ligand adsorption can be conceptualized as the sum of two dipole contributions: a contribution from the dipole formed between the surface atom of the QD and the binding group of the ligand (here referred to as $\mu^{interface}$), and a contribution from the intrinsic dipole moment of the ligand itself ($\mu^{intrinsic}$). [278] For the Lewis-basic ligands studied here, $\mu^{interface}$ points from the negatively-charged ligand to the positively-charged lead atom; $\mu^{intrinsic}$ depends on the chemical structure and binding orientation of the ligand. The z-component (normal to the PbS surface) of the total dipole (μ_z^{total}) can be expressed as $\mu_z^{total} = \mu_z^{interface} + \mu_z^{intrinsic}$, to which ΔE_{vac} is related through the Helmholtz equation:

$$\begin{aligned} \Delta E_{vac} = -\frac{\mu_z^{total}}{A\varepsilon_r\varepsilon_0} &= -\left(\frac{\mu_z^{interface}}{A\varepsilon_r\varepsilon_0} + \frac{\mu_z^{intrinsic}}{A\varepsilon_r\varepsilon_0}\right) \\ &= \Delta E_{vac}^{interface} + \Delta E_{vac}^{intrinsic}, \end{aligned} \tag{7.2}$$

where A is the area of the ligand projected into the plane of the PbS surface and ε_r is the dielectric constant of the ligand layer. [277, 284, 285, 286]

Figure 7-6 shows ΔE_{vac} for each ligand and the decomposition of ΔE_{vac} into the opposing $\Delta E_{vac}^{interface}$ and $\Delta E_{vac}^{intrinsic}$ terms. The ligand-intrinsic $\Delta E_{vac}^{intrinsic}$ terms follow trends predicted by simple electrostatics: iodide lacks an intrinsic dipole, while $\Delta E_{vac}^{intrinsic}$ for the thiols increases as the angle between C–S bonds decreases. The interfacial $\Delta E_{vac}^{interface}$ term is large for the compact iodide and BT ligands and decreases for more sterically bulky ligands. The trend in ΔE_{vac} is dominated by the influence of the ligand intrinsic dipole moment rather than the interfacial dipole, as ΔE_{vac} increases monotonically with decreasing $|\Delta E_{vac}^{intrinsic}|$. The lack of an intrinsic dipole moment in opposition to the interface dipole moment is a general feature of the halide ligands and explains the large band energy shifts observed for this class of ligands in Figure 7-1.e. The excellent agreement across multiple ligand classes with the trends observed in Figure 7-1.e lends support both to the use of UPS to reliably measure QD energy levels and to the intuitive description of energy level shifts

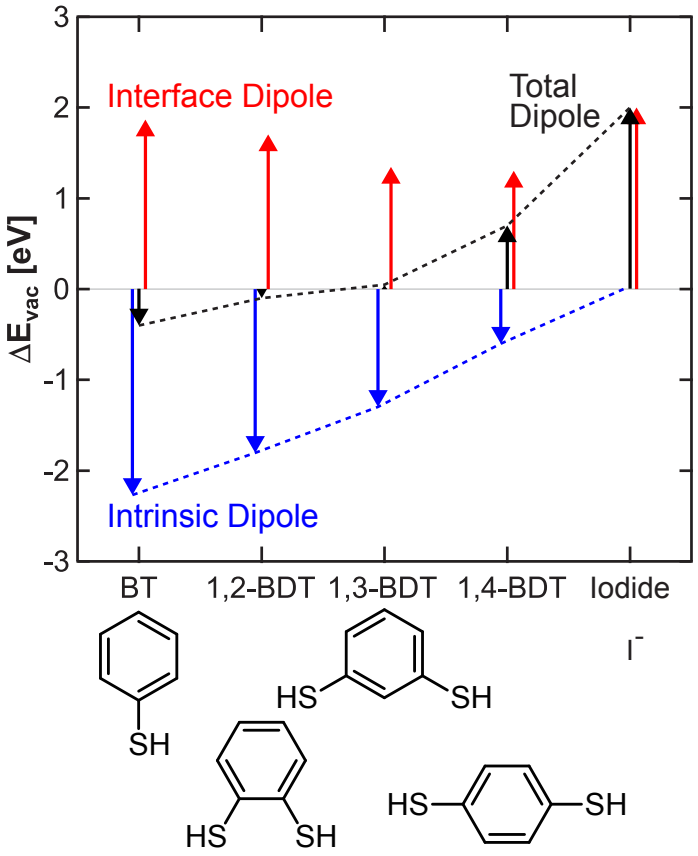

Figure 7-6: **Vacuum energy shifts at the QD/ligand interface.** The total vacuum energy shift (ΔE_{vac}) for each ligand is shown by black arrows and consists of the sum of the interface ($\Delta E_{vac}^{interface}$, red arrows) and intrinsic ligand ($\Delta E_{vac}^{intrinsic}$, blue arrows) vacuum energy shifts, calculated from electrostatic simulations as in Figure 7-5.a,b. DFT calculations performed by Donghun Kim.

presented here.

7.6 Conclusion

In summary, the band energies of colloidal QDs can be modified by ligand exchange, resulting in energy level shifts of up to 0.9 eV for PbS QDs. Trends in energy level position between different ligands are confirmed by atomistic modeling, showing that the observed shifts result from contributions from both the QD-ligand interface dipole [174] and the intrinsic dipole moment of the ligand molecule itself. [277] These energy level shifts result in predictable changes in photovoltaic device operation and provide

a guide to the optimal ligand choice and device architecture for QD photovoltaics. These findings have been employed to explain the operation of a record-efficiency (at the time of publication) PbS QD photovoltaic device employing a cascaded energy level architecture. [69] These results identify ligand-induced band-energy shifts, in complement to quantum confinement-controlled bandgap modification, as a means of predictably controlling the electronic properties of colloidal QDs and as a critical adjustable parameter in the optimization of QD optoelectronic devices.

7.7 Supplementary results and discussion

We here provide complete ultraviolet photoelectron spectra and absorption spectra of QD-ligand complexes; ligand binding simulations on a Pb-rich PbS(111) surface, monodentate and bidentate ligand binding simulations on a PbS(100) surface, and double-sided ligand binding simulations on a PbS(100) slab, performed by Donghun Kim; [119] and solar cell spectral mismatch.

7.7.1 Ultraviolet photoelectron spectra and absorption spectra of QD-ligand complexes

Figure 7-7 shows representative ultraviolet photoelectron spectra used to determine the energy levels of the ligand-exchanged PbS QDs (λ = 963 nm first excitonic absorption peak in solution) displayed in Figure 7-1 in Section 7.3. Five sequential scans collected at one-minute intervals are shown for each ligand. For an unchanging sample in equilibrium, the five scans should be identical; if the sample charges over time due to insufficient electrical contact, or if the chemical structure of the sample changes due to interaction with the 21.22 eV photon beam, the spectrum can shift over time. It is observed that the spectra of the thiols are very constant over the five-minute interval; the spectra of the halide ligands undergo a small shift ($\sim$0.1 eV) to shallower work functions. For the energy levels reported in this work, only the first scan (labeled here as "1 min") from a given sample is utilized in order to minimize

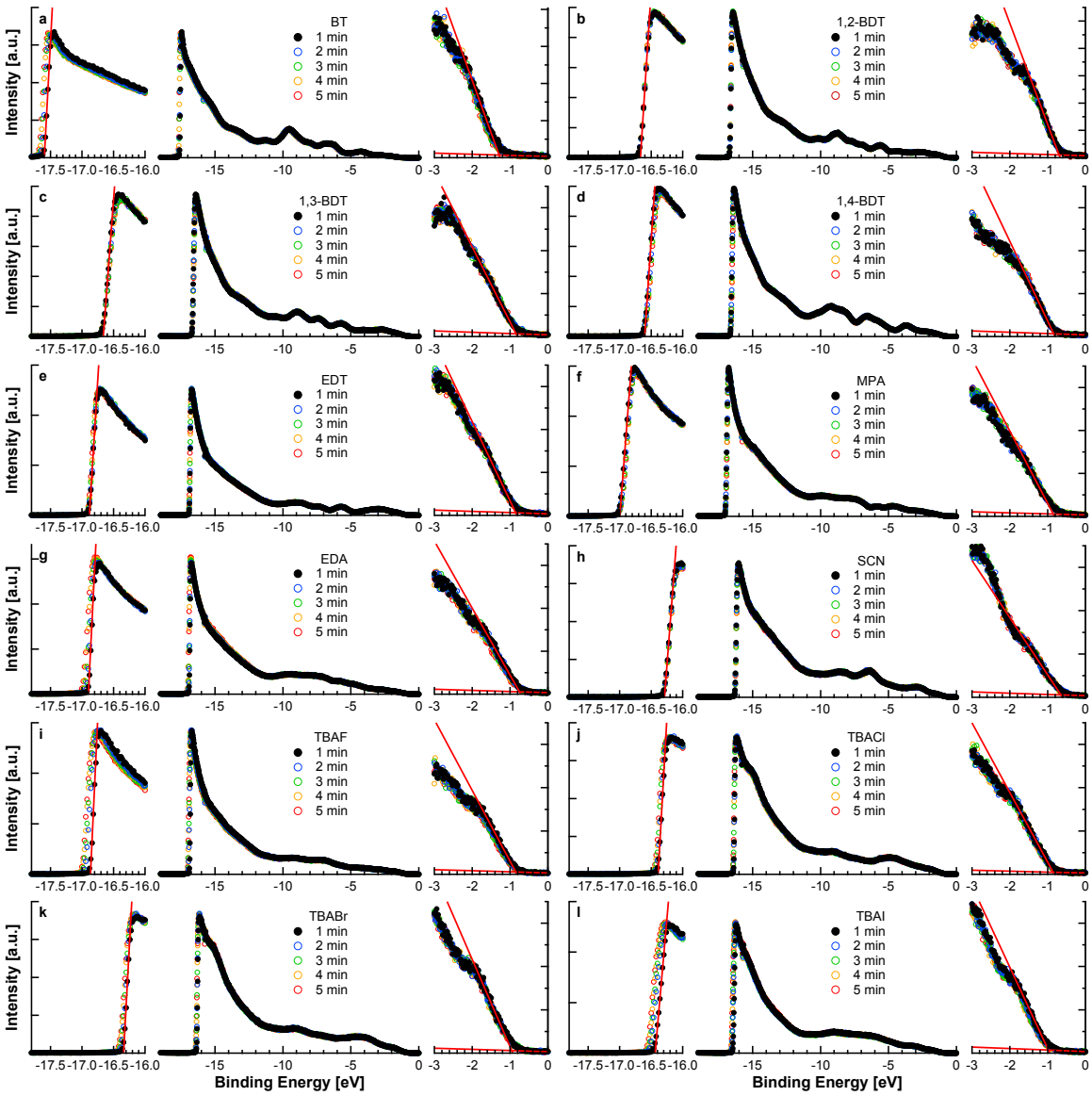

Figure 7-7: **Ultraviolet photoelectron spectra of 100 nm-thick ligand-exchanged PbS QD films on gold substrates:** **a**, benzenethiol (BT); **b**, 1,2-benzenedithiol (1,2-BDT); **c**, 1,3-benzenedithiol (1,3-BDT); **d**, 1,4-benzenedithiol (1,4-BDT); **e**, 1,2-ethanedithiol (EDT); **f**, 3-mercaptopropionic acid (MPA); **g**, ethylenediamine (EDA); **h**, ammonium thiocyanate (SCN); **i**, tetrabutylammonium fluoride (TBAF); **j**, tetrabutylammonium chloride (TBACl); **k**, tetrabutylammonium bromide (TBABr); **l**, tetrabutylammonium iodide (TBAI). Five sequential scans collected over five minutes are displayed for each sample. Red lines indicate fits to the first scan (labeled "1 min"). The Fermi energy is determined from the intercept of a linear extrapolation of the secondary electron cutoff region with the x-axis. The valence band binding energy is determined from the intercept of a linear extrapolation of the primary electron cutoff region with a linear extrapolation of the baseline.

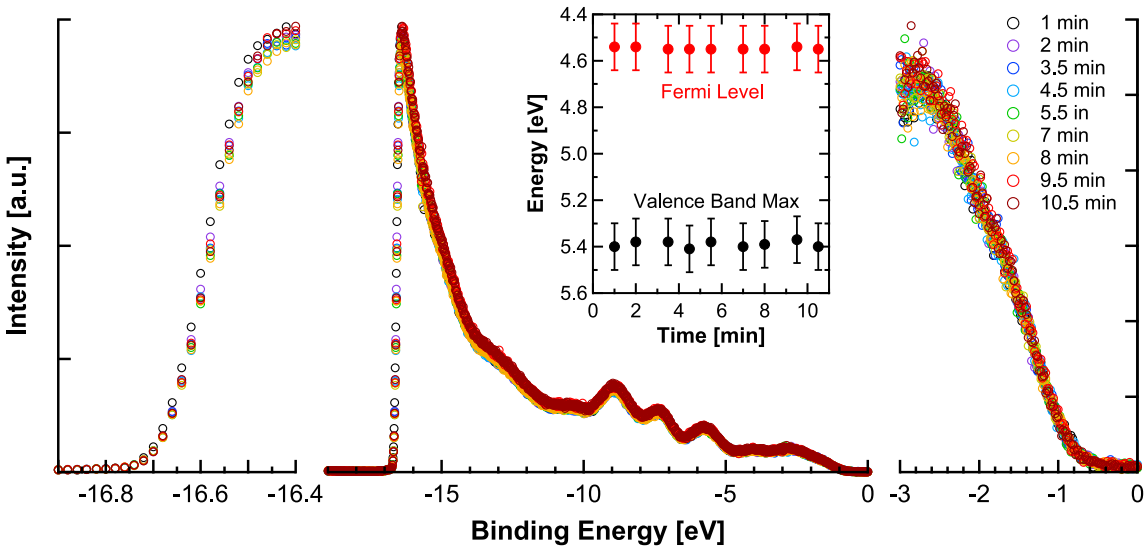

Figure 7-8: **Time-dependence of energy levels determined from UPS spectra of 1,3-BDT-treated PbS QDs** (λ = 963 nm first excitonic absorption peak in solution). Error bars indicate experimental accuracy. No significant difference in energy levels is observed for this QD/ligand combination over the time range measured here.

the influence of charging and sample damage (a common practice in UPS studies of organic or hybrid organic-inorganic materials [287]) and the energy levels of 2–4 separate samples thus determined are averaged to generate the final values presented in Figure 7-1.e.

Figure 7-8 shows the energies of the valence band maximum (VBM) and Fermi level of 1,3-BDT-exchanged PbS QDs over nine sequential scans. Neither the valence band energy nor the Fermi energy undergo significant shifts over this time interval.

Given the high sensitivity of UPS to changes in surface chemistry, it is important to verify that unintended differences in sample preparation and sample history do not influence the measured energy levels. All of the quantum dots utilized in Figure 7-1 are from a single synthetic batch, so variations in QD size across different measurements should be minimal. The surface chemistry and ligand coverage of QDs could potentially be affected by the purification procedure and the strength with which the QDs are "crashed out" of solution by non-solvent before centrifugation and resuspension. **Figure 7-9** shows energy levels determined from UPS spectra of PbS QDs exchanged with 1,3-BDT following three different crashout procedures: a "soft" crashout employing

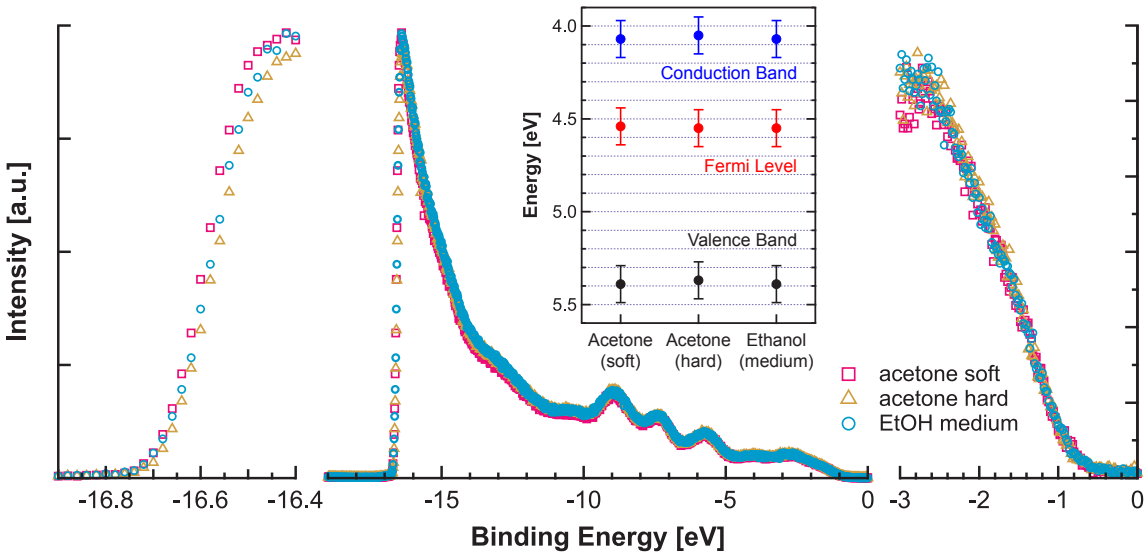

Figure 7-9: **Dependence of UPS results on QD purification procedure for 1,3-BDT-exchanged PbS QDs** (λ = 963 nm first excitonic absorption peak in solution). Error bars indicate experimental accuracy. No experimentally significant difference in energy levels is observed.

the addition of a minimal amount of acetone in the precipitation step, a "hard" crashout employing a large excess of acetone, and a crashout employing ethanol in place of acetone. It is observed that each of these different crashout procedures results in the same energy level values, indicating that the differences reported in Figure 7-1 are due to the ligands used for ligand exchange rather than differences in QD synthesis or purification. It is also worthwhile to note that the length of exposure of the samples to ultrahigh vacuum (UHV) during UPS testing is only ~1 h, comparable to the length of time that the QD samples are exposed to high vacuum during the evaporation of contacts during solar cell fabrication.

Figure 7-10 shows representative optical transmission, reflection, and absorption spectra, where $A\% = 100\% - T\% - R\%$, of 1,3-BDT-exchanged PbS QDs (λ = 963 nm first excitonic absorption peak in solution) measured during brief exposure to air. A 100 nm-thick QD film, employing 5 sequential layers of spin-cast and ligand-exchanged QDs, is deposited onto glass treated with 3-mercaptopropyltrimethoxysilane as described in Section 7.2. Reflection is measured at an incident angle of 8° from normal. Scattering is not accounted for, but does not affect the value of the bandgap

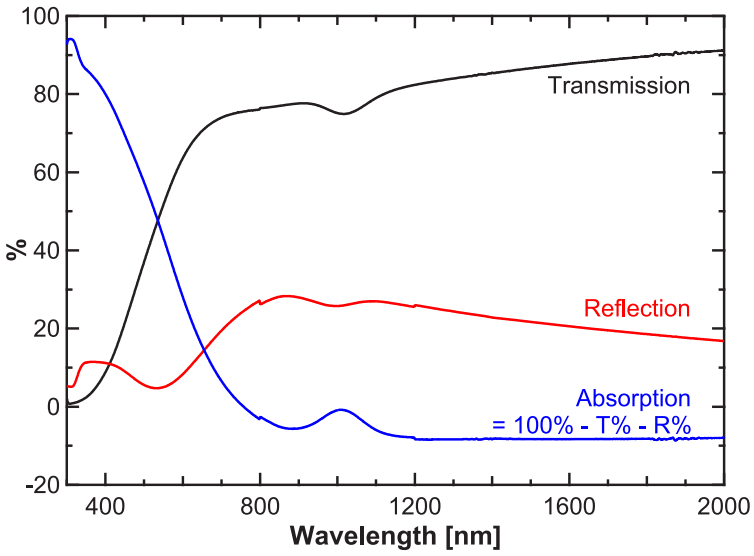

Figure 7-10: **Optical transmission, reflection, and absorption of 1,3-BDT-exchanged PbS QDs** ($\lambda = 963\,\text{nm}$ first excitonic absorption peak in solution).

determined from the first excitonic peak of the absorption spectrum.

Figure 7-11 shows the collected optical absorption spectra of PbS QDs ($\lambda = 963\,\text{nm}$ first excitonic absorption peak in solution) exchanged with each of the twelve ligands shown in Figure 7-1, collected during brief exposure to air. The optical bandgap E_g^{opt} is determined from the energy of the peak of the first absorption feature of an 11-point moving average of the presented data. As described in Section 7.3, the transport bandgap E_g is determined from the equation

$$E_g = E_g^{opt} + 1.786\frac{e^2}{4\pi\varepsilon_0\varepsilon_{QD}R}, \tag{7.3}$$

where e is the charge of the electron, ε_0 is the permittivity of free space, ε_{QD} is the optical dielectric constant of the QD core material ($\varepsilon_\infty^{PbS} = 17.2$), and R is the quantum dot radius. [268, 269] The QD radius is determined by matching the first excitonic absorption peak in solution to a power law extrapolation of the sizing curve published by Jasieniak et al. [75] An additional stabilization due to the interaction between a charge on a QD and its induced image charge across the dielectric boundary between

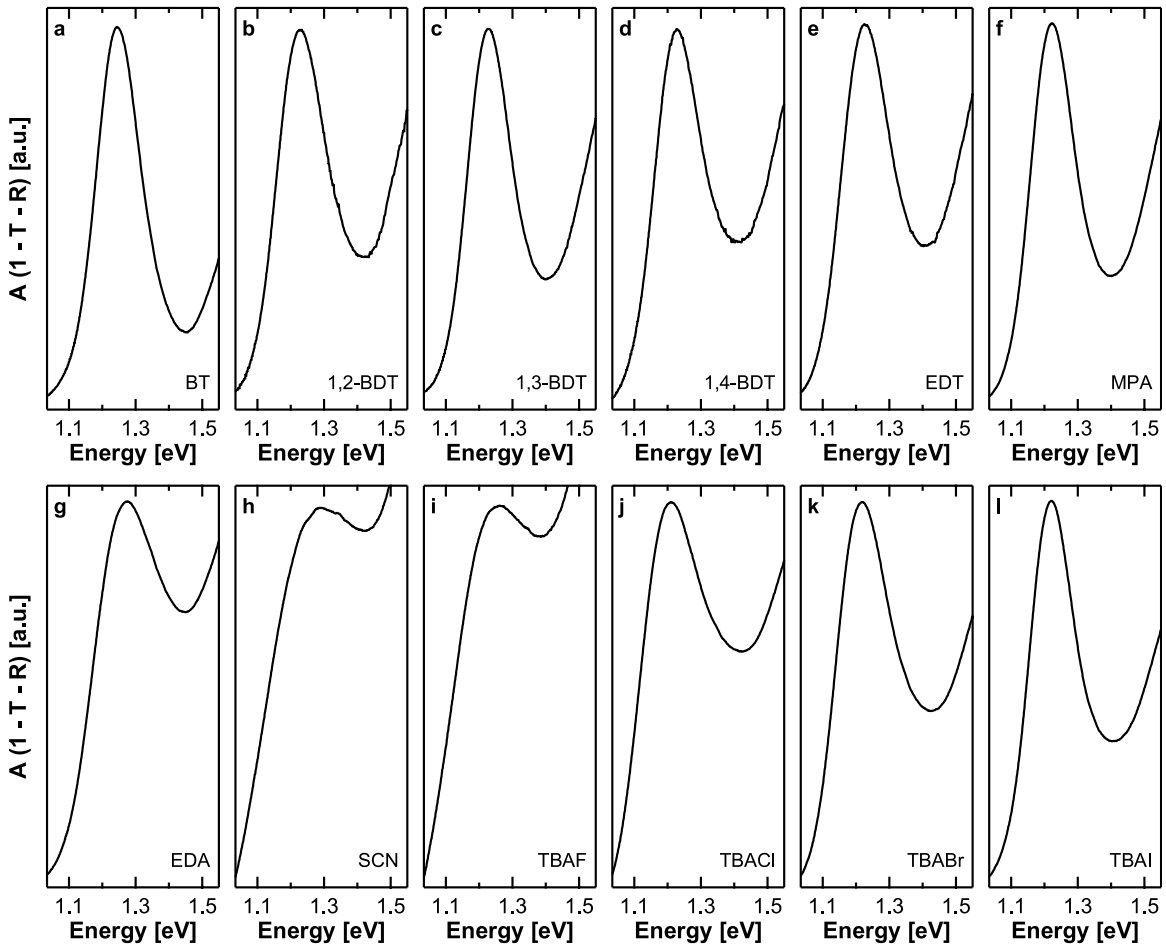

Figure 7-11: **Optical absorption spectra of ligand-exchanged PbS QDs.** Lead sulfide QDs ($\lambda = 963\,\text{nm}$ first excitonic absorption peak in solution) are exchanged with: **a**, benzenethiol; **b**, 1,2-benzenedithiol; **c**, 1,3-benzenedithiol; **d**, 1,4-benzenedithiol; **e**, 1,2-ethanedithiol; **f**, 3-mercaptopropionic acid; **g**, ethylenediamine; **h**, ammonium thiocyanate; **i**, tetrabutylammonium fluoride; **j**, tetrabutylammonium chloride; **k**, tetrabutylammonium bromide; **l**, tetrabutylammonium iodide.

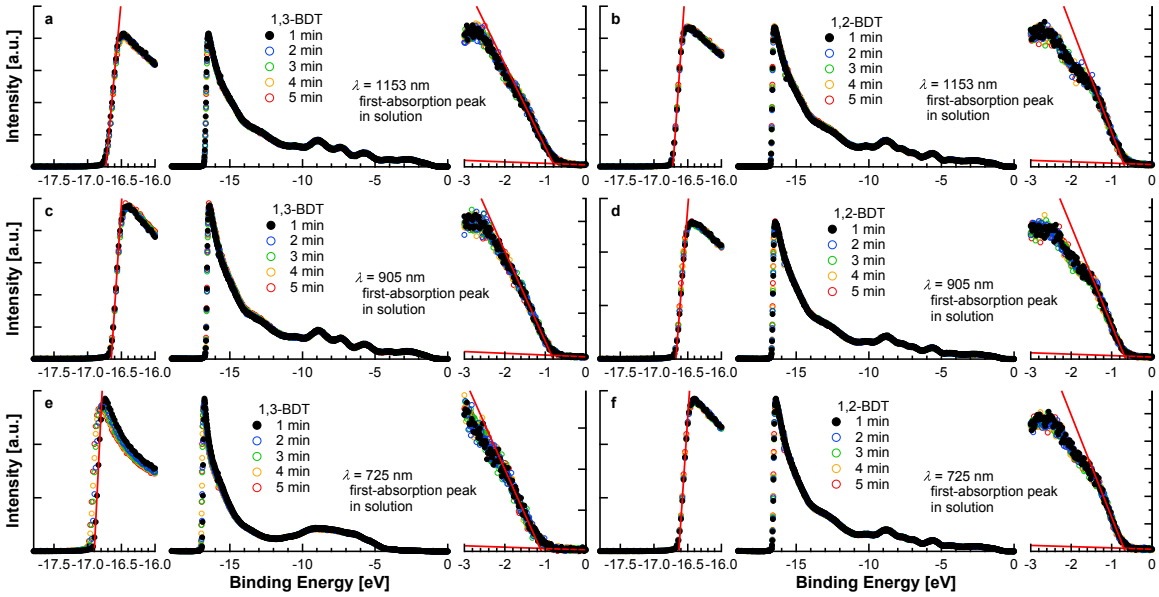

Figure 7-12: **UPS spectra of PbS QDs of varying size.** Lead sulfide QDs are deposited as ∼100 nm-thick layers (5 sequential spin-casting cycles) onto gold substrates. Samples consist of QDs with $\lambda = 1153$ nm first excitonic absorption peak in solution exchanged with 1,3-BDT (**a**) and 1,2-BDT (**b**); QDs with $\lambda = 905$ nm first excitonic absorption peak in solution exchanged with 1,3-BDT (**c**) and 1,2-BDT (**d**); and QDs with $\lambda = 725$ nm first excitonic absorption peak in solution exchanged with 1,3-BDT (**e**) and 1,2-BDT (**f**).

the QD and the ligand matrix takes the form

$$E^{pol} = \frac{e^2}{4\pi\varepsilon_0 R}\left({\varepsilon_{matrix}}^{-1} - {\varepsilon_{QD}}^{-1}\right), \tag{7.4}$$

where ε_{matrix} is the optical dielectric constant of the ligand shell; previous studies have shown that this term is negligible in ligand-exchanged QD systems, so it is neglected here. [75]

Figure 7-12 shows the collected UPS spectra of the 1,2-BDT- and 1,3-BDT-exchanged PbS QDs utilized in Figure 7-4 in Section 7.4. As in Figure 7-7, five sequential scans are shown to demonstrate the lack of considerable variation in the spectra over time; only the fit to the first scan in each case is used to determine the energy levels.

Figure 7-13 shows the optical absorption spectra of the three PbS QD sizes utilized in Figure 7-4 in Section 7.4, spin-coated onto glass and exchanged with 1,3-

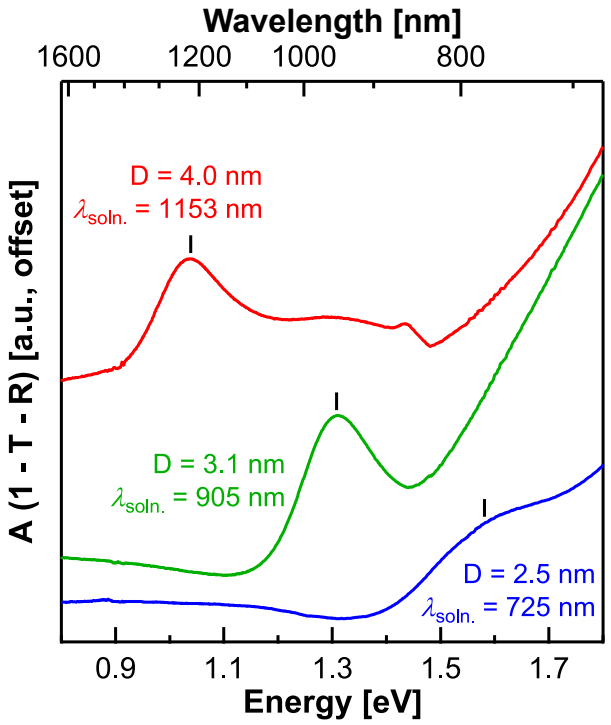

Figure 7-13: **Optical absorption spectra of 1,3-BDT-exchanged PbS QDs used in Figure 7-4 in Section 7.4**, labeled by D, the QD diameter, and λ_{soln}, the first excitonic absorption peak in solution. Spectra are vertically offset for clarity.

BDT ligands. As described above, the optical bandgaps are determined from the energy of the peak of the first excitonic absorption feature (for the highest-bandgap dots, in which only a shoulder is observed, the optical bandgap is determined from the minimum of the second derivative of the absorption profile in the shoulder region), and the transport bandgaps are determined from (7.3) using the sizing curve published by Jasieniak et al. [75]

7.7.2 Additional DFT simulations of ligand binding on the PbS surface

Ligand binding simulations on Pb-rich PbS(111) surface

Here we describe atomistic DFT simulations (performed by Donghun Kim in Brown and Kim et al. [119]) of the binding of ligands to PbS(111) surfaces to complement the discussion of binding to PbS(100) surfaces in Section 7.5, as both (100) and

(111) facets are known to be dominant for PbS QDs. [169, 279, 280] We simulate the binding of BT, 1,2-BDT, 1,3-BDT, and iodide ligands to lead-rich PbS(111) planes; the binding of 1,4-BDT to the PbS(111) surface was found to be unstable. **Figure 7-14.a** shows a schematic diagram of the modeled PbS(111) slabs. Pseudohydrogen atoms with fractional charges of $\frac{5}{3}e$ passivate the lead atoms on the right, and ligands (1,2-BDT is shown as an example in Figure 7-14.a) passivate the lead atoms on the left. Figure 7-14.b shows plane-averaged electrostatic potential plots of PbS(111) slabs with different ligands. Different ligands exhibit different vacuum level shifts (ΔE_{vac}): for iodide, 1,3-BDT, 1,2-BDT, and BT, the vacuum energy shifts are $\Delta E_{vac} = +2.58\,\text{eV}$, $+0.08\,\text{eV}$, $-0.03\,\text{eV}$, and $-0.39\,\text{eV}$, respectively. The direction of this trend in vacuum energy for binding to the lead-rich PbS(111) surface is the same as that observed in Figure 7-5 for binding to the PbS(100) surface.

Monodentate and bidentate ligand binding simulations on PbS(100) surface

The bidentate thiol ligands used here (1,2-BDT, 1,3-BDT, 1,4,-BDT, and EDT) can bind to the PbS(100) surface in multiple configurations. In monodentate attachment, one of the two thiol groups of a given ligand is bound to a single QD as thiolate; the second thiol is either protonated and unbound to a QD, or is bound to an adjacent QD. In bidentate attachment, both of the thiol groups bind to a single QD; for the PbS(100) facet, these thiols would either bind to nearest neighbor Pb atoms (with a separation of 4.2 Å along the $\langle 110 \rangle$ direction) or next-nearest neighbor Pb atoms (with a separation of 6.0 Å along the $\langle 100 \rangle$ direction).

Here we investigate the single monodentate binding mode and both bidentate binding modes of 1,2-BDT and 1,3-BDT on the PbS(100) surface. **Figure 7-15** displays the results of DFT calculations for each of these three binding modes for both ligands. For each of the three binding modes considered, ΔE_{vac} for 1,3-BDT is higher than for 1,2-BDT; this shift in ΔE_{vac} leads to a deeper valence band for 1,3-BDT-treated PbS QDs than for 1,2-BDT-treated PbS QDs, reproducing the trend observed by UPS in Figure 7-1 and by photovoltaic measurements in Figures 7-3

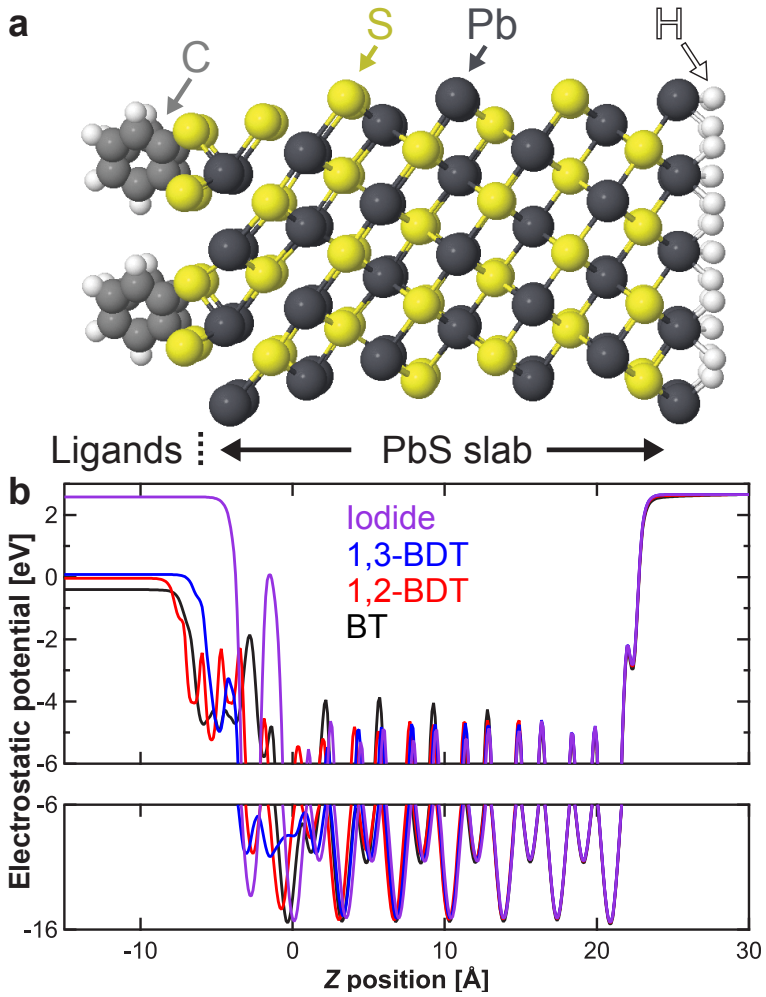

Figure 7-14: **DFT calculations of ligand-induced energy level shifts for binding to the PbS(111) surface. a**, Schematic diagram of modeled PbS(111) slab. The left side of the slab is passivated by the ligand (1,2-BDT is shown here as an example) and the right side is passivated by appropriate pseudo-hydrogen atoms to ensure charge balance. **b**, Plane-averaged electrostatic potentials of PbS(111) slabs with different ligands. The potential in the vacuum region far to the left of an unpassivated PbS slab is set to zero. The direction of the trend in energy level shifts observed here matches the trend observed in Figure 7-5 in Section 7.5. DFT calculations performed by Donghun Kim.

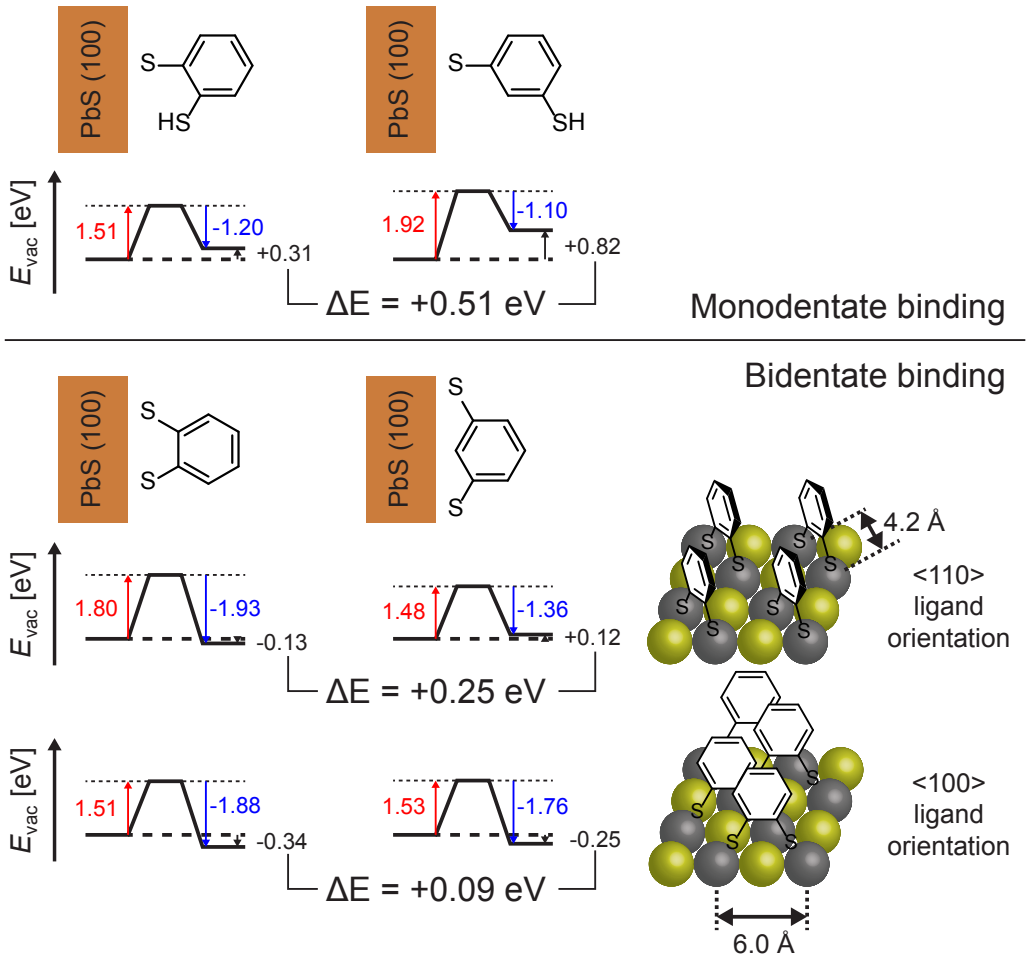

Figure 7-15: **Vacuum energy shifts for binding of 1,2-BDT and 1,3-BDT to the PbS(100) surface in various geometries.** The energy level shift ΔE_{vac} for each configuration is decomposed into components from the interfacial dipole (red; positive contribution) and the intrinsic ligand dipole (blue; negative contribution). ΔE here corresponds to the difference in vacuum energy shift between 1,2-BDT and 1,3-BDT for a given binding mode (monodentate; bidentate with $\langle 110 \rangle$ ligand orientation; or bidentate with $\langle 100 \rangle$ ligand orientation). DFT calculations performed by Donghun Kim.

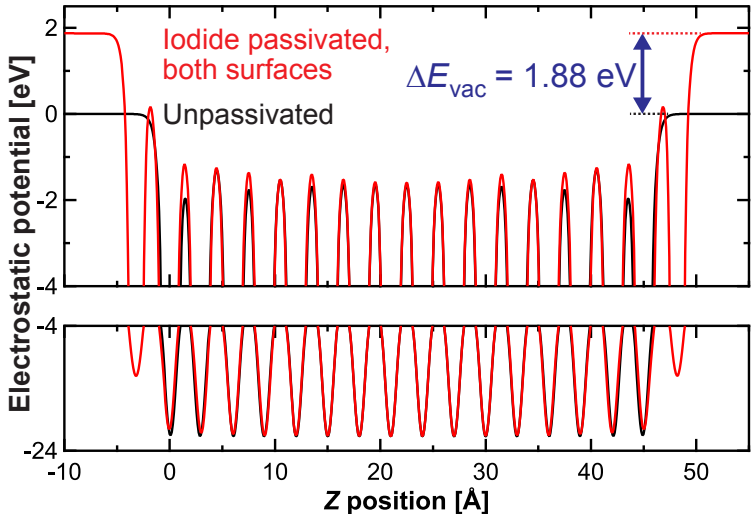

Figure 7-16: **DFT simulations of double-sided ligand binding to a PbS(100) slab.** The vacuum energy is set to zero outside the unpassivated PbS slab, and the arbitrary offset of the iodide-passivated PbS slab is chosen such that the electrostatic potentials align in the center of the slab. Close agreement is observed between the vacuum energy shift observed here for double-sided iodide passivation (ΔE_{vac} = 1.88 eV) and the vacuum energy shift observed in the main text for single-sided iodide passivation (ΔE_{vac} = 1.90 eV). DFT calculations performed by Donghun Kim.

and 7-4.

Simulations of PbS slabs with double-sided ligand passivation

The simulations described above and in Section 7.5 treat the QD surface as a semi-infinite quasi-two-dimensional slab, with ligands bound to one side of the slab and charge-balancing pseudohydrogen atoms bound to the other side. This approximation is utilized in order to increase computational efficiency and facilitate comparisons between different ligands. In reality, the entire surface of the three-dimensional QD is expected to be passivated by ligands. To verify this single-side binding model and move the simulations a step closer to physical reality, DFT simulations were performed on a PbS(100) slab passivated on both sides by iodide ligands, in comparison to an unpassivated PbS(100) slab. **Figure 7-16** shows plane-averaged electrostatic potential plots of these two systems. The arbitrary y-axis offset for each case is chosen such that the electrostatic potentials align in the center of the PbS slab and the vacuum energy outside the unpassivated slab is zero. The shift in vacuum energy observed

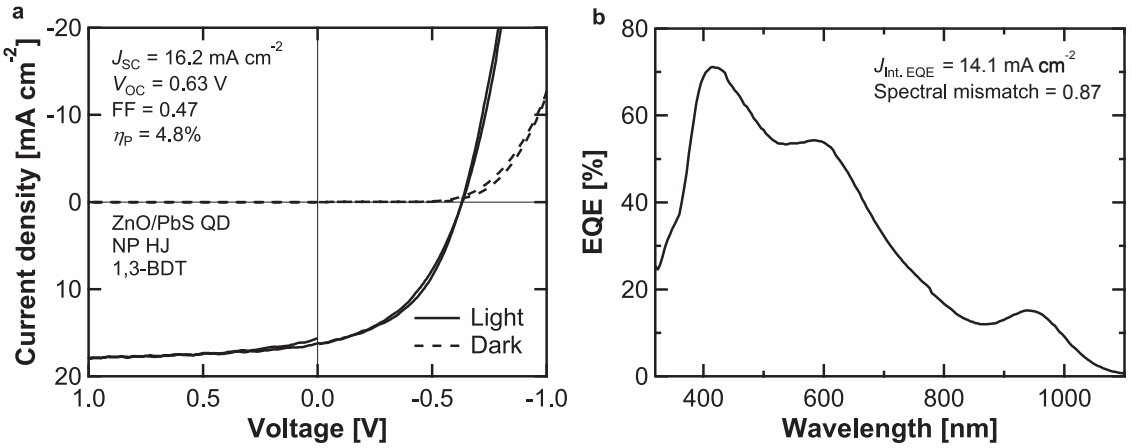

Figure 7-17: **Characteristic performance of np-HJ QD PV devices described in this chapter. a**, Current-voltage of a ZnO / PbS QD np-HJ photovoltaic device under illumination with a filtered xenon lamp. **b**, External quantum efficiency spectrum of the same device.

here for double-sided iodide passivation of $\Delta E_{vac} = 1.88\,\text{eV}$ is in close agreement with the vacuum energy shift observed in the main text for single-sided iodide passivation of $\Delta E_{vac} = 1.90\,\text{eV}$.

7.7.3 Solar cell spectral mismatch

External quantum efficiency (EQE) measurements are performed by passing chopped white light from a xenon lamp (Thermo Oriel 66921) through a monochromator into a single-core optical fiber and onto the active device in an underfilled illumination geometry; the device current is measured using a lock-in amplifier (Stanford Research Systems SR830).

Figure 7-17 shows the measured J-V and EQE response of a ZnO / PbS QD np-HJ device employing 1,3-BDT-treated QDs. Integrating the product of the EQE spectrum with the AM1.5G solar spectrum [39] yields an expected J_{SC} under solar illumination of $14.1\,\text{mA}\,\text{cm}^{-2}$; comparison with the measured J_{SC} of $16.2\,\text{mA}\,\text{cm}^{-2}$ yields a spectral mismatch of 0.87.

Chapter 8

Conclusion and Outlook

In this thesis we have identified a number of mechanisms by which the energy levels of PbS QD photovoltaic devices may be controlled and explored the effects of these energy level modifications on device performance. We here give a brief summary of the findings presented in this thesis, outline some of the work that has followed from our investigations, identify shortcomings that must be overcome for PbS QD photovoltaics to meaningfully contribute to a low-carbon future, and suggest avenues for further study.

We showed in Chapter 5 that a Schottky barrier that typically forms at the anode interface in ZnO / PbS QD n-p heterojunction photovoltaics can be alleviated through the addition of a layer of high-work-function MoO_3 between the PbS QD layer and the anode, improving the V_{OC} across a range of anode materials (Au, Ag, and ITO). [122] Using MoO_3 as an interfacial electrode layer could thus obviate the need to use expensive high-work-function electrode materials such as gold, which otherwise could significantly increase the cost of PbS QD photovoltaics. [64] Similar results were later published by Gao et al. and Wang et al. [207, 288] Later work by Jean et al. showed that MoO_3 also acts as a buffer layer in ZnO nanowire / PbS QD photovoltaic devices, preventing shorting between ZnO nanowires that extend through the PbS QD film and the hole-extracting electrode. [289] Osedach et al. showed that the transparent MoO_3 layer can be used as an optical spacer of almost arbitrary thickness in photodetectors employing extremely thin absorber layers, enabling engineering of the optical electric

field within the device to position the absorbing layer at the position of maximum field strength. [290] And Ko et al. later suggested that deep-work-function inorganic hole transport layers (CuI was used in their study, but the results could be expected to extend to MoO_3) could enable p-i-n-junction-like operation in ZnO / PbSe QD solar cells, increasing the depletion width within the PbSe QD absorber layer. [291]

At the same time, it should be noted that the extreme air sensitivity of MoO_3 may limit its utility in commercial production processes, or require careful encapsulation of PbS QD solar cells under inert conditions. The work function of MoO_3 has been observed to shift by more than 1 eV after brief exposure to ambient atmosphere. [210, 211] Chuang et al. later demonstrated efficient operation of ZnO / PbS QD photovoltaics in air without MoO_3 using a bilayer of PbS QDs treated with tetrabutylammonium iodide and ethanedithiol, suggesting that appropriate choice of ligand chemistry for the PbS QDs may eliminate the need for the MoO_3 layer.

In Chapter 6 we showed that PbS QDs can dissociate triplets generated from singlet fission in pentacene in a hybrid organic / QD solar cell. [83] Similar results were also reported by Ehrler et al. [225, 226] Thompson et al. later showed that PbS QDs can also accept triplet excitons from tetracene via nonradiative (Dexter) transfer. [76]

A major limitation of the pentacene / PbS QD devices presented here is their low (<1 %) power conversion efficiency and low external quantum efficiency (EQE) of photocurrent generation. It is possible that the surface of the pentacene film is damaged during the process of QD solution deposition or thiol ligand exchange, which may limit the ultimate efficiency that can be achieved in this architecture. Photocurrent contribution from pentacene is also only observed with very thin PbS QD layers; the EQE of PbS is already quite high in the region where pentacene absorbs. So while PbS QDs represent an attractive electron acceptor from the vantage point of pentacene-containing solar cells, adding pentacene to an already-efficient PbS QD solar cell may not lead to higher efficiencies than the current record device structure employing PbS QDs alone, at least in the present singlet fission device architecture. Future opportunities in this area include the exploration of inverted device structures, with pentacene deposited on top of the PbS QD layer to limit the

possibility of pentacene degradation through solvent exposure. Bulk heterojunction architectures employing solution-processable singlet-fission-active acene derivatives such as diphenylpentacene along with PbS QDs may also lead to improved efficiencies by decreasing the distance over which triplet excitons must diffuse in order to reach the dissociating heterojunction interface and by enabling greater amounts of the singlet fission material to be used within the device. Linking the singlet fission material directly to the QD through the use of pentacene-containing ligands could also increase the electronic coupling between the materials and enhance the efficiency of triplet transfer.

In Chapter 7 we showed that ligand exchange induces large shifts in the energy level structure of PbS QDs, and demonstrated that these shifts can both be predicted by density functional theory and have large impacts on photovoltaic device performance. [119] These findings provided insight into the operation of a certified 8.55 % efficient PbS QD device by Chuang et al. employing a cascaded QD energy level structure. [69] This PV architecture has since been widely adopted in the PbS QD PV field, and is used in the current record-holding 10.6 % efficient device by Kim et al. [116, 53]

Of course, it must be borne in mind that ligand exchange does not change just the energy levels—it can also influence the charge carrier mobility, trap density, carrier lifetime, dielectric constant, air stability, and other properties of the QD film, all of which can have large impacts on device performance. A ligand that leads to the right PbS QD energy level alignment may also decrease the charge carrier mobility or increase the trap density. So while energy level adjustments through ligand exchange are a powerful tool in the design of efficient QD photovoltaics, they must be considered in the context of all of the other implications of ligand exchange. It remains to be seen whether a ligand exchange strategy that simultaneously optimizes all of these different parameters can be found. Further work in this area could explore the influence of ligand size and structure on ligand binding density and on the resulting stoichiometry of the QD/ligand film (an approach that has begun to be explored by Yuan et al. [263]). A detailed analysis of the effects of air and moisture exposure on the chemistry, energy levels, and charge transport properties of PbS QDs with different ligand chemistries

also has yet to be performed. Chuang et al. showed that air exposure has a large effect on the efficiency of ZnO / PbS QD devices, and a deeper understanding of the oxidation processes undergone by the QD core and ligand shell during air exposure, particularly under operationally relevant illumination and temperature conditions, could lead to strategies for further efficiency enhancement. [69]

A deeper issue facing the PbS QD PV field is the low V_{OC} demonstrated by even record-efficiency PbS QD PV devices relative to the QD bandgap. To our knowledge, no PbS QD PV device has been reported in the literature with a V_{OC} greater than $\sim$50 % of the QD bandgap (a level which is significantly lower than that of other solar cell technologies). [292] Nearly all of the recent improvement in QD PV performance has arisen from enhancements in the J_{SC} and fill factor. Guyot-Sionnest and Moore et al. have noted the significant detrimental impact that a long Urbach tail—an exponential tail in the density of states extending from the valence or conduction band edge into the bandgap, arising from energetic disorder in the QDs—could have on QD solar cell performance. [161, 293] Some disagreement exists in the literature regarding the energetic disorder of PbS QDs—fluorescence spectroscopy of single PbS QDs indicates a broad single-QD linewidth, suggesting a long band tail, [294] while electronic measurements on PbS QD films suggest a sharper tail. [295] Given the critical importance of this parameter in determining the potential limiting efficiency of PbS QD photovoltaics, a direct measurement of the sub-band density of states of PbS QDs with different ligand treatments—perhaps using the sensitive absorption and photocurrent measurement techniques used by De Wolf et al. in an examination of other solar cell materials [296]—would be of great value to the field.

Perhaps the most promising approach for increasing the efficiency of solution-processed solar cells using the insights gained from this thesis would be to apply our findings on the influence of surface chemistry on PbS QD electronic structure to a new class of materials—specifically, lead halide perovskites. [297, 298, 299, 300, 301] Perovskites have upended the world of solution-processed photovoltaics over the past 7 years, rising from 3.8 % efficiency in 2009 [300] to 22.1 % efficiency today. [53] Significant challenges in this materials system remain to be overcome, particularly

with respect to long-term stability under applied bias and exposure to environmental conditions. The chemistry of high-efficiency perovskite materials, involving lead ions, halide ions, and small organic molecules, is quite similar to the chemistry of our halide-ligand-exchanged lead sulfide quantum dots. It is possible that the ligand exchange approaches explored here for PbS QDs may also provide benefit to perovskite PVs, perhaps by enabling adjustment of the interfacial energy level structure. Preliminary UPS studies of perovskite materials employing Pb:Co mixed-metal chemistries have identified significant energy level shifts depending on the metal composition that translate into predictable improvements in device operation, revealing a rich parameter space for further optimization. [302]

Appendix A

Field-Effect Mobility, Recombination Rate, and Density of States of Ligand-Exchanged PbS QDs

A.1 Introduction

As shown in Figure 7-2 in Section 7.4, PbS QDs exchanged with EDT, 1,2-BDT, and 1,3-BDT behave differently in ZnO / PbS n-p heterojunction (np-HJ) and Schottky junction (SJ) photovoltaic architectures. If trap density and carrier mobility, density, and recombination rates were the sole sources of variation between PbS QDs treated with these ligands, the same relative performance would be expected between these three ligand treatments for both architectures; if energy levels were the sole source of variation, the rank order of performance for the different ligands would be expected to be either unchanged or inverted between the two architectures. Instead, EDT shows the worst performance in both architectures; 1,3-BDT outperforms 1,2-BDT in the

[i]* These authors contributed equally to the cited work.

np-HJ architecture, and 1,2-BDT outperforms 1,3-BDT in the SJ architecture. As expected, ligand exchange brings about changes in both the trap and carrier properties and the energy levels of the QDs. Here, through a combination of field-effect mobility, recombination, and trap density measurements, we quantify differences in trap and carrier properties between the three ligands tested, showing that they can explain the poor performance of EDT but not the shift in performance for 1,2-BDT and 1,3-BDT.

A.2 Methods

A.2.1 Field-effect transistor fabrication and testing

Field-effect transistor (FET) devices utilize a bottom-contact top-gate geometry and are fabricated as described by Osedach et al. [303] Briefly, the source and drain electrodes consist of Cr(3 nm) / Au(40 nm) interdigitated arrays with length (L) and width (W) of $L = 10\,\mu m$ and $W = 12\,mm$, respectively, thermally evaporated onto glass and patterned via liftoff (Thin Film Devices). The substrates are pretreated with 3-MPTMS as described in Section 7.2, and a single layer of ligand-exchanged PbS QDs is deposited by sequential spin-casting. The gate dielectric, 950 PMMA A4 resist (Microchem), is spin-cast at 1000 rpm for a thickness of $\sim$470 nm. The top-contact aluminum gate is deposited by thermal evaporation through a shadow mask. FET measurements are performed using an Agilent 4156C semiconductor parameter analyzer. Individual current-voltage sweeps are conducted in $<$400 ms to minimize bias stress. The capacitance of the insulating gate dielectric is measured for a QD-free device using a Solartron 1260 impedance analyzer. The gate dielectric capacitance was measured by Tim Osedach.

A.2.2 Transient-V_{OC} measurements

Transient-V_{OC} measurements are performed on ZnO / PbS np-HJ devices. The device is biased by white light from a xenon lamp passed through a liquid light guide and neutral density filter onto the active area. A low-intensity perturbation is provided

by a $\lambda = 635\,\text{nm}$ laser chopped at 11 Hz and co-focused onto the active area through a variable neutral density filter. The intensity of the laser is adjusted such that the voltage perturbation ΔV is less than 5% of the V_{OC} generated by the white light bias. Transient-voltage curves are collected from the trailing edge of the perturbation pulse using the high-impedance input of a Tektronix 3054B oscilloscope.

A.2.3 Density of states measurements

Density of states measurements are performed as described by Ip et al. [304] As in the transient-V_{OC} measurements described above, white bias light of variable intensity is provided by a xenon lamp. Laser pulses of 300 ns duration, produced by modulating the output of a $\lambda = 635\,\text{nm}$ laser using an Agilent 33220A function generator, are co-focused onto the active area. The white light bias intensity and laser pulse intensity are modulated using neutral density filters such that the voltage perturbation ΔV is less than 5% of the V_{OC} generated by the white light bias. Transient responses are measured using a Tektronix 3054B oscilloscope set to an input impedance of $1\,\text{M}\Omega$: voltage traces are collected using an ADA400A high-impedance probe, and current traces are collected using a DHPCA-100 preamplifier.

A.3 Results and discussion

Carrier mobilities of ligand-exchanged PbS QD films are extracted from the FET transfer characteristics, collected in the linear regime with an absolute drain-source bias ($|V_{DS}|$) of 5 V as shown in **Figure A-1**. Electron and hole mobilities are determined from the n-channel and p-channel response, respectively, by fitting the linear regions of the I_{DS}-V_G curve to the equation

$$\left.\frac{\partial I_{DS}}{\partial V_G}\right|_{V_{DS}} = \frac{W}{L} C_i V_{SD} \mu, \tag{A.1}$$

where I_{DS} is the drain-source current, V_G is the gate bias, L and W are the length (10 µm) and width (12 mm), respectively, of the channel, and C_i is the capacitance of

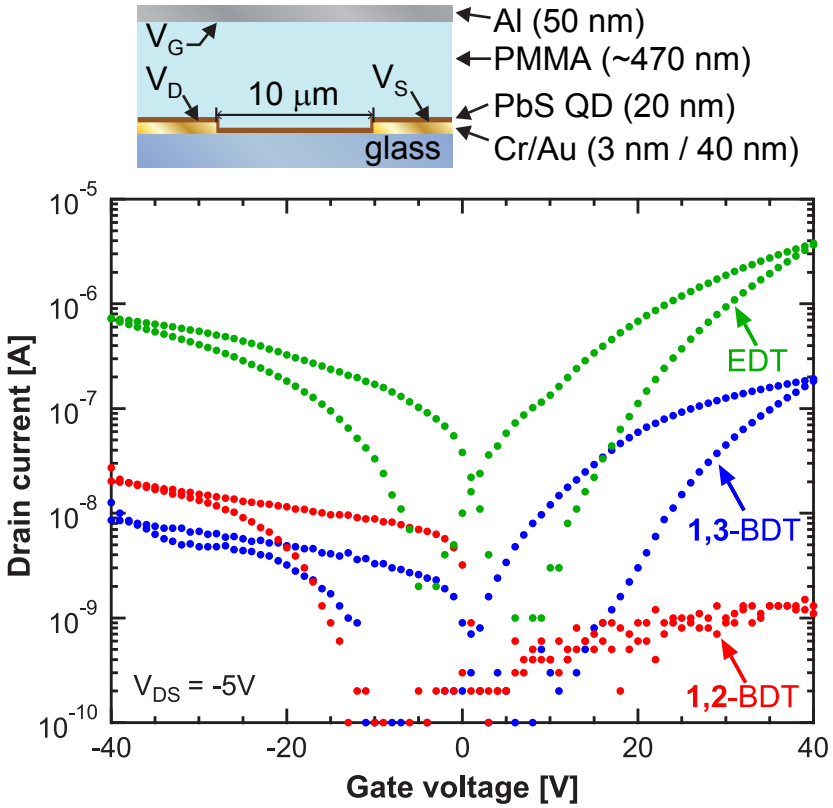

Figure A-1: **Transfer curves of PbS QD FETs.** The top panel provides a schematic cross section of the FET device structure.

the insulating gate dielectric (measured to be $5.7\,\mathrm{nF\,cm^{-2}}$). The observed hysteresis results from bias-stress within the QD channel; this phenomenon is rigorously examined elsewhere. [303] Mobilities are extracted from the branch of the transfer curve starting at $V_G = 0$ and scanning toward higher absolute gate bias. The extracted electron mobility μ_e and hole mobility μ_h for each ligand treatment are $\mu_e = 5 \times 10^{-3}\,\mathrm{cm^2\,V^{-1}\,s^{-1}}$ and $\mu_h = 6 \times 10^{-4}\,\mathrm{cm^2\,V^{-1}\,s^{-1}}$ for EDT; $\mu_h = 1 \times 10^{-5}\,\mathrm{cm^2\,V^{-1}\,s^{-1}}$ for 1,2-BDT (no n-channel turn-on observed); $\mu_e = 2 \times 10^{-4}\,\mathrm{cm^2\,V^{-1}\,s^{-1}}$ and $\mu_h = 9 \times 10^{-6}\,\mathrm{cm^2\,V^{-1}\,s^{-1}}$ for 1,3-BDT. EDT-treated PbS QD films thus demonstrate significantly higher carrier mobilities than either 1,2-BDT- or 1,3-BDT-treated films.

In the absence of other differences between ligands, a higher carrier mobility would be expected to lead to a higher performance in photovoltaics employing EDT-exchanged PbS QDs; instead, 1,2-BDT and 1,3-BDT-exchanged PbS QDs display a higher performance in both np-HJ and SJ architectures. Transient current and voltage

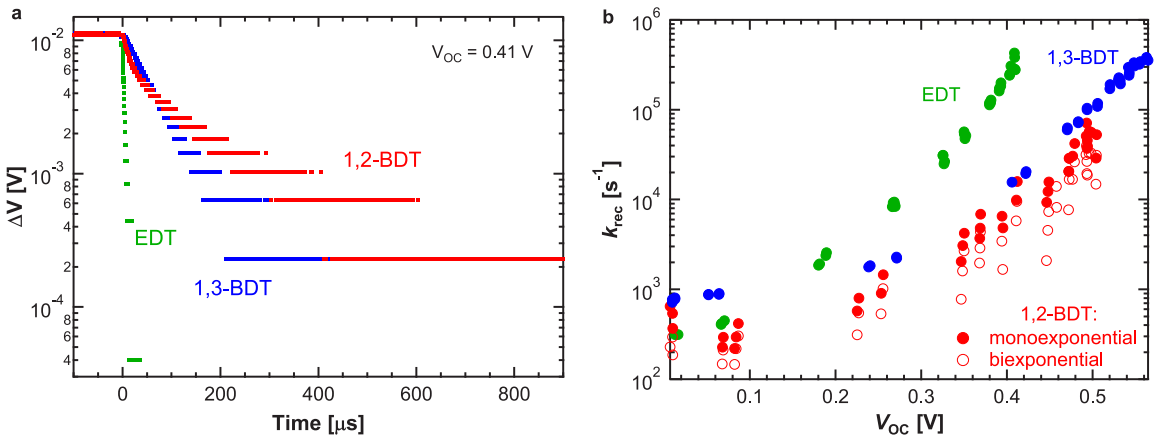

Figure A-2: **Transient-V_{OC} analysis. a**, Decay in ΔV (where ΔV is the additional V_{OC} induced by the perturbing laser pulse) following turn-off of the perturbation pulse for ZnO / PbS QD np-HJ devices employing EDT, 1,2-BDT, and 1,3-BDT ligand exchange. **b**, Extracted recombination rate coefficients k_{rec} for np-HJ photovoltaics across a range of bias light intensities and induced photovoltages. For each induced V_{OC}, the intensity of the perturbation source is adjusted such that ΔV_{max} is less than 5% of V_{OC}. Recombination rate coefficients for EDT and 1,3-BDT correspond to fits to monoexponential decay kinetics; recombination rate coefficients for both monoexponential and biexponential fits for 1,2-BDT are shown.

analysis of np-HJ photovoltaics employing 1,2-BDT-, 1,3-BDT, and EDT-exchanged QDs indicates that the higher mobility of EDT-exchanged QDs is outweighed by their higher carrier recombination rate and trap density.

Figure A-2 shows the transient voltage response, immediately after the turn-off of a perturbing illumination pulse, of ZnO / PbS QD np-HJ photovoltaics biased at $V_{OC} = 0.41$ V by white light illumination. (Note that the EDT-treated device, with its lower V_{OC} under 1-sun illumination, needs a higher bias illumination intensity in order to reach the same V_{OC} as the 1,2-BDT- and 1,3-BDT-treated devices.) EDT treatment gives rise to a much more rapid voltage decay at a given V_{OC} than 1,2-BDT and 1,3-BDT treatment. This decay can be fit to monoexponential kinetics for EDT and 1,3-BDT and biexponential kinetics for 1,2-BDT to enable calculation of the recombination rate constant k_{rec}. Figure A-2.b shows the extracted k_{rec} values for EDT-, 1,2-BDT-, and 1,3-BDT-exchanged PbS QDs in np-HJ photovoltaics across a range of bias light intensities and induced voltages. It is observed that at a given illumination-dependent V_{OC}, EDT gives rise to a larger recombination rate coefficient than either of the

benzenedithiols, in keeping with the lower V_{OC} under 1-sun illumination observed for photovoltaics employing EDT relative to those employing 1,2-BDT and 1,3-BDT in Figure 7-2.

Insight into the mechanism behind the higher recombination rate for EDT is gained by analysis of the profile of the density of electronic trap states within the bandgap, measured as described by Ip et al. [304] All measurements are performed on ZnO / PbS QD np-HJ devices. The device is held at a given V_{OC} and corresponding quasi-Fermi-level splitting through illumination with a white light bias. A short perturbation laser pulse (300 ns duration) generates an excess of carriers of density Δn, giving rise to an increase in photovoltage ΔV. The induced photovoltage ΔV for a given carrier density Δn depends on the density of states dN/dE at the quasi-Fermi level energies corresponding to the specified V_{OC}: for a given Δn, a larger density of states will result in a smaller ΔV, as the quasi-Fermi level only increases enough to fill Δn states. Thus, by plotting $\Delta n/\Delta V$ as a function of V_{OC}, the profile of the density of electronic states within the bandgap (i.e. the density of trap states) can be determined. It should be noted that this method does not specify whether the measured density of states corresponds to electron states or hole states; as the electron and hole quasi-Fermi levels both change under illumination, both electron and hole states could contribute to the response.

Figure A-3.a shows the voltage response of a 1,3-BDT-exchanged PbS QD np-HJ device at a given white light bias following excitation with a perturbation laser pulse of a given intensity. The height of the induced voltage pulse gives ΔV. To determine Δn for this perturbation intensity, the white light bias is turned off and the transient response of the device current to the perturbation pulse alone is measured, as shown in Figure A-3.b. Integration of this complete current profile provides $\Delta Q = Ae\Delta n$ (A is the device area; e is the charge of the electron) for this perturbation intensity.

A complete plot of $\Delta n/\Delta V$ as a function of quasi-Fermi-level splitting is obtained by varying the intensity of the bias light (and, correspondingly, the induced V_{OC}) and measuring ΔV and Δn at each intensity. The intensity of the perturbing laser pulse is adjusted to keep ΔV less than 5% of V_{OC} at each bias light intensity. **Figure A-4**

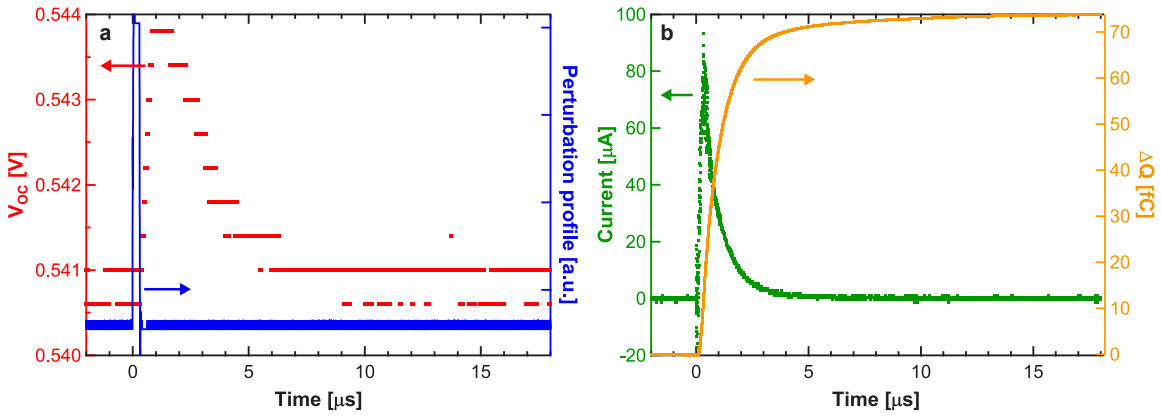

Figure A-3: **Example of transient voltage and current response at a given light bias used in determination of density of states.** **a**, Transient voltage response of a ZnO / PbS QD np-HJ photovoltaic device to a perturbation light pulse under white light bias. The voltage response is plotted in red against the left axis, and the profile of the perturbation pulse is plotted in blue against the right axis. The height of the voltage peak above the baseline yields ΔV. **b**, Transient current response of the same device to the same perturbation pulse intensity without white light bias. The current response is plotted in green against the left axis and the integrated charge is plotted in orange against the right axis. The rightmost value of the integrated charge yields the value of $\Delta Q = Ae\Delta n$ used to compute the density of states profile.

shows the calculated density of states profiles for ZnO / PbS QD np-HJ photovoltaics employing EDT-, 1,2-BDT, and 1,3-BDT-exchanged QDs. The density of states for EDT increases much more rapidly than for 1,2-BDT or 1,3-BDT as the V_{OC} under illumination increases toward the bandgap, corresponding to a greater density of trap states within the bandgap for EDT-treated PbS QDs.

The higher recombination rate and trap density for EDT-exchanged PbS QDs outweighs their higher carrier mobility, explaining why EDT-treated PbS QDs generate a lower V_{OC} in both the np-HJ and SJ architectures than 1,2-BDT and 1,3-BDT-treated PbS QDs. However, the differences in mobility, recombination rate, and trap density described here do not explain the difference in performance between 1,2-BDT and 1,3-BDT in the np-HJ and SJ architectures. These findings, in conjunction with the data reported in Sections 7.3 and 7.4, highlight the importance of taking into account both changes in carrier transport properties and dipole-induced energy level shifts in the comparison of different ligand treatments for QD optoelectronic devices.

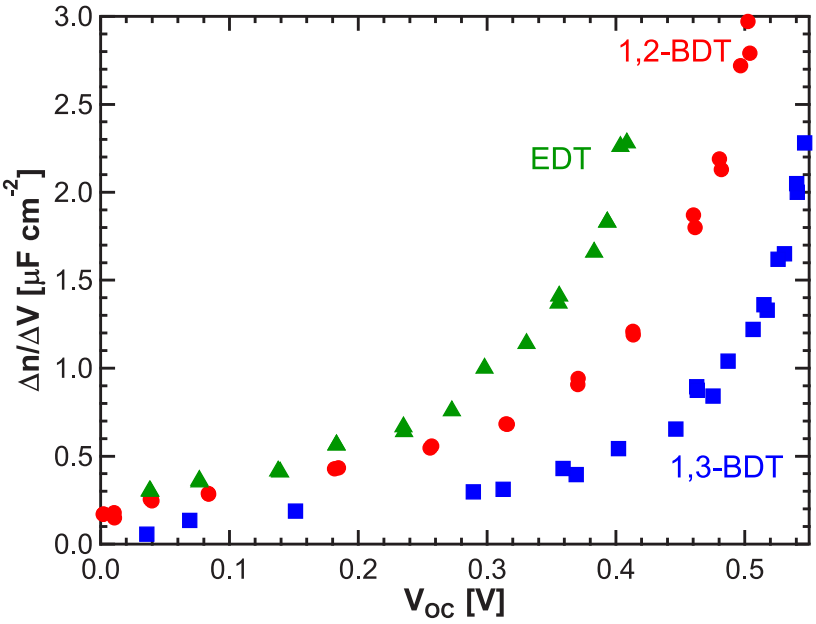

Figure A-4: **Density of states within the QD bandgap.** The DOS profile is measured in terms of $\Delta n/\Delta V$, for ZnO / PbS QD np-HJ photovoltaic devices employing ligand exchange with EDT (green triangles), 1,2-BDT (red circles), or 1,3-BDT (blue squares). A given V_{OC} corresponds to a quasi-Fermi level splitting of the same energy. The density of states increases as the electron and hole quasi-Fermi levels approach the conduction band and valence band edges, as expected for a distribution of trap states that extends as "tails" from the band edges into the bandgap.

Bibliography

[1] S. A. Marcott, J. D. Shakun, P. U. Clark, and A. C. Mix. "A Reconstruction of Regional and Global Temperature for the Past 11,300 Years." Science **339**, 1198 (2013). URL http://dx.doi.org/10.1126/science.1228026.

[2] T. Stocker, D. Qin, G.-K. Plattner, M. Tignor, S. K. Allen, J. Boschung, A. Nauels, Y. Xia, V. Bex, and P. M. Midgley. "Summary for Policymakers. In: Climate Change 2013: The Physical Science Basis. Contribution of Working Group I to the Fifth Assessment Report of the Intergovernmental Panel on Climate Change." Technical report, Intergovernmental Panel on Climate Change, Cambridge, UK and New York, NY, USA (2013). URL http://dx.doi.org/10.1017/CBO9781107415324.

[3] J. Romm. "New IPCC Report: Climatologists More Certain Global Warming Is Caused By Humans, Impacts Are Speeding Up." (2013). URL http://thinkprogress.org/climate/2013/08/18/2484711/ipcc-report-more-certain-global-warming-is-caused-by-humans-impacts-speeding-up/.

[4] Climate Interactive. "Scoreboard Science and Data." (2016). URL https://www.climateinteractive.org/tools/scoreboard/scoreboard-science-and-data/.

[5] O. Edenhofer, R. Pichs-Madruga, Y. Sokona, E. Farahani, S. Kadner, K. Seyboth, A. Adler, I. Baum, S. Brunner, P. Eickemeier, B. Kriemann, J. Savolainen, S. Schlomer, C. von Stechow, T. Zwickel, and J. C. Minx. "Climate Change 2014: Mitigation of Climate Change. Contribution of Working Group III to the Fifth Assessment Report of the Intergovernmental Panel on Climate Change." Technical report, Intergovernmental Panel on Climate Change, Cambridge, UK and New York, NY, USA (2014). URL http://www.ipcc.ch/report/ar5/wg3/.

[6] International Renewable Energy Agency. "Renewable Power Generation Costs in 2014." Technical report, IRENA (2015). URL http://www.irena.org/DocumentDownloads/Publications/IRENA_RE_Power_Costs_2014_report.pdf.

[7] U.S. Energy Information Administration. "Levelized Cost and Levelized Avoided Cost of New Generation Resources in the Annual Energy Outlook 2015." URL http://www.eia.gov/forecasts/aeo/electricity_generation.cfm.

[8] World Energy Council. "World Energy Perspective - Cost of Energy Technologies." Technical report, World Energy Council, London (2013). URL http://dx.doi.org/ISBN:9780946121304.

[9] International Technology Roadmap for Photovoltaic. "2014 Results." Technical report, International Technology Roadmap for Photovoltaic (2015). URL http://www.itrpv.net/Reports/Downloads/2015/.

[10] M. Bolinger and J. Seel. "Utility-Scale Solar 2014: An Empirical Analysis of Project Cost, Performance, and Pricing Trends in the United States." Technical report, Lawrence Berkeley National Laboratory (2015). URL https://emp.lbl.gov/publications/utility-scale-solar-2014-empirical.

[11] G. Barbose, N. Darghouth, D. Millstein, M. Spears, R. Wiser, M. Buckley, R. Widiss, and N. Grue. "Tracking the Sun VIII: The Installed Price of Residential and Non-Residential Photovoltaic Systems in the United States." Technical report, Lawrence Berkeley National Laboratory (2015). URL https://emp.lbl.gov/publications/tracking-sun-viii-installed-price.

[12] MIT Energy Initiative. "The Future of Solar Energy." Technical report, Massachusetts Institute of Technology, Cambridge, MA (2015). URL mitei.mit.edu/futureofsolar.

[13] J. E. Trancik, P. R. Brown, J. Jean, G. Kavlak, and M. Klemun. "Technology improvement and emissions reductions as mutually reinforcing efforts: Observations from the global development of solar and wind energy." Technical report, Massachusetts Institute of Technology (2015). URL http://trancik.scripts.mit.edu/home/wp-content/uploads/2015/11/Trancik_INDCReport.pdf.

[14] U.S. Energy Information Administration. "November 2015 Monthly Energy Review." Technical report, U.S. Energy Information Administration (2014). URL http://www.eia.gov/totalenergy/data/monthly.

[15] International Energy Agency. "World Energy Outlook 2006." Technical report, International Energy Agency (2006). URL http://www.worldenergyoutlook.org/media/weowebsite/2008-1994/WEO2006.pdf.

[16] International Energy Agency. "World Energy Outlook 2008." Technical report, International Energy Agency (2008). URL http://www.worldenergyoutlook.org/media/weowebsite/2008-1994/weo2008.pdf.

[17] International Energy Agency. "World Energy Outlook 2009." Technical report, International Energy Agency (2009). URL http://www.worldenergyoutlook.org/publications/weo-2009/.

[18] International Energy Agency. "World Energy Outlook 2010." Technical report, International Energy Agency (2010). URL http://www.worldenergyoutlook.org/publications/weo-2010/.

[19] International Energy Agency. "World Energy Outlook 2011." Technical report, International Energy Agency (2011). URL http://www.worldenergyoutlook.org/publications/weo-2011/.

[20] International Energy Agency. "World Energy Outlook 2012." Technical report, International Energy Agency (2012). URL http://www.worldenergyoutlook.org/publications/weo-2012/.

[21] International Energy Agency. "World Energy Outlook 2013." Technical report, International Energy Agency (2013). URL http://www.worldenergyoutlook.org/publications/weo-2013/.

[22] International Energy Agency. "World Energy Outlook 2014." Technical report, International Energy Agency (2014). URL http://www.worldenergyoutlook.org/publications/weo-2014/.

[23] U.S. Energy Information Administration. "International Energy Outlook 2010." Technical report, U.S. Energy Information Administration (2010). URL http://www.eia.gov/forecasts/archive/ieo10/index.html.

[24] U.S. Energy Information Administration. "International Energy Outlook 2011." Technical report, U.S. Energy Information Administration (2011). URL http://www.eia.gov/forecasts/archive/ieo11/.

[25] U.S. Energy Information Administration. "International Energy Outlook 2013." Technical report, U.S. Energy Information Administration (2013). URL http://www.eia.gov/forecasts/ieo/pdf/0484(2013).pdf.

[26] European Photovoltaic Industry Association. "Global Market Outlook for Photovoltaics 2014-2018." Technical report, European Photovoltaic Industry Association (2014). URL http://www.epia.org/fileadmin/user_upload/Publications/EPIA_Global_Market_Outlook_for_Photovoltaics_2014-2018_-_Medium_Res.pdf.

[27] IHS. "Solar Installations to Rise 20 Percent in 2014, Thanks to Strong Fourth Quarter." (2014). URL http://press.ihs.com/press-release/design-supply-chain/solar-installations-rise-20-percent-2014-thanks-strong-fourth-quar.

[28] REN21. "Renewable 2014 Global Status Report." Technical report, REN21 (2014). URL http://www.ren21.net/Portals/0/documents/Resources/GSR/2014/GSR2014_fullreport_lowres.pdf.

[29] U.S. Energy Information Administration. "International Energy Outlook 2009." Technical report, U.S. Energy Information Administration (2009). URL http://www.eia.gov/forecasts/archive/ieo09/pdf/0484(2009).pdf.

[30] International Energy Agency. "Energy Technology Perspectives 2014." Technical report, International Energy Agency (2014). URL http://www.iea.org/etp/etp2014/.

[31] P. R. Brown, J. Jean, R. L. Jaffe, and G. Kavlak. "Chapter 6 – PV Scaling and Materials Use." In "The Future of Solar Energy," chapter 6, pages 125–151. Massachusetts Institute of Technology Energy Initiative, Boston (2015). URL mitei.mit.edu/futureofsolar.

[32] U.S. Geological Survey. "Historical Statistics for Mineral and Material Commodities in the United States." (2014). URL http://minerals.usgs.gov/minerals/pubs/historical-statistics/.

[33] U.S. Geological Survey. "Commodity Statistics and Information." (2014). URL http://minerals.usgs.gov/minerals/pubs/commodity/.

[34] T. Lay, J. Hernlund, and B. A. Buffett. "Core–mantle boundary heat flow." Nature Geoscience **1**, 25 (2008). URL http://dx.doi.org/10.1038/ngeo.2007.44.

[35] Q. Fu. "Solar Radiation." (2002). URL http://dx.doi.org/10.1016/B0-12-227090-8/00334-1.

[36] R. L. Jaffe and W. Taylor. *The Physics of Energy*. to be published by Cambridge University Press.

[37] National Renewable Energy Laboratory. "Dynamic Maps, GIS Data, & Analysis Tools – Solar Maps." URL http://www.nrel.gov/gis/solar.html.

[38] National Renewable Energy Laboratory. "Global Horizontal Solar Radiation – Annual." URL http://en.openei.org/w/index.php?title=File:NREL-solar-glo.pdf.

[39] American Society for Testing and Materials (ASTM). "Reference Solar Spectral Irradiance: Air Mass 1.5 (ASTM G173-03 Reference Spectrum)." URL http://rredc.nrel.gov/solar/spectra/am1.5/.

[40] K. E. Trenberth, J. T. Fasullo, and J. Kiehl. "Earth's global energy budget." Bulletin of the American Meteorological Society **90**, 311 (2009). URL http://dx.doi.org/10.1175/2008BAMS2634.1.

[41] National Renewable Energy Laboratory. "Measurement and Instrumentation Data Center (MIDC)." URL http://www.nrel.gov/midc/.

[42] OpenStreetMap. "OpenStreetMap." URL http://www.openstreetmap.org.

[43] National Renewable Energy Laboratory. "National Solar Radiation Data Base - 1991-2010 Update." URL http://rredc.nrel.gov/solar/old_data/nsrdb/1991-2010/hourly/list_by_state.html.

[44] M. Albuisson, M. Lefevre, and L. Wald. "Averaged Solar Radiation 1990–2004." Technical report, Ecole des Mines de Paris / Armines (2006). URL http://www.soda-is.com/eng/map/maps_for_free.html.

[45] B. Rankin. "Radical Cartography." (2008). URL www.radicalcartography.net.

[46] National Renewable Energy Laboratory. "Solar Resources By Class Per Country." URL http://en.openei.org/datasets/dataset/solar-resources-by-class-and-country.

[47] World Bank. "World DataBank. World Development Indicators." (2014). URL http://databank.worldbank.org/data/views/reports/tableview.aspx.

[48] P. Denholm and R. M. Margolis. "Land-use requirements and the per-capita solar footprint for photovoltaic generation in the United States." Energy Policy **36**, 3531 (2008). URL http://dx.doi.org/10.1016/j.enpol.2008.05.035.

[49] A. De Vos. "Detailed balance limit of the efficiency of tandem solar cells." Journal of Physics D: Applied Physics **13**, 839 (1980). URL http://dx.doi.org/10.1088/0022-3727/13/5/018.

[50] W. Shockley and H. J. Queisser. "Detailed Balance Limit of Efficiency of p-n Junction Solar Cells." Journal of Applied Physics **32**, 510 (1961). URL http://dx.doi.org/10.1063/1.1736034.

[51] M. C. Hanna and A. J. Nozik. "Solar conversion efficiency of photovoltaic and photoelectrolysis cells with carrier multiplication absorbers." Journal of Applied Physics **100**, 074510 (2006). URL http://dx.doi.org/10.1063/1.2356795.

[52] R. R. Lunt, T. P. Osedach, P. R. Brown, J. A. Rowehl, and V. Bulović. "Practical Roadmap and Limits to Nanostructured Photovoltaics." Advanced Materials **23**, 5712 (2011). URL http://dx.doi.org/10.1002/adma.201103404.

[53] National Renewable Energy Laboratory. "Best Research-Cell Efficiencies." (2015). URL http://www.nrel.gov/ncpv/images/efficiency_chart.jpg.

[54] International Technology Roadmap for Photovoltaic. "2013 Results." Technical report, International Technology Roadmap for Photovoltaic (2014). URL http://www.itrpv.net/Reports/Downloads/2014/.

[55] National Renewable Energy Laboratory. "PVWatts Calculator - Version 5." URL http://pvwatts.nrel.gov/version_5.php.

[56] V. Fthenakis and H. C. Kim. "Land use and electricity generation: A life-cycle analysis." Renewable and Sustainable Energy Reviews **13**, 1465 (2009). URL http://dx.doi.org/10.1016/j.rser.2008.09.017.

[57] National Renewable Energy Laboratory. "Solar Summaries." URL http://www.nrel.gov/gis/data_solar.html.

[58] C. Nickerson, R. Ebel, A. Borchers, and F. Carriazo. "Major Uses of Land in the United States, 2007." (2011). URL http://www.ers.usda.gov/data-products/major-land-uses.aspx.

[59] U.S. National Park Service. "About Us." (2015). URL http://www.nps.gov/aboutus/index.htm.

[60] U.S. Department of Defense. "About Us." (2015). URL www.defense.gov/about/.

[61] SourceWatch. "The footprint of coal." (2011). URL http://www.sourcewatch.org/index.php/The_footprint_of_coal.

[62] United States Supreme Court. "Hodel v. Indiana, 452 U.S. 314." (1981). URL http://caselaw.lp.findlaw.com/scripts/getcase.pl?navby=case&court=us&vol=452&invol=314.

[63] U.S. Office of Surface Mining Reclamation and Enforcement. "Annual Reports." (2014). URL http://www.osmre.gov/resources/annualreports.shtm.

[64] J. Jean, P. R. Brown, R. L. Jaffe, T. Buonassisi, and V. Bulović. "Pathways for Solar Photovoltaics." Energy & Environmental Science **8**, 1200 (2015). URL http://dx.doi.org/10.1039/C4EE04073B.

[65] M. A. Green, K. Emery, Y. Hishikawa, W. Warta, and E. D. Dunlop. "Solar cell efficiency tables (version 39)." Progress in Photovoltaics: Research and Applications **20**, 12 (2012). URL http://dx.doi.org/10.1002/pip.2163.

[66] M. A. Green, K. Emery, Y. Hishikawa, W. Warta, and E. D. Dunlop. "Solar cell efficiency tables (version 40)." Progress in Photovoltaics: Research and Applications **20**, 606 (2012). URL http://dx.doi.org/10.1002/pip.2267.

[67] M. A. Green, K. Emery, Y. Hishikawa, W. Warta, and E. D. Dunlop. "Solar cell efficiency tables (version 41)." Progress in Photovoltaics: Research and Applications **21**, 1 (2013). URL http://dx.doi.org/10.1002/pip.2352.

[68] M. A. Green, K. Emery, Y. Hishikawa, W. Warta, and E. D. Dunlop. "Solar cell efficiency tables (version 42)." Progress in Photovoltaics: Research and Applications **21**, 827 (2013). URL http://dx.doi.org/10.1002/pip.2404.

[69] C.-H. M. Chuang, P. R. Brown, V. Bulović, and M. G. Bawendi. "Improved performance and stability in quantum dot solar cells through band alignment engineering." Nature Materials **13**, 796 (2014). URL dx.doi.org/10.1038/NMAT3984.

[70] M. A. Green, K. Emery, Y. Hishikawa, W. Warta, and E. D. Dnlop. "Solar cell efficiency tables (Version 45)." Progress in Photovoltaics: Research and Applications **23**, 1 (2015). URL http://dx.doi.org/10.1002/pip.2573.

[71] A. N. Mariano and K. L. Chopra. "Polymorphism in some IV-VI compounds induced by high pressure and thin-film epitaxial growth." Applied Physics Letters **10**, 282 (1967). URL http://dx.doi.org/10.1063/1.1754812.

[72] K. F. Cuff, M. R. Ellet, C. D. Kuglin, and L. R. Williams. In "Proc. 7th Int. Conf. Phys. Semicond.", page 677 (1964).

[73] R. Dalven. In H. Ehrenreich, F. Seitz, and D. Turnbull, editors, "Solid State Physics," volume 28, page 179. Academic Press, New York (1973).

[74] J. Gao, J. M. Luther, O. E. Semonin, R. J. Ellingson, A. J. Nozik, and M. C. Beard. "Quantum Dot Size Dependent J-V Characteristics in Heterojunction ZnO/PbS Quantum Dot Solar Cells." Nano Letters **11**, 1002 (2011). URL http://dx.doi.org/10.1021/nl103814g.

[75] J. Jasieniak, M. Califano, and S. E. Watkins. "Size-dependent valence and conduction band-edge energies of semiconductor nanocrystals." ACS Nano **5**, 5888 (2011). URL http://dx.doi.org/10.1021/nn201681s.

[76] N. J. Thompson, M. W. B. Wilson, D. N. Congreve, P. R. Brown, J. M. Scherer, T. S. Bischof, M. Wu, N. Geva, M. Welborn, T. V. Voorhis, V. Bulović, M. G. Bawendi, and M. A. Baldo. "Energy harvesting of non-emissive triplet excitons in tetracene by emissive PbS nanocrystals." Nature Materials **13**, 1039 (2014). URL http://dx.doi.org/10.1038/nmat4097.

[77] K. S. Leschkies, T. J. Beatty, M. S. Kang, D. J. Norris, and E. S. Aydil. "Solar cells based on junctions between colloidal PbSe nanocrystals and thin ZnO films." ACS Nano **3**, 3638 (2009). URL http://dx.doi.org/10.1021/nn901139d.

[78] T. Matsushima, Y. Kinoshita, and H. Murata. "Formation of Ohmic hole injection by inserting an ultrathin layer of molybdenum trioxide between indium tin oxide and organic hole-transporting layers." Applied Physics Letters **91**, 253504 (2007). URL http://dx.doi.org/10.1063/1.2825275.

[79] B.-R. Hyun, Y.-W. Zhong, A. C. Bartnik, L. Sun, H. D. Abruña, F. W. Wise, J. D. Goodreau, J. R. Matthews, T. M. Leslie, and N. F. Borrelli. "Electron injection from colloidal PbS quantum dots into titanium dioxide nanoparticles." ACS Nano **2**, 2206 (2008). URL http://dx.doi.org/10.1021/nn800336b.

[80] Y. Park, V. Choong, Y. Gao, B. R. Hsieh, and C. W. Tang. "Work function of indium tin oxide transparent conductor measured by photoelectron spectroscopy." Applied Physics Letters **68**, 2699 (1996). URL http://dx.doi.org/10.1063/1.116313.

[81] A. Kahn, N. Koch, and W. Gao. "Electronic structure and electrical properties of interfaces between metals and π-conjugated molecular films." Journal of Polymer Science Part B: Polymer Physics **41**, 2529 (2003). URL http://doi.wiley.com/10.1002/polb.10642.

[82] O. L. Griffith, J. E. Anthony, A. G. Jones, and D. L. Lichtenberger. "Electronic properties of pentacene versus triisopropylsilylethynyl- substituted pentacene: Environment-dependent effects of the silyl substituent." Journal of the American Chemical Society **132**, 580 (2010). URL http://dx.doi.org/10.1021/ja906917r.

[83] P. J. Jadhav, P. R. Brown, N. Thompson, B. Wunsch, A. Mohanty, S. R. Yost, E. Hontz, T. Van Voorhis, M. G. Bawendi, V. Bulović, and M. A. Baldo. "Triplet exciton dissociation in singlet exciton fission photovoltaics." Advanced Materials **24**, 6169 (2012). URL http://dx.doi.org/10.1002/adma.201202397.

[84] B. A. Jones, A. Facchetti, M. R. Wasielewski, and T. J. Marks. "Tuning orbital energetics in arylene diimide semiconductors. Materials design for ambient stability of n-type charge transport." Journal of the American Chemical Society **129**, 15259 (2007). URL http://dx.doi.org/10.1021/ja075242e.

[85] L. C. Picciolo, H. Murata, and Z. H. Kafafi. "Organic light-emitting devices with saturated red emission using 6,13-diphenylpentacene." Applied Physics Letters **78**, 2378 (2001). URL http://dx.doi.org/10.1063/1.1362259.

[86] J. Weaver. "Electronic structures of C_{60}, C_{70} and the fullerides: Photoemission and inverse photoemission studies." Journal of Physics and Chemistry of Solids **53**, 1433 (1992). URL http://dx.doi.org/10.1016/0022-3697(92)90237-8.

[87] J. J. Choi, Y.-F. Lim, M. B. Santiago-Berrios, M. Oh, B.-R. Hyun, L. Sun, A. C. Bartnik, A. Goedhart, G. G. Malliaras, H. D. Abruña, F. W. Wise, and T. Hanrath. "PbSe nanocrystal excitonic solar cells." Nano Letters **9**, 3749 (2009). URL http://dx.doi.org/10.1021/nl901930g.

[88] H. Usta, A. Facchetti, and T. J. Marks. "N-channel semiconductor materials design for organic complementary circuits." Accounts of Chemical Research **44**, 501 (2011). URL http://dx.doi.org/10.1021/ar200006r.

[89] J. Hwang, A. Wan, and A. Kahn. "Energetics of Metal-Organic interfaces: New experiments and assessment of the field." Materials Science and Engineering: R: Reports **64**, 1 (2009). URL http://dx.doi.org/10.1016/j.mser.2008.12.001.

[90] C. Kittel. *Introduction to Solid State Physics*. John Wiley & Sons, Inc., Hoboken, NJ, 8 edition (2005).

[91] B. L. Anderson and R. L. Anderson. *Fundamentals of Semiconductor Devices*. McGraw-Hill, New York (2005).

[92] S. H. Wei and A. Zunger. "Band offsets and optical bowings of chalcopyrites and Zn-based II-VI alloys." Journal of Applied Physics **78**, 3846 (1995). URL http://dx.doi.org/10.1063/1.359901.

[93] C. D. Clark, P. J. Dean, and P. V. Harris. "Intrinsic edge absorption in diamond." Proceedings of the Royal Society of London Series A - Mathematical and Physical Sciences **277**, 312 (1964). URL http://dx.doi.org/10.1098/rspa.1964.0025.

[94] D. M. Roessler and W. C. Walker. "Electronic spectrum of crystalline lithium fluoride." Journal of Physics and Chemistry of Solids **28**, 1507 (1967). URL http://dx.doi.org/10.1016/0038-1098(67)90807-1.

[95] T. F. Stocker, D. Qin, G.-K. Plattner, M. Tignor, S. K. Allen, J. Boschung, A. Nauels, Y. Xia, V. Bex, and P. M. Midgley. "Climate Change 2013: The Physical Science Basis. Contribution of Working Group I to the Fifth Assessment Report of the Intergovernmental Panel on Climate Change." Technical report,

Intergovernmental Panel on Climate Change, Cambridge, UK and New York, NY, USA (2013). URL http://www.climatechange2013.org/report/full-report/.

[96] C. B. Field, V. R. Barros, D. J. Dokken, K. J. Mach, M. D. Mastrandrea, T. E. Bilir, M. Chatterjee, K. L. Ebi, Y. O. Estrada, R. C. Genova, B. Girma, E. S. Kissel, A. N. Levy, S. MacCracken, P. R. Mastrandrea, and L. L. White. "Climate Change 2014: Impacts, Adaptation, and Vulnerability. Part A: Global and Sectoral Aspects. Contribution of Working Group II to the Fifth Assessment Report of the Intergovernmental Panel on Climate Change." Technical report, Intergovernmental Panel on Climate Change, Cambridge, UK and New York, NY, USA (2014). URL https://ipcc-wg2.gov/AR5/report/.

[97] V. R. Barros, C. B. Field, D. J. Dokken, M. D. Mastrandrea, K. J. Mach, T. E. Bilir, M. Chatterjee, K. L. Ebi, Y. O. Estrada, R. C. Genova, B. Girma, E. S. Kissel, A. N. Levy, S. MacCracken, P. R. Mastrandrea, and L. L. White. "Climate Change 2014: Impacts, Adaptation, and Vulnerability. Part B: Regional Aspects. Contribution of Working Group II to the Fifth Assessment Report of the Intergovernmental Panel on Climate Change." Technical report, Intergovernmental Panel on Climate Change, Cambridge, UK and New York, NY, USA (2014). URL https://ipcc-wg2.gov/AR5/report/.

[98] United Nations. "Adoption of the Paris Agreement." In "Framework Convention on Climate Change," Paris (2015). URL http://unfccc.int/resource/docs/2015/cop21/eng/l09r01.pdf.

[99] D. Archer and V. Brovkin. "The millennial atmospheric lifetime of anthropogenic CO_2." Climatic Change **90**, 283 (2008). URL http://dx.doi.org/10.1007/s10584-008-9413-1.

[100] S. Solomon, G.-K. Plattner, R. Knutti, and P. Friedlingstein. "Irreversible climate change due to carbon dioxide emissions." Proceedings of the National Academy of Sciences of the United States of America **106**, 1704 (2009). URL http://dx.doi.org/10.1073/pnas.0812721106.

[101] M. Meinshausen, N. Meinshausen, W. Hare, S. C. B. Raper, K. Frieler, R. Knutti, D. J. Frame, and M. R. Allen. "Greenhouse-gas emission targets for limiting global warming to 2 °C." Nature **458**, 1158 (2009). URL http://dx.doi.org/10.1038/nature08017.

[102] M. Allen, D. Frame, C. Huntingford, C. Jones, J. Lowe, M. Meinshausen, and N. Meinshausen. "Warming caused by cumulative carbon emissions towards the trillionth tonne." Nature **458**, 1163 (2009). URL http://dx.doi.org/10.1038/nature08019.

[103] C. McGlade and P. Ekins. "The geographical distribution of fossil fuels unused when limiting global warming to 2 °C." Nature **517**, 187 (2015). URL http://dx.doi.org/10.1038/nature14016.

[104] National Renewable Energy Laboratory. "Life Cycle Greenhouse Gas Emissions from Electricity Generation." Technical report, National Renewable Energy Laboratory (2013). URL http://nrel.gov/harmonizationhttp://www.nrel.gov/analysis/sustain_lcah.html.

[105] International Energy Agency. "PVPS Report: Snapshot of global photovoltaic markets 2015." Technical report, International Energy Agency (2016). URL http://www.iea-pvps.org/fileadmin/dam/public/report/PICS/IEA-PVPS_-__A_Snapshot_of_Global_PV_-_1992-2015_-_Final_2_02.pdf.

[106] A. McDonald and L. Schrattenholzer. "Learning rates for energy technologies." Energy Policy **29**, 255 (2001). URL http://dx.doi.org/10.1016/S0301-4215(00)00122-1.

[107] G. F. Nemet. "Interim monitoring of cost dynamics for publicly supported energy technologies." Energy Policy **37**, 825 (2009). URL http://dx.doi.org/10.1016/j.enpol.2008.10.031.

[108] M. Kaltenbrunner, M. S. White, E. D. Głowacki, T. Sekitani, T. Someya, N. S. Sariciftci, and S. Bauer. "Ultrathin and lightweight organic solar cells with high flexibility." Nature Communications **3**, 770 (2012). URL http://dx.doi.org/10.1038/ncomms1772.

[109] J. Jean, A. Wang, and V. Bulović. "In situ vapor-deposited parylene substrates for ultra-thin, lightweight organic solar cells." Organic Electronics **31**, 120 (2016). URL http://dx.doi.org/10.1016/j.orgel.2016.01.022.

[110] G. Kavlak, J. McNerney, R. L. Jaffe, and J. E. Trancik. "Metal production requirements for rapid photovoltaics deployment." Energy & Environmental Science **8**, 1651 (2015). URL http://dx.doi.org/10.1039/C5EE00585J.

[111] V. A. Akhavan, B. W. Goodfellow, M. G. Panthani, D. K. Reid, D. J. Hellebusch, T. Adachi, and B. A. Korgel. "Spray-deposited $CuInSe_2$ nanocrystal photovoltaics." Energy & Environmental Science **3**, 1600 (2010). URL http://dx.doi.org/10.1039/c0ee00098a.

[112] I. J. Kramer, J. C. Minor, G. Moreno-Bautista, L. Rollny, P. Kanjanaboos, D. Kopilovic, S. M. Thon, G. H. Carey, K. W. Chou, D. Zhitomirsky, A. Amassian, and E. H. Sargent. "Efficient Spray-Coated Colloidal Quantum Dot Solar Cells." Advanced Materials **27**, 116 (2015). URL http://dx.doi.org/10.1002/adma.201403281.

[113] J. M. Luther, M. Law, M. C. Beard, Q. Song, M. O. Reese, R. J. Ellingson, and A. J. Nozik. "Schottky solar cells based on colloidal nanocrystal films." Nano Letters **8**, 3488 (2008). URL http://dx.doi.org/10.1021/nl802476m.

[114] W.-K. Koh, S. R. Saudari, A. T. Fafarman, C. R. Kagan, and C. B. Murray. "Thiocyanate-capped PbS nanocubes: Ambipolar transport enables quantum

dot based circuits on a flexible substrate." Nano letters **11**, 4764 (2011). URL http://dx.doi.org/10.1021/nl202578g.

[115] J. M. Luther, J. Gao, M. T. Lloyd, O. E. Semonin, M. C. Beard, and A. J. Nozik. "Stability Assessment on a 3% Bilayer PbS/ZnO Quantum Dot Heterojunction Solar Cell." Advanced Materials **22**, 3704 (2010). URL http://dx.doi.org/10.1002/adma.201001148.

[116] G. H. Kim, F. P. Garcia De Arquer, Y. J. Yoon, X. Lan, M. Liu, O. Voznyy, Z. Yang, F. Fan, A. H. Ip, P. Kanjanaboos, S. Hoogland, J. Y. Kim, and E. H. Sargent. "High-Efficiency Colloidal Quantum Dot Photovoltaics via Robust Self-Assembled Monolayers." Nano Letters **15**, 7691 (2015). URL http://dx.doi.org/10.1021/acs.nanolett.5b03677.

[117] D. V. Talapin and C. B. Murray. "PbSe nanocrystal solids for n- and p-channel thin film field-effect transistors." Science **310**, 86 (2005). URL http://dx.doi.org/10.1126/science.1116703.

[118] O. Voznyy, D. Zhitomirsky, P. Stadler, Z. Ning, S. Hoogland, and E. H. Sargent. "A Charge-Orbital Balance Picture of Doping in Colloidal Quantum Dot Solids." ACS Nano **6**, 8448 (2012). URL http://dx.doi.org/10.1021/nn303364d.

[119] P. R. Brown, D. Kim, R. R. Lunt, N. Zhao, M. G. Bawendi, J. C. Grossman, and V. Bulović. "Energy Level Modification in Lead Sulfide Quantum Dot Thin Films through Ligand Exchange." ACS Nano **8**, 5863 (2014). URL http://dx.doi.org/10.1021/nn500897c.

[120] P. R. Brown. "Appendix A – The Solar Resource." In "The Future of Solar Energy," chapter Appendix A, pages 253—-270. Massachusetts Institute of Technology Energy Initiative, Boston (2015). URL http://mitei.mit.edu/futureofsolar.

[121] P. R. Brown and J. A. Macko. "Appendix B – Photovoltaics Primer." In "The Future of Solar Energy," chapter Appendix B, pages 271–284. Massachusetts Institute of Technology Energy Initiative, Boston (2015). URL mitei.mit.edu/futureofsolar.

[122] P. R. Brown, R. R. Lunt, N. Zhao, T. P. Osedach, D. D. Wanger, L.-Y. Chang, M. G. Bawendi, and V. Bulović. "Improved current extraction from ZnO/PbS quantum dot heterojunction photovoltaics using a MoO_3 interfacial layer." Nano Letters **11**, 2955 (2011). URL http://dx.doi.org/10.1021/nl201472u.

[123] W. A. Hermann. "Quantifying global exergy resources." Energy **31**, 1685 (2006). URL http://dx.doi.org/10.1016/j.energy.2005.09.006.

[124] M. I. Hoffert, K. Caldeira, A. K. Jain, E. F. Haites, L. D. D. Harvey, S. D. Potter, M. E. Schlesinger, S. H. Schneider, R. G. Watts, T. M. L. Wigley, and D. J. Wuebbles. "Energy implications of future stabilization of atmospheric CO_2 content." Nature **395**, 881 (1998). URL http://dx.doi.org/10.1038/27638.

[125] R. K. Pachauri, M. R. Allen, V. R. Barros, J. Broome, W. Cramer, R. Christ, J. A. Church, L. Clarke, Q. Dahe, P. Dasgupta, N. K. Dubash, O. Edenhofer, I. Elgizouli, C. B. Field, P. Forster, P. Friedlingstein, J. Fuglestvedt, L. Gomez-Echeverri, S. Hallegatte, G. Hegerl, M. Howden, K. Jiang, B. J. Cisneros, V. Kattsov, H. Lee, K. J. Mach, J. Marotzke, M. D. Mastrandrea, L. Meyer, J. Minx, Y. Mulugetta, K. O'Brien, M. Oppenheimer, J. J. Pereira, R. Pichs-Madruga, G.-K. Plattner, H.-O. Pörtner, S. B. Power, B. Preston, N. Ravindranath, A. Reisinger, K. Riahi, M. Rusticucci, R. Scholes, K. Seyboth, Y. Sokona, R. Stavins, T. F. Stocker, P. Tschakert, D. V. Vuuren, and J.-P. V. Ypersele. "IPCC Climate Change 2014: Synthesis Report." (2014). URL http://www.ipcc.ch/report/ar5/syr/.

[126] M. Z. Jacobson and M. A. Delucchi. "Providing all global energy with wind, water, and solar power, Part I: Technologies, energy resources, quantities and areas of infrastructure, and materials." Energy Policy **39**, 1154 (2011). URL http://dx.doi.org/10.1016/j.enpol.2010.11.040.

[127] J. Hansen, P. Kharecha, M. Sato, V. Masson-Delmotte, F. Ackerman, D. J. Beerling, P. J. Hearty, O. Hoegh-Guldberg, S.-L. Hsu, C. Parmesan, J. Rockstrom, E. J. Rohling, J. Sachs, P. Smith, K. Steffen, L. Van Susteren, K. von Schuckmann, and J. C. Zachos. "Assessing "dangerous climate change": required reduction of carbon emissions to protect young people, future generations and nature." PloS one **8**, e81648 (2013). URL http://dx.doi.org/10.1371/journal.pone.0081648.

[128] S. Glasstone and P. Dolan. *The Effects of Nuclear Weapons*. U.S. Department of Defense and Energy Research and Development Administration, Washington, D.C. (1977). URL https://www.fourmilab.ch/etexts/www/effects/.

[129] D. R. Williams. "Sun Fact Sheet." (2013). URL http://nssdc.gsfc.nasa.gov/planetary/factsheet/sunfact.html.

[130] Bureau Internaional des Poids et Mesures. "International System of Units (SI), 8th edition." (2006). URL http://dx.doi.org/10.1201/b15746.axb.

[131] D. R. Williams. "Earth Fact Sheet." (2013). URL http://nssdc.gsfc.nasa.gov/planetary/factsheet/earthfact.html.

[132] C. Fröhlich and J. Lean. "Solar radiative output and its variability: evidence and mechanisms." The Astronomy and Astrophysics Review **12**, 273 (2004). URL http://dx.doi.org/10.1007/s00159-004-0024-1.

[133] SunPower. "X-Series Solar Panels." Solar Panel Datasheet (2014). URL http://us.sunpower.com/solar-resources/.

[134] White Sands Missile Range Public Affairs Office. "White Sands Missile Range Facts Sheet." URL http://www.nasa.gov/pdf/449089main_White_Sands_Missile_Range_Fact_Sheet.pdf.

[135] United States Army. "Dugway Proving Ground Facts & Figures." URL http://www.dugway.army.mil/Facts.aspx.

[136] N. N. Ledentsov, V. M. Ustinov, V. A. Shchukin, P. S. Kop'ev, Z. I. Alferov, and D. Bimberg. "Quantum dot heterostructures: Fabrication, properties, lasers (Review)." Semiconductors **32**, 343 (1998). URL http://dx.doi.org/10.1134/1.1187396.

[137] L. E. Brus. "Electron-electron and electron-hole interactions in small semiconductor crystallites: The size dependence of the lowest excited electronic state." The Journal of Chemical Physics **9**, 4403 (1984). URL http://dx.doi.org/10.1063/1.447218.

[138] J. Q. Grim, L. Manna, and I. Moreels. "A sustainable future for photonic colloidal nanocrystals." Chemical Society Reviews **44**, 5897 (2015). URL http://dx.doi.org/10.1039/c5cs00285k.

[139] W. W. Scanlon. "Recent advances in the optical and electronic properties of PbS, PbSe, PbTe and their alloys." Journal of Physics and Chemistry of Solids **8**, 423 (1959). URL http://dx.doi.org/10.1016/0022-3697(59)90379-8.

[140] J. N. Zemel, J. D. Jensen, and R. B. Schoolar. "Electrical and optical properties of epitaxial films of PbS, PbSe, PbTe, and SnTe." Physical Review **140** (1965). URL http://dx.doi.org/10.1103/PhysRev.140.A330.

[141] T. E. Thompson, P. R. Aron, B. S. Chandrasekhar, and D. N. Langenberg. "Magnetostriction and magnetoelastic quantum oscillations in p-PbTe." Physical Review B **4**, 518 (1971). URL http://dx.doi.org/10.1103/PhysRevB.4.518.

[142] S. E. Kohn, P. Y. Yu, Y. Petroff, Y. R. Shen, Y. Tsang, and M. L. Cohen. "Electronic band structure and optical properties of PbTe, PbSe, and PbS." Physical Review B **8**, 1477 (1973). URL http://dx.doi.org/10.1103/PhysRevB.8.1477.

[143] I. Kang and F. W. Wise. "Electronic structure and optical properties of PbS and PbSe quantum dots." Journal of the Optical Society of America B **14**, 1632 (1997). URL http://dx.doi.org/10.1364/JOSAB.14.001632.

[144] A. L. Efros and M. Rosen. "The Electronic Structure of Semiconductor Nanocrystals." Annual Review of Materials Science **30**, 475 (2000). URL http://dx.doi.org/10.1146/annurev.matsci.30.1.475.

[145] D. J. Norris. "Electronic Structure in Semiconductor Nanocrystals." In V. I. Klimov, editor, "Semiconductor and Metal Nanocrystals: Synthesis and Electronic and Optical Properties," CRC Press (2003). URL http://dx.doi.org/10.1201/9780203913260.ch2.

[146] C. B. Murray, D. J. Norris, and M. G. Bawendi. "Synthesis and characterization of nearly monodisperse CdE (E = sulfur, selenium, tellurium) semiconductor nanocrystallites." Journal of the American Chemical Society **115**, 8706 (1993). URL http://dx.doi.org/10.1021/ja00072a025.

[147] C. B. Murray, C. R. Kagan, and M. G. Bawendi. "Synthesis and characterization of monodisperse nanocrystals and close-packed nanocrystal assemblies." Annual Review of Materials Science **30**, 545 (2000). URL http://dx.doi.org/10.1146/annurev.matsci.30.1.545.

[148] C. B. Murray, S. Sun, W. Gaschler, H. Doyle, T. A. Betley, and C. R. Kagan. "Colloidal synthesis of nanocrystals and nanocrystal superlattices." IBM Journal of Research and Development **45**, 47 (2001). URL http://dx.doi.org/10.1147/rd.451.0047.

[149] M. A. Hines and G. D. Scholes. "Colloidal PbS nanocrystals with size-tunable near-infrared emission: observation of post-synthesis self-narrowing of the particle size distribution." Advanced Materials **15**, 1844 (2003). URL http://dx.doi.org/10.1002/adma.200305395.

[150] L. Y. Chang, R. R. Lunt, P. R. Brown, V. Bulović, and M. G. Bawendi. "Low-temperature solution-processed solar cells based on PbS colloidal quantum dot/CdS heterojunctions." Nano Letters **13**, 994 (2013). URL http://dx.doi.org/10.1021/nl3041417.

[151] V. K. LaMer and R. H. Dinegar. "Theory, production and mechanism of formation of monodispersed hydrosols." Journal of the American Chemical Society **72**, 4847 (1950). URL http://dx.doi.org/10.1021/ja01167a001.

[152] Y. De Smet, L. Deriemaeker, and R. Finsy. "A Simple Computer Simulation of Ostwald Ripening." Langmuir **13**, 6884 (1997). URL http://dx.doi.org/10.1021/la970379b.

[153] I. Moreels, B. Fritzinger, J. C. Martins, and Z. Hens. "Surface chemistry of colloidal PbSe nanocrystals." Journal of the American Chemical Society **130**, 15081 (2008). URL http://dx.doi.org/10.1021/ja803994m.

[154] J. M. Luther and J. M. Pietryga. "Stoichiometry control in quantum dots: a viable analog to impurity doping of bulk materials." ACS Nano **7**, 1845 (2013). URL http://dx.doi.org/10.1021/nn401100n.

[155] R. S. Allgaier and W. W. Scanlon. "Mobility of electrons and holes in PbS, PbSe, and PbTe between room temperature and 4.2 K." Physical Review **111**, 1029 (1958). URL http://dx.doi.org/10.1103/PhysRev.111.1029.

[156] A. Maria, P. W. Cyr, E. J. D. Klem, L. Levina, and E. H. Sargent. "Solution-processed infrared photovoltaic devices with >10% monochromatic internal quantum efficiency." Applied Physics Letters **87**, 213112 (2005). URL http://dx.doi.org/10.1063/1.2135868.

[157] L. Kim, P. O. Anikeeva, S. A. Coe-Sullivan, J. S. Steckel, M. G. Bawendi, and V. Bulović. "Contact printing of quantum dot light-emitting devices." Nano Letters **8**, 4513 (2008). URL http://dx.doi.org/10.1021/nl8025218.

[158] M. Böberl, M. V. Kovalenko, S. Gamerith, E. J. W. List, and W. Heiss. "Inkjet-printed nanocrystal photodetectors operating up to 3 μm wavelengths." Advanced Materials **19**, 3574 (2007). URL http://dx.doi.org/10.1002/adma.200700111.

[159] J. M. Luther, M. Law, Q. Song, C. L. Perkins, M. C. Beard, and A. J. Nozik. "Structural, optical, and electrical properties of self-assembled films of PbSe nanocrystals treated with 1,2-ethanedithiol." ACS Nano **2**, 271 (2008). URL http://dx.doi.org/10.1021/nn7003348.

[160] S. A. Empedocles, D. J. Norris, and M. G. Bawendi. "Photoluminescence Spectroscopy of Single CdSe Nanocrystallite Quantum Dots." Physical Review Letters **77**, 3873 (1996). URL http://dx.doi.org/10.1103/PhysRevLett.77.3873.

[161] P. Guyot-Sionnest. "Electrical Transport in Colloidal Quantum Dot Films." The Journal of Physical Chemistry Letters **3**, 1169 (2012). URL http://dx.doi.org/10.1021/jz300048y.

[162] A. Miller and E. Abrahams. "Impurity conduction at low concentrations." Physical Review **120**, 745 (1960). URL http://dx.doi.org/10.1103/PhysRev.120.745.

[163] Y. Liu, M. Gibbs, J. Puthussery, S. Gaik, R. Ihly, H. W. Hillhouse, and M. Law. "Dependence of carrier mobility on nanocrystal size and ligand length in PbSe nanocrystal solids." Nano letters **10**, 1960 (2010). URL http://dx.doi.org/10.1021/nl101284k.

[164] B. Shklovskii and A. Efros. *Electronic properties of doped semiconductors*. Springer-Verlag (1984). URL http://dx.doi.org/10.1007/978-3-662-02403-4.

[165] E. J. D. Klem, D. D. MacNeil, P. W. Cyr, L. Levina, and E. H. Sargent. "Efficient solution-processed infrared photovoltaic cells: Planarized all-inorganic bulk heterojunction devices via inter-quantum-dot bridging during growth from solution." Applied Physics Letters **90**, 183113 (2007). URL http://dx.doi.org/10.1063/1.2735674.

[166] A. G. Pattantyus-Abraham, I. J. Kramer, A. R. Barkhouse, X. Wang, G. Konstantatos, R. Debnath, L. Levina, I. Raabe, M. K. Nazeeruddin, M. Grätzel, and E. H. Sargent. "Depleted-heterojunction colloidal quantum dot solar cells." ACS Nano **4**, 3374 (2010). URL http://dx.doi.org/10.1021/nn100335g.

[167] A. T. Fafarman, W.-k. Koh, B. T. Diroll, D. K. Kim, D.-K. Ko, S. J. Oh, X. Ye, V. Doan-Nguyen, M. R. Crump, D. C. Reifsnyder, C. B. Murray, and C. R. Kagan. "Thiocyanate-capped nanocrystal colloids: vibrational reporter of surface chemistry and solution-based route to enhanced coupling in nanocrystal solids." Journal of the American Chemical Society **133**, 15753 (2011). URL http://dx.doi.org/10.1021/ja206303g.

[168] J. Tang, K. W. Kemp, S. Hoogland, K. S. Jeong, H. Liu, L. Levina, M. Furukawa, X. Wang, R. Debnath, D. Cha, K. W. Chou, A. Fischer, A. Amassian, J. B. Asbury, and E. H. Sargent. "Colloidal-quantum-dot photovoltaics using atomic-ligand passivation." Nature Materials **10**, 765 (2011). URL http://dx.doi.org/10.1038/nmat3118.

[169] J. J. Choi, C. R. Bealing, K. Bian, K. J. Hughes, W. Zhang, D.-M. Smilgies, R. G. Hennig, J. R. Engstrom, and T. Hanrath. "Controlling nanocrystal superlattice symmetry and shape-anisotropic interactions through variable ligand surface coverage." Journal of the American Chemical Society **133**, 3131 (2011). URL http://dx.doi.org/10.1021/ja110454b.

[170] D. Kim, D.-H. Kim, J.-H. Lee, and J. C. Grossman. "Impact of Stoichiometry on the Electronic Structure of PbS Quantum Dots." Physical Review Letters **110**, 196802 (2013). URL http://dx.doi.org/10.1103/PhysRevLett.110.196802.

[171] D. A. R. Barkhouse, A. G. Pattantyus-Abraham, L. Levina, and E. H. Sargent. "Thiols passivate recombination centers in colloidal quantum dots leading to enhanced photovoltaic device efficiency." ACS Nano **2**, 2356 (2008). URL http://dx.doi.org/10.1021/nn800471c.

[172] S. J. Oh, N. E. Berry, J.-H. Choi, E. A. Gaulding, T. Paik, S.-H. Hong, C. B. Murray, and C. R. Kagan. "Stoichiometric control of lead chalcogenide nanocrystal solids to enhance their electronic and optoelectronic device performance." ACS Nano **7**, 2413 (2013). URL http://dx.doi.org/10.1021/nn3057356.

[173] S. J. Oh, N. E. Berry, J.-H. Choi, E. A. Gaulding, H. Lin, T. Paik, B. T. Diroll, S. Muramoto, C. B. Murray, and C. R. Kagan. "Designing High-Performance PbS and PbSe Nanocrystal Electronic Devices through Stepwise, Post-Synthesis, Colloidal Atomic Layer Deposition." Nano Letters **14**, 1559 (2014). URL http://dx.doi.org/10.1021/nl404818z.

[174] M. Soreni-Harari, N. Yaacobi-Gross, D. Steiner, A. Aharoni, U. Banin, O. Millo, and N. Tessler. "Tuning energetic levels in nanocrystal quantum dots through surface manipulations." Nano Letters **8**, 678 (2008). URL http://dx.doi.org/10.1021/nl0732171.

[175] B. A. Timp and X.-Y. Zhu. "Electronic energy alignment at the PbSe quantum dots/ZnO($10\bar{1}0$) interface." Surface Science **604**, 1335 (2010). URL http://dx.doi.org/10.1016/j.susc.2010.04.026.

[176] A. M. Munro, B. Zacher, A. Graham, and N. R. Armstrong. "Photoemission spectroscopy of tethered CdSe nanocrystals: Shifts in ionization potential and local vacuum level as a function of nanocrystal capping ligand." ACS Applied Materials & Interfaces **2**, 863 (2010). URL http://dx.doi.org/10.1021/am900834y.

[177] D. D. W. Grinolds, P. R. Brown, D. K. Harris, V. Bulović, and M. G. Bawendi. "Quantum-Dot Size and Thin-Film Dielectric Constant: Precision Measurement

and Disparity with Simple Models." Nano Letters **15**, 21 (2015). URL http://dx.doi.org/10.1021/nl5024244.

[178] T. C. Choy. *Effective Medium Theory: Principles and Applications*. Oxford University Press, Oxford, 1 edition (1999).

[179] K. W. Johnston, A. G. Pattantyus-Abraham, J. P. Clifford, S. H. Myrskog, S. Hoogland, H. Shukla, E. J. D. Klem, L. Levina, and E. H. Sargent. "Efficient Schottky-quantum-dot photovoltaics: The roles of depletion, drift, and diffusion." Applied Physics Letters **92**, 122111 (2008). URL http://dx.doi.org/10.1063/1.2896295.

[180] K. W. Johnston, A. G. Pattantyus-Abraham, J. P. Clifford, S. H. Myrskog, D. D. MacNeil, L. Levina, and E. H. Sargent. "Schottky-quantum dot photovoltaics for efficient infrared power conversion." Applied Physics Letters **92**, 151115 (2008). URL http://dx.doi.org/10.1063/1.2912340.

[181] K. Szendrei, W. Gomulya, M. Yarema, W. Heiss, and M. A. Loi. "PbS nanocrystal solar cells with high efficiency and fill factor." Applied Physics Letters **97**, 203501 (2010). URL http://dx.doi.org/10.1063/1.3518067.

[182] H. Lee, H. C. Leventis, S.-J. Moon, P. Chen, S. Ito, S. A. Haque, T. Torres, F. Nüesch, T. Geiger, S. M. Zakeeruddin, M. Grätzel, and M. K. Nazeeruddin. "PbS and CdS Quantum Dot-Sensitized Solid-State Solar Cells: "Old Concepts, New Results"." Advanced Functional Materials **19**, 2735 (2009). URL http://dx.doi.org/10.1002/adfm.200900081.

[183] A. Kongkanand, K. Tvrdy, K. Takechi, M. Kuno, and P. V. Kamat. "Quantum dot solar cells. Tuning photoresponse through size and shape control of CdSe-TiO2 architecture." Journal of the American Chemical Society **130**, 4007 (2008). URL http://dx.doi.org/10.1021/ja0782706.

[184] S. W. Tsang, H. Fu, R. Wang, J. Lu, K. Yu, and Y. Tao. "Highly efficient cross-linked PbS nanocrystal/C_{60} hybrid heterojunction photovoltaic cells." Applied Physics Letters **95**, 183505 (2009). URL http://dx.doi.org/10.1063/1.3257729.

[185] A. C. Arango, D. C. Oertel, Y. Xu, M. G. Bawendi, and V. Bulović. "Heterojunction photovoltaics using printed colloidal quantum dots as a photosensitive layer." Nano Letters **9**, 860 (2009). URL http://dx.doi.org/10.1021/nl803760j.

[186] N. Zhao, T. P. Osedach, L.-Y. Chang, S. M. Geyer, D. Wanger, M. T. Binda, A. C. Arango, M. G. Bawendi, and V. Bulović. "Colloidal PbS quantum dot solar cells with high fill factor." ACS Nano **4**, 3743 (2010). URL http://dx.doi.org/10.1021/nn100129j.

[187] S. A. McDonald, G. Konstantatos, S. Zhang, P. W. Cyr, E. J. D. Klem, L. Levina, and E. H. Sargent. "Solution-processed PbS quantum dot infrared photodetectors and photovoltaics." Nature Materials **4**, 138 (2005). URL http://dx.doi.org/10.1038/nmat1299.

[188] S.-W. Tsang, H. Fu, J. Ouyang, Y. Zhang, K. Yu, J. Lu, and Y. Tao. "Self-organized phase segregation between inorganic nanocrystals and $PC_{61}BM$ for hybrid high-efficiency bulk heterojunction photovoltaic cells." Applied Physics Letters **96**, 243104 (2010). URL http://dx.doi.org/10.1063/1.3454923.

[189] X. Lan, O. Voznyy, A. Kiani, F. P. García de Arquer, A. S. Abbas, G.-H. Kim, M. Liu, Z. Yang, G. Walters, J. Xu, M. Yuan, Z. Ning, F. Fan, P. Kanjanaboos, I. Kramer, D. Zhitomirsky, P. Lee, A. Perelgut, S. Hoogland, and E. H. Sargent. "Passivation Using Molecular Halides Increases Quantum Dot Solar Cell Performance." Advanced Materials **28**, 299 (2015). URL http://dx.doi.org/10.1002/adma.201503657.

[190] J. J. Choi, J. Luria, B.-R. Hyun, A. C. Bartnik, L. Sun, Y.-F. Lim, J. A. Marohn, F. W. Wise, and T. Hanrath. "Photogenerated Exciton Dissociation in Highly Coupled Lead Salt Nanocrystal Assemblies." Nano letters pages 1805–1811 (2010). URL http://dx.doi.org/10.1021/nl100498e.

[191] E. Talgorn, Y. Gao, M. Aerts, L. T. Kunneman, J. M. Schins, T. J. Savenije, M. A. van Huis, H. S. J. van der Zant, A. J. Houtepen, and L. D. A. Siebbeles. "Unity quantum yield of photogenerated charges and band-like transport in quantum-dot solids." Nature Nanotechnology **6**, 733 (2011). URL http://dx.doi.org/10.1038/nnano.2011.159.

[192] M. H. Zarghami, Y. Liu, M. Gibbs, E. Gebremichael, C. Webster, and M. Law. "p-Type PbSe and PbS quantum dot solids prepared with short-chain acids and diacids." ACS Nano **4**, 2475 (2010). URL http://dx.doi.org/10.1021/nn100339b.

[193] J. Pan, M. Gloeckler, and J. R. Sites. "Hole current impedance and electron current enhancement by back-contact barriers in CdTe thin film solar cells." Journal of Applied Physics **100**, 124505 (2006). URL http://dx.doi.org/10.1063/1.2400799.

[194] M. Kröger, S. Hamwi, J. Meyer, T. Riedl, W. Kowalsky, and A. Kahn. "Role of the deep-lying electronic states of MoO_3 in the enhancement of hole-injection in organic thin films." Applied Physics Letters **95**, 123301 (2009). URL http://dx.doi.org/10.1063/1.3231928.

[195] V. Shrotriya, G. Li, Y. Yao, C.-W. Chu, and Y. Yang. "Transition metal oxides as the buffer layer for polymer photovoltaic cells." Applied Physics Letters **88**, 073508 (2006). URL http://dx.doi.org/10.1063/1.2174093.

[196] D. Y. Kim, J. Subbiah, G. Sarasqueta, F. So, H. Ding, and Y. Gao. "The effect of molybdenum oxide interlayer on organic photovoltaic cells." Applied Physics Letters **95**, 093304 (2009). URL http://dx.doi.org/10.1063/1.3220064.

[197] N. Li, B. E. Lassiter, R. R. Lunt, G. Wei, and S. R. Forrest. "Open circuit voltage enhancement due to reduced dark current in small molecule photovoltaic

cells." Applied Physics Letters **94**, 023307 (2009). URL http://dx.doi.org/10.1063/1.3072807.

[198] I. Hancox, K. V. Chauhan, P. Sullivan, R. A. Hatton, A. Moshar, C. P. A. Mulcahy, and T. S. Jones. "Increased efficiency of small molecule photovoltaic cells by insertion of a MoO_3 hole-extracting layer." Energy & Environmental Science **3**, 107 (2010). URL http://dx.doi.org/10.1039/b915764f.

[199] C. Tao, S. Ruan, X. Zhang, G. Xie, L. Shen, X. Kong, W. Dong, C. Liu, and W. Chen. "Performance improvement of inverted polymer solar cells with different top electrodes by introducing a MoO_3 buffer layer." Applied Physics Letters **93**, 193307 (2008). URL http://dx.doi.org/10.1063/1.3026741.

[200] J. H. Lee, S. Cho, A. Roy, H.-T. Jung, and A. J. Heeger. "Enhanced diode characteristics of organic solar cells using titanium suboxide electron transport layer." Applied Physics Letters **96**, 163303 (2010). URL http://dx.doi.org/10.1063/1.3409116.

[201] Y. Sun, C. J. Takacs, S. R. Cowan, J. H. Seo, X. Gong, A. Roy, and A. J. Heeger. "Efficient, Air-Stable Bulk Heterojunction Polymer Solar Cells Using MoO_x as the Anode Interfacial Layer." Advanced Materials **23**, 2226 (2011). URL http://dx.doi.org/10.1002/adma.201100038.

[202] M. C. Gwinner, R. D. Pietro, Y. Vaynzof, K. J. Greenberg, P. K. H. Ho, R. H. Friend, and H. Sirringhaus. "Doping of Organic Semiconductors Using Molybdenum Trioxide: a Quantitative Time-Dependent Electrical and Spectroscopic Study." Advanced Functional Materials **21**, 1432 (2011). URL http://dx.doi.org/10.1002/adfm.201002696.

[203] H. Lin, W. Xia, H. N. Wu, and C. W. Tang. "CdS/CdTe solar cells with MoO_x as back contact buffers." Applied Physics Letters **97**, 123504 (2010). URL http://dx.doi.org/10.1063/1.3489414.

[204] R. H. Bube and A. L. Fahrenbruch. *Advances in Electronics and Electron Physics*. Academic, New York (1981).

[205] D. J. Milliron, I. G. Hill, C. Shen, A. Kahn, and J. Schwartz. "Surface oxidation activates indium tin oxide for hole injection." Journal of Applied Physics **87**, 572 (2000). URL http://dx.doi.org/10.1063/1.371901.

[206] D. A. R. Barkhouse, I. J. Kramer, X. Wang, and E. H. Sargent. "Dead zones in colloidal quantum dot photovoltaics: evidence and implications." Optics Express **18**, A451 (2010). URL http://www.ncbi.nlm.nih.gov/pubmed/21165075.

[207] J. Gao, C. L. Perkins, J. M. Luther, M. C. Hanna, H.-Y. Chen, O. E. Semonin, A. J. Nozik, R. J. Ellingson, and M. C. Beard. "n-Type transition metal oxide as a hole extraction layer in PbS quantum dot solar cells." Nano Letters **11**, 3263 (2011). URL http://dx.doi.org/10.1021/nl2015729.

[208] H. B. Michaelson. "The work function of the elements and its periodicity." Journal of Applied Physics **48**, 4729 (1977). URL http://dx.doi.org/10.1063/1.323539.

[209] X. Qi, N. Li, and S. R. Forrest. "Analysis of metal-oxide-based charge generation layers used in stacked organic light-emitting diodes." Journal of Applied Physics **107**, 014514 (2010). URL http://dx.doi.org/10.1063/1.3275050.

[210] Irfan, H. Ding, Y. Gao, C. Small, D. Y. Kim, J. Subbiah, and F. So. "Energy level evolution of air and oxygen exposed molybdenum trioxide films." Applied Physics Letters **96**, 243307 (2010). URL http://dx.doi.org/10.1063/1.3454779.

[211] J. Meyer, A. Shu, M. Kröger, and A. Kahn. "Effect of contamination on the electronic structure and hole-injection properties of MoO_3/organic semiconductor interfaces." Applied Physics Letters **96**, 133308 (2010). URL http://dx.doi.org/10.1063/1.3374333.

[212] J. Nelson, J. Kirkpatrick, and P. Ravirajan. "Factors limiting the efficiency of molecular photovoltaic devices." Physical Review B **69**, 035337 (2004). URL http://dx.doi.org/10.1103/PhysRevB.69.035337.

[213] F. Pfisterer. "The wet-topotaxial process of junction formation and surface treatments of Cu_2S-CdS thin-film solar cells." Thin Solid Films **431-432**, 470 (2003). URL http://dx.doi.org/10.1016/S0040-6090(03)00166-4.

[214] J. Poortmans and V. Arkhipov. *Thin Film Solar Cells Fabrication, Characterization and Applications*. John Wiley & Sons, Ltd, West Sussex, England (2006).

[215] S. M. Sze and K. K. Ng. *Physics of Semiconductor Devices*. John Wiley & Sons, Inc., Hoboken, N.J., 3 edition (2007).

[216] G. G. Malliaras, J. R. Salem, P. J. Brock, and J. C. Scott. "Photovoltaic measurement of the built-in potential in organic light emitting diodes and photodiodes." Journal of Applied Physics **84**, 1583 (1998). URL http://dx.doi.org/10.1063/1.368227.

[217] J. Tang, L. Brzozowski, D. A. R. Barkhouse, X. Wang, R. Debnath, R. Wolowiec, E. Palmiano, L. Levina, A. G. Pattantyus-Abraham, D. Jamakosmanovic, and E. H. Sargent. "Quantum dot photovoltaics in the extreme quantum confinement regime: the surface-chemical origins of exceptional air- and light-stability." ACS Nano **4**, 869 (2010). URL http://dx.doi.org/10.1021/nn901564q.

[218] R. Schaller and V. Klimov. "High Efficiency Carrier Multiplication in PbSe Nanocrystals: Implications for Solar Energy Conversion." Physical Review Letters **92**, 1 (2004). URL http://dx.doi.org/10.1103/PhysRevLett.92.186601.

[219] R. J. Ellingson, M. C. Beard, J. C. Johnson, P. Yu, O. I. Micic, A. J. Nozik, A. Shabaev, and A. L. Efros. "Highly efficient multiple exciton generation in

colloidal PbSe and PbS quantum dots." Nano letters **5**, 865 (2005). URL http://dx.doi.org/10.1021/nl0502672.

[220] O. E. Semonin, J. M. Luther, S. Choi, H.-Y. Chen, J. Gao, A. J. Nozik, and M. C. Beard. "Peak external photocurrent quantum efficiency exceeding 100% via MEG in a quantum dot solar cell." Science **334**, 1530 (2011). URL http://dx.doi.org/10.1126/science.1209845.

[221] D. N. Congreve, J. Lee, N. J. Thompson, E. Hontz, S. R. Yost, P. D. Reusswig, M. E. Bahlke, S. Reineke, T. Van Voorhis, and M. A. Baldo. "External Quantum Efficiency Above 100% in a Singlet-Exciton-Fission-Based Organic Photovoltaic Cell." Science **340**, 334 (2013). URL http://dx.doi.org/10.1126/science.1232994.

[222] W. A. Tisdale, K. J. Williams, B. A. Timp, D. J. Norris, E. S. Aydil, and X.-Y. Zhu. "Hot-electron transfer from semiconductor nanocrystals." Science **328**, 1543 (2010). URL http://dx.doi.org/10.1126/science.1185509.

[223] A. Luque and A. Martí. "Increasing the Efficiency of Ideal Solar Cells by Photon Induced Transitions at Intermediate Levels." Physical Review Letters **78**, 5014 (1997). URL http://dx.doi.org/10.1103/PhysRevLett.78.5014.

[224] R. E. Merrifield, P. Avakian, and R. P. Groff. "Fission of singlet excitons into pairs of triplet excitons in tetracene crystals." Chemical Physics Letters **3**, 155 (1969). URL http://dx.doi.org/10.1016/0009-2614(69)80122-3.

[225] B. Ehrler, B. J. Walker, M. L. Böhm, M. W. B. Wilson, Y. Vaynzof, R. H. Friend, and N. C. Greenham. "In situ measurement of exciton energy in hybrid singlet-fission solar cells." Nature Communications **3**, 1019 (2012). URL http://dx.doi.org/10.1038/ncomms2012.

[226] B. Ehrler, M. W. B. Wilson, A. Rao, R. H. Friend, and N. C. Greenham. "Singlet exciton fission-sensitized infrared quantum dot solar cells." Nano Letters **12**, 1053 (2012). URL http://dx.doi.org/10.1021/nl204297u.

[227] J. Y. Kim, K. Lee, N. E. Coates, D. Moses, T.-Q. Nguyen, M. Dante, and A. J. Heeger. "Efficient tandem polymer solar cells fabricated by all-solution processing." Science **317**, 222 (2007). URL http://dx.doi.org/10.1126/science.1141711.

[228] J. J. Choi, W. N. Wenger, R. S. Hoffman, Y.-F. Lim, J. Luria, J. Jasieniak, J. A. Marohn, and T. Hanrath. "Solution-Processed Nanocrystal Quantum Dot Tandem Solar Cells." Advanced Materials **23**, 3144 (2011). URL http://dx.doi.org/10.1002/adma.201100723.

[229] X. Wang, G. I. Koleilat, J. Tang, H. Liu, I. J. Kramer, R. Debnath, L. Brzozowski, D. A. R. Barkhouse, L. Levina, S. Hoogland, and E. H. Sargent. "Tandem colloidal quantum dot solar cells employing a graded recombination layer." Nature Photonics **5**, 480 (2011). URL http://dx.doi.org/10.1038/nphoton.2011.123.

[230] J. You, L. Dou, K. Yoshimura, T. Kato, K. Ohya, T. Moriarty, K. Emery, C.-C. Chen, J. Gao, G. Li, and Y. Yang. "A polymer tandem solar cell with 10.6% power conversion efficiency." Nature communications **4**, 1446 (2013). URL http://dx.doi.org/10.1038/ncomms2411.

[231] X. Che, X. Xiao, J. D. Zimmerman, D. Fan, and S. R. Forrest. "High-efficiency, vacuum-deposited, small-molecule organic tandem and triple-junction photovoltaic cells." Advanced Energy Materials **4**, 1400568 (2014). URL http://dx.doi.org/10.1002/aenm.201400568.

[232] C. D. Bailie, M. G. Christoforo, J. P. Mailoa, A. R. Bowring, E. L. Unger, W. H. Nguyen, J. Burschka, N. Pellet, J. Z. Lee, M. Grätzel, R. Noufi, T. Buonassisi, A. Salleo, and M. D. McGehee. "Semi-transparent perovskite solar cells for tandems with silicon and CIGS." Energy & Environmental Science **8**, 956 (2014). URL http://dx.doi.org/10.1039/C4EE03322A.

[233] J. P. Mailoa, C. D. Bailie, E. C. Johlin, E. T. Hoke, A. J. Akey, W. H. Nguyen, M. D. McGehee, and T. Buonassisi. "A 2-terminal perovskite/silicon multijunction solar cell enabled by a silicon tunnel junction." Applied Physics Letters **106**, 121105 (2015). URL http://dx.doi.org/10.1063/1.4914179.

[234] M. C. Beard, K. P. Knutsen, P. Yu, J. M. Luther, Q. Song, W. K. Metzger, R. J. Ellingson, and A. J. Nozik. "Multiple exciton generation in colloidal silicon nanocrystals." Nano letters **7**, 2506 (2007). URL http://dx.doi.org/10.1021/nl071486l.

[235] M. C. Beard, A. G. Midgett, M. C. Hanna, J. M. Luther, B. K. Hughes, and A. J. Nozik. "Comparing Multiple Exciton Generation in Quantum Dots To Impact Ionization in Bulk Semiconductors: Implications for Enhancement of Solar Energy Conversion." Nano Letters **10**, 3019 (2010). URL http://dx.doi.org/10.1021/nl101490z.

[236] B. L. Wehrenberg, C. Wang, and P. Guyot-Sionnest. "Interband and Intraband Optical Studies of PbSe Colloidal Quantum Dots." The Journal of Physical Chemistry B **106**, 10634 (2002). URL http://dx.doi.org/10.1021/jp021187e.

[237] P. Guyot-Sionnest, M. Shim, and C. Wang. "Intraband Spectroscopy and Dynamics of Colloidal Semiconductor Quantum Dots." In V. I. Klimov, editor, "Semiconductor and Metal Nanocrystals: Synthesis and Electronic and Optical Properties," pages 133–145. CRC Press (2003). URL http://dx.doi.org/10.1201/9781420079272-c4.

[238] A. J. Nozik, M. C. Beard, J. M. Luther, M. Law, R. J. Ellingson, and J. C. Johnson. "Semiconductor quantum dots and quantum dot arrays and applications of multiple exciton generation to third-generation photovoltaic solar cells." Chemical reviews **110**, 6873 (2010). URL http://dx.doi.org/10.1021/cr900289f.

[239] D. Bozyigit, N. Yazdani, M. Yarema, O. Yarema, W. M. M. Lin, S. Volk, K. Vuttivorakulchai, M. Luisier, F. Juranyi, and V. Wood. "Soft surfaces of nanomaterials enable strong phonon interactions." Nature **531**, 618 (2016). URL http://dx.doi.org/10.1038/nature16977.

[240] G. D. Scholes and G. Rumbles. "Excitons in nanoscale systems." Nature Materials **5**, 683 (2006). URL http://dx.doi.org/10.1038/nmat1710.

[241] H. Rademaker, A. J. Hoff, R. Van Grondelle, and L. N. Duysens. "Carotenoid triplet yields in normal and deuterated Rhodospirillum rubrum." Biochimica et Biophysica Acta (BBA) - Bioenergetics **592**, 240 (1980). URL http://dx.doi.org/10.1016/0005-2728(80)90185-1.

[242] C. C. Gradinaru, J. T. Kennis, E. Papagiannakis, I. H. van Stokkum, R. J. Cogdell, G. R. Fleming, R. A. Niederman, and R. van Grondelle. "An unusual pathway of excitation energy deactivation in carotenoids: Singlet-to-triplet conversion on an ultrafast timescale in a photosynthetic antenna." Proceedings of the National Academy of Sciences of the United States of America **98**, 2364 (2001). URL http://dx.doi.org/10.1073/pnas.051501298.

[243] G. Lanzani, S. Stagira, G. Cerullo, S. D. Silvestri, and D. Comoretto. "Triplet exciton generation and decay in a red polydiacetylene studied by femtosecond spectroscopy." Chemical Physics Letters **313**, 525 (1999). URL http://dx.doi.org/10.1016/S0009-2614(99)01104-5.

[244] M. B. Smith and J. Michl. "Singlet fission." Chemical reviews **110**, 6891 (2010). URL http://dx.doi.org/10.1021/cr1002613.

[245] S. T. Roberts, R. E. McAnally, J. N. Mastron, D. H. Webber, M. T. Whited, R. L. Brutchey, M. E. Thompson, and S. E. Bradforth. "Efficient singlet fission discovered in a disordered acene film." Journal of the American Chemical Society **134**, 6388 (2012). URL http://dx.doi.org/10.1021/ja300504t.

[246] B. J. Walker, A. J. Musser, D. Beljonne, and R. H. Friend. "Singlet exciton fission in solution." Nature Chemistry **5**, 1019 (2013). URL http://dx.doi.org/10.1038/nchem.1801.

[247] R. E. Merrifield. "Theory of Magnetic Field Effects on the Mutual Annihilation of Triplet Excitons." The Journal of Chemical Physics **48**, 4318 (1968). URL http://dx.doi.org/10.1063/1.1669777.

[248] R. C. Johnson and R. E. Merrifield. "Effects of magnetic fields on the mutual annihilation of triplet excitons in anthracene crystals." Physical Review B **1**, 896 (1970). URL http://dx.doi.org/10.1103/PhysRevB.1.896.

[249] A. Suna. "Kinematics of exciton-exciton annihilation in molecular crystals." Physical Review B **1**, 1716 (1970). URL http://dx.doi.org/10.1103/PhysRevB.1.1716.

[250] W.-L. Chan, M. Ligges, A. Jailaubekov, L. Kaake, L. Miaja-Avila, and X.-Y. Zhu. "Observing the multiexciton state in singlet fission and ensuing ultrafast multielectron transfer." Science **334**, 1541 (2011). URL http://dx.doi.org/10.1126/science.1213986.

[251] A. Rao, M. W. B. Wilson, J. M. Hodgkiss, S. Albert-Seifried, H. Bässler, and R. H. Friend. "Exciton fission and charge generation via triplet ecitons in pentacene/C_{60} bilayers." Journal of the American Chemical Society **132**, 12698 (2010). URL http://dx.doi.org/10.1021/ja1042462.

[252] M. W. B. Wilson, A. Rao, J. Clark, R. S. S. Kumar, D. Brida, G. Cerullo, and R. H. Friend. "Ultrafast dynamics of exciton fission in polycrystalline pentacene." Journal of the American Chemical Society **133**, 11830 (2011). URL http://dx.doi.org/10.1021/ja201688h.

[253] M. C. Beard, J. M. Luther, O. E. Semonin, and A. J. Nozik. "Third generation photovoltaics based on multiple exciton generation in quantum confined semiconductors." Accounts of Chemical Research **46**, 1252 (2013). URL http://dx.doi.org/10.1021/ar3001958.

[254] J. Lee, P. Jadhav, and M. A. Baldo. "High efficiency organic multilayer photodetectors based on singlet exciton fission." Applied Physics Letters **95**, 033301 (2009). URL http://dx.doi.org/10.1063/1.3182787.

[255] P. J. Jadhav, A. Mohanty, J. Sussman, J. Lee, and M. A. Baldo. "Singlet Exciton Fission in Nanostructured Organic Solar Cells." Nano Letters **11**, 1495 (2011). URL http://dx.doi.org/10.1021/nl104202j.

[256] J. Lee, P. Jadhav, P. D. Reusswig, S. R. Yost, N. J. Thompson, D. N. Congreve, E. Hontz, T. Van Voorhis, and M. A. Baldo. "Singlet Exciton Fission Photovoltaics." Accounts of Chemical Research **46**, 1300 (2013). URL http://dx.doi.org/10.1021/ar300288e.

[257] S. R. Saudari and C. R. Kagan. "Electron and hole transport in ambipolar, thin film pentacene transistors." Journal of Applied Physics **117** (2015). URL http://dx.doi.org/10.1063/1.4906145.

[258] S. Chai, S.-H. Wen, J.-D. Huang, and K.-L. Han. "Density functional theory study on electron and hole transport properties of organic pentacene derivatives with electron-withdrawing substituent." J. Comput. Chem. **32**, 3218 (2011). URL http://dx.doi.org/10.1002/jcc.21904.

[259] J. Burgos, M. Pope, C. E. Swenberg, and R. R. Alfano. "Heterofission in pentacene-doped tetracene single crystals." Physica Status Solidi (b) **83**, 249 (1977). URL http://dx.doi.org/10.1002/pssb.2220830127.

[260] K. O. Lee and T. T. Gan. "Influence of substrate temperature on the optical properties of evaporated films of pentacene." Chemical Physics Letters **51**, 120 (1977). URL http://dx.doi.org/10.1016/0009-2614(77)85368-2.

[261] L. Sebastian, G. Weiser, and H. Bässler. "Charge transfer transitions in solid tetracene and pentacene studied by electroabsorption." Chemical Physics **61**, 125 (1981). URL http://dx.doi.org/10.1016/0301-0104(81)85055-0.

[262] G. M. Akselrod, P. B. Deotare, N. J. Thompson, J. Lee, W. A. Tisdale, M. A. Baldo, V. M. Menon, and V. Bulović. "Visualization of exciton transport in ordered and disordered molecular solids." Nature Communications **5**, 3646 (2014). URL http://dx.doi.org/10.1038/ncomms4646.

[263] M. Yuan, D. Zhitomirsky, V. Adinolfi, O. Voznyy, K. W. Kemp, Z. Ning, X. Lan, J. Xu, J. Y. Kim, H. Dong, and E. H. Sargent. "Doping control via molecularly engineered surface ligand coordination." Advanced Materials **25**, 5586 (2013). URL http://dx.doi.org/10.1002/adma201302802.

[264] K. Katsiev, A. H. Ip, A. Fischer, I. Tanabe, X. Zhang, A. R. Kirmani, O. Voznyy, L. R. Rollny, K. W. Chou, S. M. Thon, G. H. Carey, X. Cui, A. Amassian, P. Dowben, E. H. Sargent, and O. M. Bakr. "The complete in-gap electronic structure of colloidal quantum dot solids and its correlation with electronic transport and photovoltaic performance." Advanced Materials **26**, 937 (2014). URL http://dx.doi.org/10.1002/adma.201304166.

[265] G. I. Koleilat, L. Levina, H. Shukla, S. H. Myrskog, S. Hinds, A. G. Pattantyus-Abraham, and E. H. Sargent. "Efficient , Stable Infrared Photovoltaics Based on Solution-Cast Colloidal Quantum Dots." ACS Nano **2**, 833 (2008). URL http://dx.doi.org/10.1021/nn800093v.

[266] D. Zhitomirsky, M. Furukawa, J. Tang, P. Stadler, S. Hoogland, O. Voznyy, H. Liu, and E. H. Sargent. "N-type colloidal-quantum-dot solids for photovoltaics." Advanced Materials **24**, 6181 (2012). URL http://dx.doi.org/10.1002/adma.201202825.

[267] L.-Y. Chang, R. R. Lunt, P. R. Brown, V. Bulović, and M. G. Bawendi. "Low-temperature solution-processed solar cells based on PbS colloidal quantum dot/CdS heterojunctions." Nano Letters **13**, 994 (2013). URL http://dx.doi.org/10.1021/nl3041417.

[268] L. Brus. "Electronic wave functions in semiconductor clusters: experiment and theory." The Journal of Physical Chemistry **90**, 2555 (1986). URL http://dx.doi.org/10.1021/j100403a003.

[269] R. Dalven. "Electronic structure of PbS, PbSe, and PbTe." Solid State Physics **28**, 179 (1974). URL http://dx.doi.org/10.1016/S0081-1947(08)60203-9.

[270] Y. Zhou, C. Fuentes-Hernandez, J. Shim, J. Meyer, A. J. Giordano, H. Li, P. Winget, T. Papadopoulos, H. Cheun, J. Kim, M. Fenoll, A. Dindar, W. Haske, E. Najafabadi, T. M. Khan, H. Sojoudi, S. Barlow, S. Graham, J.-L. Brédas, S. R. Marder, A. Kahn, and B. Kippelen. "A universal method to produce

low-work function electrodes for organic electronics." Science **336**, 327 (2012). URL http://dx.doi.org/10.1126/science.1218829.

[271] K. S. Jeong, J. Tang, H. Liu, J. Kim, A. W. Schaefer, K. Kemp, L. Levina, X. Wang, S. Hoogland, R. Debnath, L. Brzozowski, E. H. Sargent, and J. B. Asbury. "Enhanced mobility-lifetime products in PbS colloidal quantum dot photovoltaics." ACS Nano **6**, 89 (2012). URL http://dx.doi.org/10.1021/nn2039164.

[272] W. Ma, S. L. Swisher, T. Ewers, J. Engel, V. E. Ferry, H. A. Atwater, and A. P. Alivisatos. "Photovoltaic Performance of Ultrasmall PbSe Quantum Dots." ACS Nano **5**, 8140 (2011). URL http://dx.doi.org/10.1021/nn202786g.

[273] N. Koch, A. Kahn, J. Ghijsen, J.-J. Pireaux, J. Schwartz, R. L. Johnson, and A. Elschner. "Conjugated organic molecules on metal versus polymer electrodes: Demonstration of a key energy level alignment mechanism." Applied Physics Letters **82**, 70 (2003). URL http://dx.doi.org/10.1063/1.1532102.

[274] S. E. Shaheen, G. E. Jabbour, M. M. Morrell, Y. Kawabe, B. Kippelen, N. Peyghambarian, M.-F. Nabor, R. Schlaf, E. A. Mash, and N. R. Armstrong. "Bright blue organic light-emitting diode with improved color purity using a LiF/Al cathode." Journal of Applied Physics **84**, 2324 (1998). URL http://dx.doi.org/10.1063/1.368299.

[275] J. Tang, X. Wang, L. Brzozowski, D. A. R. Barkhouse, R. Debnath, L. Levina, and E. H. Sargent. "Schottky quantum dot solar cells stable in air under solar illumination." Advanced Materials **22**, 1398 (2010). URL http://dx.doi.org/10.1002/adma.200903240.

[276] C. J. Brabec, S. E. Shaheen, C. Winder, N. S. Sariciftci, and P. Denk. "Effect of LiF/metal electrodes on the performance of plastic solar cells." Applied Physics Letters **80**, 1288 (2002). URL http://dx.doi.org/10.1063/1.1446988.

[277] G. Heimel, L. Romaner, E. Zojer, and J.-L. Brédas. "Toward control of the metal-organic interfacial electronic structure in molecular electronics: a first-principles study on self-assembled monolayers of pi-conjugated molecules on noble metals." Nano letters **7**, 932 (2007). URL http://dx.doi.org/10.1021/nl0629106.

[278] S. Yang, D. Prendergast, and J. B. Neaton. "Tuning semiconductor band edge energies for solar photocatalysis via surface ligand passivation." Nano Letters **12**, 383 (2012). URL http://dx.doi.org/10.1021/nl203669k.

[279] K.-S. Cho, D. V. Talapin, W. Gaschler, and C. B. Murray. "Designing PbSe nanowires and nanorings through oriented attachment of nanoparticles." Journal of the American Chemical Society **127**, 7140 (2005). URL http://dx.doi.org/10.1021/ja050107s.

[280] C. R. Bealing, W. J. Baumgardner, J. J. Choi, T. Hanrath, and R. G. Hennig. "Predicting nanocrystal shape through consideration of surface-ligand interactions." ACS Nano **6**, 2118 (2012). URL http://dx.doi.org/10.1021/nn3000466.

[281] M. Law, J. M. Luther, Q. Song, B. K. Hughes, C. L. Perkins, and A. J. Nozik. "Structural, optical, and electrical properties of PbSe nanocrystal solids treated thermally or with simple amines." Journal of the American Chemical Society **130**, 5974 (2008). URL http://dx.doi.org/10.1021/ja800040c.

[282] N. Yaacobi-Gross, N. Garphunkin, O. Solomeshch, A. Vaneski, A. S. Susha, A. L. Rogach, and N. Tessler. "Combining Ligand-Induced Quantum- Confined Stark Effect with Type II Heterojunction Bilayer Structure in CdTe and CdSe Nanocrystal-Based Solar Cells." Nano Letters **6**, 3128 (2012). URL http://dx.doi.org/10.1021/nn204910g.

[283] N. Yaacobi-Gross, M. Soreni-Harari, M. Zimin, S. Kababya, A. Schmidt, and N. Tessler. "Molecular control of quantum-dot internal electric field and its application to CdSe-based solar cells." Nature Materials **10**, 974 (2011). URL http://dx.doi.org/10.1038/nmat3133.

[284] R. W. Zehner, B. F. Parsons, R. P. Hsung, and L. R. Sita. "Tuning the Work Function of Gold with Self-Assembled Monolayers Derived from X−[C_6H_4−C≡C−]$_n$$C_6H_4$−SH ($n$ = 0, 1, 2; X = H, F, CH_3, CF_3, and OCH_3)." Langmuir **15**, 1121 (1999). URL http://dx.doi.org/10.1021/la981114f.

[285] D. M. Alloway, M. Hofmann, D. L. Smith, N. E. Gruhn, A. L. Graham, R. Colorado, V. H. Wysocki, T. R. Lee, P. A. Lee, and N. R. Armstrong. "Interface Dipoles Arising from Self-Assembled Monolayers on Gold: UV-Photoemission Studies of Alkanethiols and Partially Fluorinated Alkanethiols." The Journal of Physical Chemistry B **107**, 11690 (2003). URL http://dx.doi.org/10.1021/jp034665+.

[286] B. de Boer, A. Hadipour, M. M. Mandoc, T. van Woudenbergh, and P. W. M. Blom. "Tuning of Metal Work Functions with Self-Assembled Monolayers." Advanced Materials **17**, 621 (2005). URL http://dx.doi.org/10.1002/adma.200401216.

[287] M. T. Greiner, M. G. Helander, W.-M. Tang, Z.-B. Wang, J. Qiu, and Z.-H. Lu. "Universal energy-level alignment of molecules on metal oxides." Nature Materials **11**, 76 (2012). URL http://dx.doi.org/10.1038/nmat3159.

[288] X. Wang, G. I. Koleilat, A. Fischer, J. Tang, R. Debnath, L. Levina, and E. H. Sargent. "Enhanced open-circuit voltage in visible quantum dot photovoltaics by engineering of carrier-collecting electrodes." ACS Applied Materials & Interfaces **3**, 3792 (2011). URL http://dx.doi.org/10.1021/am201097p.

[289] J. Jean, S. Chang, P. R. Brown, J. J. Cheng, P. H. Rekemeyer, M. G. Bawendi, S. Gradečak, and V. Bulović. "ZnO nanowire arrays for enhanced photocurrent in PbS quantum dot solar cells." Advanced Materials **25**, 2790 (2013). URL http://dx.doi.org/10.1002/adma.201204192.

[290] T. P. Osedach, A. Iacchetti, R. R. Lunt, T. L. Andrew, P. R. Brown, G. M. Akselrod, and V. Bulović. "Near-infrared photodetector consisting of J-aggregating

cyanine dye and metal oxide thin films." Applied Physics Letters **101**, 113303 (2012). URL http://dx.doi.org/10.1063/1.4752434.

[291] D. K. Ko, P. R. Brown, M. G. Bawendi, and V. Bulović. "p-i-n heterojunction solar cells with a colloidal quantum-dot absorber layer." Advanced Materials **26**, 4845 (2014). URL http://dx.doi.org/10.1002/adma.201401250.

[292] C.-H. M. Chuang, A. Maurano, R. E. Brandt, G. W. Hwang, J. Jean, T. Buonassisi, V. Bulović, and M. G. Bawendi. "Open-circuit voltage deficit, radiative sub-bandgap states, and prospects in quantum dot solar cells." Nano Letters **15**, 3286 (2015). URL http://dx.doi.org/10.1021/acs.nanolett.5b00513.

[293] D. T. Moore, B. Gaskey, A. Robbins, and T. Hanrath. "A detailed balance analysis of conversion efficiencies limits for nanocrystal solar cells—Relating the shape of the excitonic peak to conversion efficiencies." Journal of Applied Physics **115**, 054313 (2014). URL http://dx.doi.org/10.1063/1.4864066.

[294] J. J. Peterson and T. D. Krauss. "Fluorescence spectroscopy of single lead sulfide quantum dots." Nano Letters **6**, 510 (2006). URL http://dx.doi.org/10.1021/nl0525756.

[295] P. T. Erslev, H.-Y. Chen, J. Gao, M. C. Beard, A. J. Frank, J. van de Lagemaat, J. C. Johnson, and J. M. Luther. "Sharp exponential band tails in highly disordered lead sulfide quantum dot arrays." Physical Review B **86**, 155313 (2012). URL http://dx.doi.org/10.1103/PhysRevB.86.155313.

[296] S. De Wolf, J. Holovsky, S. J. Moon, P. Löper, B. Niesen, M. Ledinsky, F. J. Haug, J. H. Yum, and C. Ballif. "Organometallic halide perovskites: Sharp optical absorption edge and its relation to photovoltaic performance." Journal of Physical Chemistry Letters **5**, 1035 (2014). URL http://dx.doi.org/10.1021/jz500279b.

[297] J. Burschka, N. Pellet, S.-J. Moon, R. Humphry-Baker, P. Gao, M. K. Nazeeruddin, and M. Grätzel. "Sequential deposition as a route to high-performance perovskite-sensitized solar cells." Nature **499**, 316 (2013). URL http://dx.doi.org/10.1038/nature12340.

[298] M. M. Lee, J. Teuscher, T. Miyasaka, T. N. Murakami, and H. J. Snaith. "Efficient hybrid solar cells based on meso-superstructured organometal halide perovskites." Science **338**, 643 (2013). URL http://dx.doi.org/10.1126/science.1228604.

[299] M. Liu, M. B. Johnston, and H. J. Snaith. "Efficient planar heterojunction perovskite solar cells by vapour deposition." Nature **501**, 395 (2013). URL http://dx.doi.org/10.1038/nature12509.

[300] A. Kojima, K. Teshima, Y. Shirai, and T. Miyasaka. "Organometal halide perovskites as visible-light sensitizers for photovoltaic cells." Journal of the American Chemical Society **131**, 6050 (2009). URL http://dx.doi.org/10.1021/ja809598r.

[301] H.-S. Kim, C.-R. Lee, J.-H. Im, K.-B. Lee, T. Moehl, A. Marchioro, S.-J. Moon, R. Humphry-Baker, J.-H. Yum, J. E. Moser, M. Grätzel, and N.-G. Park. "Lead Iodide Perovskite Sensitized All-Solid-State Submicron Thin Film Mesoscopic Solar Cell with Efficiency Exceeding 9%." Scientific Reports **2**, 591 (2012). URL http://dx.doi.org/10.1038/srep00591.

[302] M. T. Klug, A. Osherov, S. D. Stranks, P. R. Brown, X. Dang, V. Bulović, and A. M. Belcher. "Influence of secondary metal species on material properties and photovoltaic performance of methylammonium mixed-metal triiodide perovskites." submitted (2016).

[303] T. P. Osedach, N. Zhao, T. L. Andrew, P. R. Brown, D. D. Wanger, D. B. Strasfeld, L.-Y. Chang, M. G. Bawendi, and V. Bulović. "Bias-stress effect in 1,2-ethanedithiol-treated PbS quantum dot field-effect transistors." ACS Nano **6**, 3121 (2012). URL http://dx.doi.org/10.1021/nn3008788.

[304] A. H. Ip, S. M. Thon, S. Hoogland, O. Voznyy, D. Zhitomirsky, R. Debnath, L. Levina, L. R. Rollny, G. H. Carey, A. Fischer, K. W. Kemp, I. J. Kramer, Z. Ning, A. J. Labelle, K. W. Chou, A. Amassian, and E. H. Sargent. "Hybrid passivated colloidal quantum dot solids." Nature Nanotechnology **7**, 577 (2012). URL http://dx.doi.org/10.1038/nnano.2012.127.